Dynamic Response of Cohesive-frictional Soils Under Thermo-Controlled Constant Water Content Cyclic Simple Shear Testing

by

Daniel R. C. Green

Presented to the Faculty of the Graduate School of

The University of Texas at Arlington in Partial Fulfillment

of the Requirements

for the Degree of

Doctor of Philosophy in Civil Engineering

The University of Texas at Arlington

August 2023

Acknowledgements

I would like to express my deepest gratitude to my research advisor, Dr. Laureano R. Hoyos, for his guidance throughout this process. Additionally, I would like to recognize my dissertation committee members, Dr. Xinbao Yu, Dr. Sahadat Hossain, and Dr. Nur Yazdani, who generously provided their time, knowledge, and expertise. I am extremely grateful for the financial assistance provided by the University of Texas at Arlington Civil Engineering Department, who gave me the opportunity to work as a GTA while conducting my research.

I am grateful to VJ Tech for providing the testing equipment and training without which this research would not have been possible. Specifically, I would like to recognize Mr. Adrian Rose and Dr. Vasileios Matziaris for their help during the training and thermo-modification processes. I would also like to extend my sincere thanks to Mr. Scott Eichmann, in the UTA Mechanical and Aerospace Engineering shop, for fabricating the many parts I needed for device modification and testing.

Lastly, this endeavor would not have been possible without my parents. Their unending support allowed me to pursue my dreams and I will forever be grateful.

Abstract

Dynamic Response of Cohesive-Frictional Soils Under Thermo-Controlled Constant Water Content Cyclic Simple Shear Testing

Daniel R. C. Green

The University of Texas at Arlington, 2023

Supervising Professor: Dr. Laureano R. Hoyos

A considerable portion of the emerging geothermal infrastructure in the country is located in earthquake prone areas while being supported and/or surrounded by soil deposits located well above the groundwater table. Geotechnical earthquake research in the country, however, continues to be mostly focused on soil response under saturated conditions, especially soil liquefaction phenomena, while most of the work on dynamic response of compacted soils has not taken thermal conditioning of pore-fluids into account as critical environmental factors. To date, there is hardly any comprehensive study at the laboratory scale that has focused on a thorough assessment of the dynamic properties of compacted soils, particularly shear modulus and material damping ratio of cohesive-frictional soils, for a relatively large range of cyclic shear strain amplitudes (0.001% to 10.0% shear strain amplitudes) under controlled moisture content and simultaneous thermal conditioning of pore-fluids.

In the present study, an existing Cyclic Simple Shear (CSS) apparatus has been upgraded to investigate the dynamic response of three distinct types of cohesive-frictional soils, namely, CL (w=9.0%), CL (w=13.6%), CL (w=17.0%), ML (w=14.8%), SC (w=10.0%), particularly in terms of shear modulus and damping ratio, under controlled moisture, confinement, and thermal conditioning of the pore-fluids, from 23°C (room temperature) to 60°C. A digital convection heater, featuring two heating elements and a thermocouple, was adapted to the main cell of the CSS apparatus for measurement and control of thermal gradients in the test samples. However, because thermocouple probes cannot be inserted into the sample during testing, for risk of disturbing the compacted soil and puncturing the latex membrane, a thorough thermo-calibration of the upgraded CSS chamber was necessary prior to thermo-controlled testing to ensure proper heating and heat distribution within the soil samples.

After thermo-calibration, a comprehensive testing plan was followed to investigate the effects of increased temperatures on shear modulus and damping ratio of all three test soils for a wide array of shear strain amplitudes (from 0.001% to 10.0%). Experimental variables and procedures are described in detail. Experimental results are presented and analyzed via the Bilinear and Ramberg-Osgood Models. Results and analysis suggest that increased temperatures caused a decrease in peak shear stress under a fixed shear strain amplitude, suggesting a decrease in shear modulus and an increase in material damping ratio.

Table of Contents

List of Figures

List of Tables

Chapter 1: Introduction

1.1 - Background and Scope

Geothermal power is a continually developing trend in green energy that has been growing rapidly in the United States and in countries around the world since the late 1970s. Globally, geothermal capacity of existing geothermal power plants totaled 11,700 megawatts as of 2013, with an additional 11,700 megawatts in additional capacity either in early stages of development or currently under construction in 70 countries around the world. Existing plants produced approximately 68 billion kilowatt-hours of electricity, enough to meet the demands of nearly 6 million homes in the United States (Geothermal Energy Association, 2013). Currently, 3386 megawatts of the global geothermal power infrastructure reside in the United States, making it the global leader in geothermal capacity. Eighty percent of the United States geothermal capacity is located in California where 40 power plants provide close to 7 percent of the state's electricity (Geothermal Energy Association, 2013).

High underground temperatures are a necessity for geothermal power. The areas with the highest underground temperatures are located in regions with active or young volcanoes where tectonic plate boundaries and thin layers in the earth's crust allow for harvesting of geothermal reservoirs. These favorable locations and identified hydrothermal sites can be seen in Figure 1.1. These regions with the highest potential for geothermal power are seismically active. Earthquakes cause movement and stress in the rock which allows naturally heated water to circulate more freely, sometimes leading to geysers and natural hot springs. Geothermal power plants tap into these geothermal reservoirs drawing hot water or steam from the earth and convert the heated fluid into electricity for commercial use.

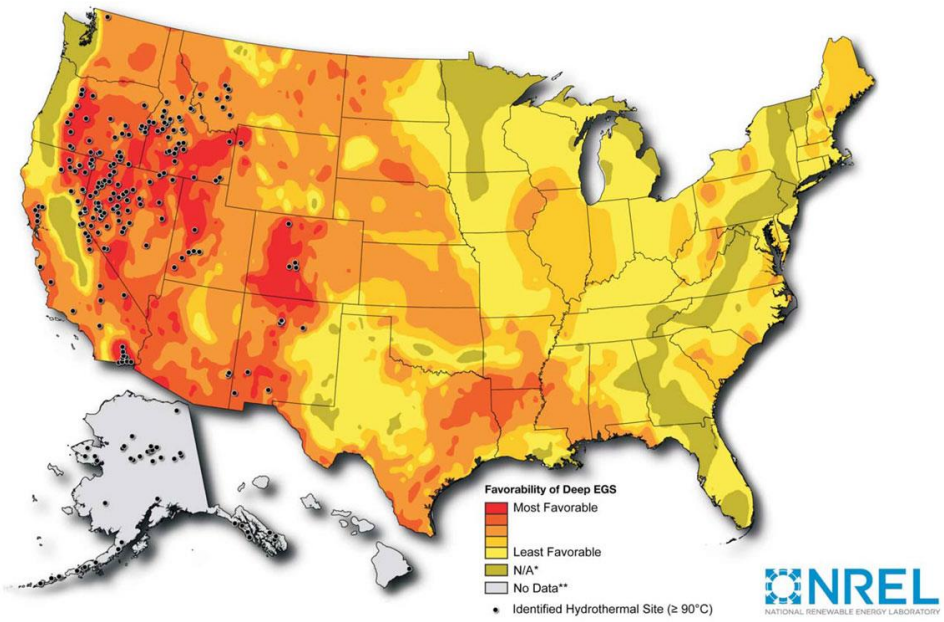

Figure 1.1: U.S. geothermal resources. (Fichman, U.S. Energy Information Administration, Annual Energy Review, 2011)

While geothermal energy has the potential for electrical power generation on a large scale, it also is being used in heating and cooling systems for homes and buildings through the use of ground source heat pumps. Geothermal power generation requires high underground temperatures; however, geothermal heating and cooling systems utilize the constant temperature zone located anywhere from five feet to a few hundred feet below the ground where the temperature remains about 55°F regardless of seasonal changes. In residential areas or small buildings these geothermal systems can be installed at relatively shallow depths of five feet in a horizontal configuration or at deeper depths of a few hundred feet for vertical configurations.

For larger structures, geothermal energy is harvested primarily through energy piles, heat exchanger piles, or geothermal piles. The idea of geothermal piles is the same as the ground source heating and cooling previously stated. However, instead of having a separate pipe system underground, the heat exchanger pipes are located in the foundation itself by adding one or more loops of plastic pipes down the length of the pile inside of the rebar reinforcement cage. A common geothermal pile schematic is shown in Figure 1.2. The circulation loops located in the structural support piles are connected to a ground source heat pump that provides heating and cooling to the building. The ground source heat pump functions the same way as the more common air source heat pump, however it has the advantage of the ground being warmer than the air in the winter (therefore able to provide more heat) and cooler than the air in the summer (therefore able to absorb more heat). These dual-purpose piles provide an efficient and renewable source of energy potential with great environmental and economic benefits.

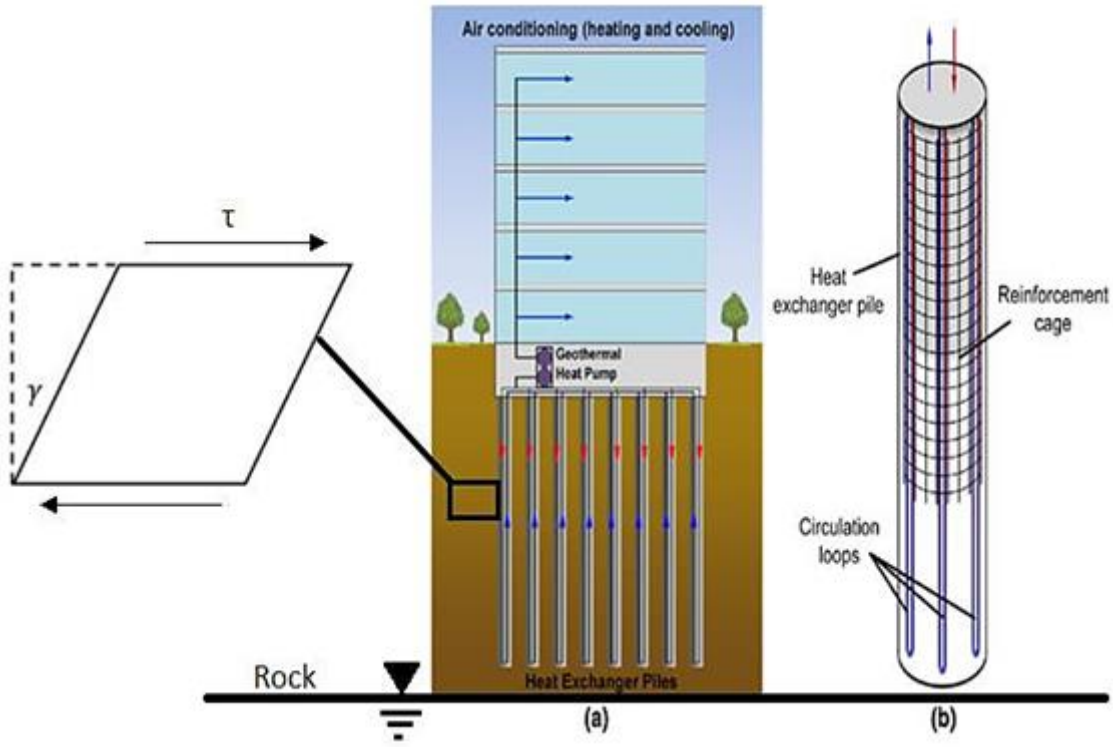

Figure 1.2: a) Building supported by heat exchanger piles as the soil is subject to shear-wave induced cyclic stresses, b) typical configuration of a heat exchanger pile with integrated circulation loops. (Olgun et al., 2015)

Even though geothermal energy is more environmentally friendly and economical than traditional energy generation methods, it is not without its challenges. The addition of cyclic thermal loading applications to foundation systems and soil requires further investigation to fully understand the effects of heat on soil properties. While the heat induced effects of thermo-active structures like geothermal power plants and geothermal piles on soil is a primary concern, increased surface soil temperatures caused by solar radiation or increased subsurface soil temperatures caused by underground compressed gas storage also have potential to compromise critical geotechnical infrastructure. Pavements, slopes, and geomembranes are all subjected to significant temperature increases in the form of solar radiation. Underground compressed gas storage causes an increase in temperature that can be transferred to the surrounding soil structures. As gas is compressed the pressure increases, the increase in pressure causes the internal energy of the gas to increase, which must be transferred to the surrounding environment potentially causing an increase in soil temperature (Cooper et al., 2011). While earthquakes remain a chief concern, traffic, vibratory machinery, and rotary machinery such as windmills are a few additional examples of potential dynamic loading sources in soil.

While numerous thermo-controlled soil tests have been performed and the results are well documented, the majority of these tests are focused on how temperature influences the strength properties and preconsolidation pressure of soil using thermo-controlled triaxial and thermo-controlled oedometer experiments. Cekerevac and Laloui studied the effects of temperatures ranging from 22 to 90°C on the mechanical behavior of a saturated clay (Cekerevac and Laloui, 2003). To complete their work, they developed and calibrated a new thermo-controlled triaxial device specifically focused on the thermo-mechanical testing of saturated soil (Cekerevac and Laloui, 2005). Tang et al. developed an isotropic cell to study the thermo-mechanical behavior of unsaturated soils (Tang et al., 2007). Uchaipichat and Khalili modified a triaxial apparatus for testing of unsaturated soils at elevated temperatures from 20 to 60°C (Uchaipichat and Khalili, 2009). Alsherif and McCartney used drained triaxial compression tests to study the effects of temperature and suction on the hardening mechanisms of soil under different testing paths (Alsherif and McCartney, 2015).

Stiffness properties of soil, such as damping ratio and shear modulus, have also been well documented through the use of cyclic triaxial, resonant column, and cyclic simple shear testing. Ashmawy et al. thoroughly reviews material damping ratio and resonant column testing (Ashmawy et al., 1995). Lanzo and Vucetic established trends between plasticity index and damping ratio of soils (Lanzo and Vucetic, 1999). Vucetic and Dobry studied the effects of soil plasticity on cyclic response and stiffness properties to potentially aid in seismic microzonation of earthquake prone areas (Vucetic and Dobry, 1991). Suction controlled dynamic soil testing has also been thorough. Suprunenko used a suction controlled cyclic triaxial device to study strain-dependent dynamic shear modulus of unsaturated sand (Suprunenko, 2015). Vassallo et al. used a suction controlled resonant column apparatus to investigate the effect of suction history on small strain stiffness of a clayey silt (Vassallo et al., 2007). Le and Ghayoomi used a suction controlled cyclic simple shear apparatus to measure the dynamic response of unsaturated soils (Le and Ghayoomi, 2016). Despite the advances mentioned, there is a distinct lack of information on the stiffness properties of soil under thermo-controlled cyclic loading conditions. However, as renewable energy like geothermal and wind becomes more prevalent, surface temperatures continue to increase, and geothermal piles become more common the demand for this information will continue to grow.

For the purposes of this research, data will be gathered using a thermo-controlled cyclic simple shear device from VJ Tech, a civil engineering focused materials testing equipment manufacturer located in the

United Kingdom. The data will be used in conjunction with data previously gathered using a thermo-controlled resonant column device in order to better understand the effects of increased temperature on stiffness for strains ranging from very small (γ < 0.0001%) to large (γ > 1.0%). There are two main advantages in using a cyclic simple shear test. Cyclic simple shear devices provide a more accurate representation of field conditions since the soil samples can be confined in the K_0 state, and they allow for tests to be conducted over a wide range of strain amplitudes. Figure 1.3 shows a standard normalized shear modulus degradation curve and the typical range of shear strain values which are valid for resonant column (γ < 0.005%) and cyclic simple shear tests (γ > 0.005%).

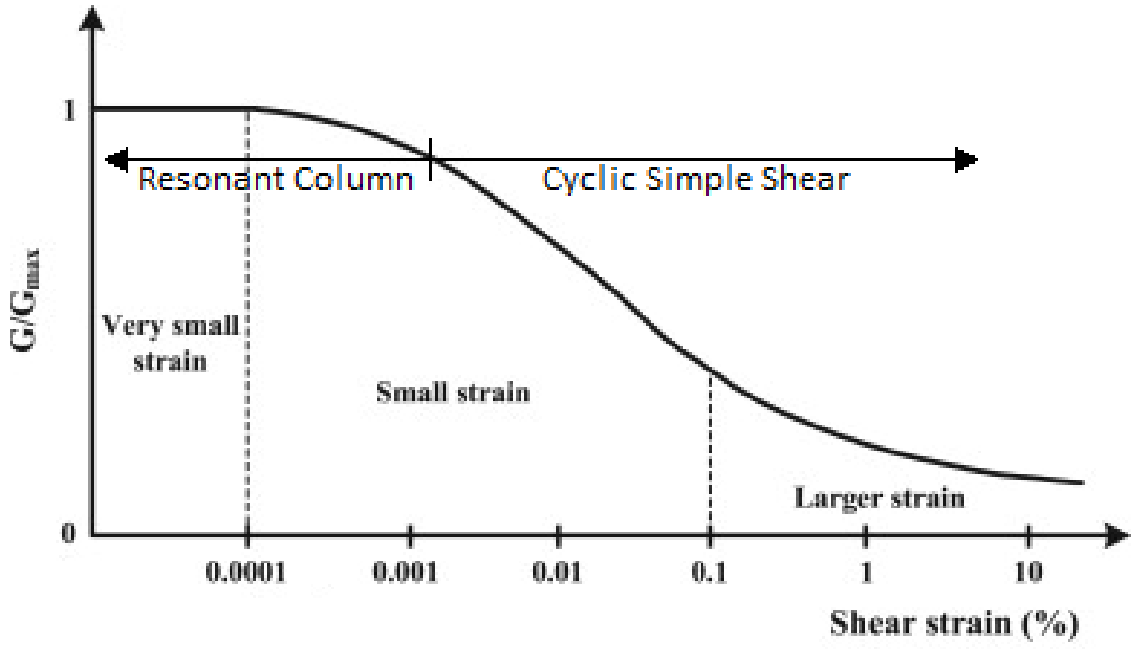

Figure 1.3: Range and applicability of laboratory tests as a function of shear strain amplitude.

1.2 - Objectives

The main objective of the present research work is to upgrade an existing cyclic simple shear device for thermo-controlled testing and then investigate the effects of temperature on shear modulus and damping for three soil types. The three soil types being studied are low plasticity clay, CL, low plasticity silt, ML, and clayey sand, SC. The research will be comprehensive, encompassing a range of values for key experimental variables that act as parameters for the cyclic simple shear device. Experimental variables will consist of moisture content, confinement, temperature, frequency, and number of cycles. Shear modulus and damping ratio of the soil will be analyzed over a wide array of shear strain percentages for each variable combination with the use of the Bilinear and Ramberg-Osgood models. The cyclic simple shear data will then be used in conjunction with resonant column data to plot a complete shear modulus reduction curve with increasing shear strain amplitude. Specific tasks required to complete this study are outlined below.

- Identify the need for a better understanding of soil stiffness properties under thermo-controlled cyclic loading conditions.
- Review literature on previous thermo-controlled testing devices and studies.
- Use the new cyclic simple shear device to investigate known trends to ensure proper functionality.
- Clearly outline a comprehensive testing plan.
- Upgrade the existing device for thermo-controlled testing.
- Calibrate the upgraded cyclic simple shear device to establish heating trends.
- Conduct thermo-controlled cyclic simple shear tests following the testing plan.
- Analyze test data with the use of the Bilinear and Ramberg-Osgood models.
- Distill findings into a concise conclusion with recommendations for future testing.

1.3 - Thesis Organization

A brief summary of the chapters included in this doctoral thesis are as follows:

Chapter 2 – Literature Review: Chapter 2 restates the importance of pursuing and investigating thermo-controlled soil testing by examining growth trends in geothermal and wind energy. Previous thermo-controlled soil testing devices are examined to show different methods of thermo-control. Stiffness properties of soils, such as shear modulus and damping ratio, are discussed to provide a basis for understanding dynamic soil studies. Studies using thermo-controlled cyclic triaxial, thermo-controlled resonant column, and thermo-controlled cyclic simple shear devices are reviewed as a foundation for the experimentation conducted and discussed in this thesis. During the review of thermo-controlled dynamic soil testing systems, unmodified and suction-controlled systems are reviewed to provide a baseline understanding of specific dynamic soil tests and expected results.

Chapter 3 – Experimental Program and Variables: Chapter 3 provides basic information on soils used for thermo-controlled testing, discusses variables chosen, and outlines the process of the thermo-controlled testing program. Basic room temperature cyclic simple shear test results are presented to show functionality of the device and repeatability of results.

Chapter 4 – Thermo-Controlled Cyclic Simple Shear System: Chapter 4 covers all aspects of the thermo-controlled cyclic simple shear system including the main components of the device, sample preparation, a step-by-step assembly process, thermo-calibration, and software controls. Numerous photos are included with each of these four sections to fully detail and explain the entire thermo-controlled cyclic simple shear device and thermo-calibration process.

Chapter 5 – Experimental Results from Thermo-Controlled Cyclic Simple Shear Testing: Chapter 5 presents detailed experimental results from thermo-controlled tests pertaining to the experimental program detailed in Chapter 3. Results are presented on the basis of shear strain amplitude and temperature, with specific loading cycles highlighted to give a clear picture of the effect that increased temperature has on shear modulus. Results from all three soil types are examined and explained thoroughly.

Chapter 6 – Bilinear Modeling of Shear Modulus: Chapter 6 focuses on analysis of experimental results at larger shear strain amplitudes ($\gamma > 1.0\%$) with the use of the Bilinear model proposed by Thiers and Seed in 1968. The framework of the Bilinear model is discussed, and results are presented to show the effect of increased temperatures on the cyclic degradation of shear modulus.

Chapter 7 – Nonlinear Modeling of Shear Modulus and Damping Ratio: Chapter 7 presents the shear modulus degradation curve and material damping ratio for all three soil types. The Ramberg-Osgood model proposed by Ramberg and Osgood in 1943 is reviewed and fit to the experimental data for qualitative analysis purposes.

Chapter 8 – Conclusions and Recommendations: Chapter 8 includes a summary of the thesis and results obtained from thermo-calibration and thermo-controlled testing. Key points of data analysis are restated to highlight the most important findings from the research. Conclusions pertaining to the data obtained are stated and recommendations for improvements to methods used are given to provide guidance for future research.

Chapter 2: Literature Review

2.1 - Introduction

This chapter discusses the growing need for a better understanding of how elevated temperatures affect the dynamic and stiffness properties of soil, in particular shear modulus, G, and damping ratio, D. Advancements in thermo-mechanical testing of soils are reviewed not only to show that temperature has a significant effect on mechanical and strength properties of soil, but also to look at different heating methods used in thermo-controlled soil testing. Differences between heating methods used, mediums for heat transfer, and challenges faced are examined to provide a basis for thermo-calibration of the thermo-controlled cyclic simple shear device. Previous dynamic soil studies, suction-controlled dynamic soil studies, and thermo-controlled dynamic soil studies are presented to establish a base understanding of dynamic soil testing, with a focus on cyclic triaxial, resonant column, and cyclic simple shear soil testing.

2.2 - Growing Trends in Renewable Energy.

The Geothermal Energy Association reported in 2013 that 11,765 Megawatts (MW) of geothermal power are operating globally with 11,766 MW of additional capacity either in development or in early stages of construction across 70 countries (Geothermal Energy Association, 2013). Figure 2.1, from the 2016 Geothermal Energy Association report showed that the global market reached 13.3 Gigawatts of operating capacity as of January 2016 with 12.5 Gigawatts of additional planned capacity across 82 countries. Current installed capacity is growing at a rate of 3.5% annually, reaching a total capacity of 16 Gigawatts (GW) in 2021 (International Renewable Energy Agency, 2023). The United Nations and the International Renewable Energy Agency pledged a five-fold growth increase in geothermal capacity and two-fold growth increase in geothermal heating by 2030 compared to current levels. The Geothermal Energy Association estimates that countries around the world have only tapped into 6 to 7 percent of the total global potential for geothermal power based on current geologic knowledge and technology. The untapped resources are vast and could provide renewable energy to power grids across the globe (Geothermal Energy Association, 2016).

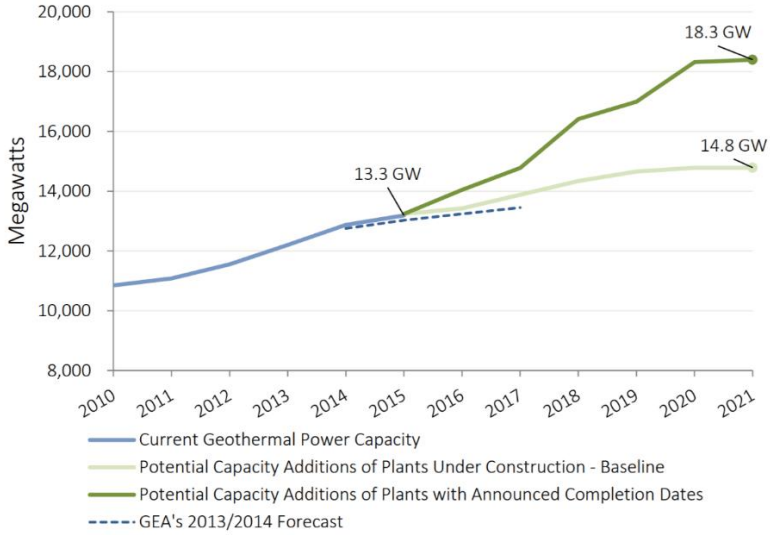

Figure 2.1: International geothermal power nameplate capacity (MW).
(Geothermal Energy Association, 2016)

The majority of current geothermal power capacity is located in the United States. Figure 2.2 shows the United States has approximately 3,386 MW of installed geothermal capacity. Furthermore, 3,250 MW of the United States current geothermal capacity are in two of the most seismically active states. California contains over 80 percent of the current geothermal capacity, with an additional 15 percent located in Nevada. California will continue to be a national leader in geothermal power due to their 2005 Energy Action Plan, which proposes a goal of 33 percent of electricity generation from renewable sources by 2020. The plan was codified in 2011. Geothermal energy in Nevada is also expected to continue growing. Nevada currently has 517 Megawatts of geothermal capacity with 2,275 MW in development over 75 projects (Geothermal Energy Association, 2013).

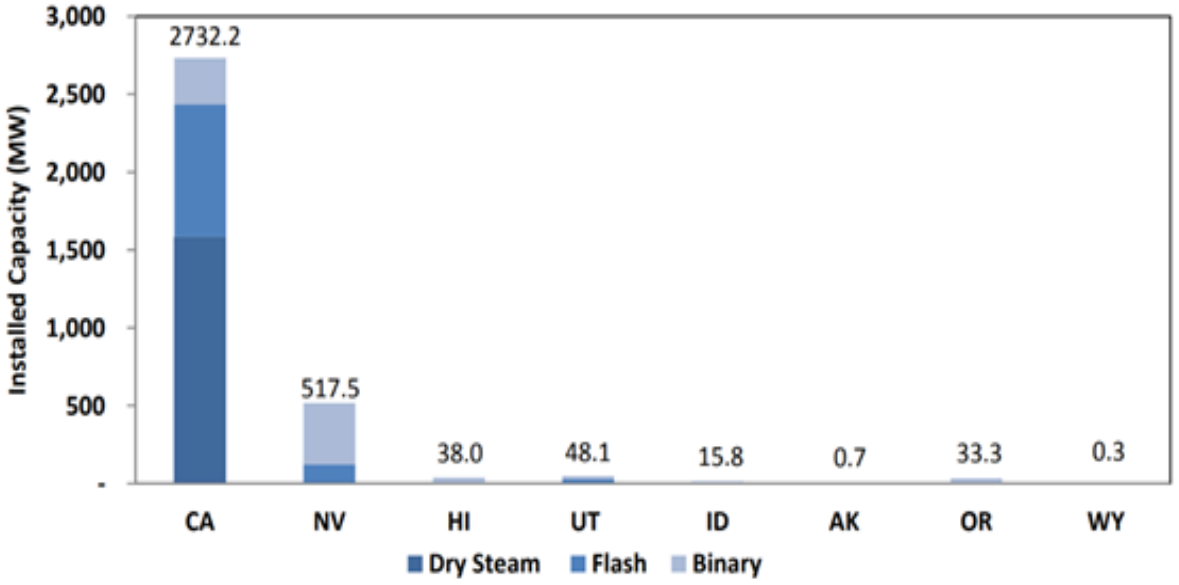

Figure 2.2: February 2013, US Geothermal Installed Capacity by State (MW).
(Geothermal Energy Association, 2013)

Wind electricity generation has also increased significantly. Figure 2.3 shows total annual United States electricity generation from wind energy increased from 6 billion kWh in 2000 to 380 billion kWh in 2021. In 2022, wind turbines were the source of about 10.2% of total United States electricity generation (U.S. Energy Information Administration, 2023). In 2008, the United States Department of Energy published a report that investigated the feasibility of generating 20% of the nation's electricity using wind energy. The report concluded that to generate 20% of the nation's electricity via wind energy, turbine installations would need to increase 2000 per year to 7000 per year (U.S. Department of Energy, 2008). This massive increase in installations makes wind turbines an important element of the country's electrical infrastructure. The soil beneath a wind turbine is subjected to not only environmental impacts but also continuous vibrations transmitted from the superstructure. Wind induced dynamic load transferred from the superstructure to the soil creates a continuous vibrating effect. Figure 2.4 shows continuous vibrations have a deteriorative effect on the strength of soil (Zhou et al., 2021).

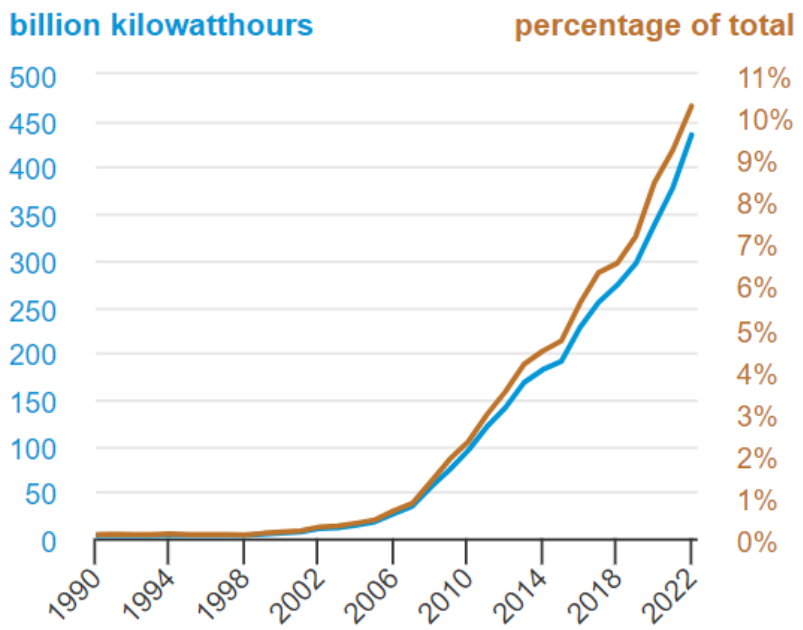

Figure 2.3: Wind electricity generation and share of total U.S. electricity generation, 1990-2022. (U.S. Energy Information Administration, 2023)

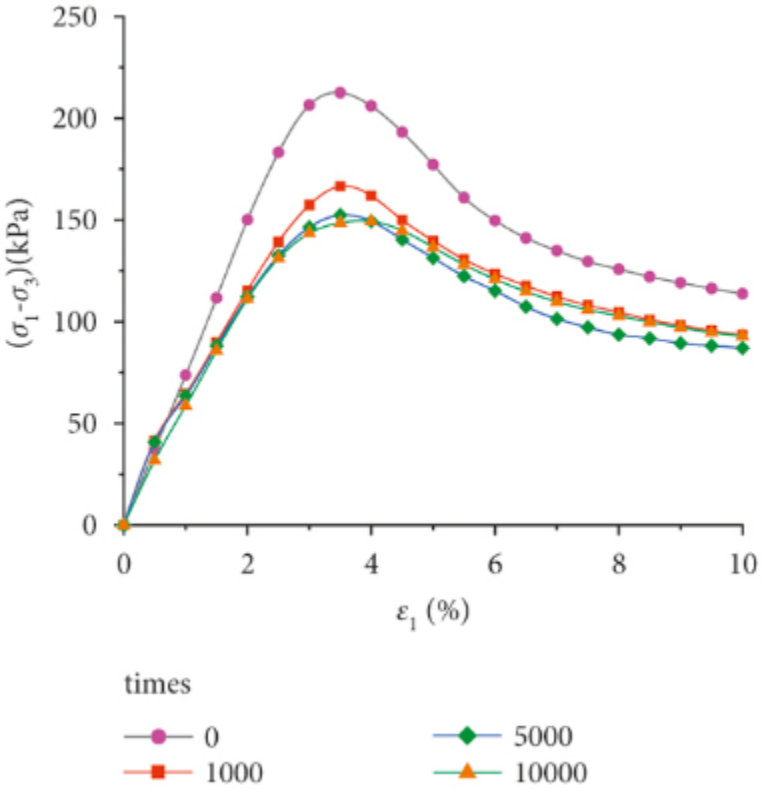

Figure 2.4: Stress-strain curves of specimens affected by vibrations. (Zhou et al., 2021)

As renewable energy continues to grow, a complete understanding of elevated temperatures on strength and stiffness properties of soil will be crucial to ensure safe and cost-effective designs of the country's infrastructure. For geothermal structures, the increased soil temperatures resulting from energy generation could overlap with cyclic loads from an earthquake. For wind turbines, increased surface soil temperatures could lead to reduced soil stiffness when subjected to vibrations occurring during energy generation. Potential environmental and economic benefits of renewable energy have made the use of geothermal pile support systems and wind turbines more popular all over the world. However, despite the growing popularity of harvesting shallow geothermal energy through building foundation systems, the present design practices use empirical methods and high factors of safety, which undermine the economic and environmental benefits associated with renewable geothermal energy (Ghasemi-Fare and Basu, 2015).

2.3 - Review of Thermo-Mechanical Soil Testing and Devices

Thermal effects on the mechanical behavior of saturated soil are well documented. The first soil testing devices modified for thermo-mechanical testing were oedometers. The apparatus was usually modified with a heating element located in the water bath surrounding the sample. The heating element would heat up the water which would heat up the sample. Oedometers operate under an assumption of zero lateral strain. However, with thermo-induced volume change, that assumption is invalid. Difficulty with analysis of thermo-controlled oedometer results led to the development of temperature controlled triaxial cells (Cekerevac and Laloui, 2005).

Many thermo-controlled triaxial devices have been used with different heating methods, however, most heating methods fall into two categories: heating by circulating fluid or heating with internal heaters. Despite their differences, both methods use water as the confining fluid and medium for heat transfer. Triaxial cells that heat via circulating fluid have an external heat pump that circulates hot water into the chamber. The hot water being circulated into the cell was used both as a heat source and confining fluid. Triaxial cells with internal heaters submerge heating elements directly into the water filled cell and use a motorized propeller to evenly distribute heat throughout the water. Heating elements have varied from metal rods to coils that surround the sample like a cage (Cekerevac and Laloui, 2005).

Cekerevac and Laloui conducted a thorough study on clay using a temperature controlled triaxial device. Triaxial shear, consolidation, and drained thermal heating experiments were conducted for temperatures between 20 and 90°C. They developed a new thermo-mechanical triaxial system with the following requirements in mind: the heating system should work independently from the other parts of the cell, the heating system should impose a uniform temperature field to the sample, the time needed to bring the sample to a uniform temperature should be as short as possible, and the heater should be as close to the sample as possible to improve temperature control.

The triaxial device they designed incorporated both heating by circulating fluid through a heat pump and heating by an internal submerged heat source. The closed loop system is attached to a 2000-watt heater that uses a pump to circulate hot water through coiled tubing around the soil sample. A diagram of the triaxial cell designed by Cekerevac and Laloui is shown in Figure 2.5 below (Cekerevac and Laloui, 2005).

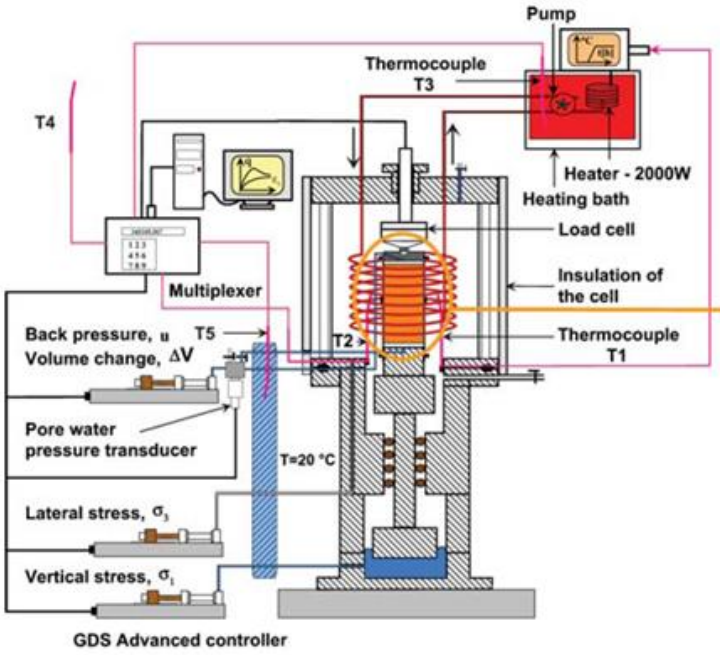

Figure 2.5: Triaxial apparatus with controlled temperatures. (Cekerevac and Laloui, 2005)

To calibrate their triaxial device they used three main thermocouples, one to control the temperature of the circulating fluid, one to measure water temperature near the sample, and one inserted into the middle of the sample to measure the soil temperature. The calibration tests showed small differences between the temperature of the water and the sample that ranged from 0.3°C at an imposed temperature of 30°C to 1.0°C at 90°C. Figure 2.6 shows the calibration data. For temperature increases of 10°C, 60 minutes were required for thermo-equalization (Cekerevac and Laloui, 2005).

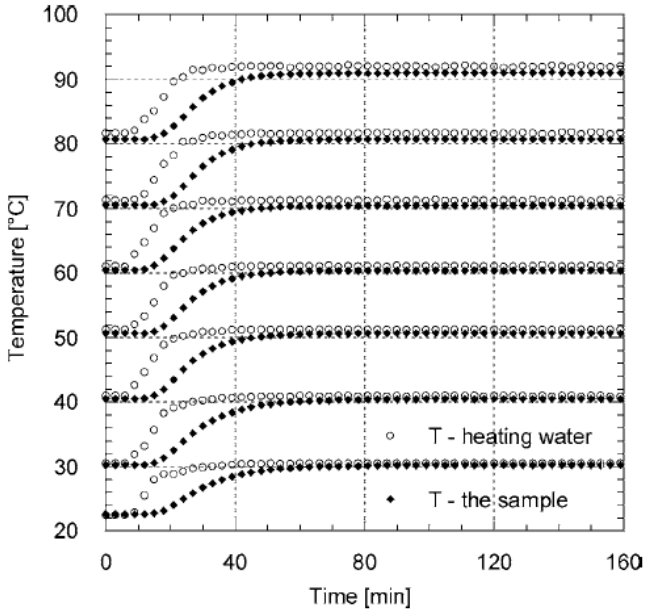

Figure 2.6: Temperature changes of heating water and the sample during the heating from 20-90°C; confining pressure 600kPa. (Cekerevac and Laloui, 2005)

Temperature increases in heating water can have unforeseen consequences. High temperatures cause water to expand, which can manifest in a dilation of the drainage system or contraction of the sample. High temperatures can also compromise the integrity of the latex membrane surrounding the sample, allowing a significant inflow of water into the sample.

Figure 2.7 shows that isotropic drained heating produces volume changes that can be expansive or contractive depending on the overconsolidation ratio of the soil. Densification was observed for heating of normally consolidated samples and dilation was observed for heating of overconsolidated samples (Cekerevac and Laloui, 2005). Figure 2.8 shows an increase in deviator stress at failure for samples tested at higher temperatures under drained heating conditions, indicating an increase in shear strength (Cekerevac and Laloui, 2003).

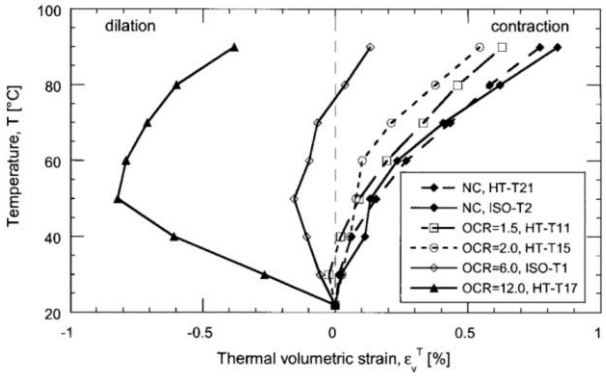

Figure 2.7: Volumetric strain of Kaolin during heating from 22 to 90°C.
(Cekerevac and Laloui, 2005)

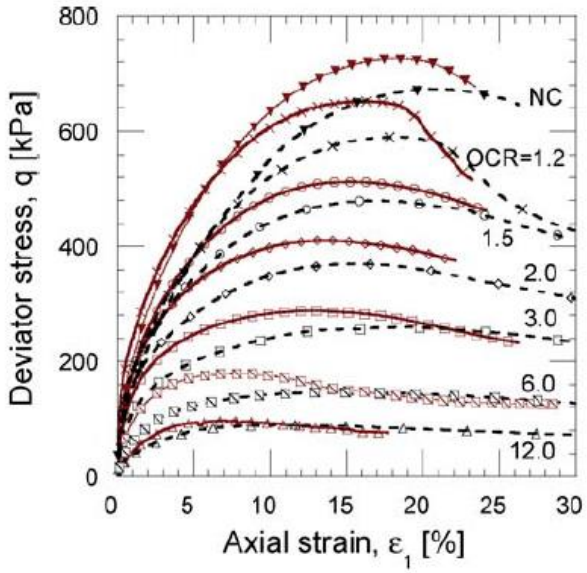

Figure 2.8: Drained triaxial tests at ambient (22°C) and high (90°C) temperatures; Consolidation pressure 600 kPa, 22°C – dashed lines, 90°C – solid lines; Deviator stress vs axial strain. (Cekerevac and Laloui, 2003)

Tang et al. describe similar findings in their paper detailing the development of an isotropic cell capable of high suction (500 MPa), high temperature (20 – 80°C), and high pressure (64 MPa). Heating is achieved by placing the entire isotropic cell into a temperature-controlled bath with thermocouples monitoring the water temperature inside and outside the chamber. A schematic of the isotropic cell is shown in Figure 2.9. The results showed a similar thermal dilation effect as previously mentioned. Preconsolidation pressure showed a significant dependence on temperature, decreasing from 1.9 MPa to 0.8 MPa under undrained heating conditions when temperature was increased from 20 to 60°C (Tang et al., 2007).

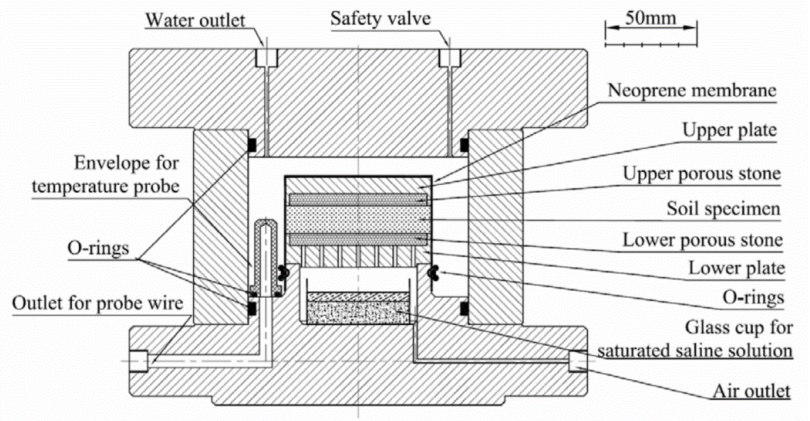

Figure 2.9: Basic scheme of the suction-temperature controlled isotropic cell. (Tang et al., 2007)

Uchaipichat and Khalili investigated the thermo-mechanical behavior of an unsaturated silt. For their experiments, a standard suction controlled triaxial device was modified to allow temperature control by means of a heating element and motorized agitator. The motorized agitator acts like a propeller and circulates the confining water to achieve a uniform heat distribution. A schematic of the modified triaxial cell is shown in Figure 2.10 (Uchaipichat and Khalili, 2009).

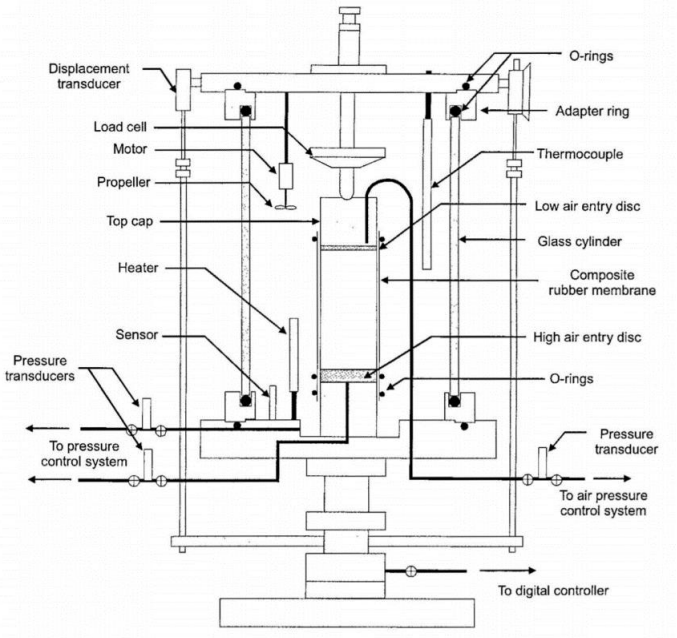

Figure 2.10: Modified Bishop-Wesley cell. (Uchaipichat and Khalili, 2009)

Uchaipichat and Khalili report similar findings to the previously mentioned studies. For high overconsolidation ratios dilation occurred. For normal and low overconsolidation ratios contraction occurred. Increasing temperature under undrained conditions produced a similar thermal softening effect, with preconsolidation pressure decreasing. The findings pertaining to shear strength show thermal softening trends under undrained heating, which can be seen in Figure 2.11. At all suction values, peak deviator stress at failure and thus shear strength clearly decreases as temperature increases (Uchaipichat and Khalili, 2009).

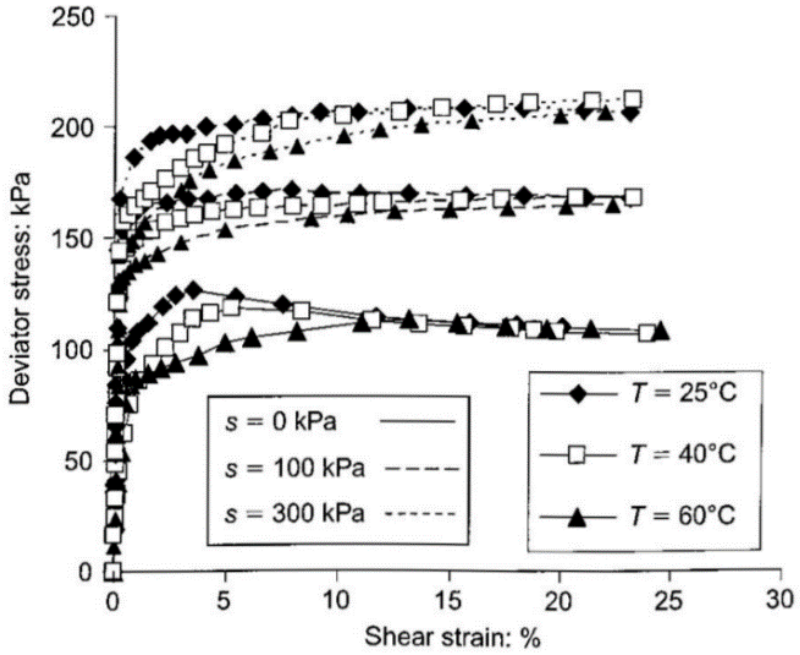

Figure 2.11: Suction and temperature controlled conventional compression shear tests at initial mean effective stress of 50 kPa. (Uchaipichat and Khalili, 2009)

Alsherif and McCartney further investigated the effects of high temperatures and high suction on soil. They used a thermo-hydro-mechanical triaxial cell to conduct their experiments. Figure 2.12 shows the schematic of the thermo-controlled triaxial cell. The samples were heated using heating elements submerged in the confining fluid with a pump to circulate the water to achieve uniform heat distribution. The thermal softening trends are similar to those observed in previous studies. Elevated temperatures caused a reduction in preconsolidation pressure and shear strength (Alsherif and McCartney, 2015).

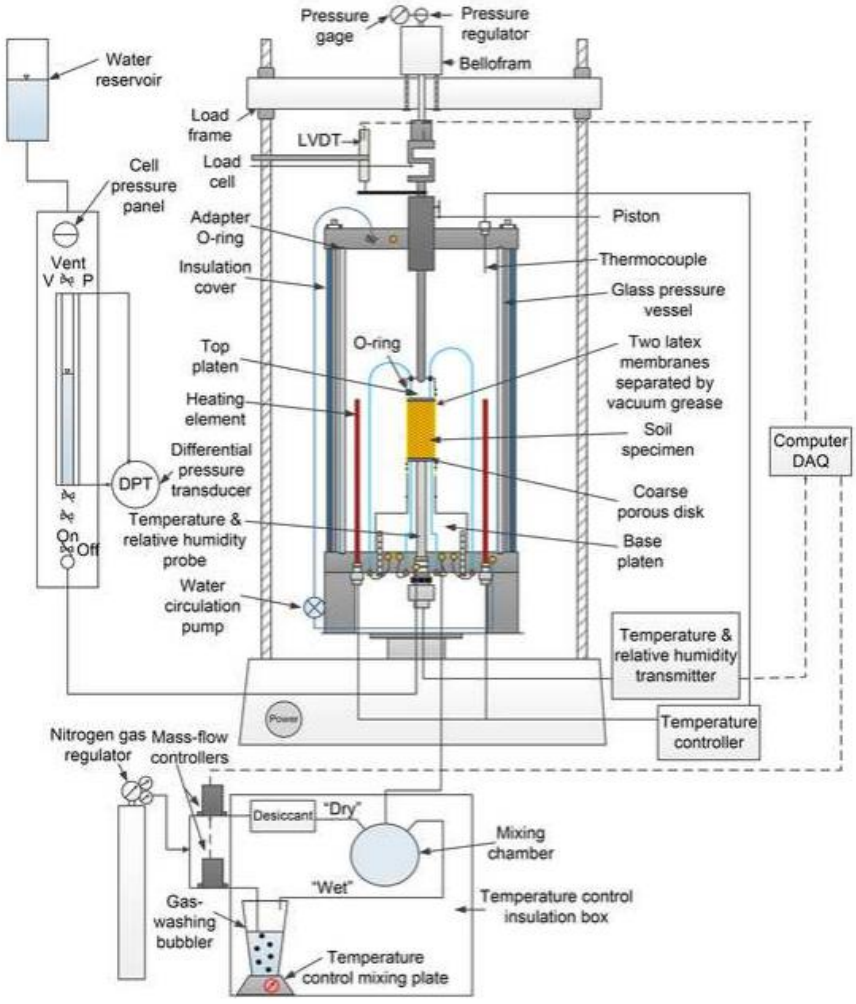

Figure 2.12: Thermo-controlled triaxial cell. (Alsherif and McCartney, 2015)

2.4 - Review of Stiffness Properties of Soils

Shear modulus, G, and damping ratio, D, are two of the main properties needed to evaluate the dynamic response of soil. The determination of shear modulus can be made from experimental results similar to Figure 2.13, which shows the small strain shear modulus, G_{max}, and the secant shear modulus, G. These values are determined by the slope of the hysteresis loop generated from the shear strain amplitude imposed on the soil specimen. Due to the highly nonlinear nature of shear strain response in soils, shear modulus changes dramatically depending on shear strain amplitude. As the peak shear strain amplitude increases, the slope of the generated hysteresis loop decreases indicating a decrease in the shear modulus of the soil.

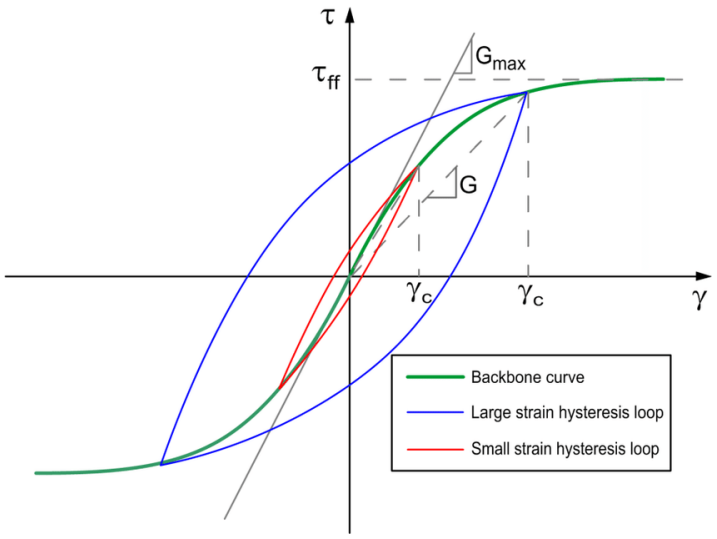

Figure 2.13: Schematic illustration of backbone curve and small strain and large strain hysteresis loops. (Stewart et al., 2014)

Proper evaluation of shear modulus is necessary for geotechnical engineers to safely design deep foundation systems and any other structure subject to dynamic soil structure interaction; especially when the area is prone to stability problems or is located in earthquake prone or seismically active areas where dynamic interaction is more common.

Once soil is subjected to dynamic or cyclic loading from an earthquake, damping ratio, D, is the soil property responsible for the dissipation of energy propagating through the material. Material damping ratio is the proportion of dissipated energy to the maximum retained strain energy during a cyclic load application. Damping is defined as the loss of energy within a vibrating or cyclically loaded system, usually dissipated in the form of heat. There are two types of damping, internal and external. Internal damping refers to the energy dissipation within the material itself. For soils, internal damping can be attributed to inter-particle sliding and friction, structural rearrangement, and pore fluid viscosity. Internal damping is an inherent soil material property and is usually the term being referred to by “damping ratio”. External damping, also called system damping, is not an inherent material property and refers to a transmission of energy away from the source via radiation (Ashmawy et al., 1995). The damping ratio of soils also changes dramatically under different shear strain amplitudes due to the nonlinear nature of shear response in soil. However, instead of decreasing as strain amplitudes increase, damping ratio increases under higher shear strain amplitudes, signifying a larger dissipation of energy under successive cyclic loading cycles.

The effect of various parameters on the dynamic properties of soils has been investigated thoroughly. These parameters include shear strain amplitude (Silver and Seed, 1971), confining stress (Darendeli et al., 2001), vertical stress (Das, 1993), time of confinement (Anderson and Stokoe, 1978), number of loading cycles (Thiers and Seed, 1968), loading frequency (Nong et al., 2020), overconsolidation ratio (Vucetic and Dobry, 1987), void ratio (Hardin and Drnevich, 1972), degree of saturation (Shahbaz, 1993), and plasticity index (Vucetic and Dobry, 1991).

Temperature is also a key variable in determining soil response to dynamic loading. The effect of temperature seems to depend on the method of heat application. When the sample is allowed to drain during heat application the volume contracts and the absorbed water barrier around the clay particles is weakened. The increasing temperature creates more solid to solid contact surfaces and thus results in an increase in shear strength. If the sample is not allowed to drain during heating, the heat induced pore pressure significantly reduces effective stress. This reduction in effective stress results in a decrease of shear strength (Kuntiwattanakul, 1995). Currently, there are very few comprehensive soil studies investigating the effect of temperature on soil stiffness properties under dynamic loading. The majority of temperature-controlled studies either involve static loading or dynamic testing of soils at subzero temperatures.

2.5 - Thermo-Controlled Cyclic Triaxial Testing

Cyclic triaxial tests are performed to determine the modulus of elasticity, E, and the damping ratio, D, of soils. Typically, the soil sample is subjected to a confining pressure, after which an axial cyclic stress is applied to the soil specimen. Cyclic triaxial tests generate hysteresis loops that provide the basis for determination of elastic modulus and damping. Figure 2.14 shows how modulus of elasticity is determined from the slope of the hysteresis loop using Equation 2.1, and damping is determined from the ratio of the area of the hysteresis loop (A_L) to the area of the triangle (A_T) using Equation 2.2. Once modulus of elasticity is determined, shear modulus can be calculated by assuming a representative value of Poisson's ratio (μ), shown in equation 2.3 (Das, 1993).

$$E = \frac{\Delta\sigma_d}{\varepsilon} \tag{2.1}$$

$$D = \frac{A_L}{4\pi A_T} \tag{2.2}$$

$$G = \frac{E}{2(1+\mu)} \tag{2.3}$$

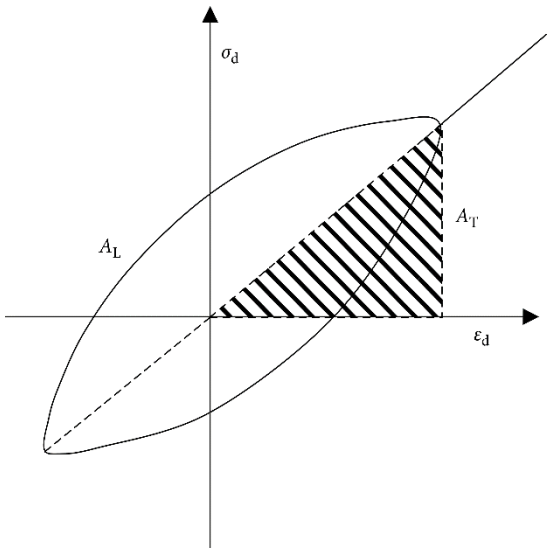

Figure 2.14: Determination of elastic modulus and damping via cyclic triaxial testing. (Zhou, 2018)

There are few experimental studies concerning thermo-controlled cyclic triaxial soil testing. Ng and Zhou investigated the cyclic behavior of an unsaturated silt at various suctions and temperatures. To achieve thermo-control, a suction and temperature-controlled cyclic triaxial apparatus was developed. Figure 2.15 shows a schematic of the device. The device was used to measure axial strain, volumetric strain, and resilient modulus for suctions ranging from 0 to 60 kPa and temperatures ranging from 20°C to 60°C.

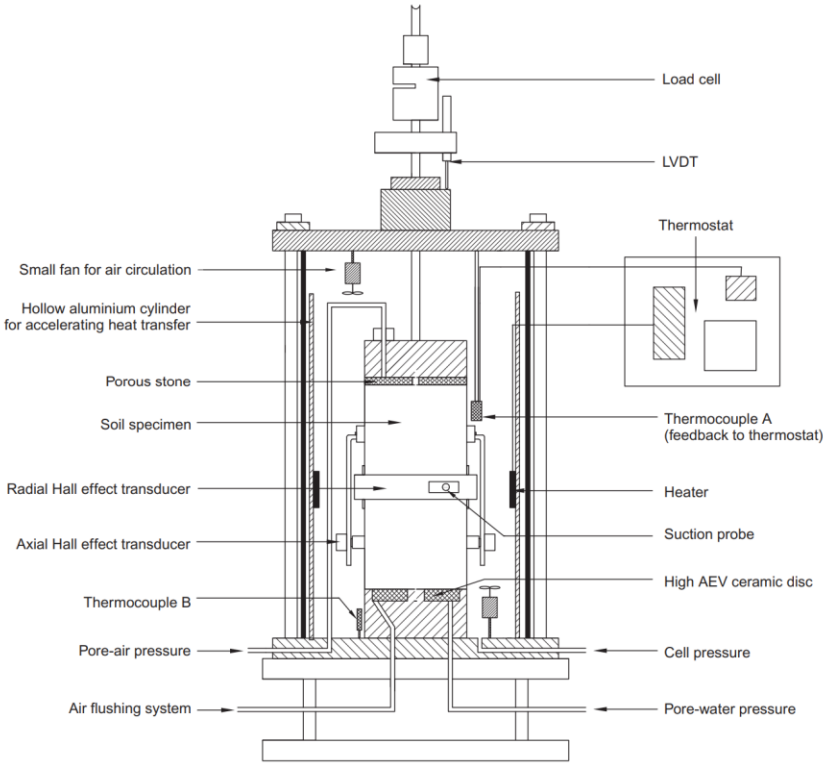

Figure 2.15: Schematic of thermo-controlled cyclic triaxial device. (Ng and Zhou, 2014)

Experimental results of the study showed that yield stress increased with suction (suction-induced hardening) but decreased with temperature (thermal-induced softening). For a given temperature, resilient modulus significantly increases when suction increases, however, the influence of temperature on resilient modulus depends on the level of applied suction. Figure 2.16 shows at zero suction resilient modulus was slightly affected by temperature. Figure 2.17 shows at larger suctions increasing temperatures caused a significant decrease in resilient modulus. The study concluded that thermal effects were much more pronounced on unsaturated soils possibly due to the decrease in Bishop's stress between soil particles and the decrease in the meniscus water stabilization effect (Ng and Zhou, 2014).

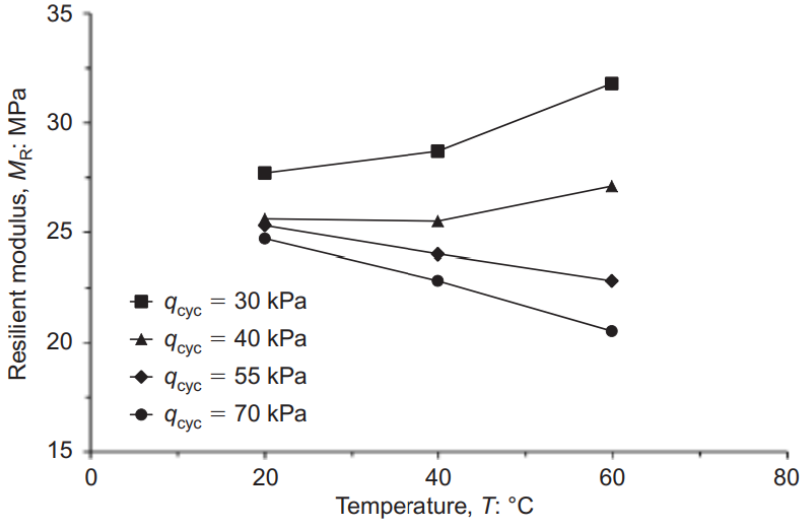

Figure 2.16: Influence of temperature on resilient modulus at zero suction. (Ng and Zhou, 2014)

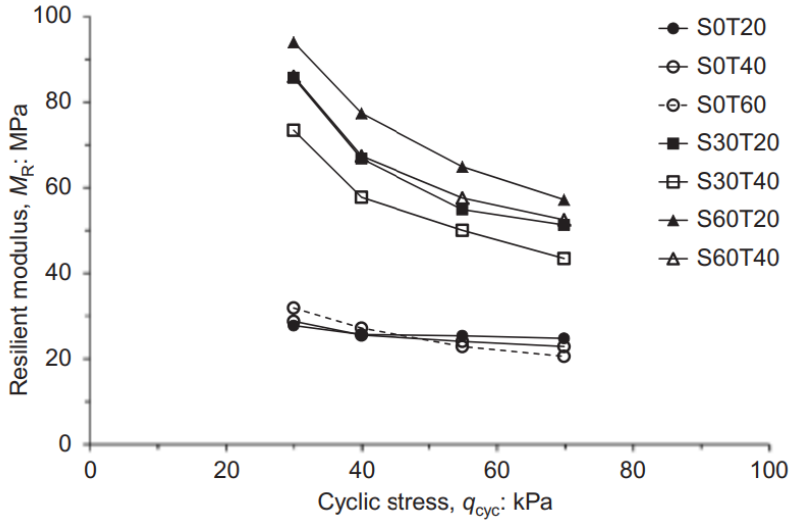

Figure 2.17: Influence of temperature on resilient modulus at different suctions. (Ng and Zhou, 2014)

2.6 - Thermo-Controlled Resonant Column Testing

The resonant column test consists of a soil column that has torque applied at one end. The frequency of the torque application is increased generating a frequency response curve. Once the frequency response curve is obtained the frequency at resonance can be determined from the peak of the curve, allowing for shear modulus and damping ratio calculations. To determine shear modulus using the resonant column test, shear wave velocity is calculated from the first mode resonant frequency and multiplied by soil density. Equations 2.4 and 2.5 show the process for calculating shear modulus via the resonant column test:

$$\frac{I}{I_0} = \frac{2\pi h f_n}{v_s} \tan\left(\frac{2\pi h f_n}{v_s}\right) \tag{2.4}$$

$$G = \rho v_s^2 \tag{2.5}$$

where I is the sum of the mass moment of inertia of the soil specimen and membrane, I_0 is the mass moment of inertia of the rigid end mass at the top of the sample, h is the sample height, f_n is the resonant frequency of the specimen, v_s is the shear wave velocity, ρ is the density of the soil, and G is the shear modulus.

In the resonant column test, two methods of damping measurement are typically used: the logarithmic decrement method and the half-power bandwidth method. The logarithmic decrement method refers to imposing an initial vibratory condition on the soil sample then allowing the sample to vibrate freely while recording the decay in peak amplitude. The half-power bandwidth method refers to using the steady state peak amplitude at resonance to determine the damping ratio. Logarithmic decrement and half-power bandwidth methods are depicted in Figures 2.18 and 2.19. Damping ratio can be calculated from either the logarithmic decay curve using Equations 2.6 and 2.7, or the frequency response curve using Equation 2.8:

$$D = \frac{1}{\sqrt{1 + \left(\frac{2\pi}{\delta}\right)^2}} \tag{2.6}$$

$$\delta = \frac{1}{n} \ln \frac{A(t_0)}{A(t_0 + nT)} \tag{2.7}$$

$$D = \frac{f_2 - f_1}{2f_0} \tag{2.8}$$

where δ is logarithmic decay, A is amplitude, n is the number of cycles, f_0 is the resonant frequency corresponding to the peak of the frequency response curve, and f_1 and f_2 are the frequencies corresponding to 0.707 of the peak amplitude of the frequency response curve.

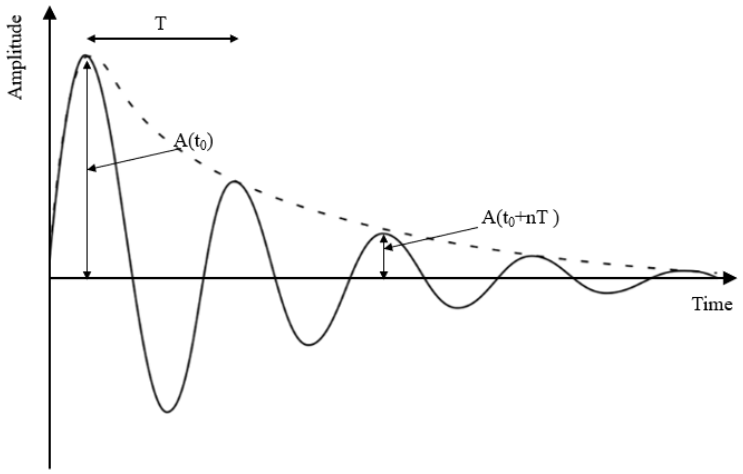

Figure 2.18: Conceptual illustration of typical logarithmic free-vibration decay curve. (Bilesavar, 2020)

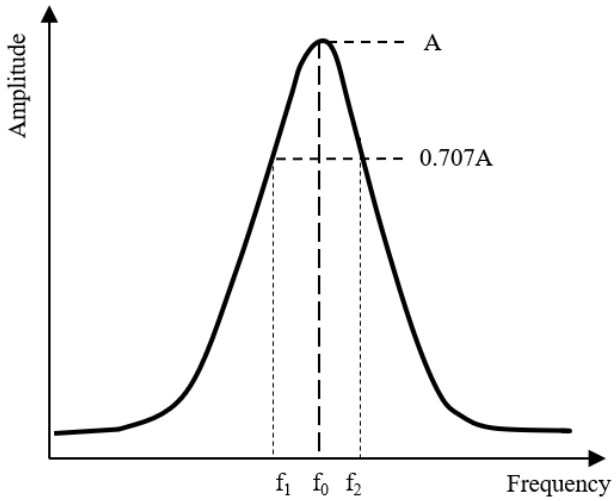

Figure 2.19: Conceptual illustration of typical frequency response curve. (Bilesavar, 2020)

Currently there are few thermo-controlled resonant column studies. Al-Hunaidi used the resonant column method to determine the dynamic shear modulus and damping ratio of undisturbed frozen (-9°C) and thawed soil samples (22°C) under a 14 kPa confining pressure. The results show that at low strains the shear modulus of the frozen samples was 50 times that of the thawed samples (Al-Hunaidi et al., 1996). Yu used a resonant column device to test frozen silt. Samples were tested at temperatures ranging from -15°C to 25°C under a 100 kPa confining pressure. The results showed a significant increase in initial shear modulus with decreasing temperatures. The experimental results identified a sensitive stage and a stable stage for initial shear modulus. During the sensitive stage (25°C to -4°C) decreases in temperature caused large increases in initial shear modulus, however, during the stable stage (<-4°C) additional decreases in temperature had little effect on the initial shear modulus of the frozen soil sample (Yu et al., 2016).

Bilesavar used an upgraded thermo-controlled resonant column testing device to investigate the cohesive-frictional soil response to cyclic torsional excitations under independently controlled environmental factors, including soil moisture, ambient temperature, and isotropic confinement. An existing resonant column device was upgraded and calibrated for temperature control using two 120V heating elements and two 12V fans to circulate the temperature inside the testing chamber, shown in Figure 2.20.

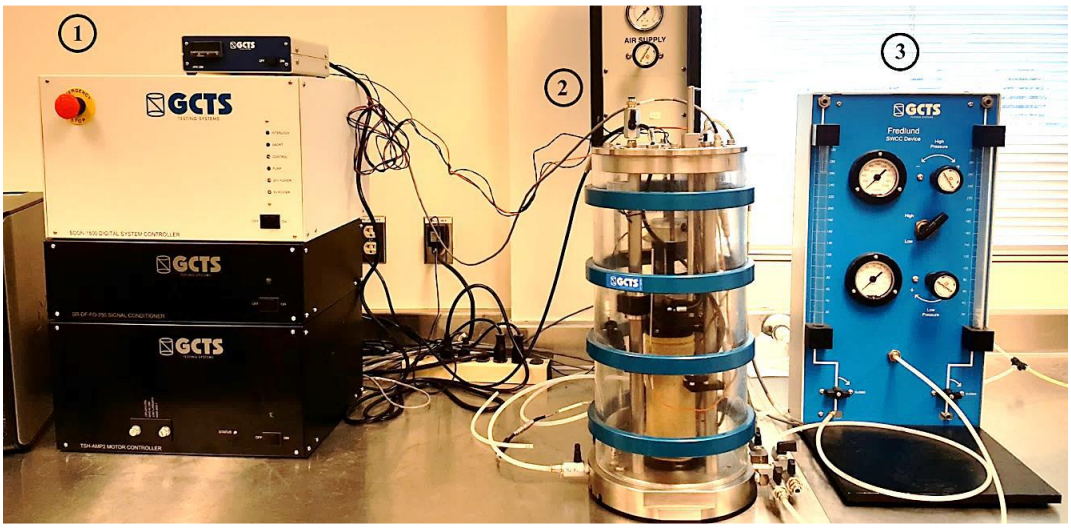

Figure 2.20: Thermo/servo-controlled RC test setup. (Bilesavar, 2020)

Testing was conducted at temperatures of 23°C, 40°C, 50°C, and 60°C for confinements of 5, 10, 15, and 20 psi. The dynamic response of clayey CL, silty ML, and sandy soils SC was evaluated. Analysis of experimental results showed increased temperatures had a detrimental effect on initial shear modulus (G_{max}) and minimum damping ratio (D_{min}) caused by thermal softening of the soil samples in an undrained heating environment. The thermal softening effect can be seen in Figure 2.21, which shows that hysteresis loops generated from RC tests expanded in size with increasing temperature. The expansion in loop size indicated a reduction in shear modulus and increase in damping ratio. Figure 2.22 shows the reduction in shear modulus was more pronounced in the drier clay samples. Figure 2.23 shows threshold strain of all test soils decreased with increasing temperatures, with higher water content samples experiencing a greater reduction (Bilesavar, 2020).

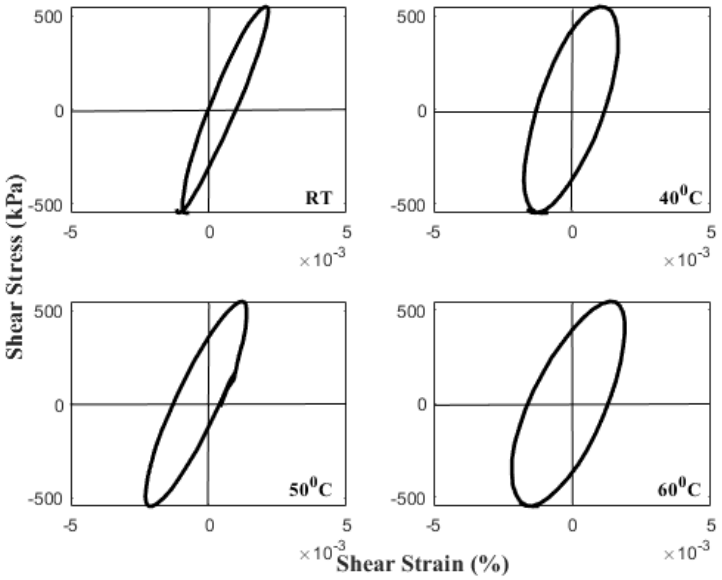

Figure 2.21: Effect of temperature on CL soil response to cyclic torsional loading at 17% moisture content and 20 psi confinement. (Bilesavar, 2020)

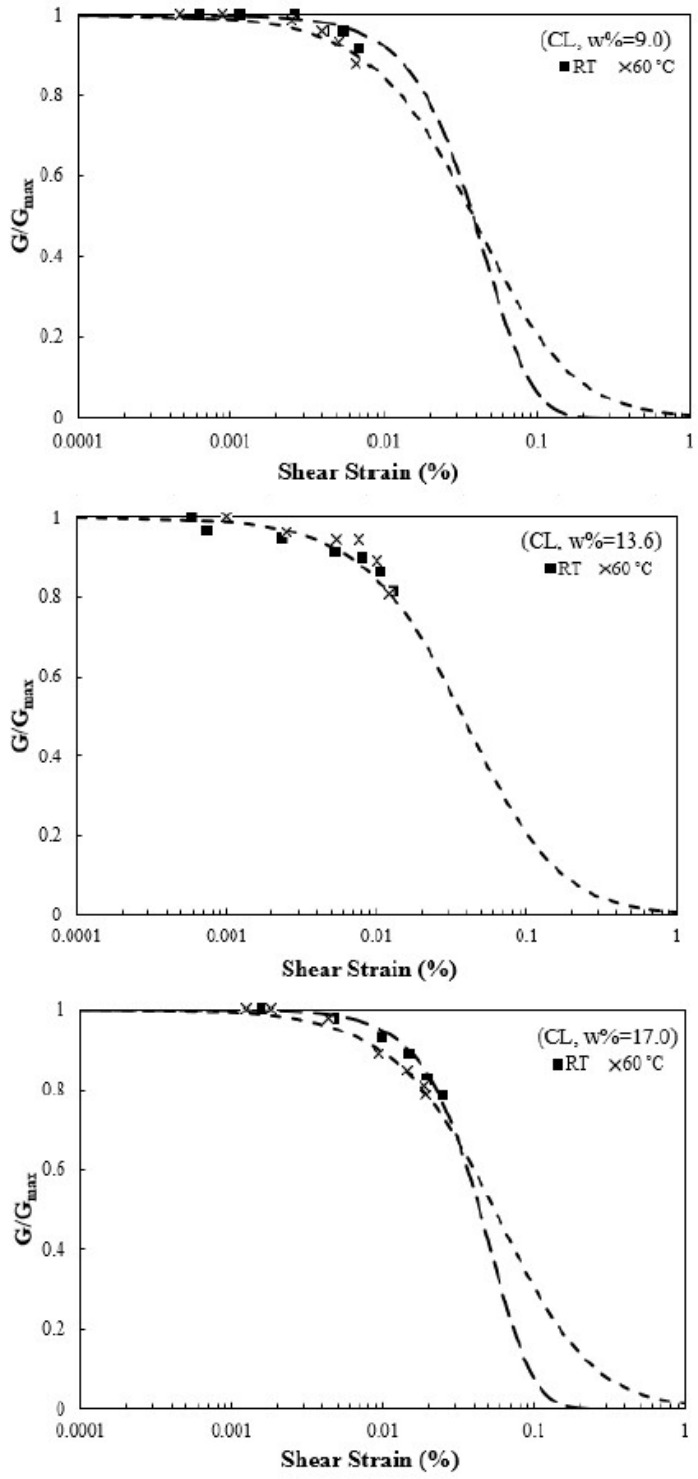

Figure 2.22: Reduction of shear modulus with heat application. (Bilesavar, 2020)

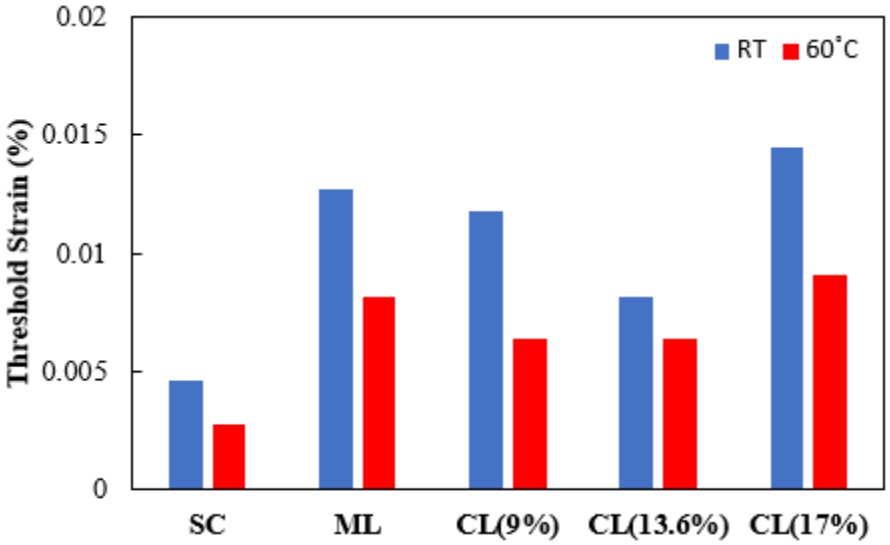

Figure 2.23: Effect of temperature on threshold shear strain of test materials. (Bilesavar, 2020)

2.7 - Cyclic Simple Shear Testing

Cyclic simple shear testing is a convenient method for determining shear modulus, damping ratio, and liquefaction parameters of soils. During a cyclic simple shear test a soil specimen is subjected to confinement and vertical stress with an additional application of cyclic shear stress. The horizontal load and shear deformation of the soil sample is measured and used to calculate shear modulus and damping ratio. There are two main advantages of cyclic simple shear soil testing. The tests are more representative of field conditions since the device allows for soils to be consolidated under K_0 conditions, and cyclic simple shear tests can be conducted for a wider range of strain amplitudes.

The shear modulus and damping ratio is determined from hysteresis loops similar to an ideal case shown in Figure 2.24. Shear modulus, G, is calculated from the slope of the hysteresis loop. Damping ratio, D, is calculated similarly to the method used for cyclic triaxial testing, from the ratio of the area of hysteresis loop A(l) to the area of triangle A(t). Equations 2.9 and 2.10 show shear modulus and damping calculations respectively:

$$G = \frac{\text{amplitude of cyclic shear stress } \tau}{\text{amplitude of cyclic shear strain } \gamma} \tag{2.9}$$

$$D = \frac{A(l)}{4\pi A(t)} \tag{2.10}$$

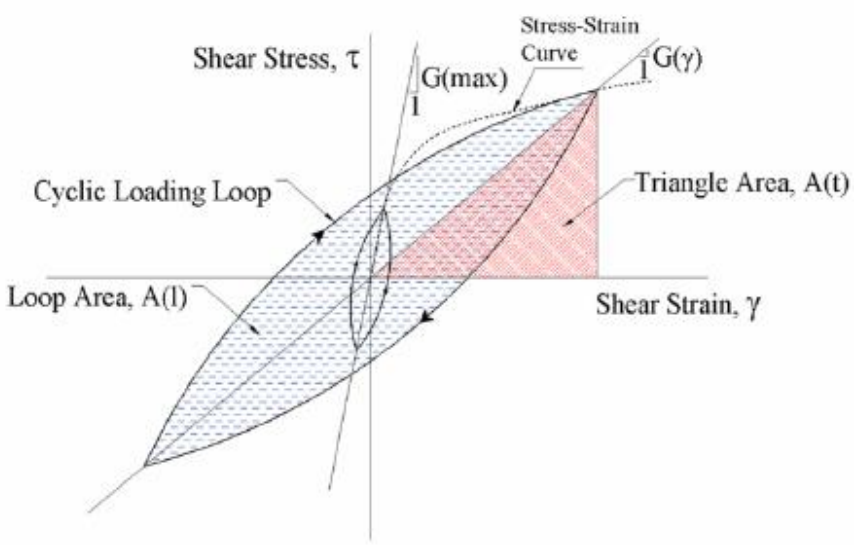

Figure 2.24: Hysteretic shear stress – shear strain relationship. (M. Meidani et al., 2008)

Cyclic simple shear soil studies are quite prevalent and provide a thorough understanding of soil behavior under dynamic loading conditions. Silver and Seed used a modified Norwegian Geotechnical Institute (NGI) simple shear device to study the effects of shear strain amplitude and vertical stress on a medium dense sand. Figure 2.25 shows two important dynamic soil testing trends. Shear modulus decreases with an increase in shear strain amplitude and increases with an increase in vertical stress (Silver and Seed, 1971). Thiers and Seed used a similar device to investigate the cyclic degradation of shear modulus for clay. Figure 2.26 shows that shear modulus decreases as number of cycles increases (Thiers and Seed, 1968).

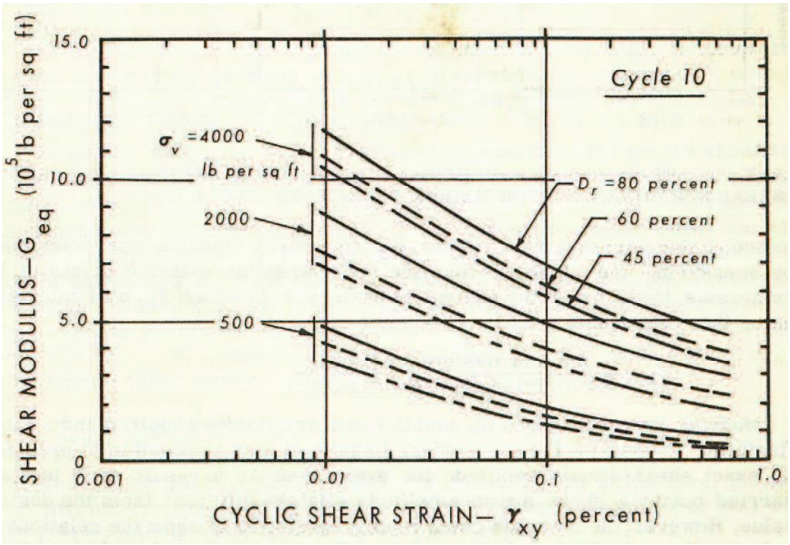

Figure 2.25: Effect of vertical stress and relative density on shear modulus in tenth loading cycle. (Silver and Seed, 1971)

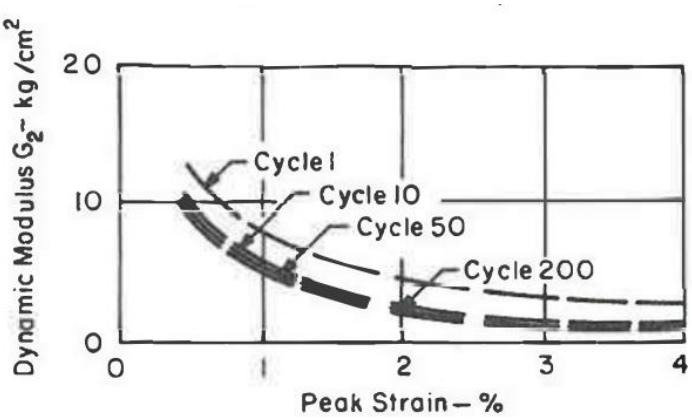

Figure 2.26: Effect of cyclic loading on shear modulus. (Thiers and Seed, 1968)

Suction-controlled cyclic simple shear studies are less prevalent and need further experimentation to provide a complete understanding of how suction affects the dynamic response of soil. Le and Ghayoomi developed a suction-controlled cyclic simple shear device to examine shear modulus and damping ratio of an unsaturated, poorly graded, fine sand. Various dry, partially saturated, and fully saturated samples were tested at a shear strain amplitude of 0.032% and matric suction values of 4, 6, 8, and 10 kPa. Figures 2.27 and 2.28 show that an increase in suction results in an increase in shear modulus and a decrease in damping ratio (Le and Ghayoomi, 2016).

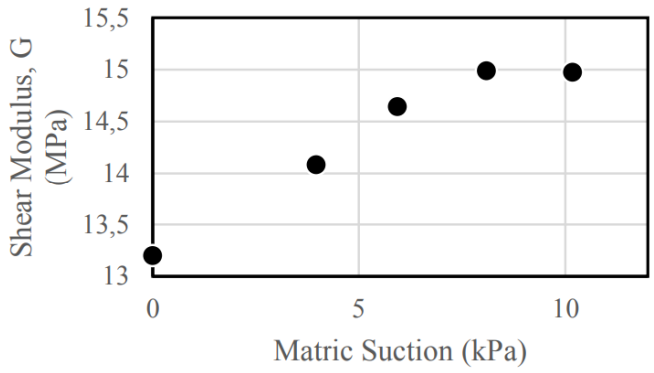

Figure 2.27: Effects of matric suction on shear modulus. (Le and Ghayoomi, 2016)

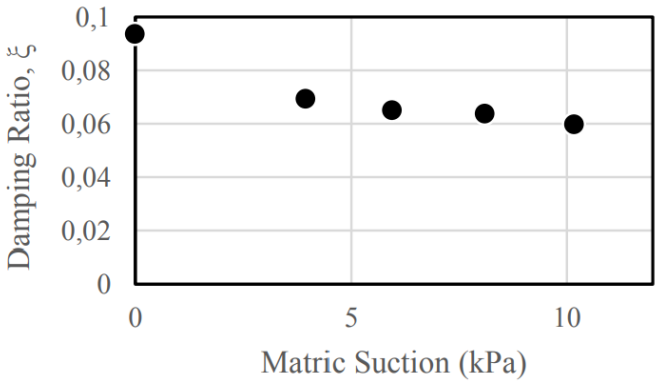

Figure 2.28: Effect of matric suction on damping properties. (Le and Ghayoomi, 2016)

Guo used a modified direct shear device to investigate soil-structure interface behavior under monotonic and cyclic thermal loading conditions. Figure 2.29 shows a schematic of the direct shear device, modified with a heat pump to control temperature (Guo et al., 2023). The study focuses on the soil-structure interface and does investigate how temperature affects shear modulus or damping ratio.

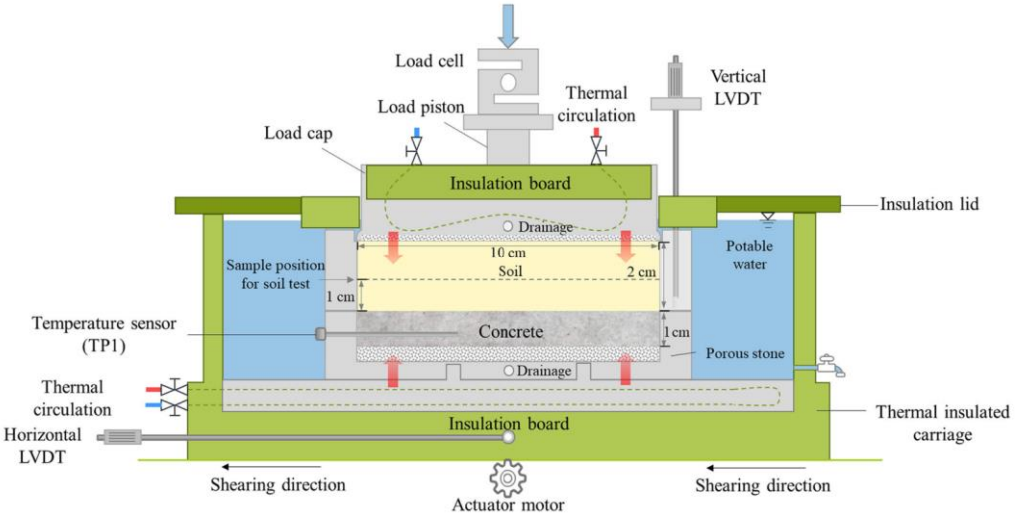

Figure 2.29: Schematic view of temperature controlled direct shear box. (Guo 2023)

At the time of this study there are no known thermo-controlled cyclic simple shear studies investigating the shear modulus and damping response of soils under increased temperatures.

Chapter 3: Experimental Program and Variables

3.1 - Test Soils

Tests will be conducted on three different soil types: low plasticity clay (CL), nonplastic silt (ML), and clayey sand (SC), per the Unified System for Classification of Soils (USCS). All samples were collected from Denison, Texas, near the Red River on the border of Texas and Oklahoma. Figure 3.1 shows the general location for sample collection. The specific properties of the soils being used are shown in Table 3.1. All properties shown below except internal friction angle (ϕ) were obtained experimentally using Atterberg limits, pycnometer, and standard proctor tests according to ASTM standards D3418e1, D854-14, and D698-12e2 respectively. Internal friction angle was estimated using established values from similar soil types. Lateral earth pressure coefficient (K_0) was calculated from Equation 3.1 using the corresponding friction angle (ϕ). An average value of 0.53 is used to determine the proper horizontal to vertical pressure ratio used during anisotropic consolidation for all soils.

$$K_0 = 1 - \sin\varphi \tag{3.1}$$

Table 3.1: Soil Properties

Property	**CL**	**ML**	**SC**
Sand (%)	20	4	64
Silt (%)	28	86	30
Clay (%)	52	10	6
Maximum dry unit weight, γ_{dmax} (kN/m^3)	17.8	16.6	19.7
Optimum moisture content, w_{opt} (%)	13.6	14.8	10
Plasticity Index (PI)	11	NP*	NP*
Specific Gravity, G_s	2.67	2.68	2.67
Friction Angle, ϕ’	28	27	32
Earth pressure coefficient, K_0	0.53	0.55	0.47

*Nonplastic

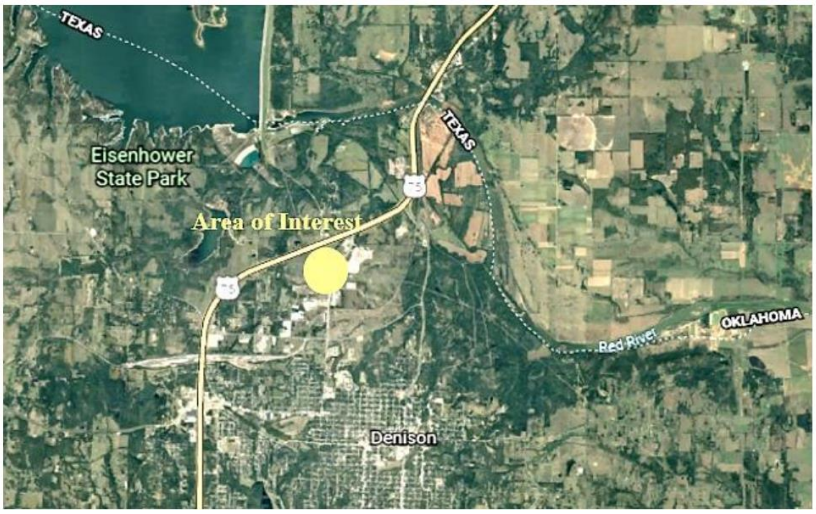

Figure 3.1: Sampling location of cohesive-frictional test soils.

3.2 - Test Variables

Table 3.2 shows the variables being considered for this research. The effects of these variables on the shear modulus and damping ratio of soil, except for temperature, are well documented. The effect of elevated temperature on shear modulus and damping ratio, and the interactions between temperature and the other variables needs to be investigated further.

Table 3.2: Test Variables

Soil Type	Moisture Content, w (%)	Total Vertical Stress, σ_v (psi)	Temperature (^oC)	Shear strain, γ (%)	Frequency, f (Hz)	Number of cycles (N)
CL	9.0	20.0	RT, 40, 50, 60	0.001 - 10	0.1	1, 5, 10
	13.6 (OMC)	20.0	RT, 40, 50, 60	0.001 - 10	0.1	1, 5, 10
	17.0	20.0	RT, 40, 50, 60	0.001 - 10	0.1	1, 5, 10
ML	14.8 (OMC)	20.0	RT, 40, 50, 60	0.001 - 10	0.1	1, 5, 10
SC	10 (OMC)	20.0	RT, 40, 50, 60	0.001 - 10	0.1	1, 5, 10

Tests will be conducted at optimum moisture content (OMC) for each of the three different soil types. However, the clay will have two additional series of tests conducted for samples compacted dry (w=9.0%) and wet (w=17.0%) of optimum moisture content. These two moisture content values were chosen because they correspond to the same dry unit weight value on the proctor curve. It has been shown that an increase in matric suction causes an increase in shear modulus. As the water content of the soil specimen decreases, the matric suction increases. This increase in matric suction causes an increase in the effective stress of the sample, which relates to an increase in shear modulus and decrease in damping ratio.

The following section shows preliminary testing of clay soil (CL) samples to ensure the CSS device is functioning properly and results are repeatable. To determine proper device functionality known trends are investigated to ensure the CSS device is producing expected results. Functionality will be evaluated through effects of vertical stress, shear strain amplitude, and number of cycles. Repeatability will be evaluated by testing three identically prepared clay soil (CL) samples and comparing the shear modulus of the generated hysteresis loops.

3.3 – Performance Verification: Effect of Vertical Stress (σ_v)

Samples will be compacted at a specific moisture content and dry density before being confined under K_0 conditions, maintaining the desired ratio of horizontal to vertical stress throughout the testing process. Tests will be conducted at a vertical stress of 20 psi. The effect of increasing vertical stress and confinement is documented. At a constant shear strain amplitude, shear modulus increases with an increase in vertical stress, which can be seen in Figure 3.2. Shear modulus calculations for cyclic simple shear tests are shown in Chapter 2, visually represented by the slope of the hysteresis loops. As the vertical stress on the sample increases from 2.5 psi (17.2 kPa) to 20 psi (137.9 kPa), the slope of the hysteresis loops also increases, signifying an increase in shear modulus. The present experimental CSS program was accomplished only for a relatively high level of confinement, namely 20 psi (137.9 kPa), which would be reasonably close to the typical average of overburden pressures reported in a wide variety of geosystems subject to thermal gradients in the field.

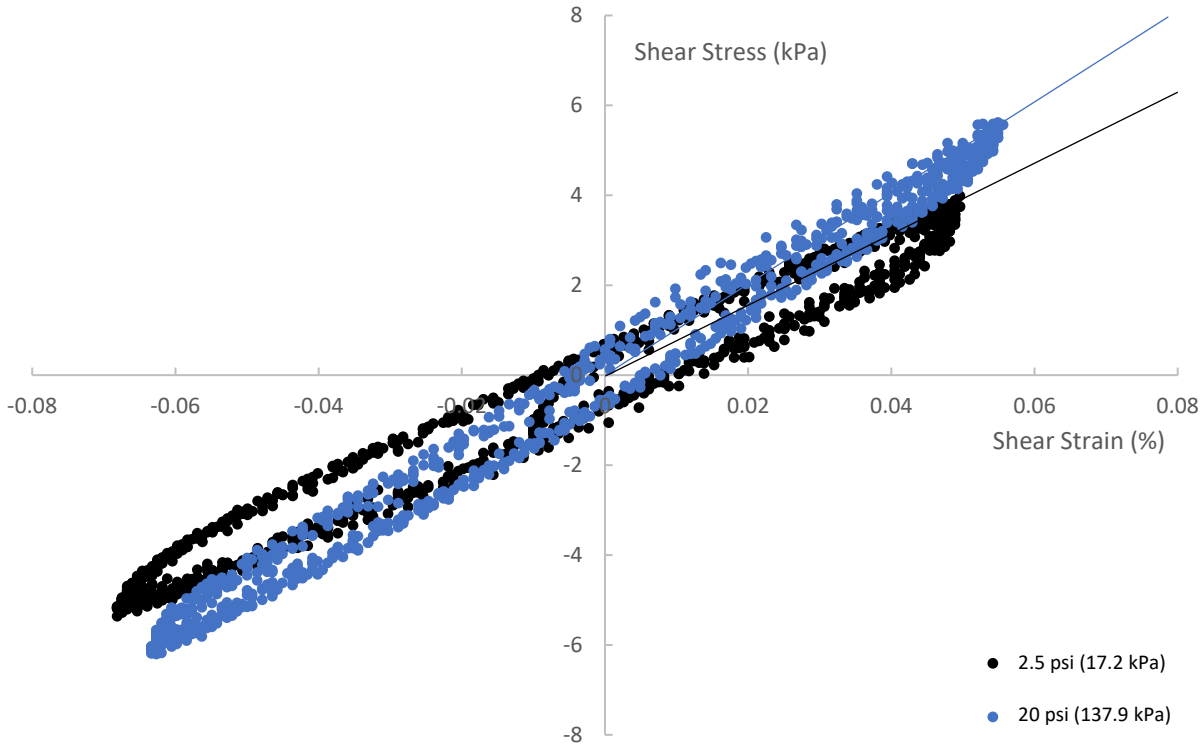

Figure 3.2: Effect of vertical stress on shear modulus for γ = 0.05%.

3.4 – Performance Verification: Effect of Shear Strain Amplitude (γ)

Tests will be conducted for a wide array of shear strain amplitudes. The effect of increasing shear strain amplitude is well documented. An increase in shear strain amplitude should result in a decrease in shear modulus. With the cyclic simple shear device, it is possible to obtain shear modulus values for strains ranging from 0.001% to over 5.0%. This large range of shear modulus values will allow for fairly accurate plotting of the shear modulus reduction curve, G/G_{max}. The effect of shear strain on shear modulus is shown in Figure 3.3 and Figure 3.4. Figure 3.3 shows the degradation of shear modulus for relatively small strain values, comparing 0.01% strain to 0.05% strain. Figure 3.4 shows a more pronounced degradation

for large strain values, comparing 1.0% strain to 5.0% strain. In both cases shear modulus decreases as the amplitude of shear strain increases.

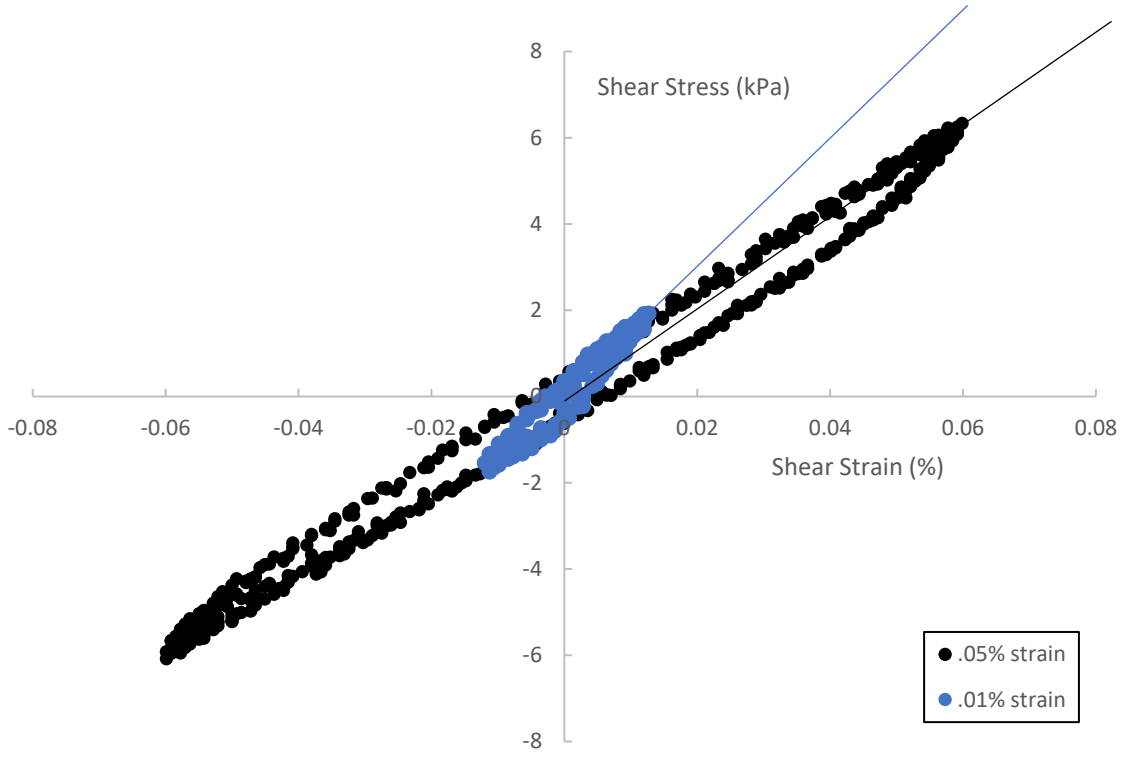

Figure 3.3: Effect of shear strain amplitude on shear modulus for small deformations.

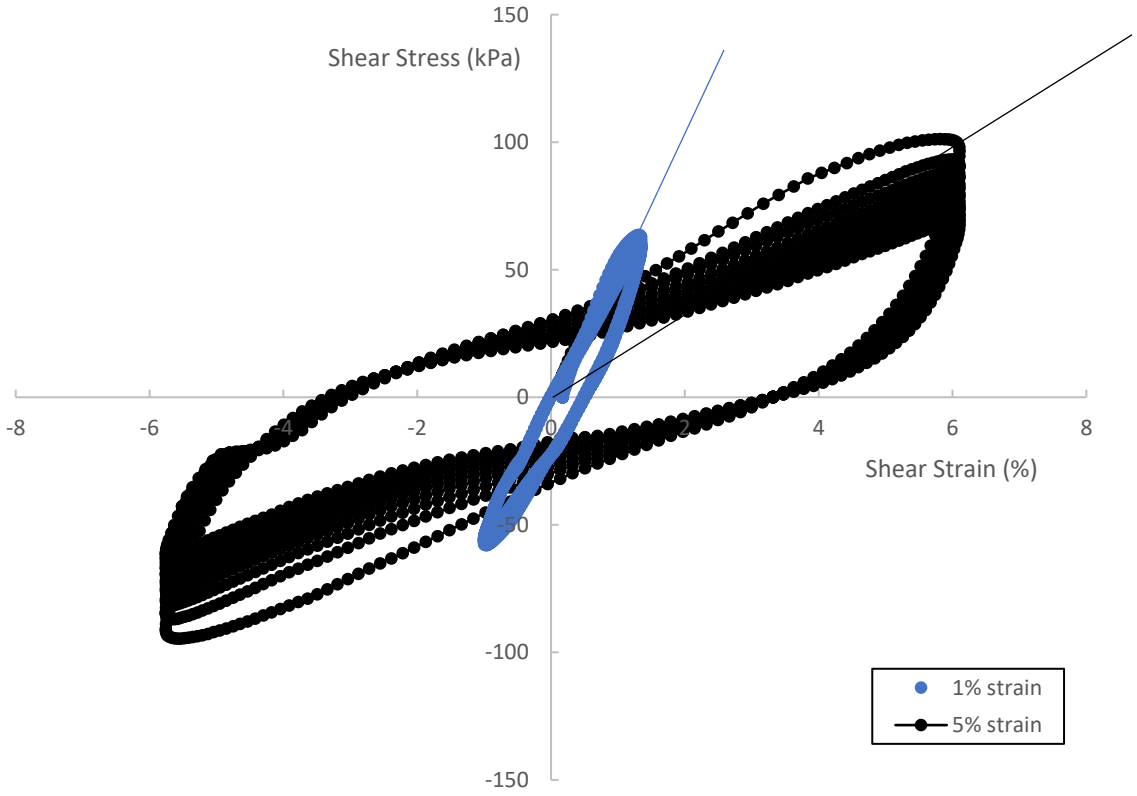

Figure 3.4: Effect of shear strain amplitude on shear modulus for large deformations.

3.5 – Performance Verification: Effect of Number of Cycles (N)

Each test will be conducted for N=10 cycles to observe the effect temperature has on the degradation of shear modulus during cyclic loading. It has been shown that under undrained cyclic loading conditions, the stiffness and strength of the soil degrades as the number of cycles increases, causing a decrease in the shear modulus of the soil specimen. The rate of decrease becomes more pronounced as the strain applied to the sample increases (Vucetic and Dobry, 1991). This effect is illustrated in Figure 3.5 and Figure 3.6. At large shear strain values, deformation increases rapidly with the number of cycles. However, at smaller shear strain values, the effect of cyclic loading is less significant.

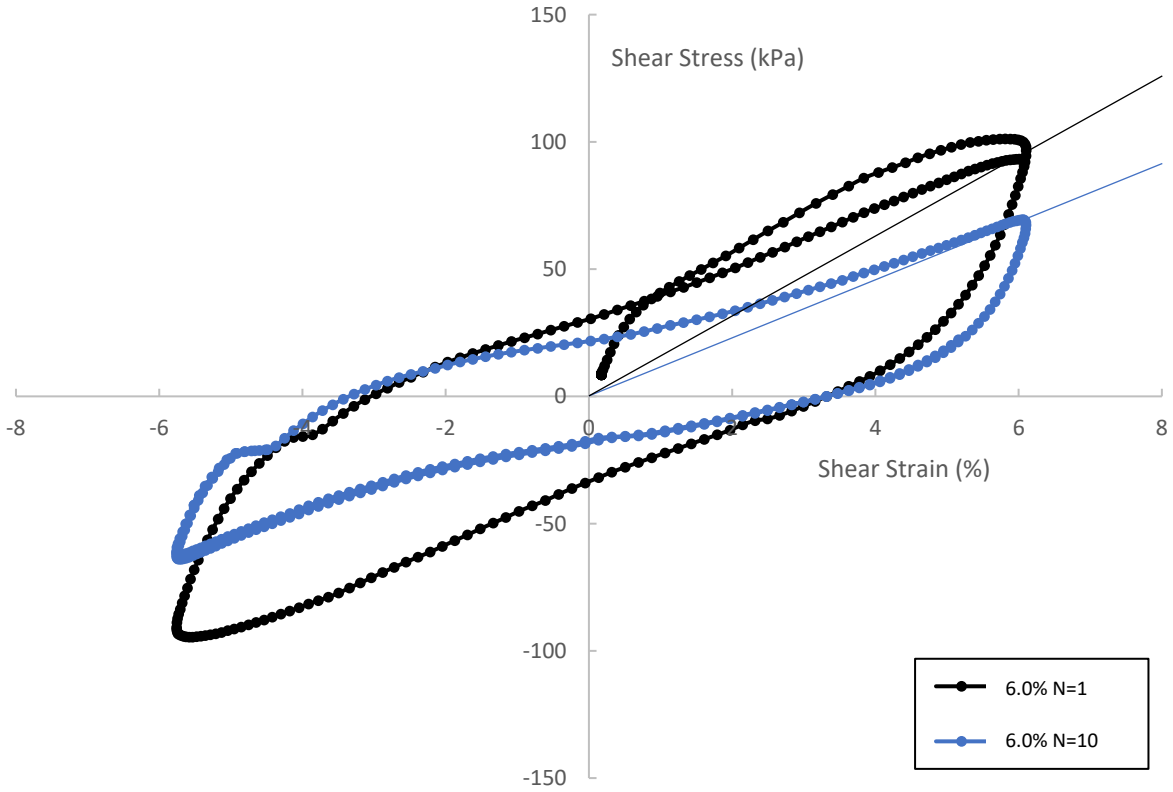

Figure 3.5: Degradation of shear modulus with number of cycles, N, for large strains.

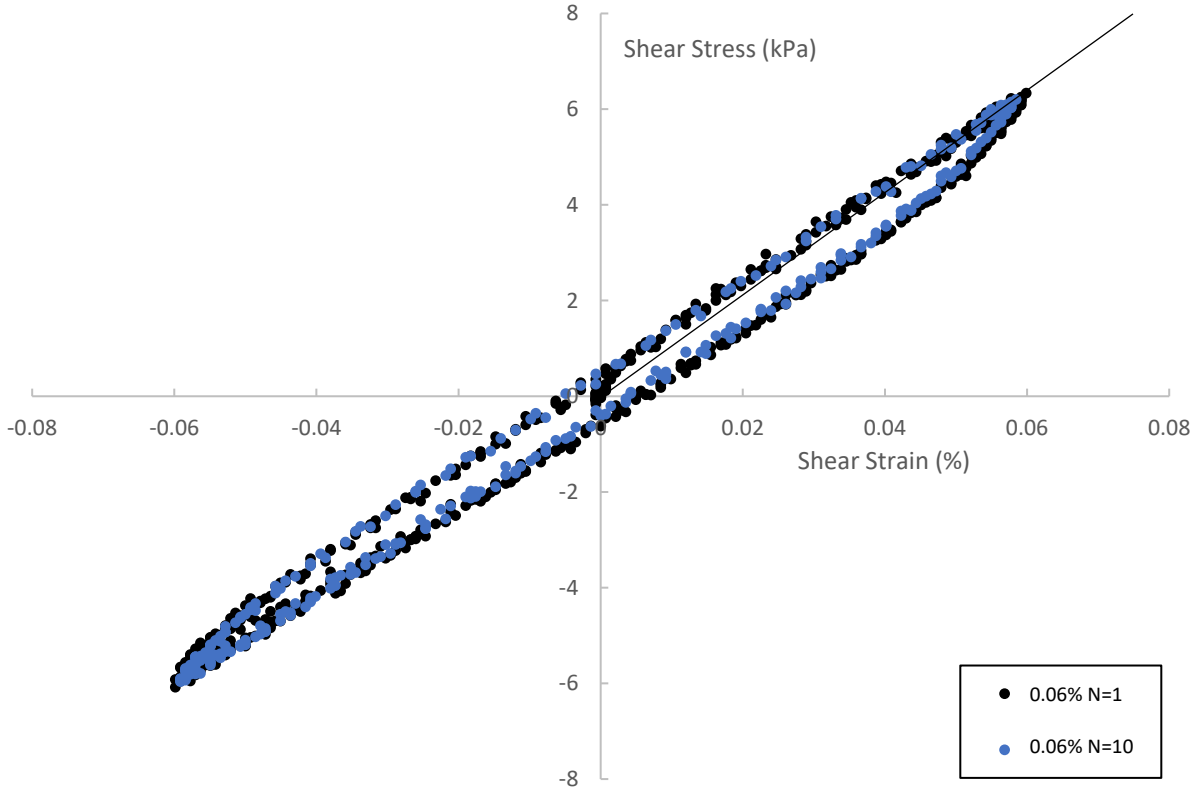

Figure 3.6: Degradation of shear modulus with number of cycles, N, for small strains.

3.6 – Performance Verification: Effect of Frequency (*f*)

While frequency is kept constant in this study, observed effects of cyclic frequency on soil stiffness are briefly reviewed. The planned testing frequency for all samples is 0.1 Hz or 1 revolution per 10 seconds. The effect of loading frequency on the cyclic response of soils varies between studies. For sand, an increase in loading frequency caused a decrease in accumulated shear strain and pore water pressure leading to a significant increase in liquefaction resistance (Nong et al., 2020). A similar trend was shown in silts. For undrained conditions, deformation accumulates faster at slower frequencies (Normandeau and Zimmie, 1991). A contradictory trend has been shown in clay. For normally consolidated, high plasticity clay, the rate of cyclic degradation increases with frequency (Mortezaie and Vucetic 2013).

3.7 – Performance Verification: Repeatability

It is important that the CSS device produces consistent results. To evaluate the consistency and repeatability of the device, three identically prepared clay soil (CL) samples were subjected to the same testing procedure and the results were compared. Figure 3.7 shows three identical cyclic simple shear tests conducted at a shear strain amplitude of 1.0%. The first cycle is highlighted for each test. The results were extremely similar with the hysteresis stress-strain response overlapping for all three tests. Shear modulus was calculated and presented along with standard deviation and coefficient of variation in Table 3.3. The low standard deviation and coefficient of variation show the consistency of the CSS device.

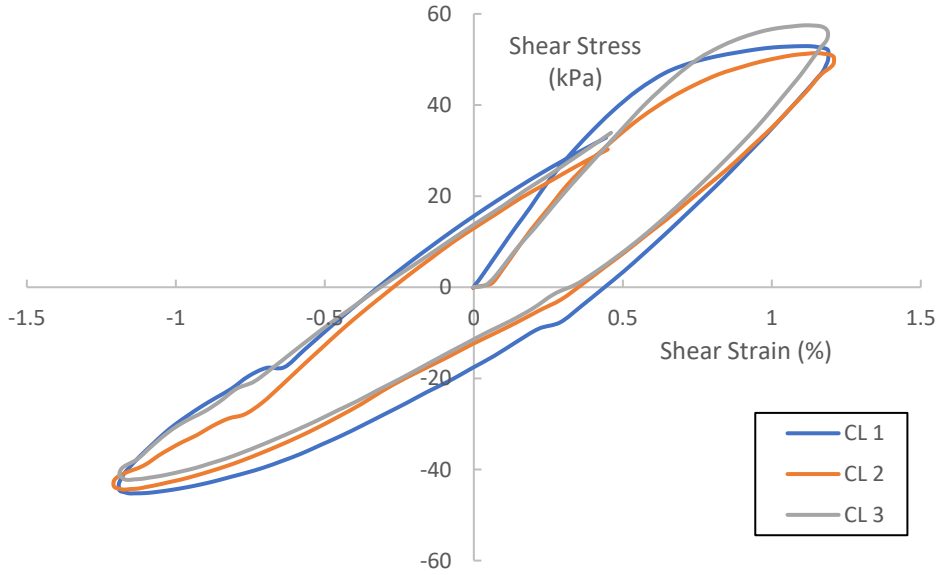

Figure 3.7: Evaluating consistency of CSS device via repeatable results from clay soil (CL) samples.

Table 3.3: Shear Modulus Deviation of CL Samples

	CL 1	CL 2	CL 3
Shear Modulus, G (MPa)	4.024	3.982	4.089
Standard Deviation	0.44		
Coefficient of Variation	0.011		

3.8 – Thermo-Controlled Test Procedure

Each test iteration requires a 24-hour period of consolidation and a 24-hour period of heating prior to testing. The soil will be consolidated under K_0 = 0.53 conditions at a total vertical stress of 20 psi (137.9 kPa) and a corresponding confinement of 10.6 psi (73.1 kPa). Vertical stress and confinement are slowly increased at a constant and proportional rate over a period of ten minutes until the desired values are reached. During the 24-hour consolidation period, the drainage valve is left open allowing dissipation of any increased pore pressure. After consolidation, the drainage valve is closed, and the heater is turned on. The soil undergoes a 24-hour period of undrained heating. After heating, the soil sample is subject to twenty cyclic loading tests of increasing shear strain amplitudes from 0.001% to 10.0%. Each cyclic loading test involves ten cyclic load applications. After completion of all twenty cyclic loading tests, the device is disassembled and prepared for the next sample at an increased temperature. Tests were conducted for temperature values of 23°C (room temperature RT), 40°C, 50°C, and 60°C at 20 psi for all three soil types: CL (dry), CL, CL (wet), ML, and SC. Figure 3.8 shows a visual depiction of the stress/thermal history induced on the soil samples prior to testing.

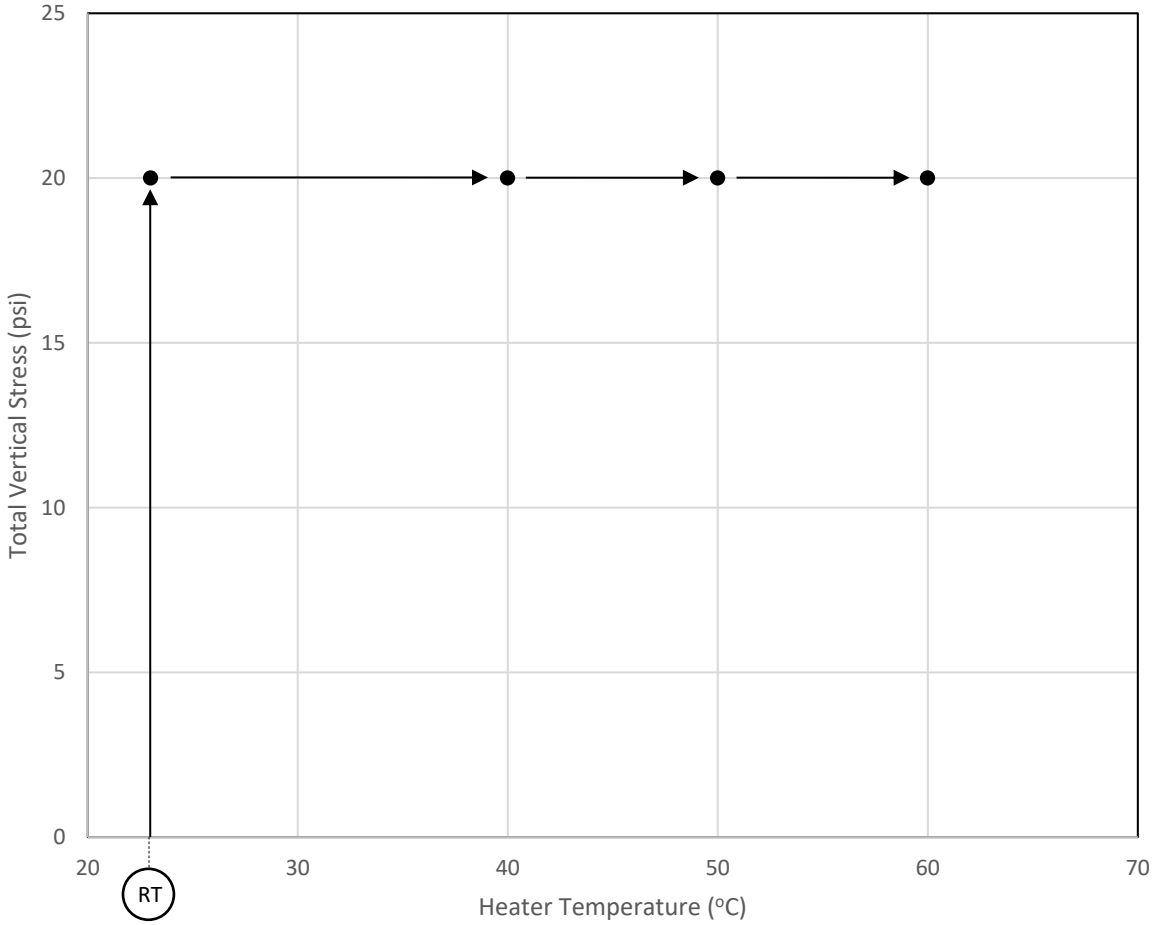

Figure 3.8: Stress/thermal history to be induced on soil samples prior to CSS testing.

Chapter 4: Thermo-Controlled Cyclic Simple Shear System

4.1 - Cyclic Simple Shear Device Main Components

The present section briefly describes the main components of the Cyclic Simple Shear Device, providing an overview of their purpose and functionality. The three main components of the Cyclic Simple Shear Device are shown in Figure 4.1. From left to right the components are: Dynamic Servo Controller, Simple Shear Frame, and Pro Dual Automatic Pressure Controller.

The Dynamic Servo Controller (DSC3000MM), left component, is a state-of-the-art dual axis electro-mechanical servo controller for dual axis dynamic testing. The device features two DSCs mounted in a cabinet. One DSC is responsible for controlling axial force or displacement and the other has the ability to dynamically control cell pressure. Key features of the DSC3000MM are built in signal conditioning, adaptive peak and trough control, numerous waveforms, fast processing and data logging, sensor and machine limit control for device protection, and high-speed USB and Ethernet connections. Figure 4.2 shows a closer view of the servo controller (VJ Tech, 2023).

The Cyclic Simple Shear frame, middle component, is composed of a stainless-steel simple shear apparatus with vertical and horizontal electromechanical dynamic actuators and an adapted triaxial type cell. The vertical and horizontal actuators are used to apply load to the sample and are controlled by the DSC3000MM. Key features of the Cyclic Simple Shear device are static or dynamic testing via servo controlled high speed motors, axial and shear stress-strain control, movable confining cell for easy sample assembly, and confining pressures up to 2000 kPa (290 psi). A detailed schematic of the Cyclic Simple Shear device is shown in Figure 4.3. The schematic shows the main components of the Cyclic Simple Shear device such as the vertical and horizontal actuators, vertical and horizontal load cells, external pressure transducer, and confinement cell (VJ Tech, 2023).

The Pro Dual Automatic Pressure Controller (Pro Dual APC), right component, is specifically designed to work with the triaxial cell used in the Cyclic Simple Shear device. It provides two independent channels for pressure control. The two independent channels allow for both cell and back pressure to be controlled from a single piece of equipment. Key features of the Pro Dual APC are compact design, touchscreen display for standalone control, two independent pressure channels, upright cylinders for easy de-airing, and built-in auto protection via sensors and limit switches. Figure 4.4 shows a closer view of the pressure controller (VJ Tech, 2023).

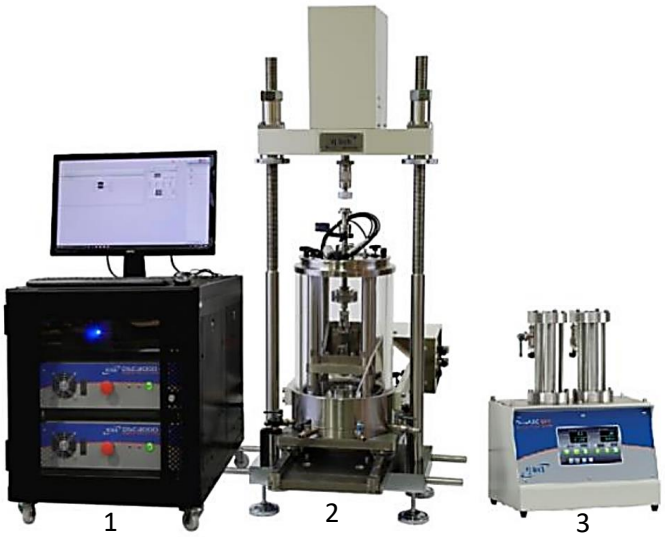

Figure 4.1: Cyclic Simple Shear Device – Main Components: 1) Dynamic Servo Controller (DSC3000MM), 2) Cyclic Simple Shear Device, 3) Pro Dual Automatic Pressure Controller (Pro Dual APC).

Figure 4.2: Dynamic Servo Controller (DSC3000MM).

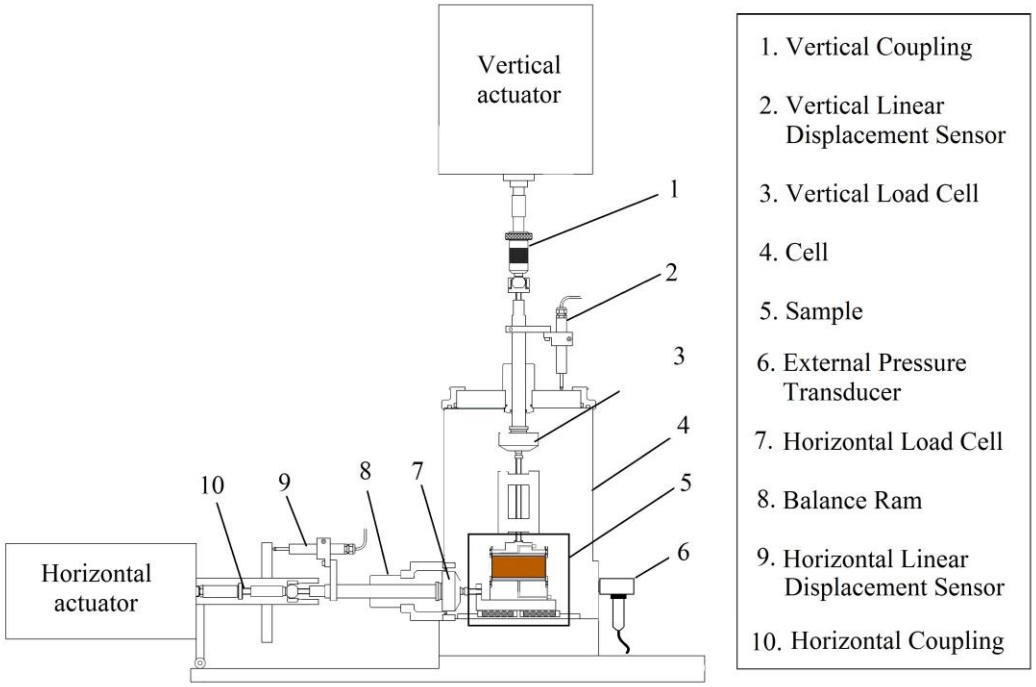

Figure 4.3: Detailed schematic of the cyclic simple shear device. (VJ Tech, 2023)

Figure 4.4: Pro Dual APC.

4.2 - Sample Preparation

Remolded soil samples were used for all three soil types. The cyclic simple shear device shipped with two devices for soil preparation. The first is the small stainless-steel ring shown below. The steel ring was designed to be pressed into a soil boring to extract an undisturbed soil sample. The second is a series of rings used to test sand.

The components shown below were designed and fabricated to allow for compaction of remolded soil samples. The components consist of the original stainless-steel ring, hollow cylindrical compaction sleeve, base plate, top plate, and solid compaction cylinder. The hollow compaction sleeve fits securely over the steel ring and into the groove in the base plate. The sleeve allows for the mold to hold loose soil prior to compacting into the steel ring. The top cap fits over the sleeve to keep it secure during the compaction process. The solid aluminum cylinder fits into the sleeve and is used to compact the soil into the steel ring.

Figures 4.5 – 4.12 show the complete sample preparation process from soil mold components, mold assembly, method of compaction, and soil extraction.

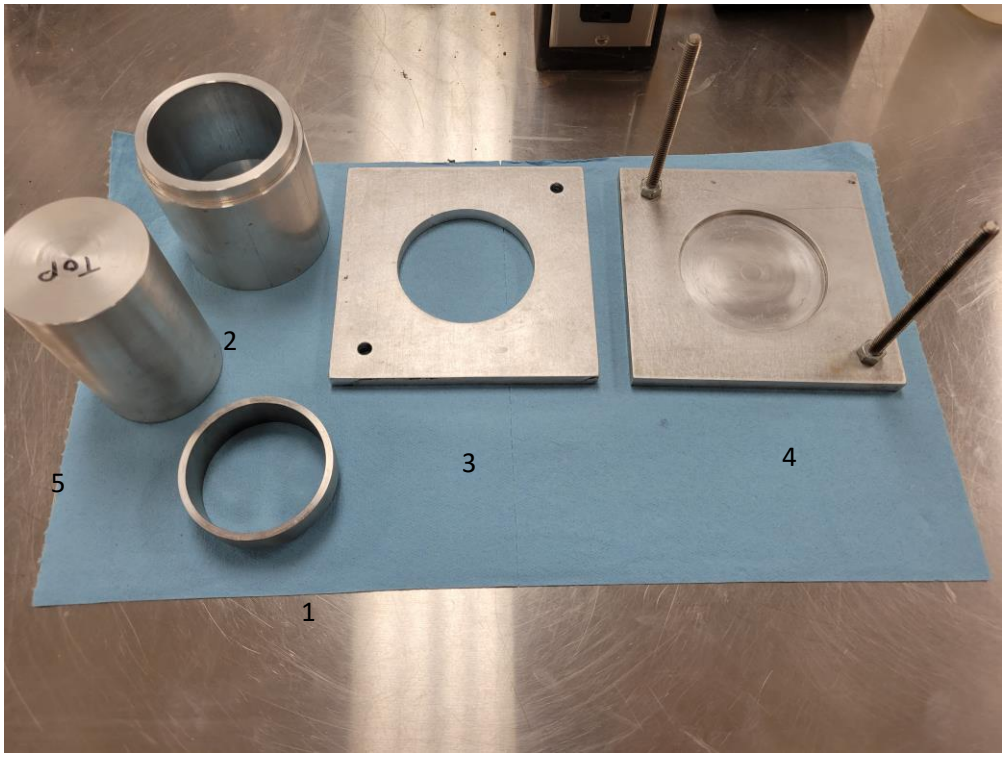

Figure 4.5: Soil compaction mold components: 1) steel ring, 2) hollow aluminum sleeve, 3) base plate, 4) top plate, 5) solid aluminum compaction cylinder.

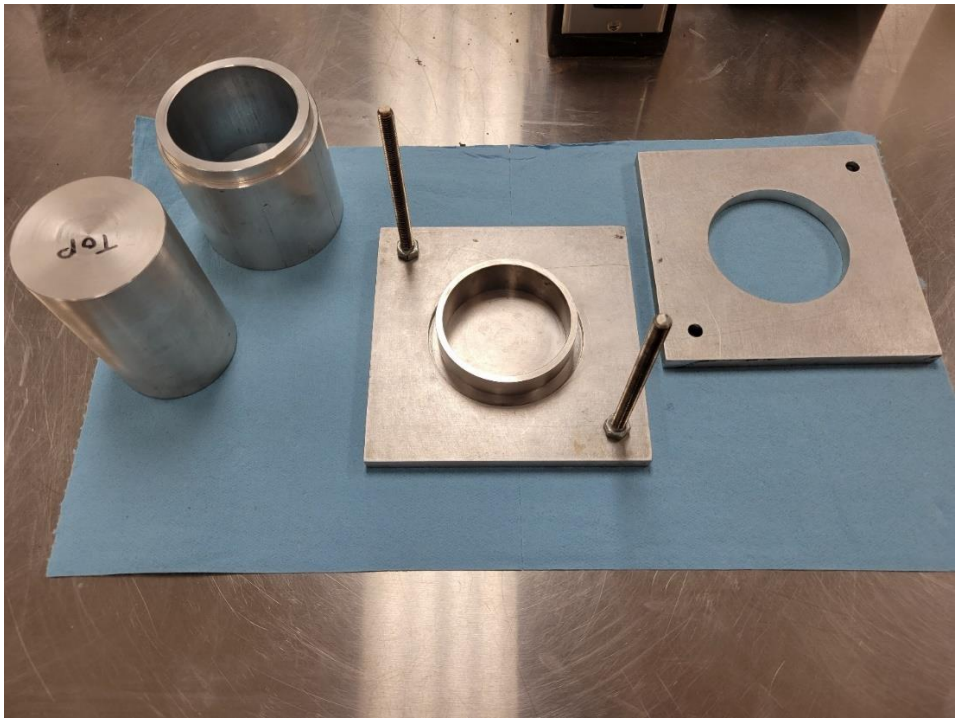

Figure 4.6: Soil compaction mold assembly process step 1: place steel ring onto base plate.

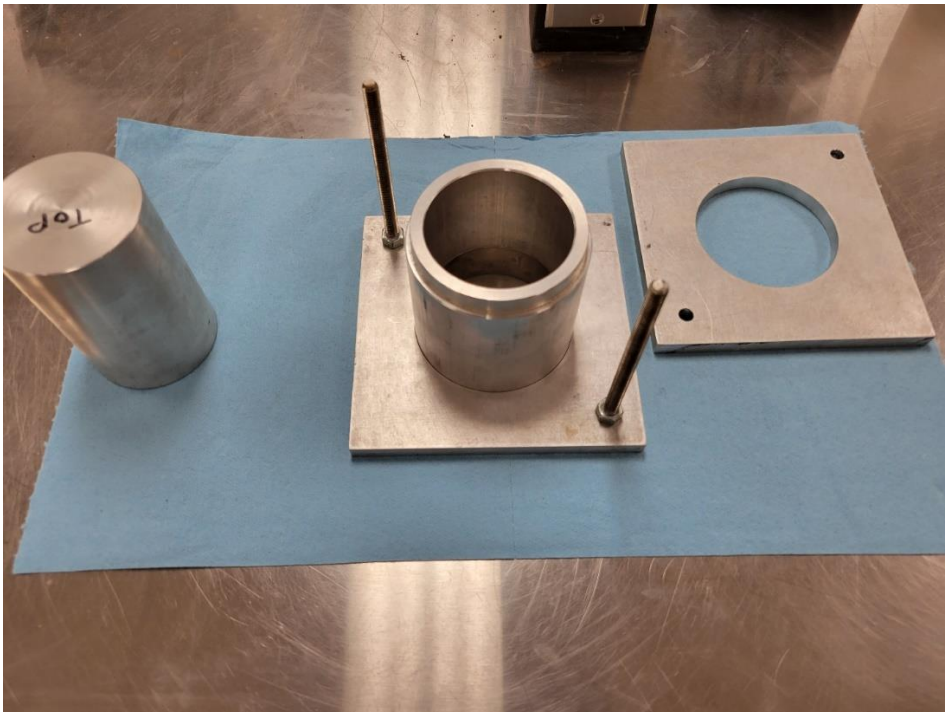

Figure 4.7: Soil compaction mold assembly process step 2: fit hollow aluminum sleeve over steel ring and securely into groove on base plate.

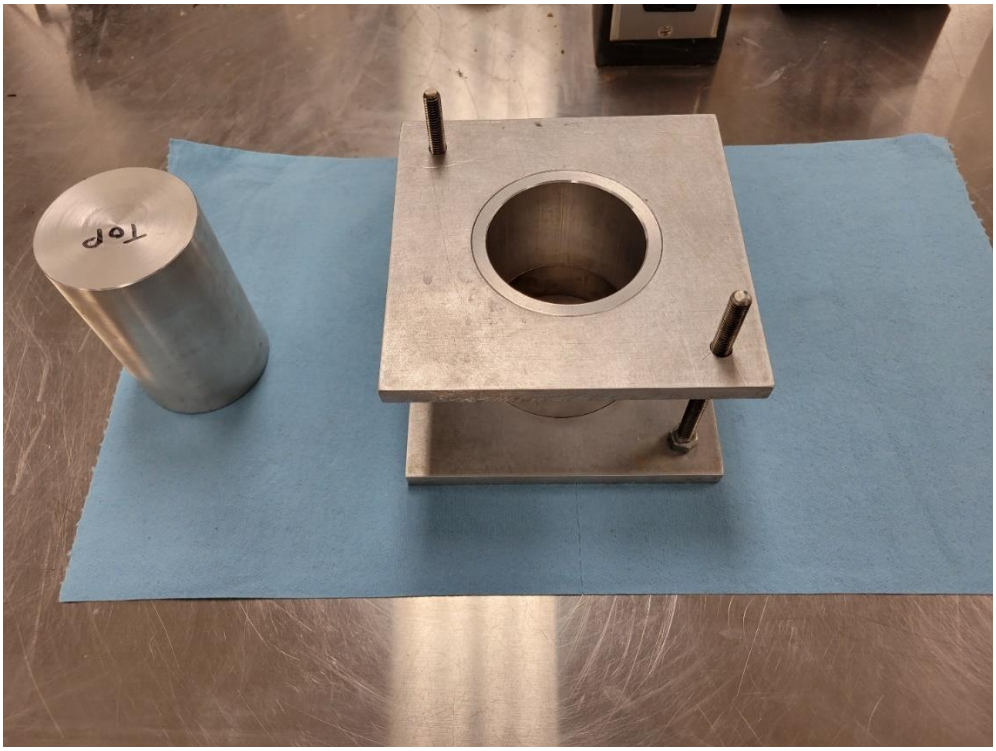

Figure 4.8: Soil compaction mold assembly process step 3: place top plate onto mold, fitting securely onto lip of hollow cylinder.

Figure 4.9: Fill mold with calculated amount of soil to achieve desired dry density after compaction.

Figure 4.10: Place solid aluminum cylinder into the mold and place mold into the compaction device.

Figure 4.11: Disassemble compaction mold to reveal steel ring with compacted soil sample.

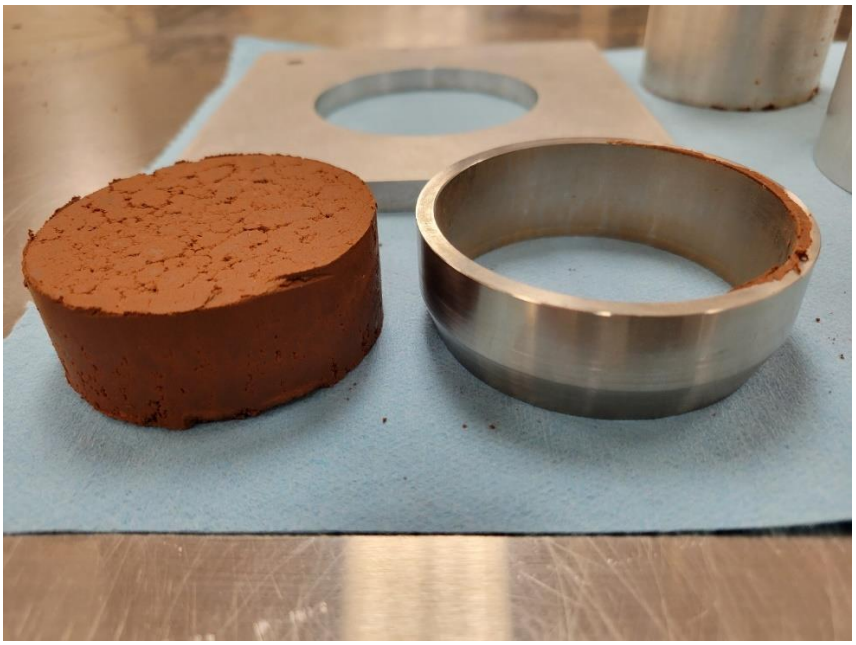

Figure 4.12: Extracted soil sample.

Table 4.1 shows the data used for determining the proper amount of soil per sample. A constant dry unit weight of 109 pcf was chosen for all three water content variations of the low plasticity clay soil (CL). Keeping dry density constant for all three clay soil samples is essential for observing the effect of water content during the heating and cyclic simple shear process. The necessary soil weight for the low plasticity silt (ML) and clayey sand (SC) samples was calculated using optimum moisture content (OMC) and maximum dry density.

The height (1.022 inches) and diameter (2.755 inches) of the soil ring was determined using a dial gauge caliper. Volume of the ring mold was calculated using Equation 4.1 and then converted to cubic feet for simplicity:

$$\text{Volume} = \text{Height} * \text{Area} \tag{4.1}$$

$$\text{Volume} = \text{Height} * \pi * r^2$$

$$\text{Volume} = 1.022 * 3.14 * 2.7552 = 6.092 \text{ in}^3 = 0.00353 \text{ ft}^3$$

Water content, w (%), and dry unit weight, γ_d (pcf), values were chosen using the compaction curve obtained from a standard proctor test. Moist unit weight, γ, was calculated using Equation 4.2:

$$\gamma = \gamma_d * (1 + w) \tag{4.2}$$

$$\gamma = 109.0 * (1 + 0.136) = 123.8 \text{ pcf}$$

Soil weight needed for each sample was calculated using Equation 4.3:

$$\text{Soil weight} = \gamma * \text{Volume} \tag{4.3}$$

$$\text{Soil weight} = 123.8 * 0.00353 = 0.4365 \text{ lbs}$$

Table 4.1: Data for Soil Weight Calculation

Soil Type	w(%)	γ_d (pcf)	γ (pcf)	Volume Mold (ft^3)	Soil Weight (lbs)
CL	OMC (13.6)	109.0	123.8	0.00353	0.4365
	Dry (9.0)	109.0	118.8		0.4190
	Wet (17.0)	109.0	127.5		0.4500
ML	OMC (14.8)	106.6	122.4		0.4280
SC	OMC (10.0)	126.5	139.2		0.4860

Table 4.2 highlights the soil weight needed per sample for each soil type. The values in the table represent moist weight and assume the soil has already been mixed with the necessary amount of water to achieve the desired moisture content. Water is added to one pound of dry soil and mixed thoroughly. To determine the amount of water required for each moisture content Equation 4.4 is used:

$$w = \frac{\text{weight of water}}{\text{weight of dry soil}} \tag{4.4}$$

$$0.136 = \frac{\text{weight of water}}{1 \text{ lbs}}$$

$$\text{weight of water} = 0.136 \text{ lbs}$$

Table 4.2: Soil Weight Needed Per Sample

Soil Weight (lbs.) per Sample				
CL			ML	SC
OMC (13.6%)	Dry (9%)	Wet (17%)	OMC (14.8%)	OMC (10%)
0.4365	0.4190	0.4500	0.4280	0.4860

4.3 - Step by Step Assembly Process

Figures 4.12 - 4.14 show the components of the sample pedestal, vertical bearing assembly, and confining cell.

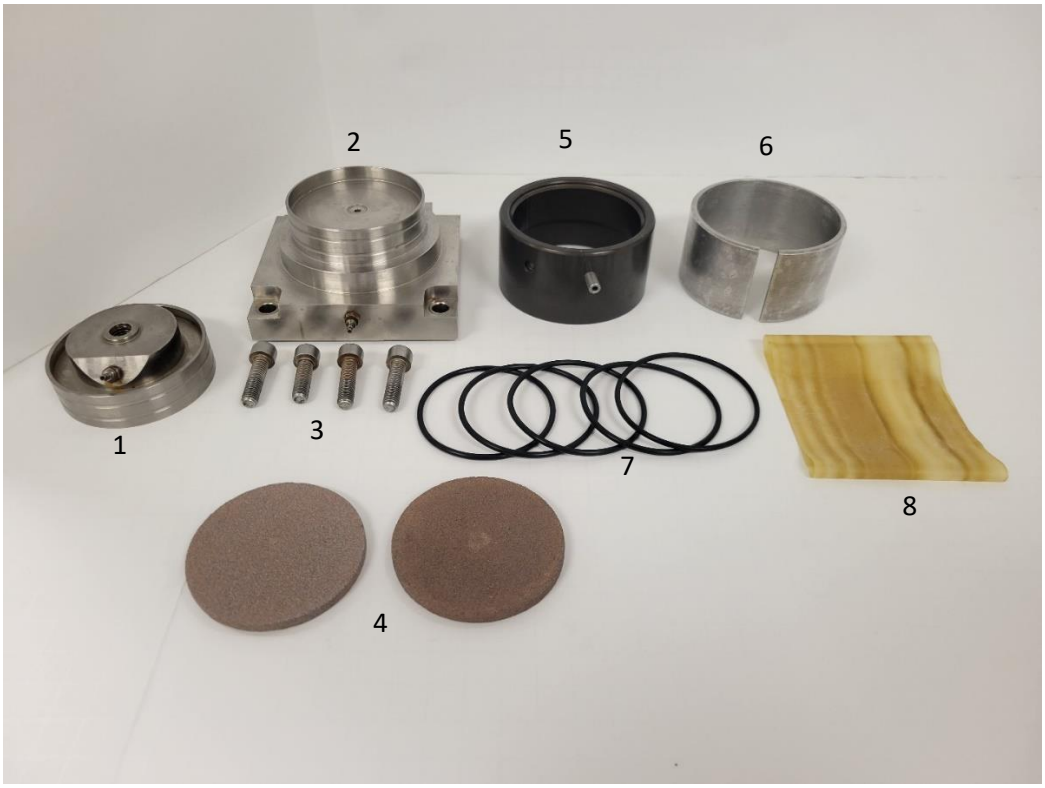

Figure 4.13: Sample pedestal components: 1) skirted top cap, 2) skirted base pedestal, 3) 4 screws, 4) 2 porous discs, 5) sample former, 6) O-Ring tool, 7) 5 rubber O-Rings, 8) standard latex membrane.

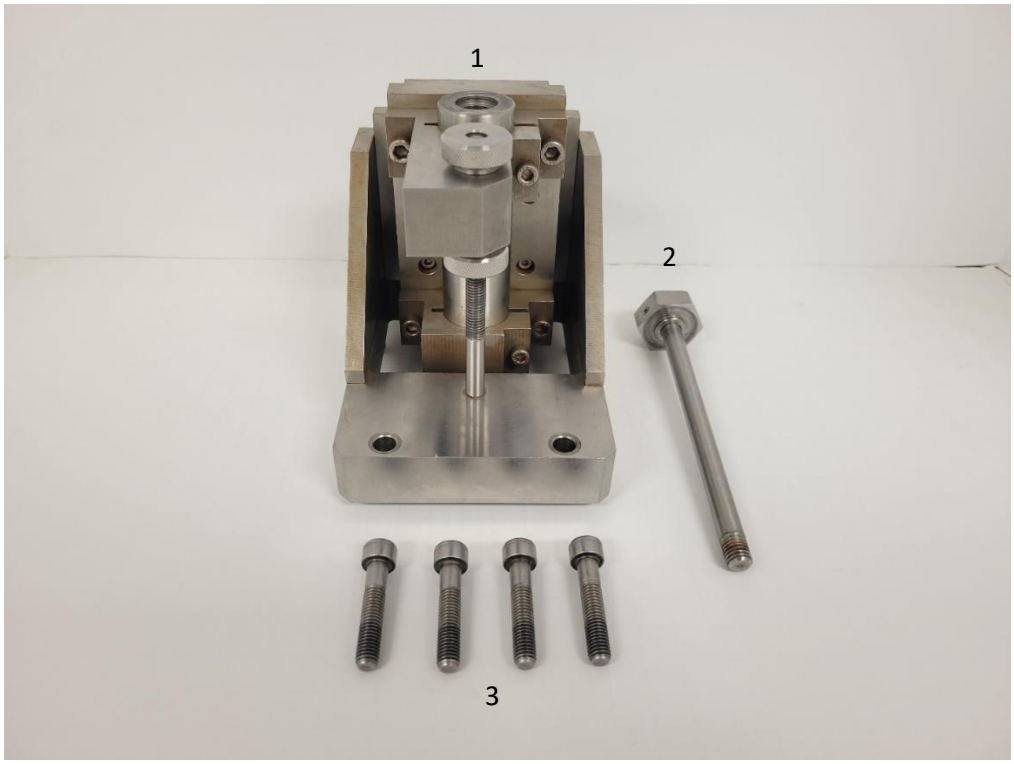

Figure 4.14: 1) Vertical bearing assembly, 2) top cap spindle, 3) 4 screws.

Figure 4.15: 1) Plexiglass cell wall, 2) cell top, 3) 4 washers and nuts.

Figures 4.15 – 4.41 show the step-by-step assembly process of the sample pedestal and confining cell. Detailed instructions are provided with each picture to clearly explain how to properly assemble the device.

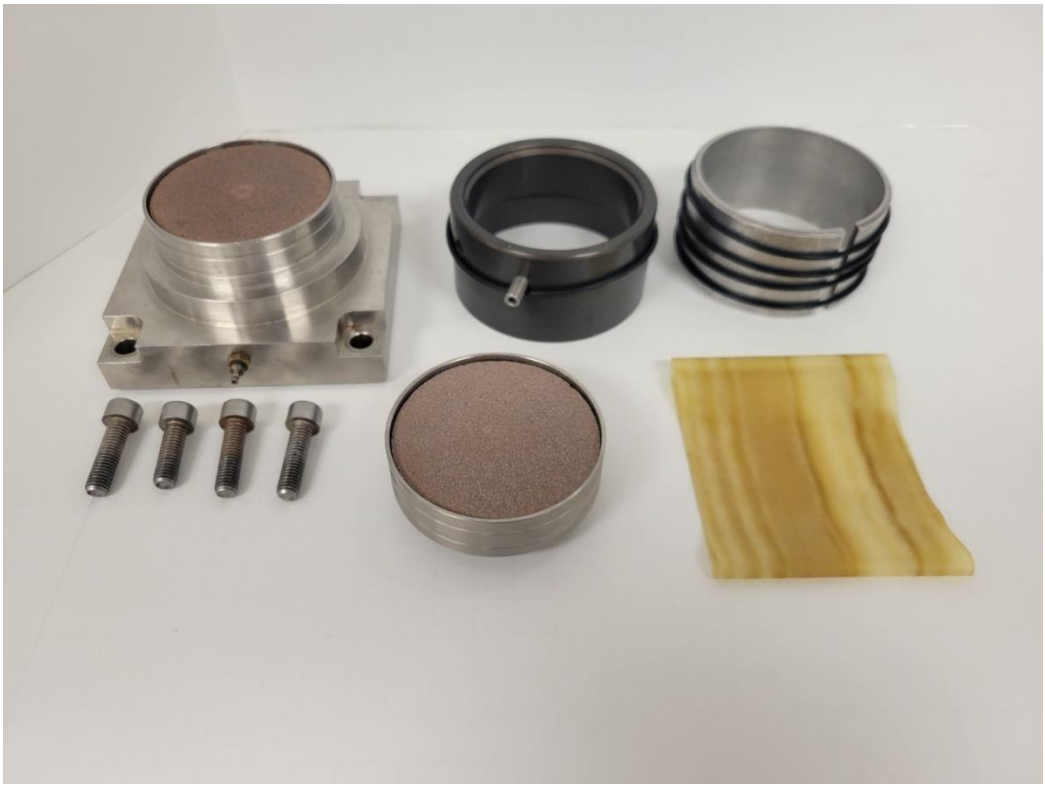

Figure 4.16: Sample pedestal assembly step 1: place porous discs in top cap and base pedestal, place 4 rubber O-Rings on O-Ring tool and 1 rubber O-Ring on the sample former.

Figure 4.17: Sample pedestal assembly step 2: place standard latex membrane on base pedestal and use O-Ring tool to place 2 rubber O-Rings over the membrane and into the grooves in the base pedestal, firmly securing the membrane to the base.

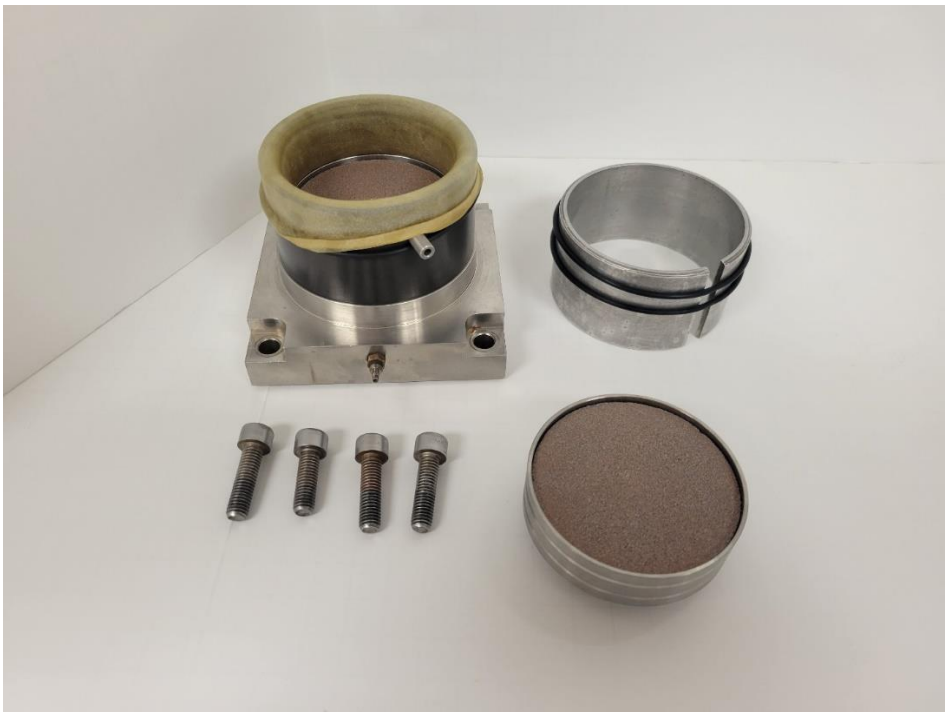

Figure 4.18: Sample pedestal assembly step 3: place the sample former over the membrane onto the base pedestal, fold the top of the membrane over the sample former as shown.

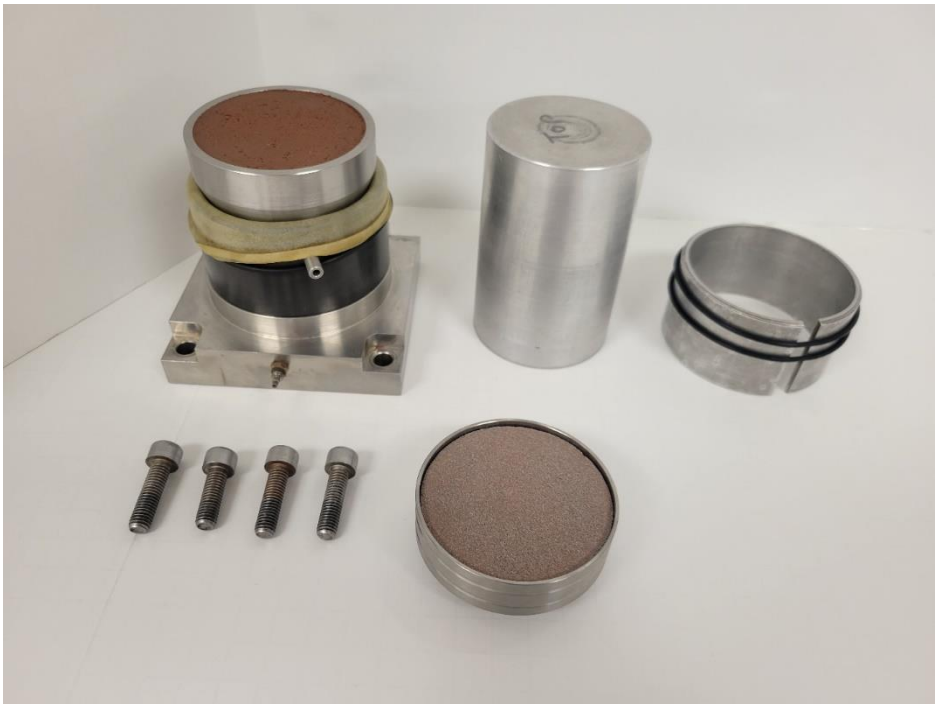

Figure 4.19: Sample pedestal assembly step 4: place the sample ring with the remolded soil sample onto the sample former.

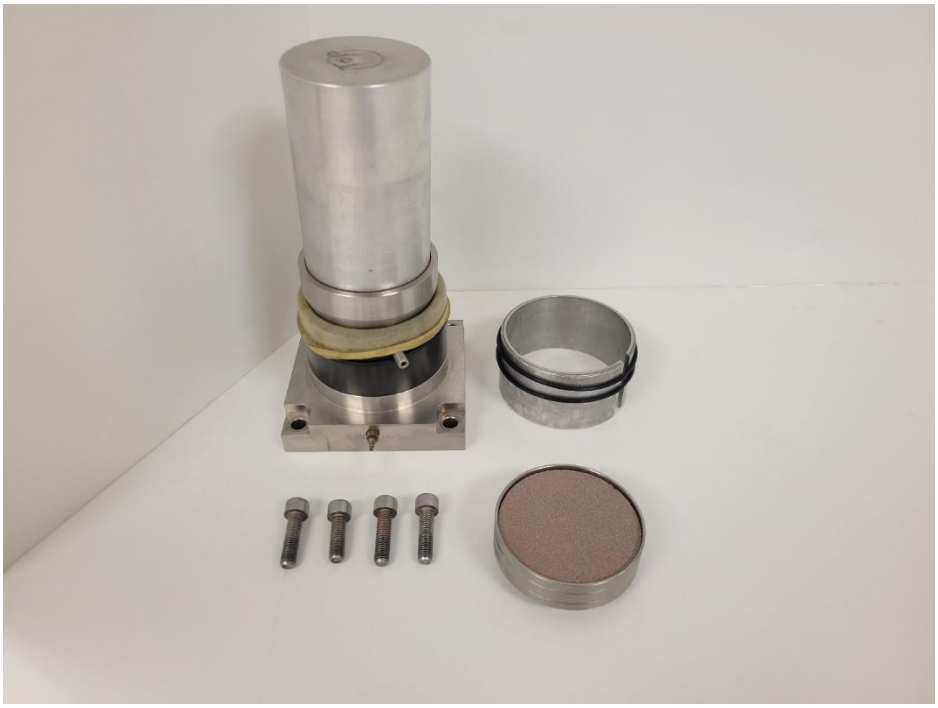

Figure 4.20: Sample pedestal assembly step 5: place solid aluminum compaction cylinder on top of sample and push on the compaction cylinder to force the remolded sample out of the sample ring and into the sample former and latex membrane.

Figure 4.21: Sample pedestal assembly step 6: remove solid aluminum compaction cylinder and sample ring from the sample pedestal.

Figure 4.22: Sample pedestal assembly step 7: place top cap onto sample former and press down lightly to seat top cap onto sample. Take care to ensure that the valve on the base plate is pointing the same direction as the valve on the top cap for easy assembly.

Figure 4.23: Sample pedestal assembly step 8: pull latex membrane over top cap and remove sample former. To remove sample former, roll rubber O-Ring down off of the sample former and onto the base plate as shown. May need to carefully adjust membrane and top cap to ensure membrane is pulled tight with no creases or folds.

Figure 4.24: Sample pedestal assembly step 9: Use the O-Ring tool to place the last 2 rubber O-Rings onto the latex membrane and into the grooves in the top cap, firmly securing the membrane to the top cap. Fold the membrane down to expose the valve in the top cap.

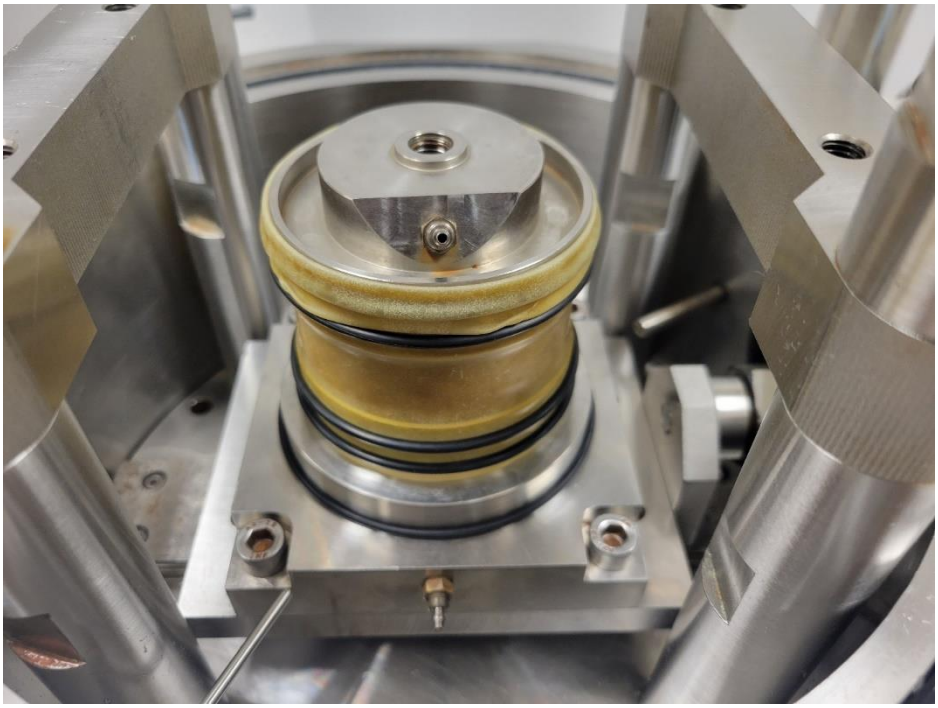

Figure 4.25: Confining cell assembly step 1: place the assembled sample pedestal onto the horizontal carriage and use the 4 screws to securely attach the two pieces. Take care to ensure the 2 valves are pointed to the side of the cell for easy connection to the back pressure and pore pressure lines.

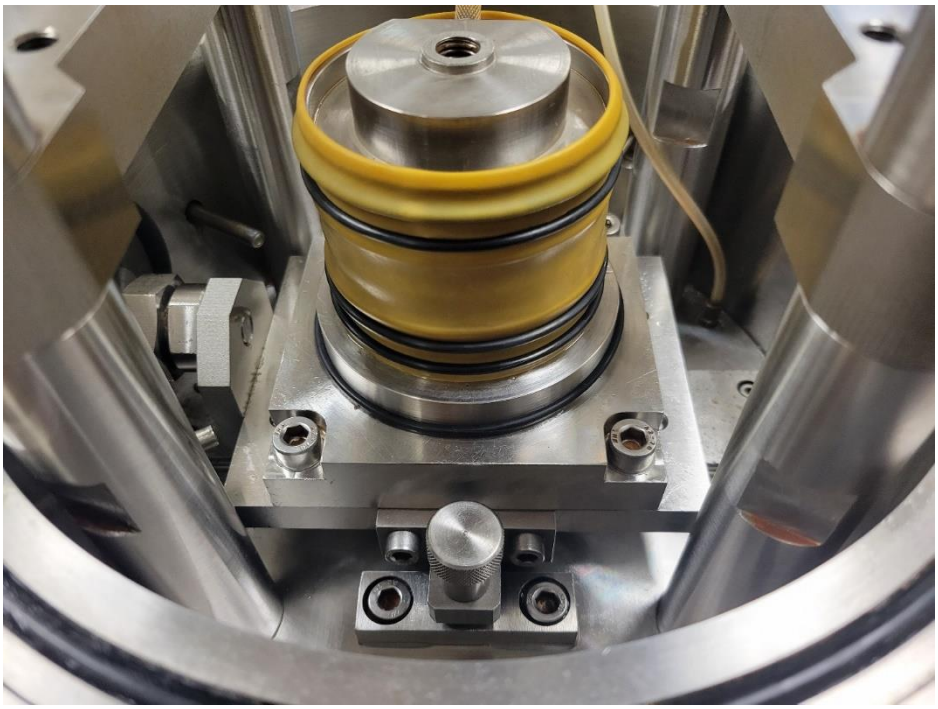

Figure 4.26: Confining cell assembly step 2: move the horizontal carriage into a central position and use the securing pin to lock the carriage in place for the next few steps of the assembly process.

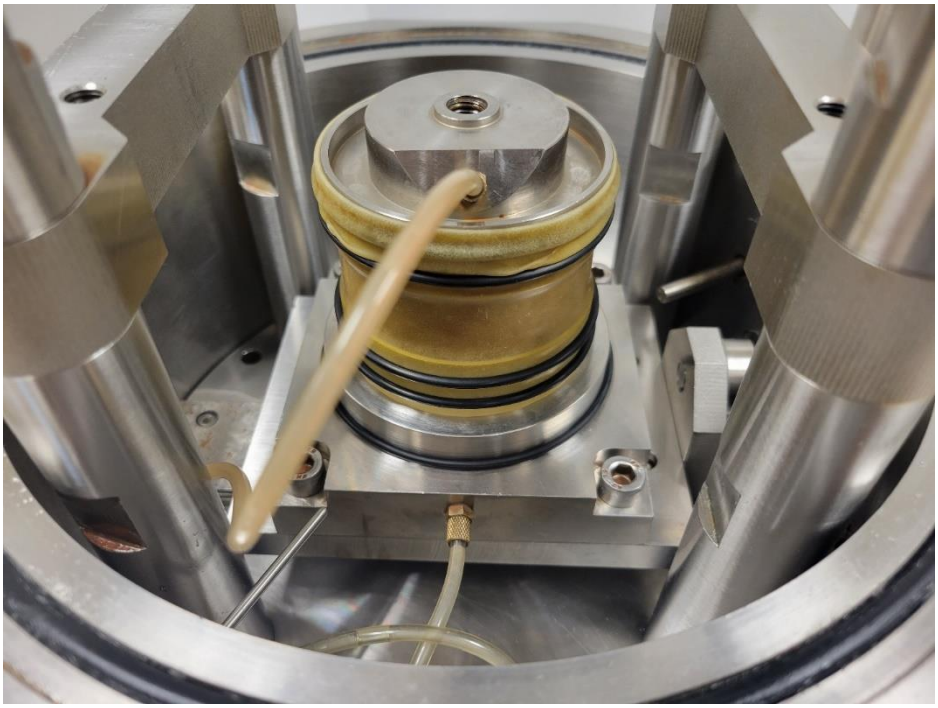

Figure 4.27: Confining cell assembly step 3: connect the pore water pressure line to the valve in the base pedestal and connect the back pressure line to the valve in the top cap. Tighten the milled nuts securely by hand.

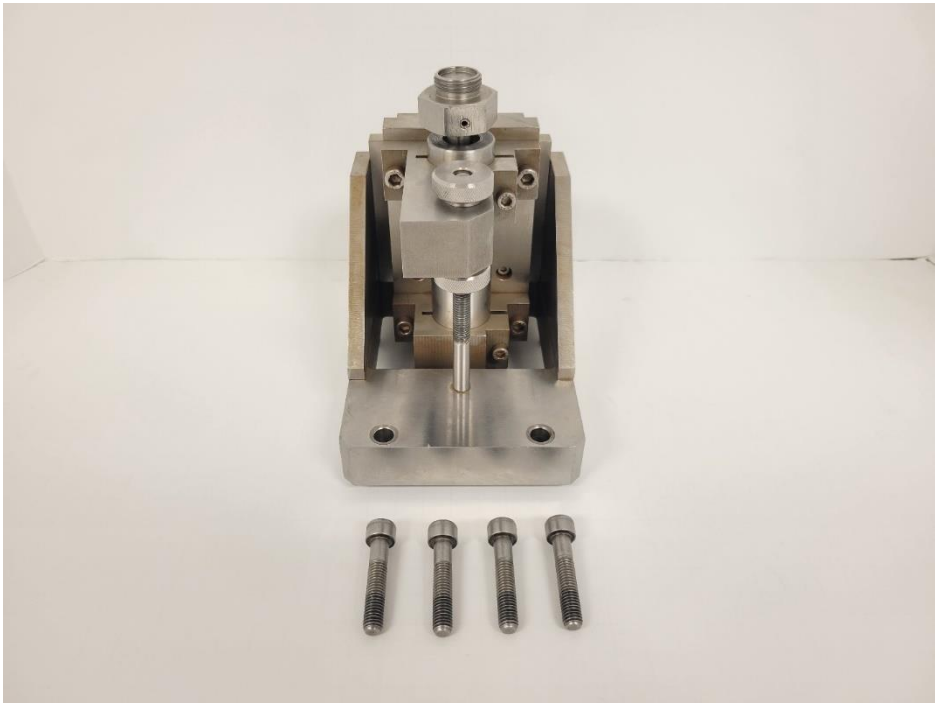

Figure 4.28: Confining cell assembly step 4: insert the top cap spindle into the vertical bearing assembly and use the two milled knobs to lock the vertical bearing assembly into its highest position.

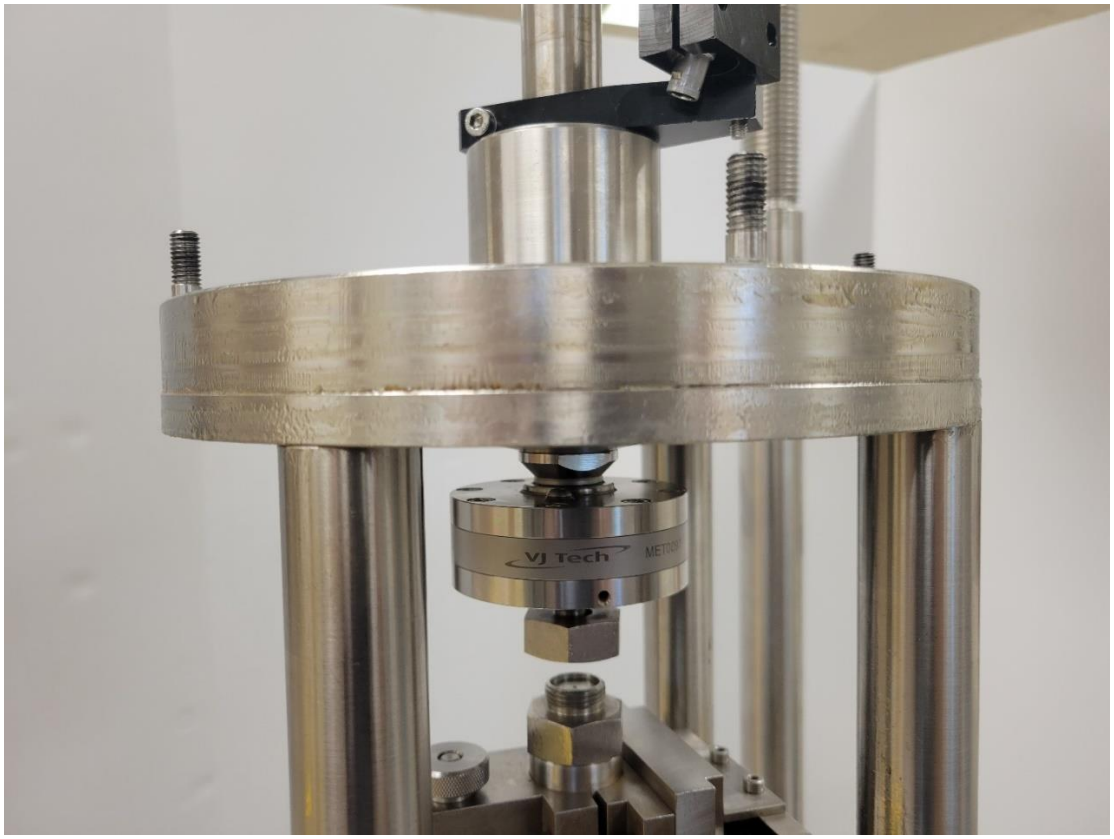

Figure 4.29: Confining cell assembly step 5: lift the vertical load ram as high as possible and lock the ram into position using the bracket as shown.

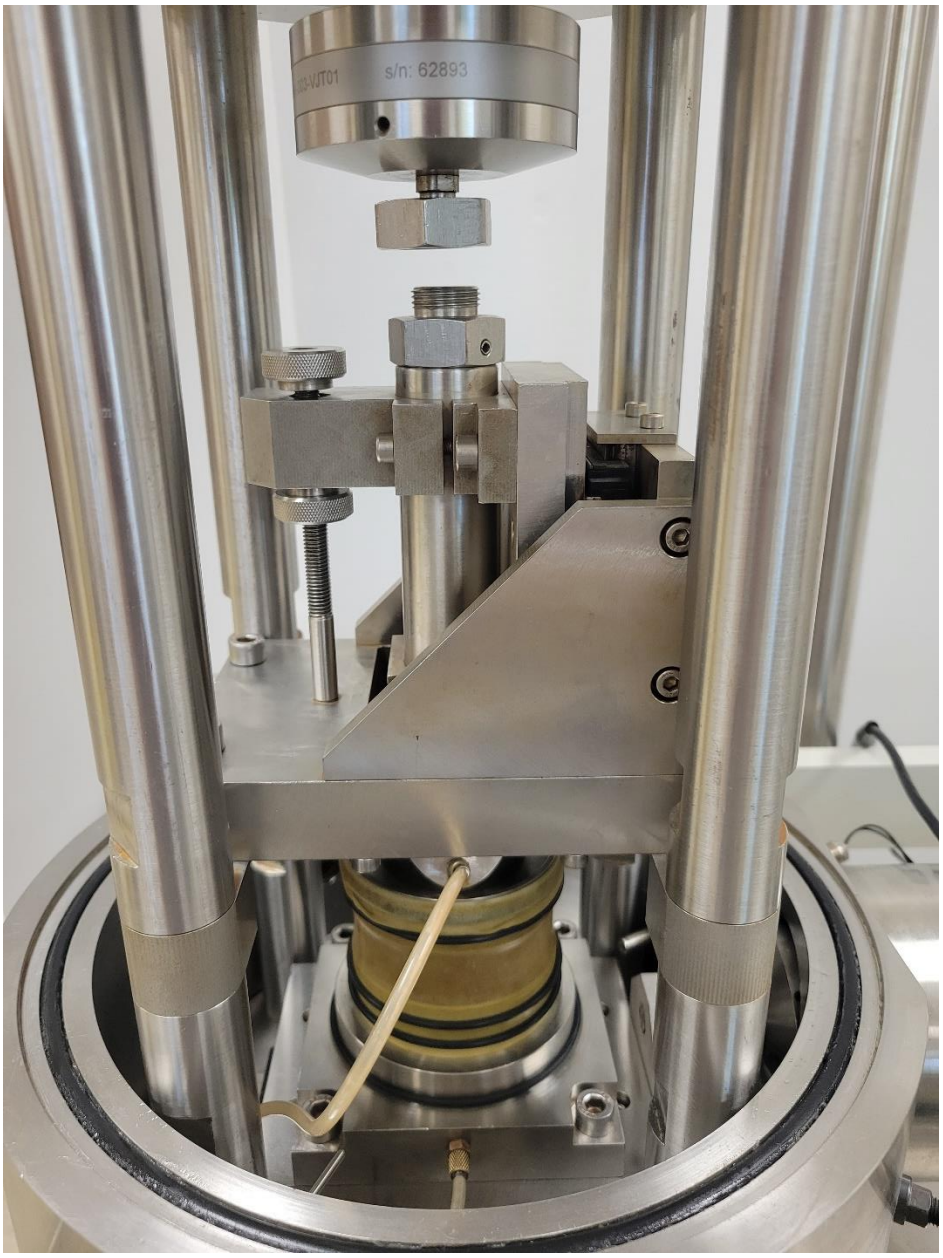

Figure 4.30: Confining cell assembly step 6: insert the 4 screws into the vertical bearing assembly and loosely attach the vertical bearing assembly to the confining cell frame.

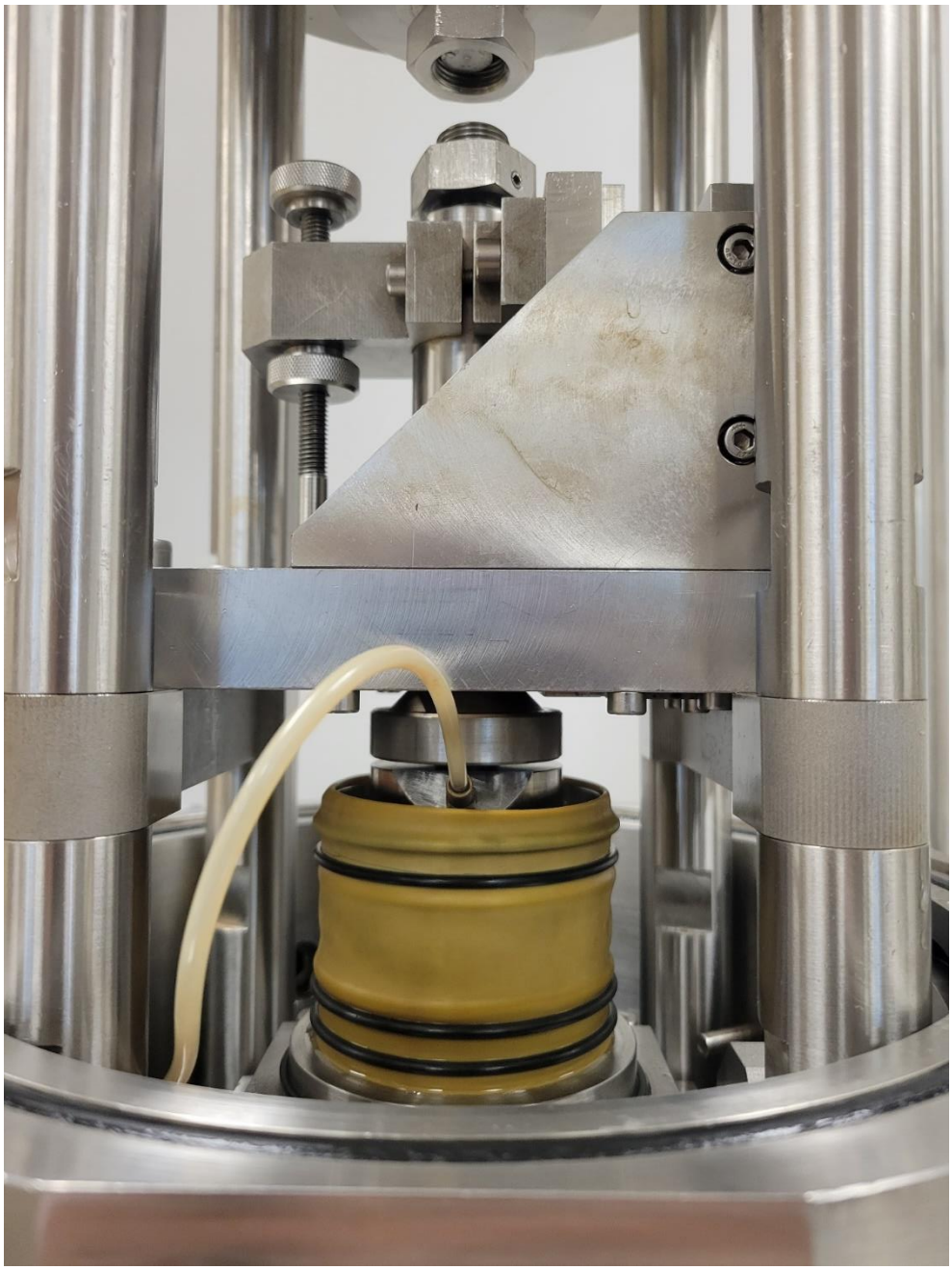

Figure 4.31: Confining cell assembly step 7: use the bottom milled knob to carefully lower the vertical bearing assembly onto the sample top cap.

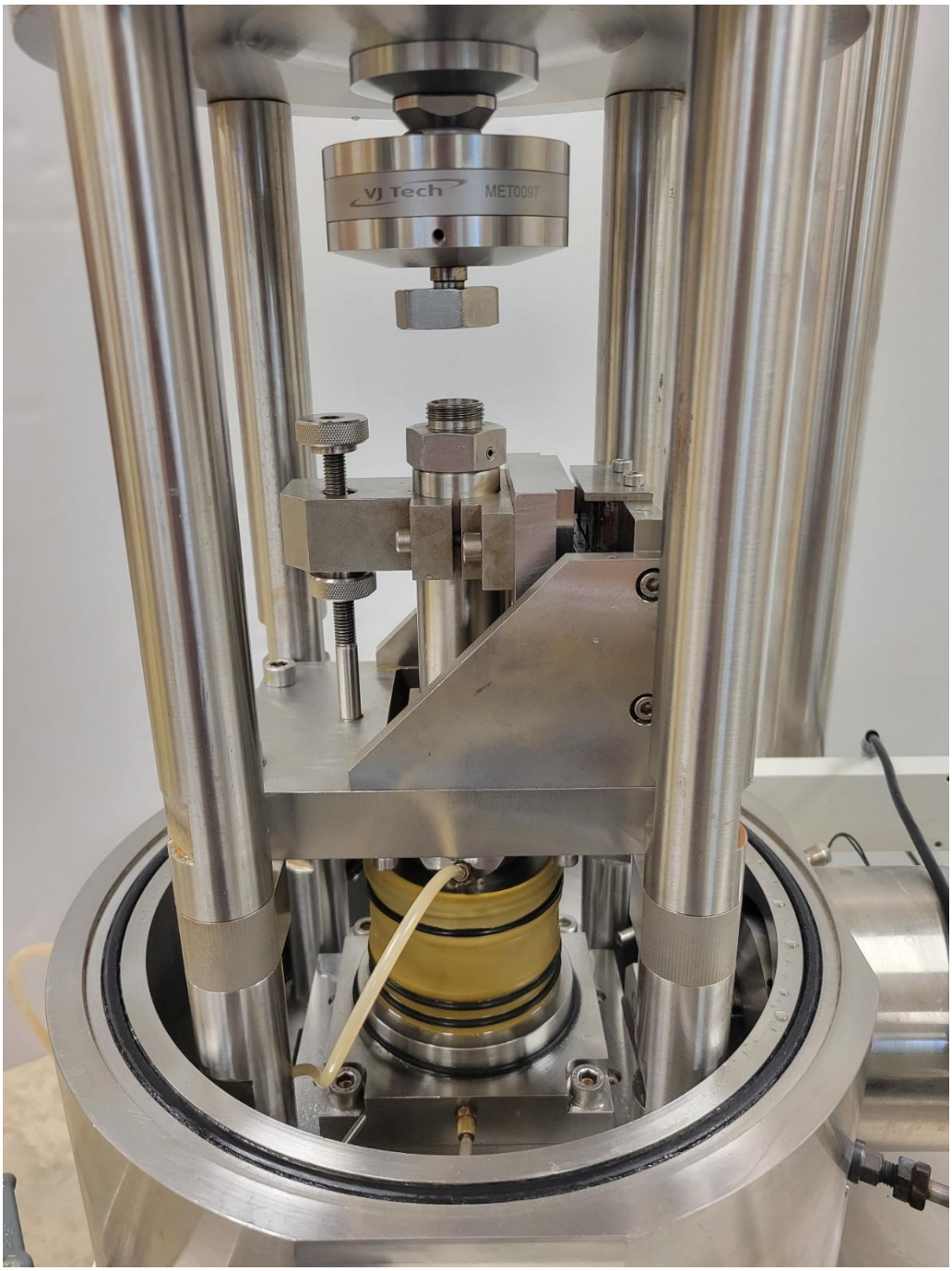

Figure 4.32: Confining cell assembly step 8: tighten the top cap spindle securing it firmly to the sample top cap. This should be as tight as possible. Finish tightening the 4 screws securing the vertical bearing assembly.

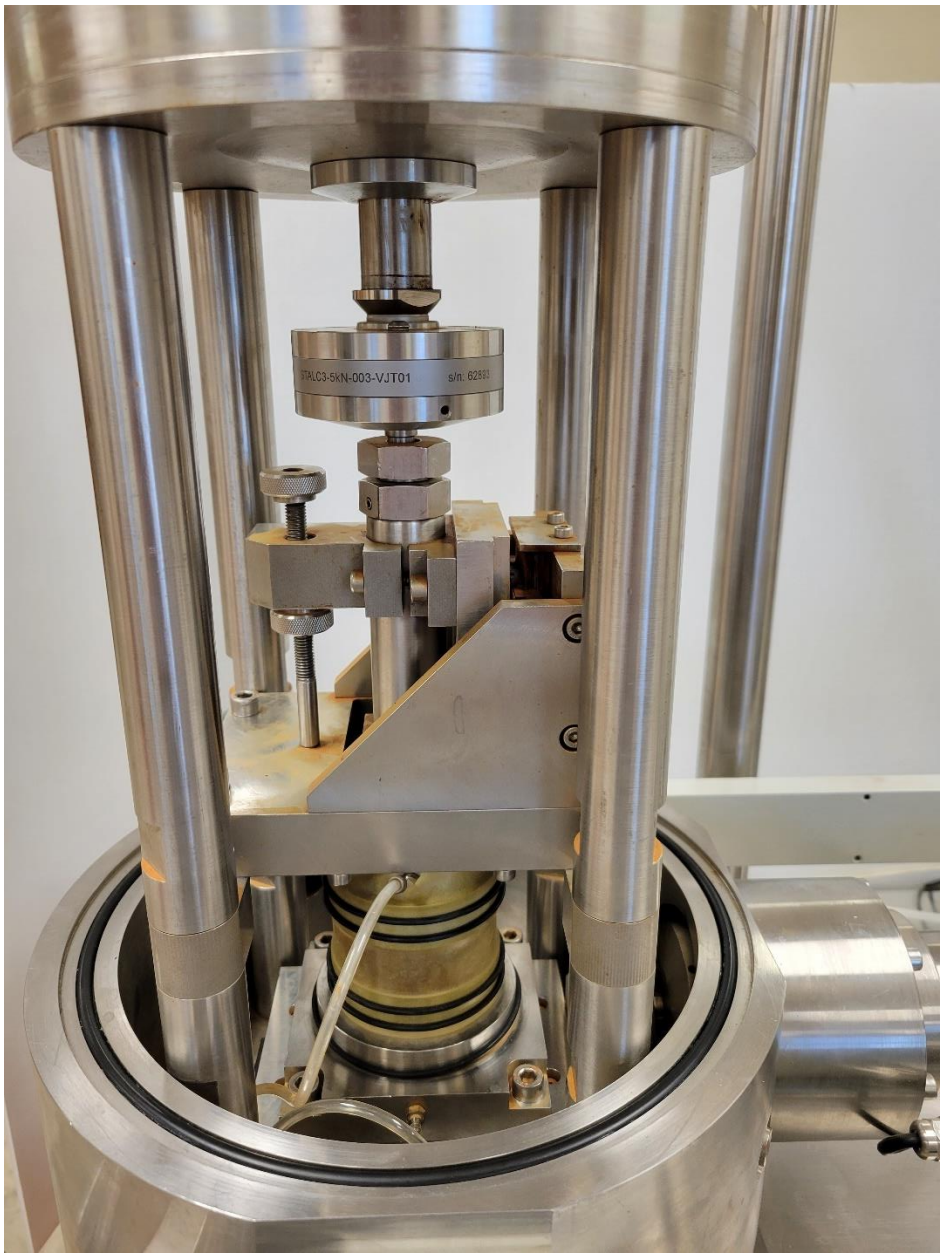

Figure 4.33: Confining cell assembly step 9: loosen the top bracket and gently slide the vertical load ram onto the vertical bearing assembly. Secure the vertical load ram to the vertical bearing assembly. Securely tighten the top bracket again.

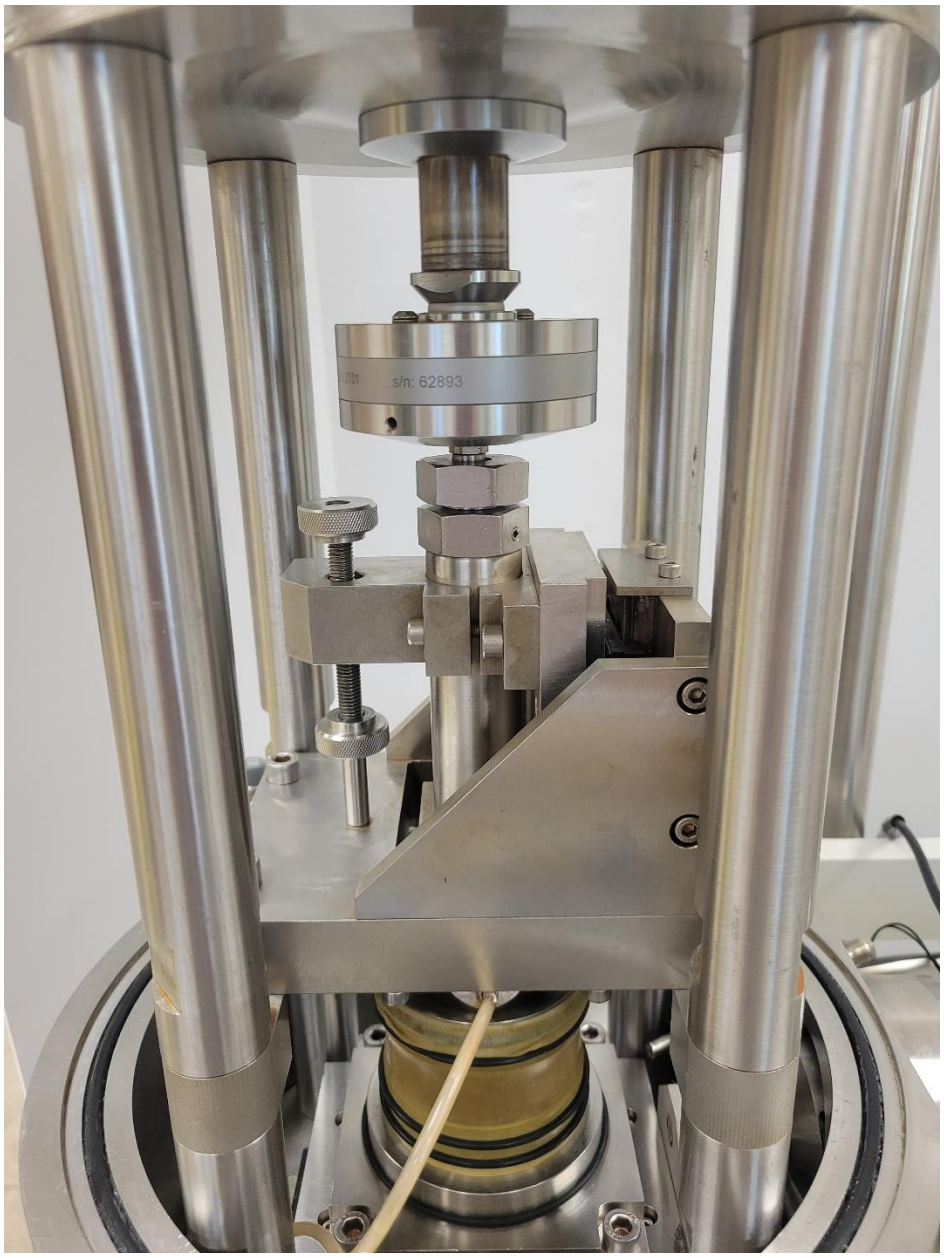

Figure 4.34: Confining cell assembly step 10: move the two milled knobs on the vertical bearing into the highest and lowest positions possible. The top knob should be as high as possible, the bottom knob should be as low as possible. Remove the horizontal carriage securing pin.

Figure 4.35: Confining cell assembly step 11: place the cell wall over the cell base. Make sure the cell wall is seated centrally on the base.

Figure 4.36: Confining cell assembly step 12: place the cell top onto the cell wall such that the 4 screw heads on the cell body come out of the 4 holes in the cell top. Push down on the cell top until it drops down into a secure position. Place a washer and nut on each screw head and cross tighten to seal the top cap.

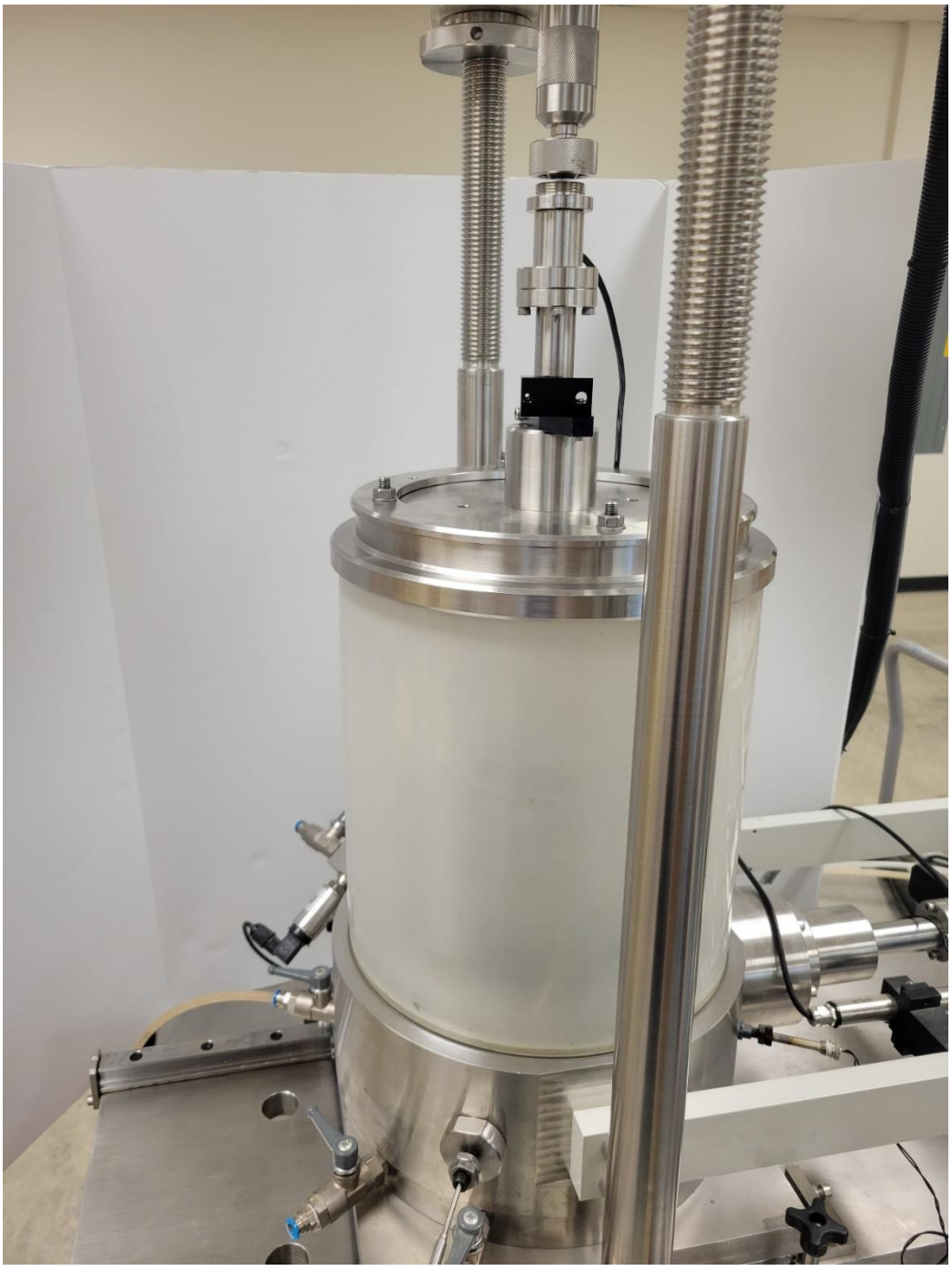

Figure 4.37: Confining cell assembly step 13: push the cell back into position under the cross beam of the vertical servo.

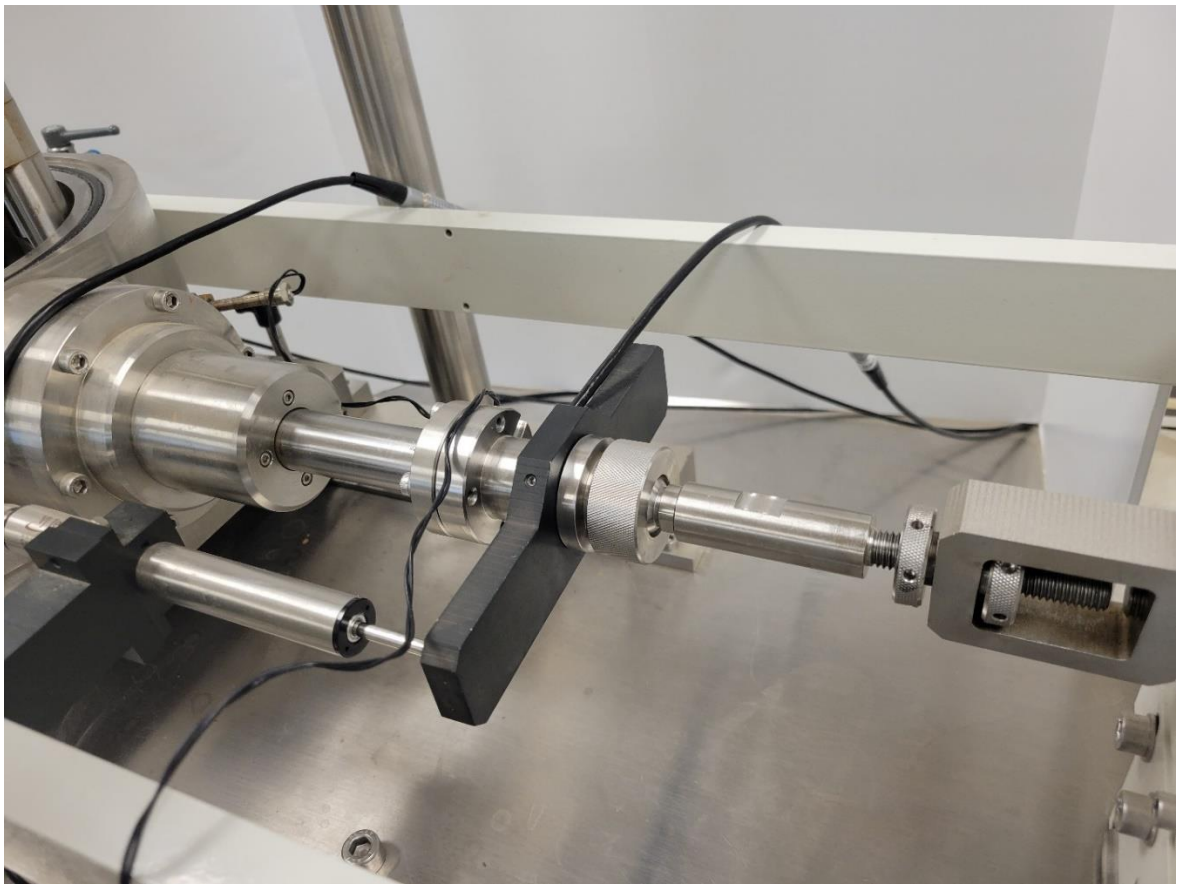

Figure 4.38: Confining cell assembly step 14: connect the horizontal ram to the horizontal servo. Adjust the adapter until the ball and cup joint are touching then use the milled nut to secure the ram. Make sure not to apply load to the sample.

Figure 4.39: Confining cell assembly step 15: connect the vertical ram to the vertical servo. Adjust the adapter until the ball and cup joint are touching then use the milled nut to secure the vertical ram similar to the process followed for the horizontal ram. Do not apply load to the sample. Loosen the top bracket and move into a neutral position.

Figure 4.40: Confining cell assembly step 16: fit the two securing clamps onto the confining cell carriage to securely lock the cell into testing position.

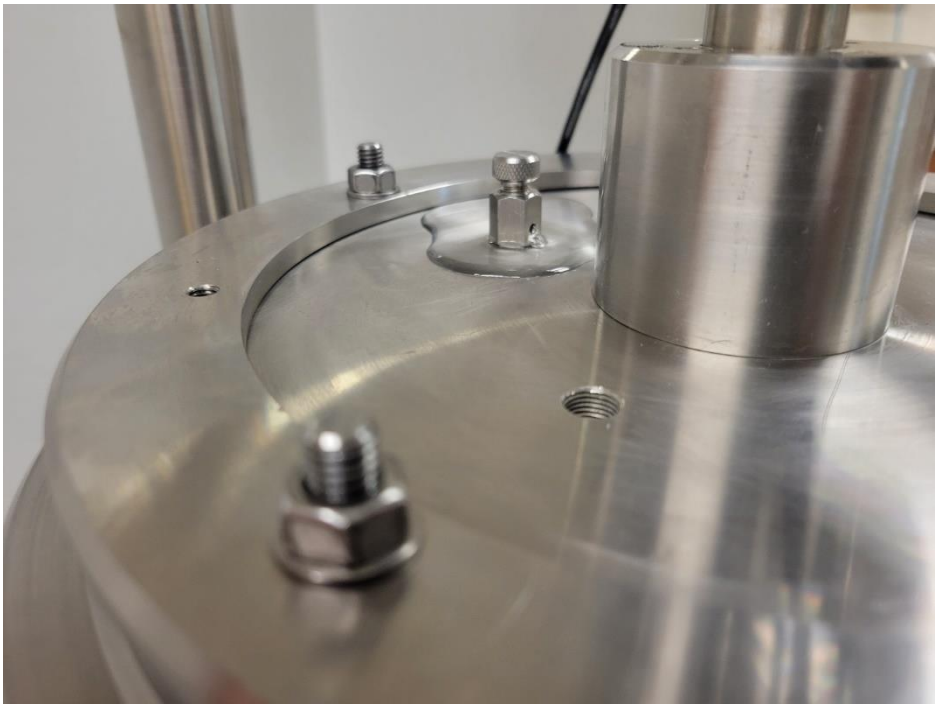

Figure 4.41: Confining cell assembly step 17: loosen top bleed valve and fill cell with water. Tighten top bleed valve once the cell is full.

Figure 4.42: Confining cell assembly step 18: connect cell pressure line from Pro Dual APC to cell pressure valve. The sample is now ready for testing.

4.4 - Device Modification and Calibration for Thermal Control

The existing cyclic simple shear device was upgraded with the GCTS HTC-250 Heating Controller shown in Figure 4.42. The heating controller consists of two heating elements and one thermocouple which communicates through the HTC-250 control box to regulate the temperature inside the plexiglass chamber. Figure 4.43 shows the configuration of the heating elements and the thermocouple inside the cyclic simple shear chamber. This configuration consists of the heating elements and thermocouple located at the bottom of the chamber near the sample, allowing for a relatively uniform heat distribution inside the plexiglass chamber. The chosen configuration also makes use of three previously unused openings at the bottom of the chamber, achieving thermo-control without any major modifications to the stainless-steel base.

Figure 4.43: GCTS HTC-250 Heater Control Unit components: 1) control box, 2) 2 heating elements, 3) thermocouple

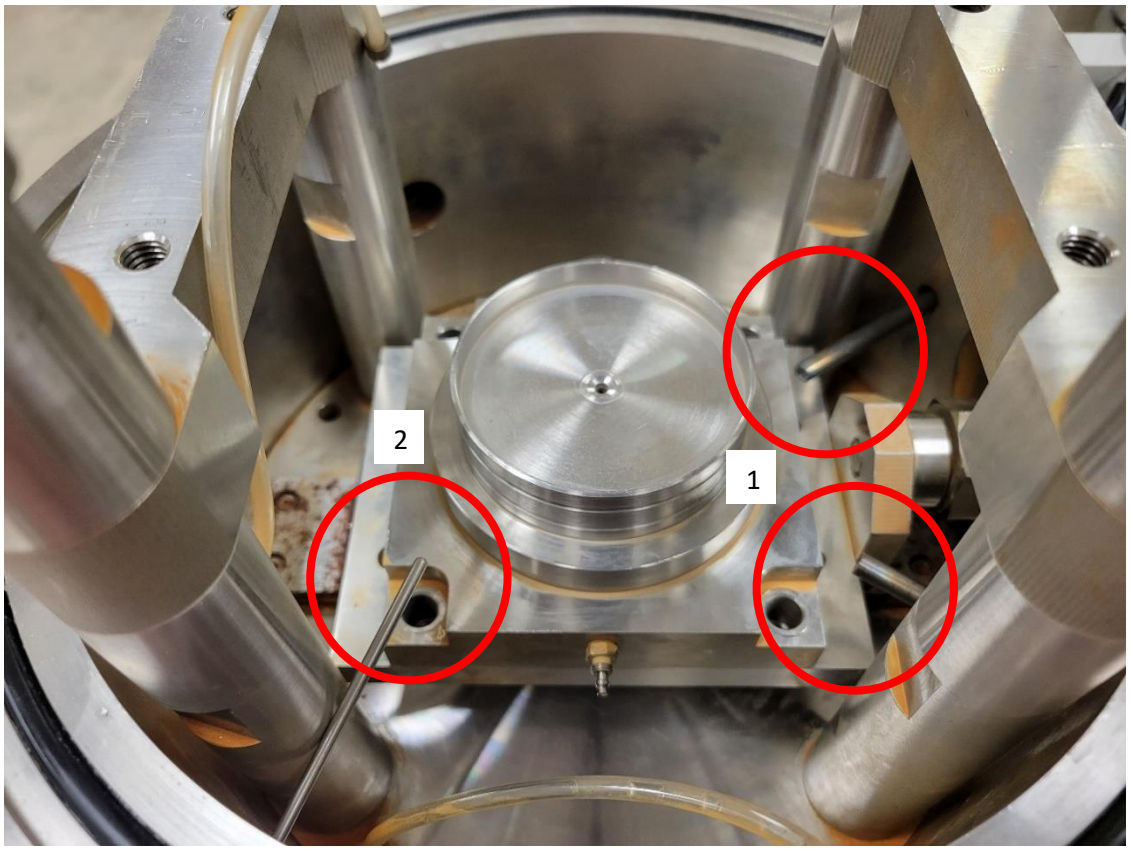

Figure 4.44: Heating configuration for CSS device showing: 1) 2 heating elements, 2) thermocouple

The thermo-calibration process was conducted using the Extech 4-Channel data logging thermometer shown in Figure 4.44. This thermometer allows for constant monitoring and recording of the soil temperature at multiple points in the sample to account for any temperature variation within the sample. Figure 4.45 shows the components used for thermo-calibration and Figures 4.46 – 4.50 show the step-by-step assembly process. A special aluminum top cap was fabricated to allow for three wire probes to be inserted into the sample without infiltration of the confining water. The soil sample will be monitored during the heating process at three points to determine the time it takes for temperature to equalize, the discrepancy between the heater and soil temperatures, and the temperature variation inside the soil sample.

Figure 4.45: Extech 4-Channel Data Logging Thermometer components: 1) power cable, 2) thermometer, 3) 3 thermocouple wire probes

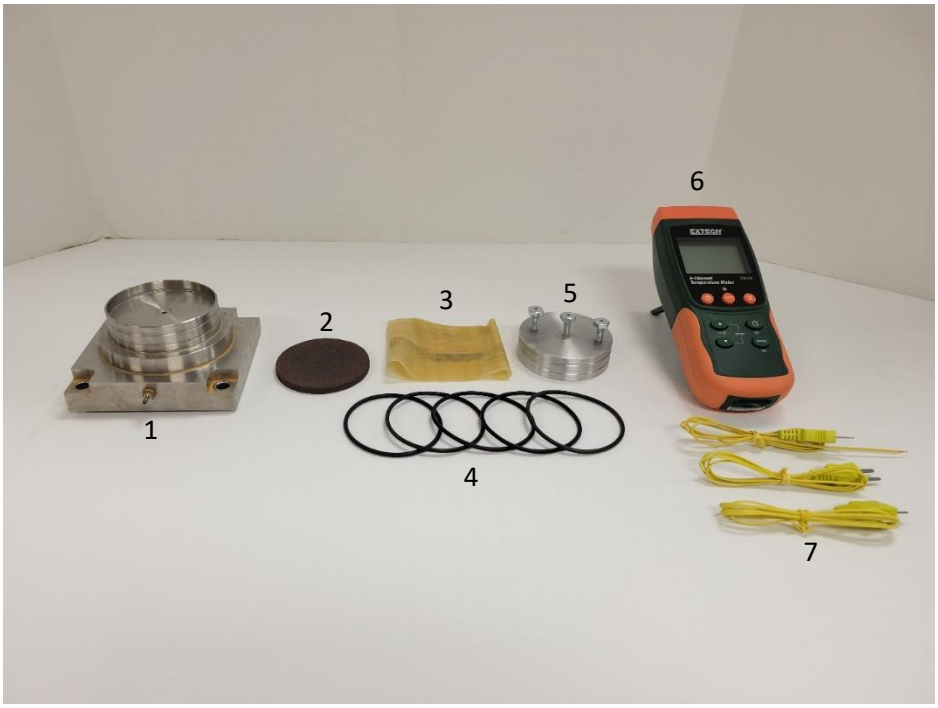

Figure 4.46: Thermo-calibration components: 1) sample base pedestal, 2) porous disk, 3) latex membrane, 4) 5 rubber O-rings, 5) sample top cap, 6) Extech thermometer, 7) 3 thermocouple wire probes.

Figure 4.47: Thermo-calibration assembly step 1: secure latex membrane to base pedestal using 2 rubber O-rings and add soil sample.

Figure 4.48: Thermo-calibration assembly step 2: firmly place top cap onto soil sample and secure latex membrane to top cap using 2 rubber O-rings.

Figure 4.49: Thermo-calibration assembly step 3: insert three wire probes into soil sample using the corresponding three holes in the top cap.

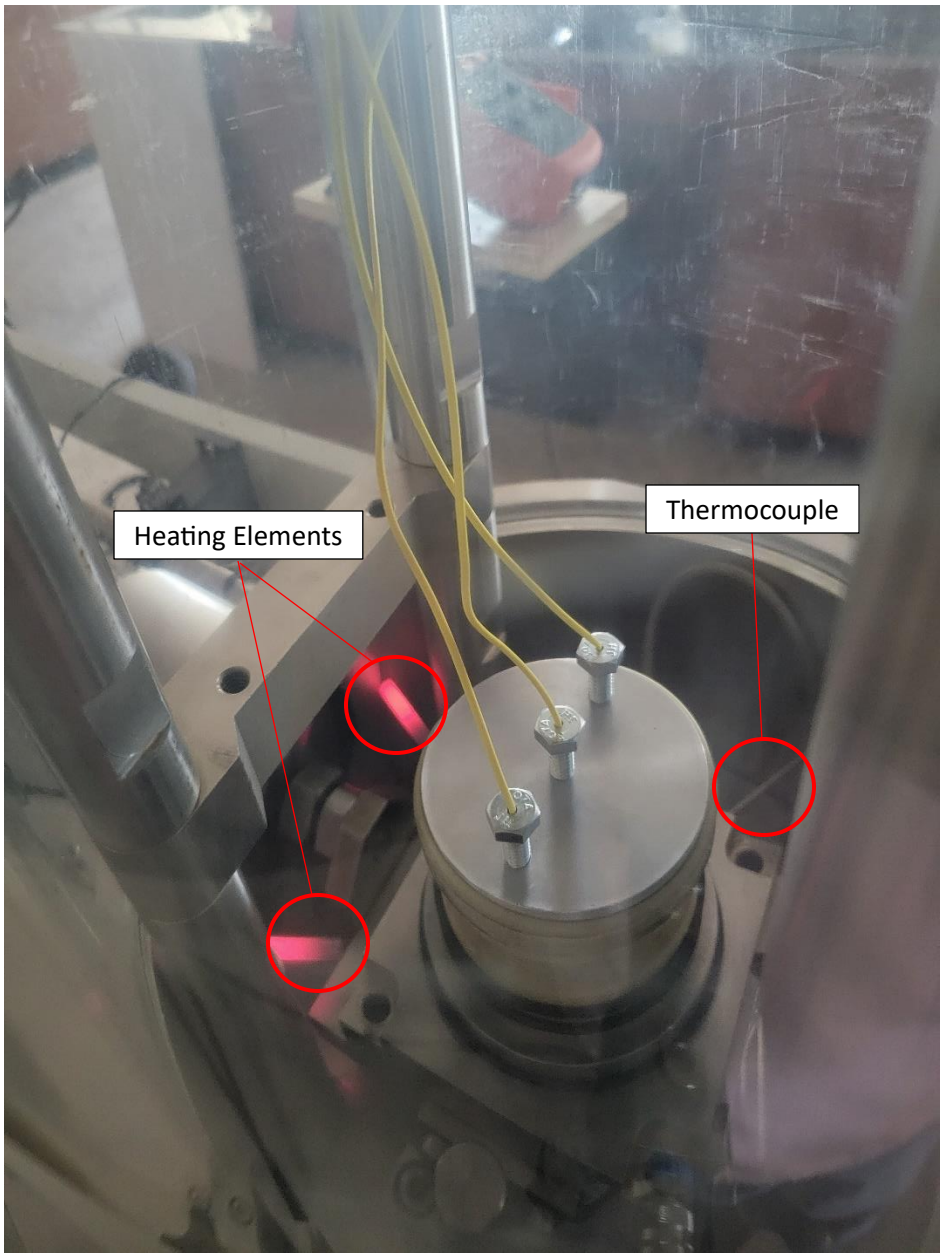

Figure 4.50: Thermo-calibration assembly step 4: place sample assembly into chamber.

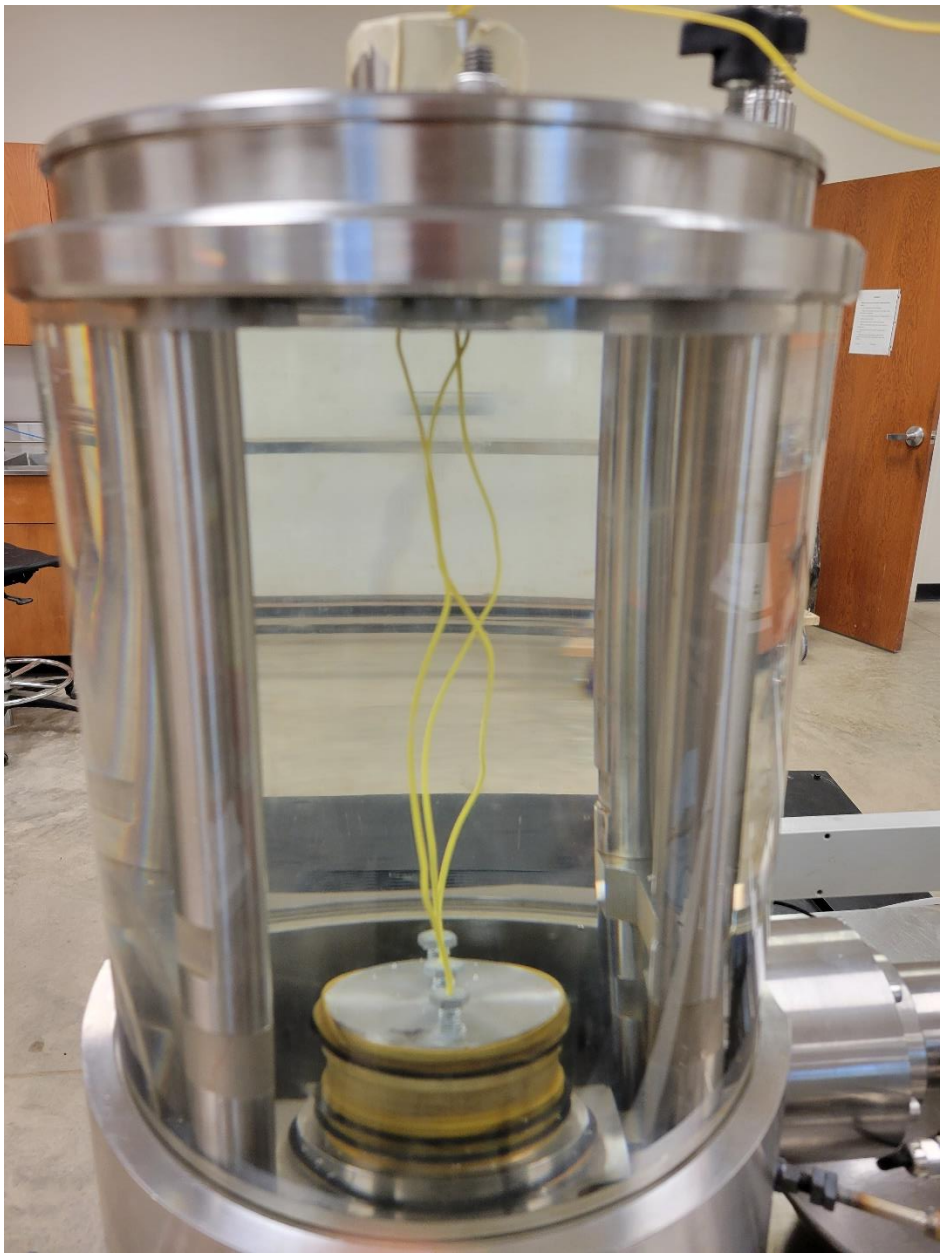

Figure 4.51: Thermo-calibration assembly step 5: fill chamber with water.

4.5 - Thermal Calibration

Thermo-calibration was conducted on all three soil types being used: CL dry (w=9.0%), CL OMC (w=13.6%), CL wet (w=17.0%), ML (w=14.8%), and SC (w=10.0%). To determine each soil's thermo-calibration curve, soil samples were heated to 40°C, 50°C, and 60°C for a period of 24 hours. Figures 4.51 – 4.55 show the thermo-calibration results for all soil types. Due to the small size of the soil sample, the heat distribution inside the sample was relatively constant, and the three thermocouple wire probes recorded similar temperature values. Data from all three wire probes is shown for each calibration test with the left, middle, and right probe temperatures labeled TL, TM, and TR respectively.

The individual heating test data shows that there is a small discrepancy between heater setting and measured soil temperature for all soil types. This discrepancy is similar for all soil types. For the 40°C heating test, soil temperature equalizes at 38°C. For the 50°C heating test, soil temperature equalizes at 46°C. For the 60°C heating test, soil temperature equalizes at 53°C. To calibrate the heating controller for this discrepancy, heater temperature was plotted against the peak equalization temperature for each test. The slope-intercept equation displayed on each calibration curve figure takes the form of Equation 4.5:

$$\text{Soil Temp} = \text{m}(\text{Heater Temp}) + \text{b} \tag{4.5}$$

where Soil Temp is the desired soil temperature, Heater Temp is the required heater temperature, and m and b represent the slope and y-intercept of the calibration line. Figure 4.51(d) shows the resulting calibration curve and equation for CL dry (w=9.0%). The exact same process was followed for the other four soil types with the resulting calibration values shown in Table 4.3. This table shows the required heater input values for each soil type to cause a desired soil temperature of 40°C, 50°C, and 60°C. For example, the HTC heating unit would need to be set at 68.8°C to cause a ML soil sample to reach a peak equalization temperature of 60°C. Finally, a feasibility test was run to verify the heating unit's functionality. Figure 4.56 shows the device is capable of heating soil samples to 60°C. Three SC soil samples were used to measure water content before and after thermo-controlled CSS testing. Table 4.4 shows that water content remained relatively constant throughout testing, verifying the CSS device is capable of thermo-controlled constant water testing.

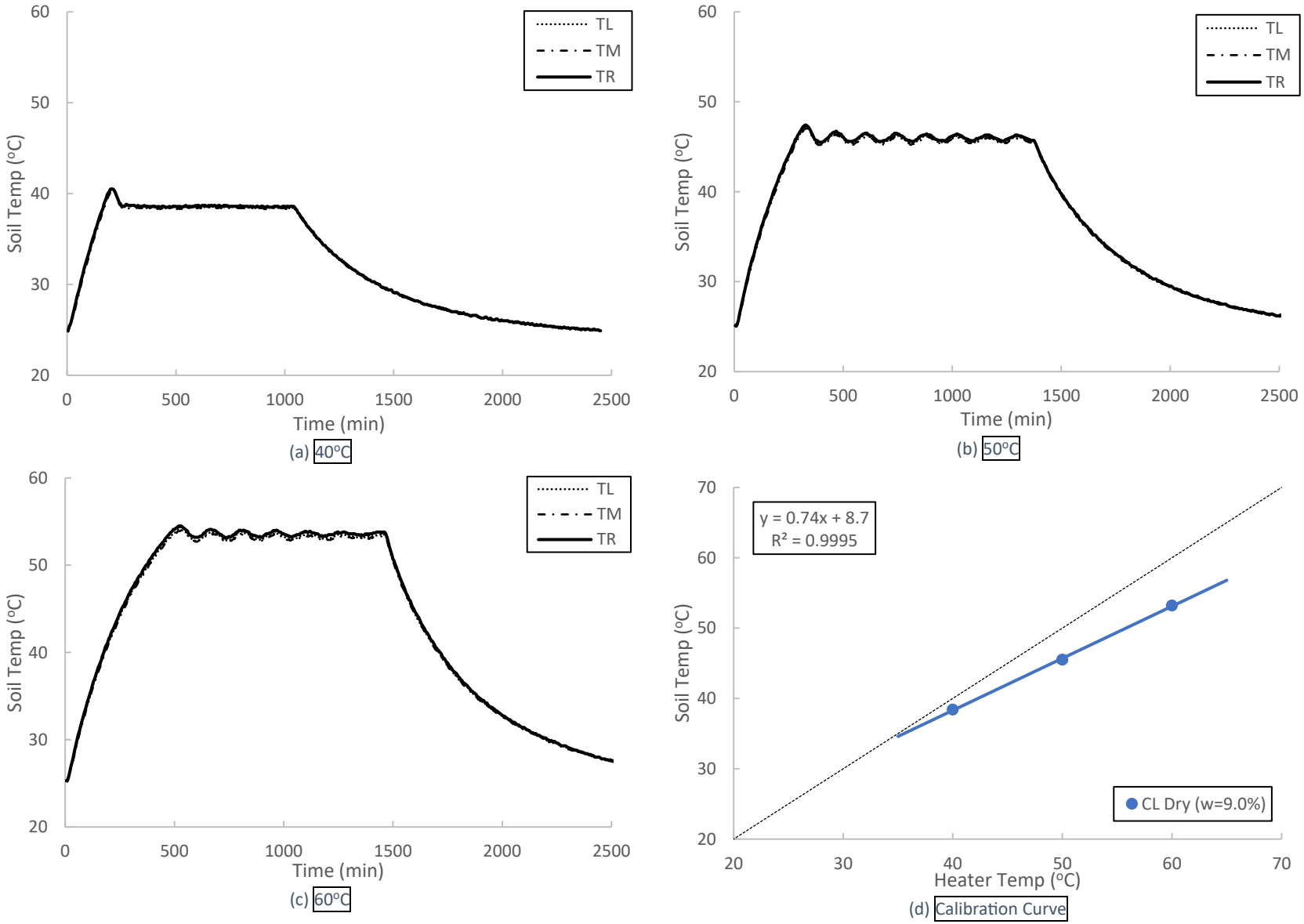

Figure 4.52: Thermal Calibration for Clayey Soil CL Dry (w=9.0%)

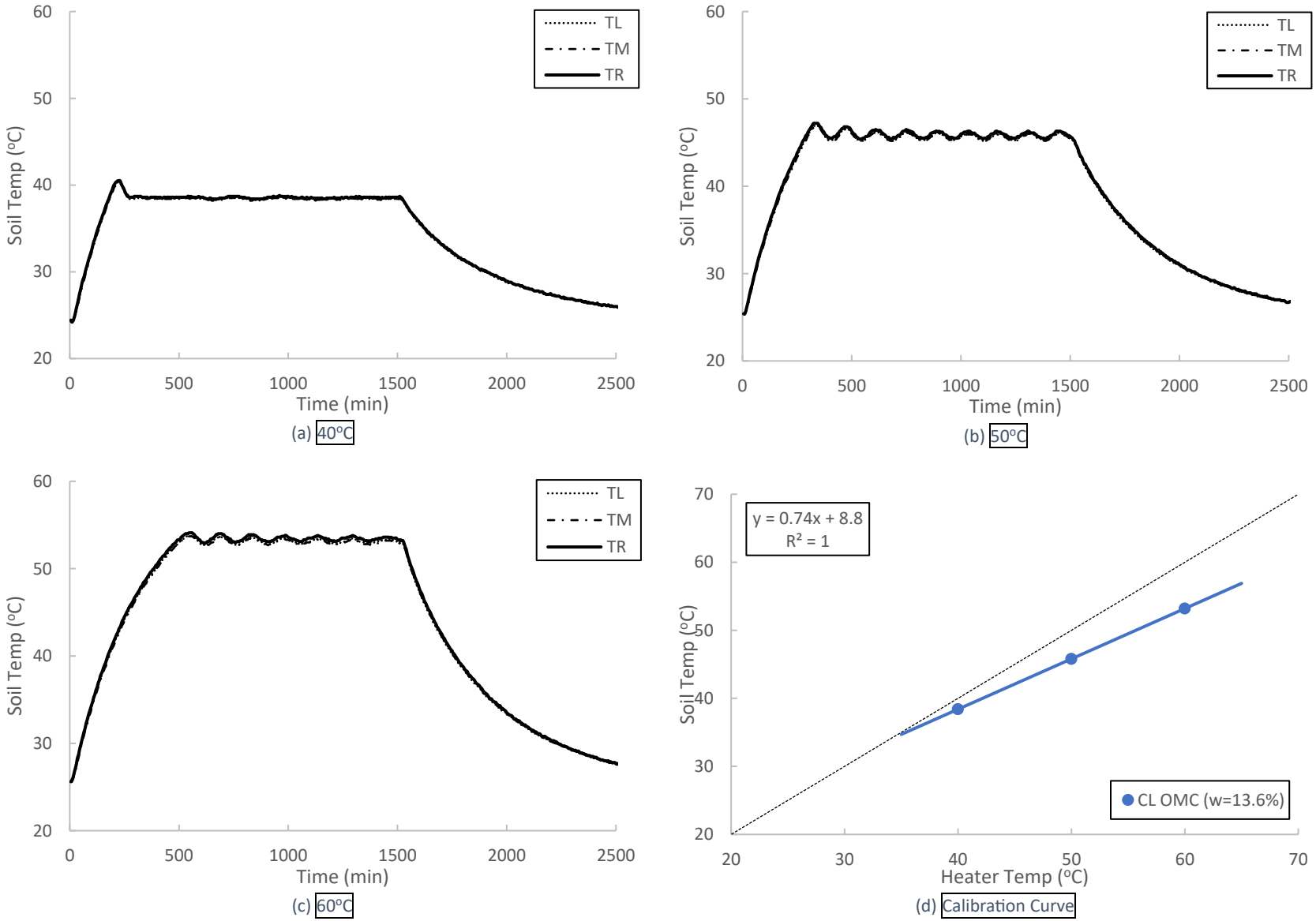

Figure 4.53: Thermal Calibration for Clayey Soil CL OMC (w=13.6%)

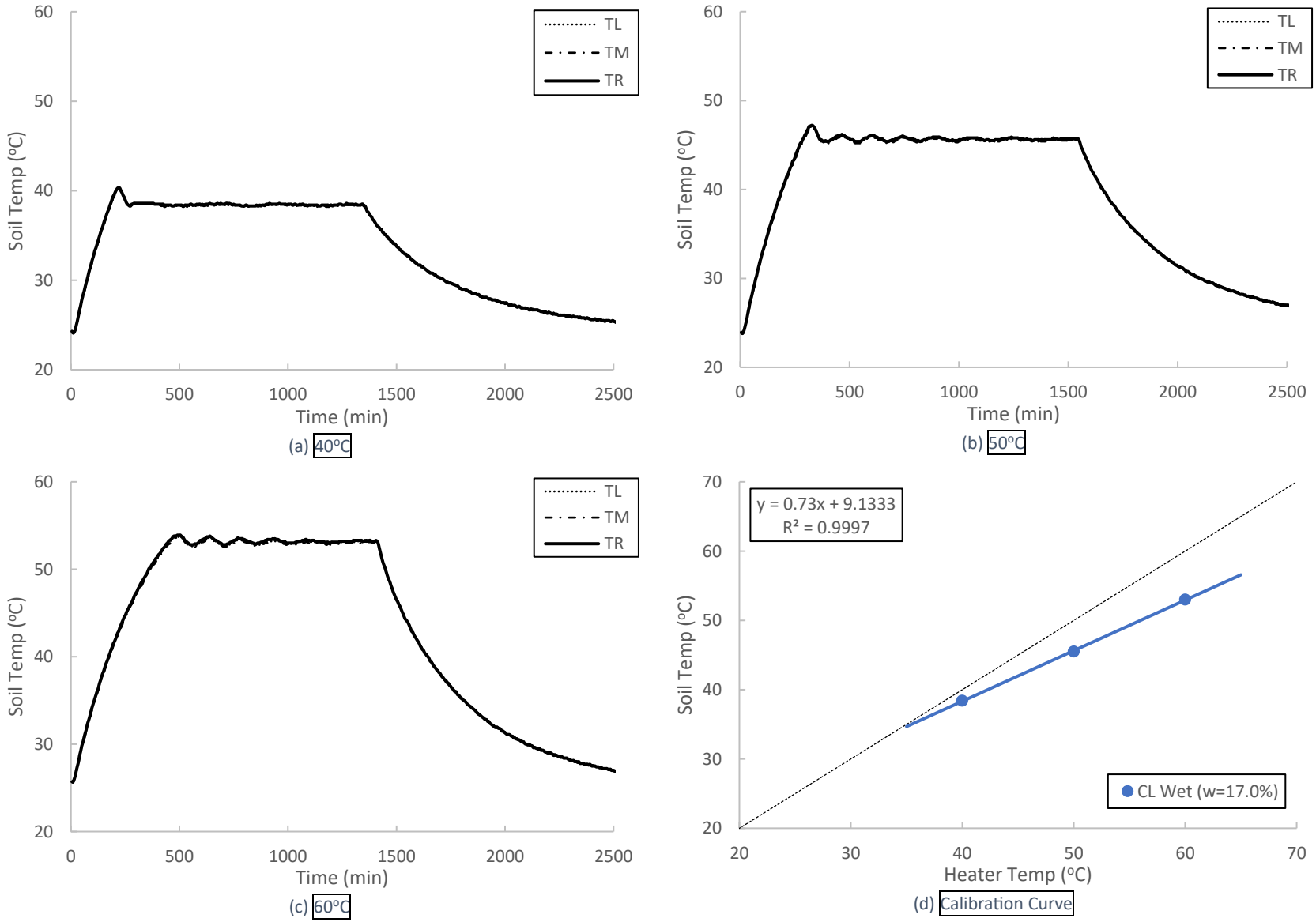

Figure 4.54: Thermal Calibration for Clayey Soil Wet (w=17.0%)

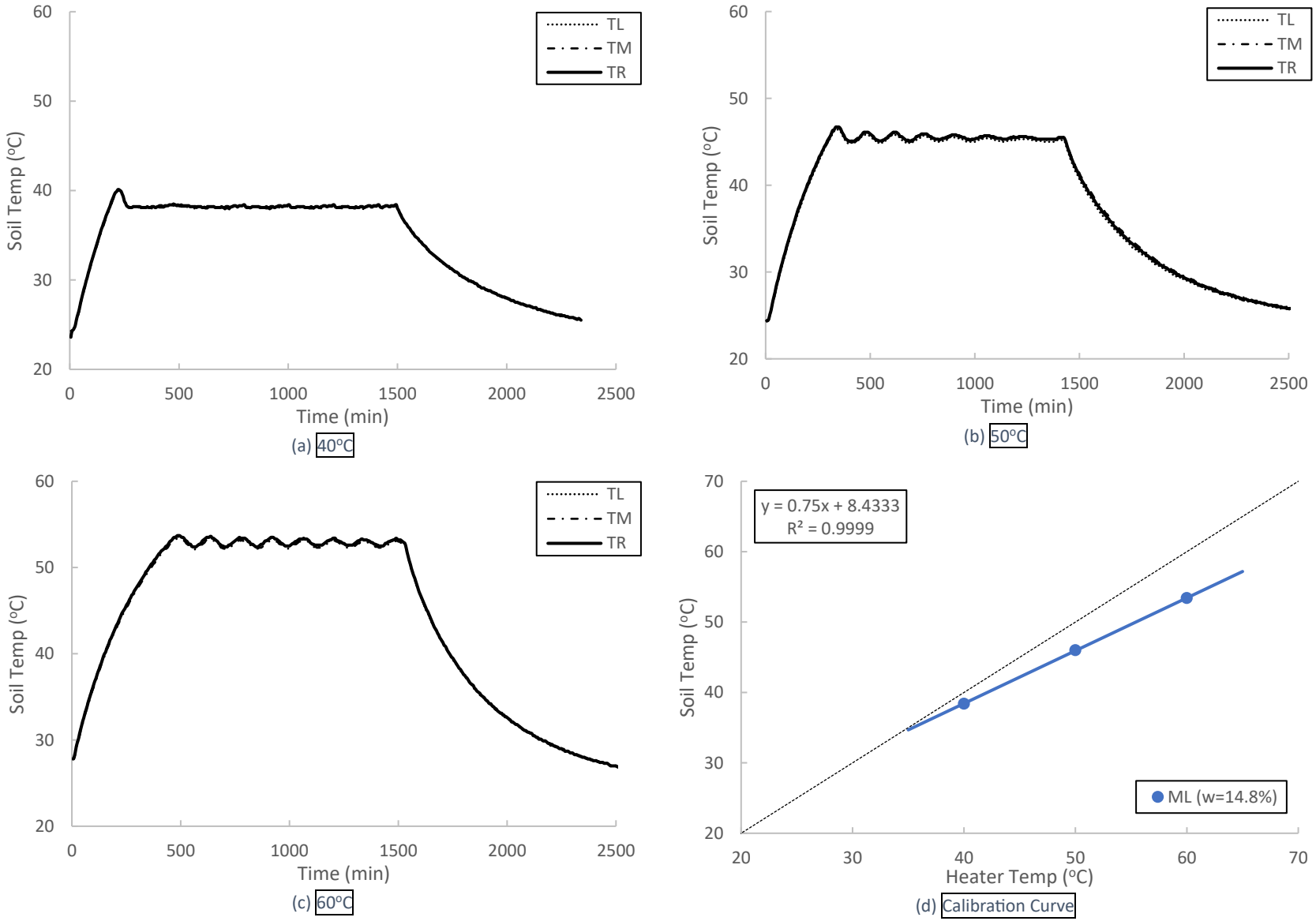

Figure 4.55: Thermal Calibration for Silty Soil ML (w=14.8%)

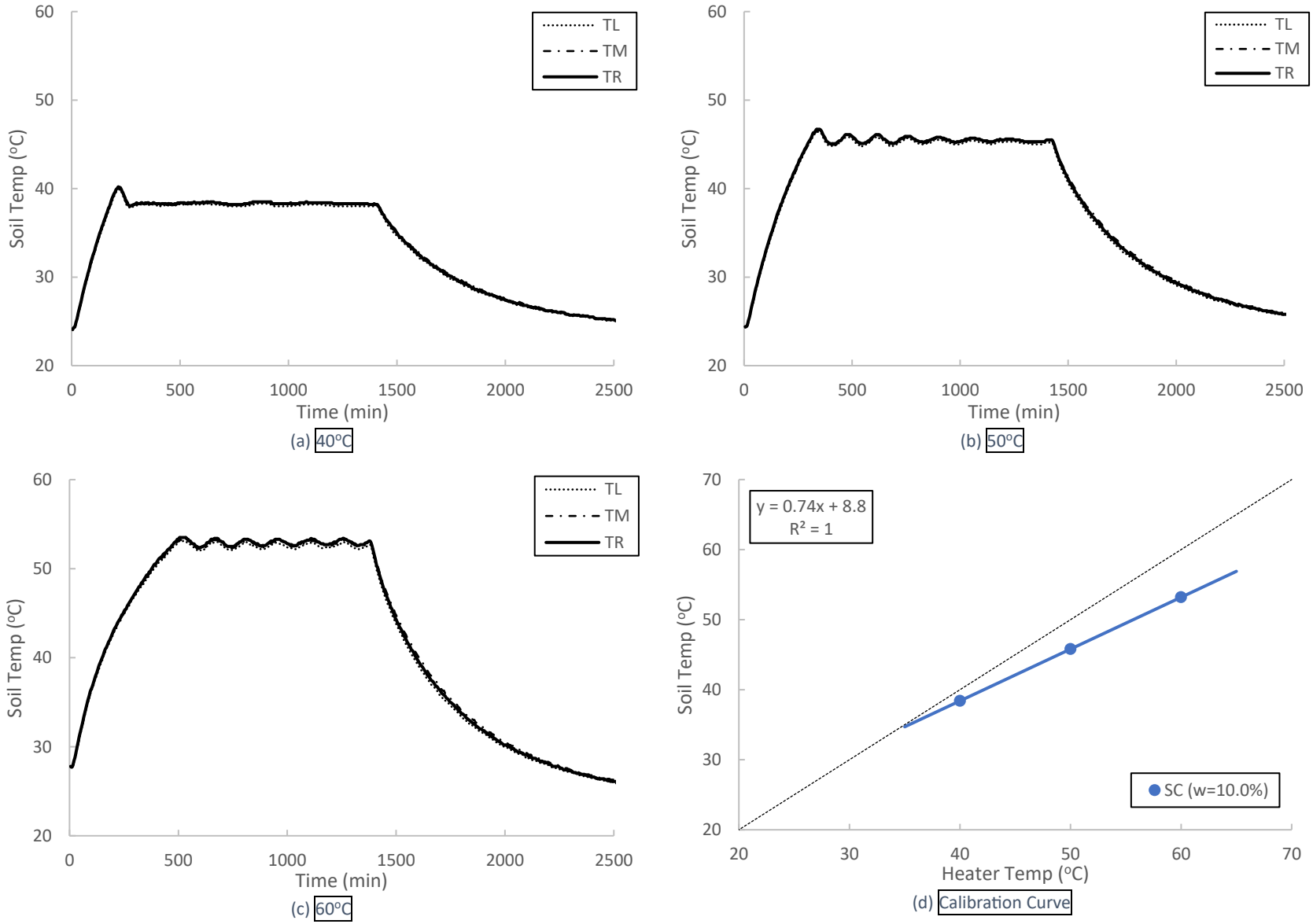

Figure 4.56: Thermal Calibration for Sandy Soil SC (w=10.0%)

Table 4.3 shows the resultant data from the thermo-calibration process. The variation between the heating calibration data of the three soil types is negligible due to the small size of the soil sample and the sample proximity to heating elements. The device uses water for confinement. Even though water is a poor conductor of heat, water is vastly superior to air and allows for a uniform temperature distribution inside the plexiglass chamber. Figure 4.56 shows a trial heating test for clayey soil CL at optimum moisture content. The data shows the system is capable of achieving 60°C soil temperatures. To verify, tests were conducted under constant water conditions, moisture contents were taken before and after testing for three clayey sand SC soil samples. The results presented in Table 4.4 demonstrate moisture content remained relatively constant during thermo-controlled testing indicating the system is functioning properly.

Table 4.3: Heater Calibration

Target Soil Temp (°C)	Heater Temp (°C)				
	Clay			Silt	Sand
	OMC	Dry	Wet	OMC	OMC
40	42.2	42.3	42.3	42.1	42.2
50	55.7	55.8	56.0	55.4	55.7
60	69.2	69.3	69.7	68.8	69.2

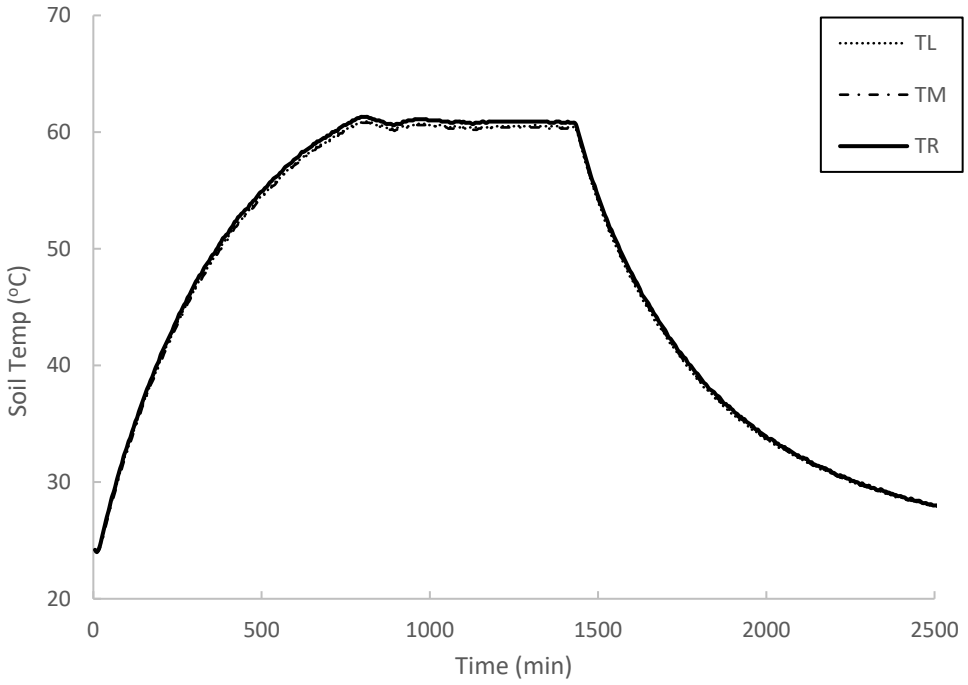

Figure 4.57: Heater feasibility test.

Table 4.4: Constant Water Verification

	SC Sample 1	SC Sample 2	SC Sample 3
MC Before (%)	10.21	9.85	10.13
MC After (%)	10.52	9.65	10.57
Difference (%)	2.99	2.05	4.25

4.6 - Infrared Pictures

The following pictures were taken with an infrared camera during and after a thermo-controlled 60°C cyclic simple shear test. Figure 4.57 shows the entire cyclic shear device. The fairly constant coloration of the plexiglass testing chamber suggests a relatively uniform heat distribution inside the cell. Figure 4.58 shows the base pedestal, soil sample, and top cap immediately after a thermo-controlled 60°C cyclic simple shear test. Similar to the previous picture, the slight orange to red color variation further suggests a uniform heat distribution between the base pedestal and top cap. Figure 4.59 shows the soil sample immediately following a 60°C cyclic simple shear test. The soil sample was removed from the sample pedestal and latex membrane to show a clear picture of the temperature variation of the soil. The slight variations in color further demonstrate that thermo-control of the CSS system is functioning properly.

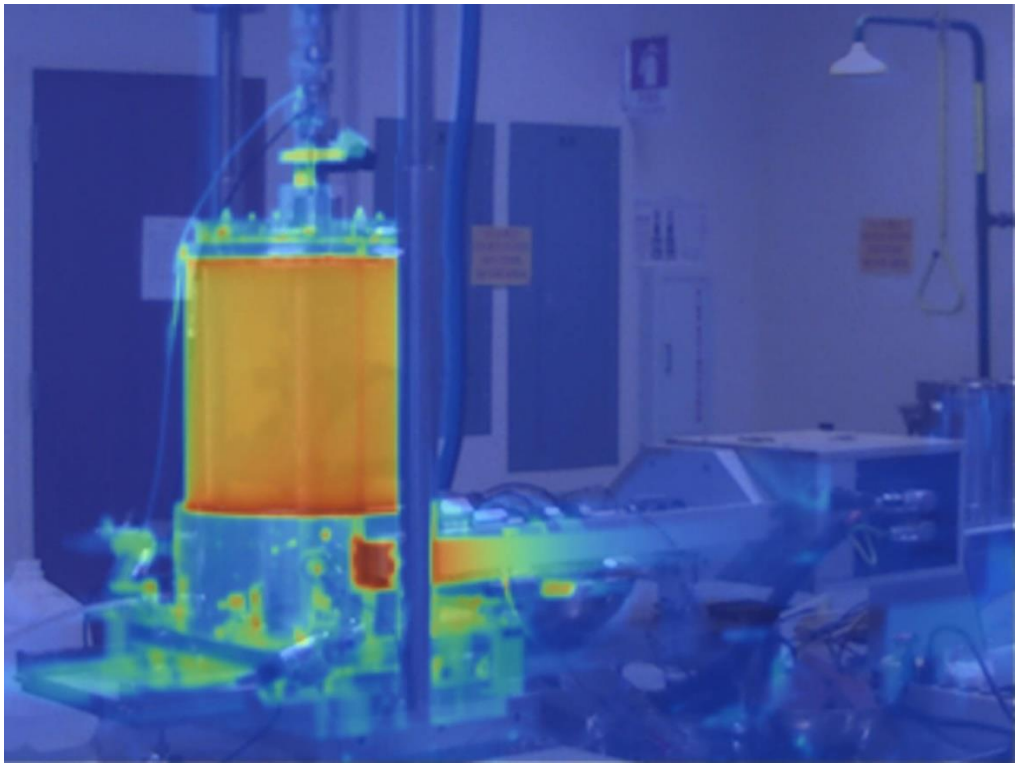

Figure 4.58: Infrared picture of thermo-controlled CSS system after heating.

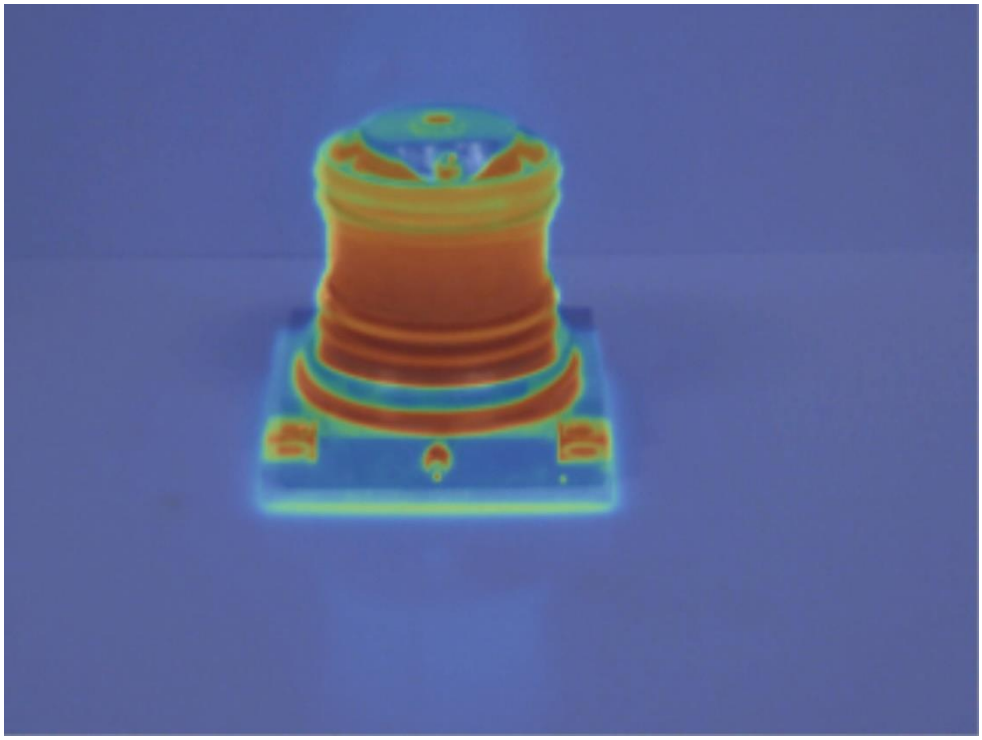

Figure 4.59: Infrared picture of sample pedestal immediately following 60°C heating test.

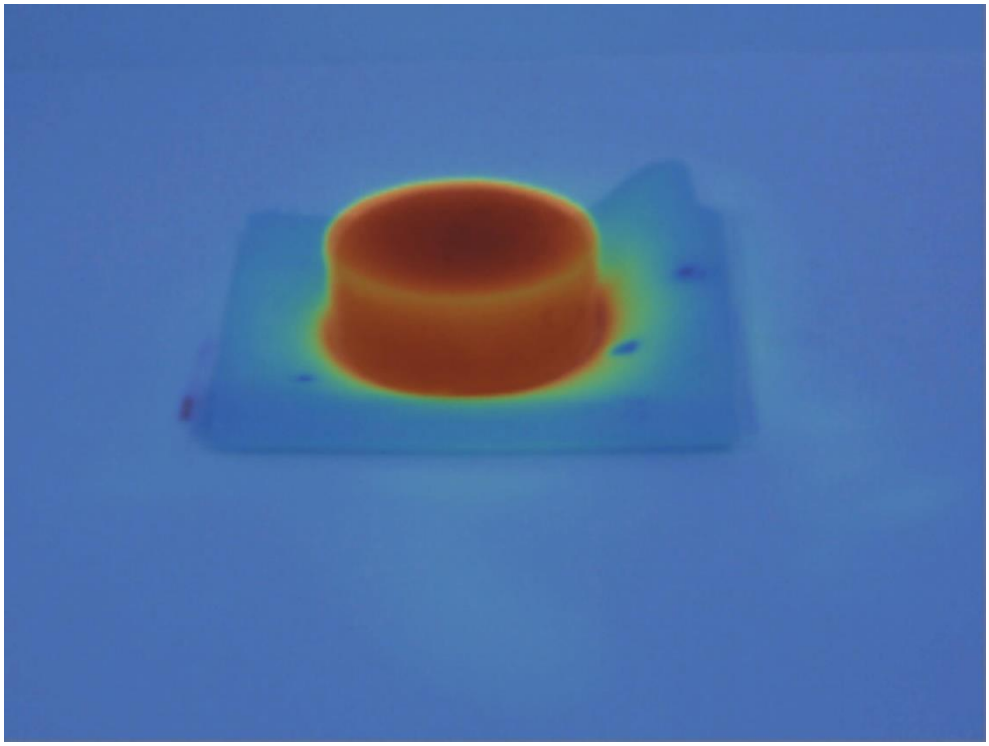

Figure 4.60: Infrared picture of soil sample immediately following 60°C heating test.

4.7 – Data Acquisition and Process Control (DA/PC) Software

The software used for testing is CLISP Studio, a Combined Laboratory Integrated Software Package developed by VJ Tech. CLISP Studio can control complex instruments and continually gather data at high speeds for thorough analysis. CLISP Studio is simple to use as test modules have an assistant function that guides the testing process from setup to results analysis. Test modules are automatic, allowing for tests to be started and run independently, requiring minimal user interaction. The software module used for cyclic simple shear testing was the CLISP Studio DSS with confining pressure software module (VJT-csDYNSS-C). Key features of the software include a saturation stage, various consolidation options (isotropic, anisotropic, K0), static loading stage, simple cyclic shear stage, liquefaction cyclic shear stage, and live data views and graphical displays. The stages used for thermo-controlled cyclic simple shear testing were the saturation stage, consolidation stage, and simple cyclic shear stage. It is important to note that the saturation stage window is not shown. Because the purpose of the research was to evaluate the cyclic response of thermo-controlled unsaturated soil, the saturation stage was not used in a meaningful way. The back pressure valve was kept closed throughout testing with the back pressure line disconnected from the cell to ensure no additional water was introduced into the sample. The following figures show the software controls used for thermo-controlled cyclic simple shear testing (VJ Tech, 2023).

Figure 4.60 shows the graphical display of the pressure control unit. Cell and back pressure can be controlled through this window. The software allows for either a target pressure or a pressure rate to be set for either the cell or back pressure valves. The software also allows for emptying or filling of the valves as it becomes necessary. During repeated use it may be necessary to refill the water supply in the pressure valves with the fill function or deair the system with the help of the empty function. Typically, precise pressure control is done through the various stages in the testing cycle and not directly through the pressure control window.

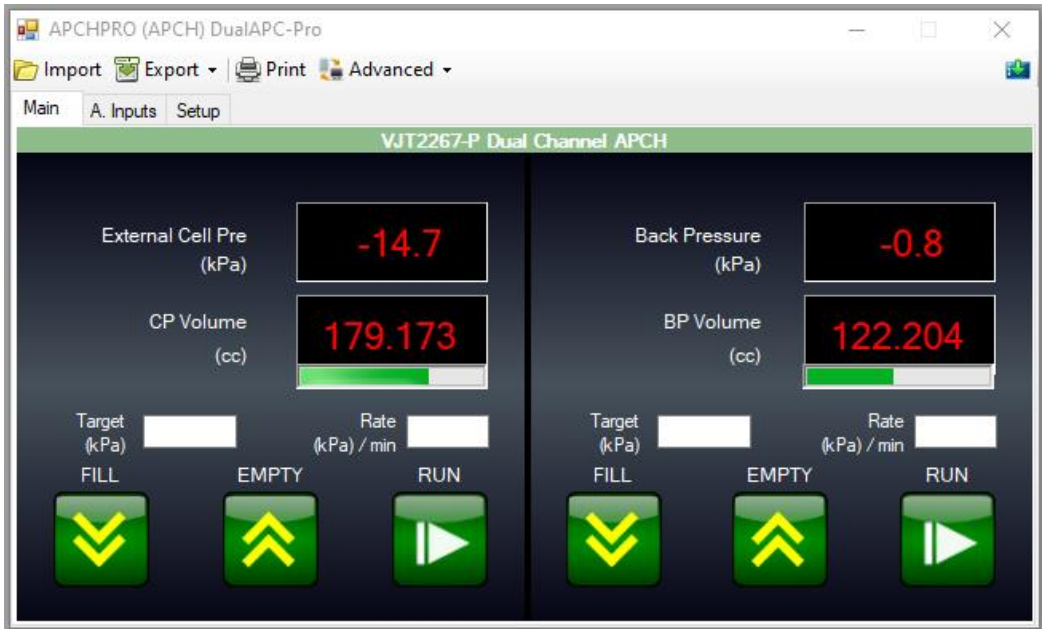

Figure 4.61: Pressure Control window.

Figure 4.61 shows the graphical display of the DSC3000MM dynamic servo controller. The dynamic servo control window displays the current position of both the vertical and horizontal servos as well as the load on the vertical and horizontal load cells. The window has a speed input as well as back, forward, and stop controls typically used prior to testing to ensure the sample is in a neutral position by zeroing out the load on the vertical and horizontal load cells. The window also features a home button which is used between tests to return the servos to their default factory positions. Typically, precise load control is done through the various stages in the testing cycle and not directly through the DSC3000MM control window.

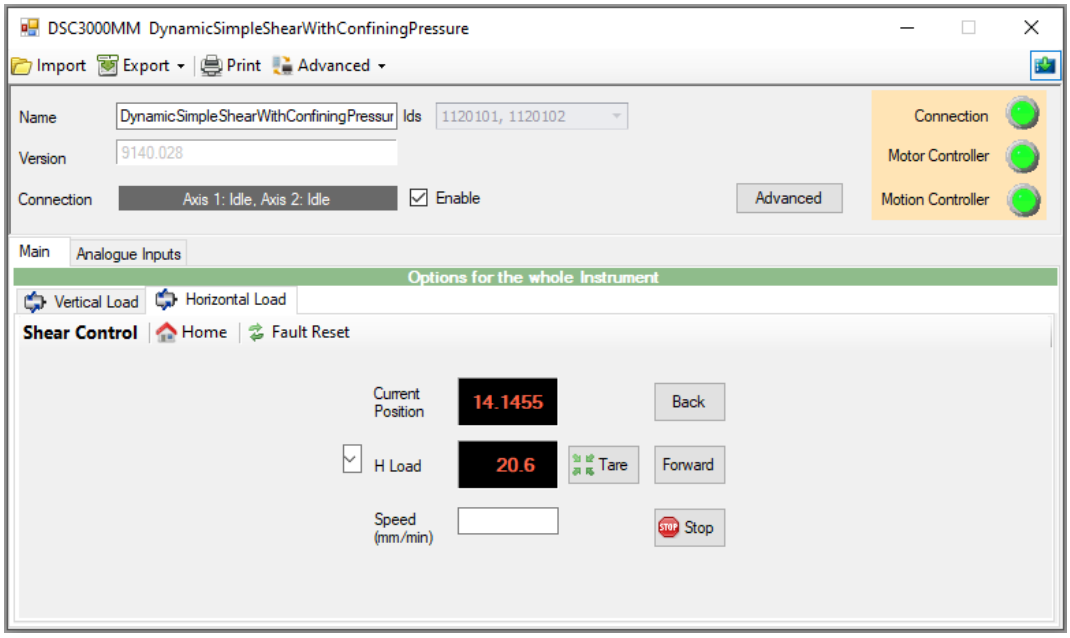

Figure 4.62: DSC3000MM Control window.

Figure 4.62 shows the Consolidation Setup window. CLISP Studio has three consolidation options: isotropic, anisotropic, and K0. The anisotropic consolidation option was exclusively used for this research to consolidate soil samples under equivalent K0 conditions. The anisotropic consolidation stage allows for control of starting conditions, logging conditions, and stopping conditions. The starting condition window lets the user set back pressure, total vertical stress and total horizontal stress. A total vertical stress of 137.9 kPa (20 psi), a total horizontal stress of 73.1 (10.6 psi), and a ramp time of ten minutes were used for all tests. Logging conditions and stopping conditions can be set according to the user's preference. All tests used a logging interval of two minutes and a stopping condition of 99 hours to ensure the device would not automatically proceed to the next step without user input.

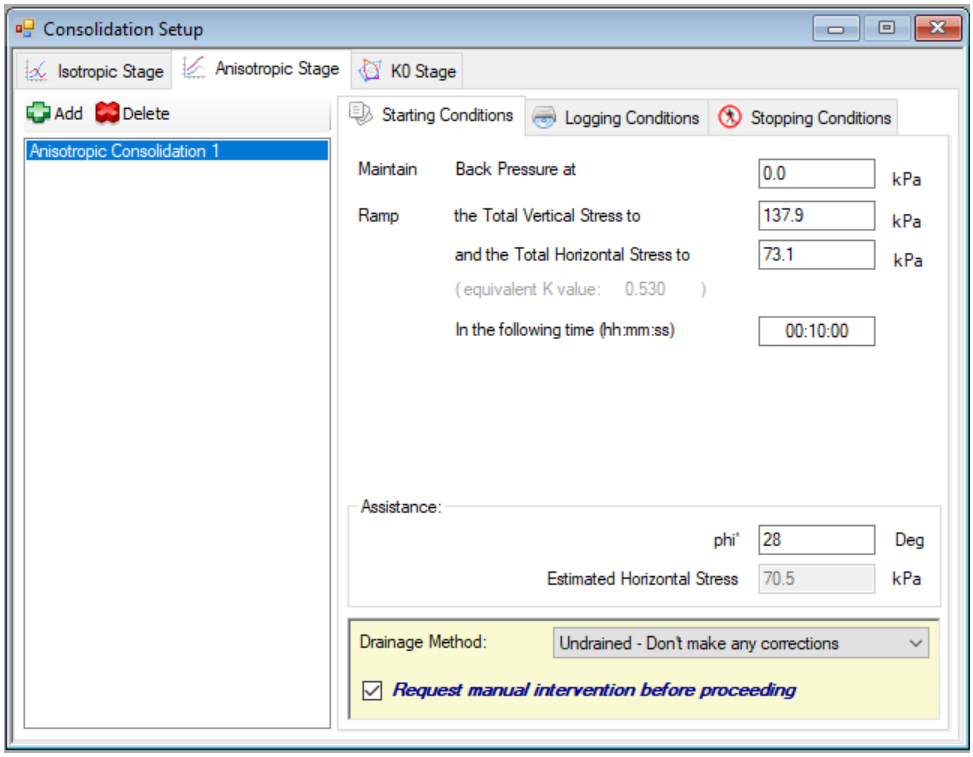

Figure 4.63: Consolidation Setup window.

Figure 4.63 shows the Cyclic Loading Configuration window. CLISP Studio has three cyclic loading stages: drained pre-shearing, cyclic loading, and monotonic shearing. Only the cyclic loading stage was used to gather data for this research. The cyclic loading stage allows for setting of initial conditions, logging conditions, and stopping conditions. The initial conditions window lets the user select the type of cyclic test (undrained or drained), number of cycles, type of waveform, measurement unit (stress or displacement), wave amplitude, and frequency. All settings were kept constant throughout the research and testing process except for the two-way amplitude. Shear strain is controlled through the two-way displacement amplitude.

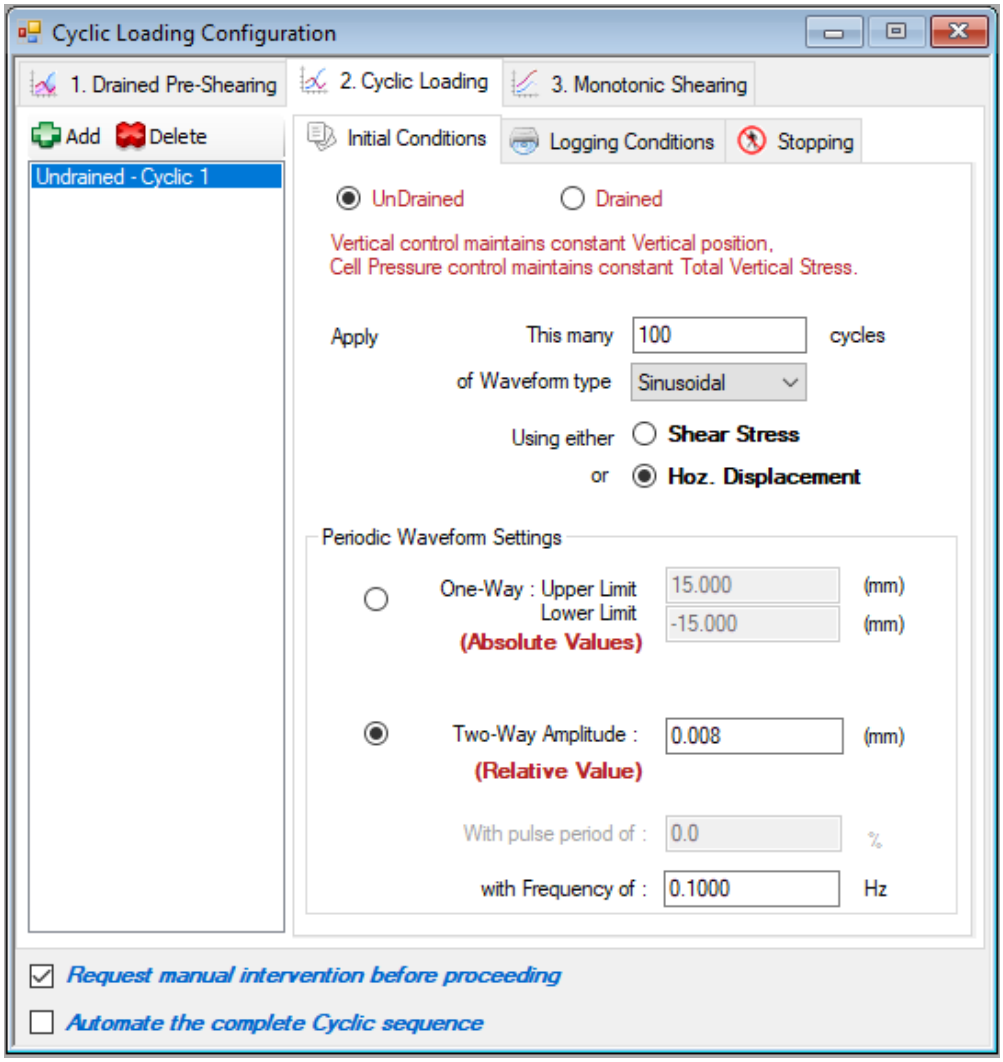

Figure 4.64: Cyclic Loading Configuration window.

4.8 – Typical DA/PC Outputs

The following figures show example outputs from the CLISP Studio software. The majority of data generated through the testing process was exported into various excel files for analysis; however, the software provides a few useful output windows that allow for real time observation of test phenomena. The three output windows used are transducer live readings, anisotropic consolidation over time curve, cyclic loading over time curve, and cyclic loading shear strain curve. These three curves provide instant feedback to let the user determine if a given test is running in an expected manner.

Figure 4.64 shows the Transducer Live Readings window. The window gives current output readings from multiple transducers located around the device. The live readings show pressure values, vertical and horizontal load values, and vertical and horizontal displacement positions. The transducer live readings allow for real time monitoring of the entire cyclic simple shear system during testing.

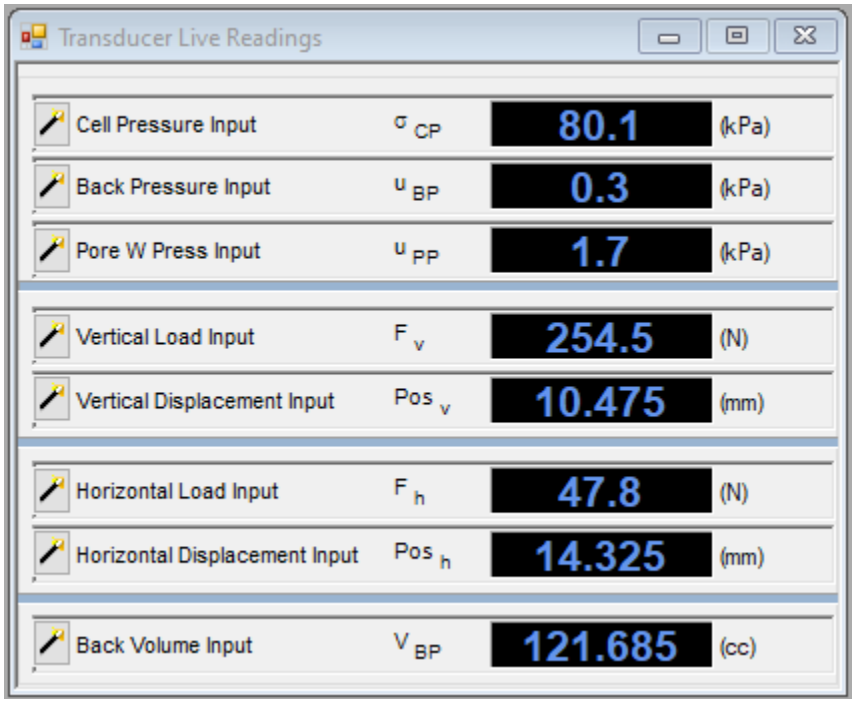

Figure 4.65: Transducer Live Readings.

Figure 4.65 shows the Anisotropic Consolidation Time Related Curve window. The window lets the user observe the consolidation process over time. The window shown in Figure 6 is set to report total vertical stress, but the primary axis can be changed to various measured values of the user's choosing.

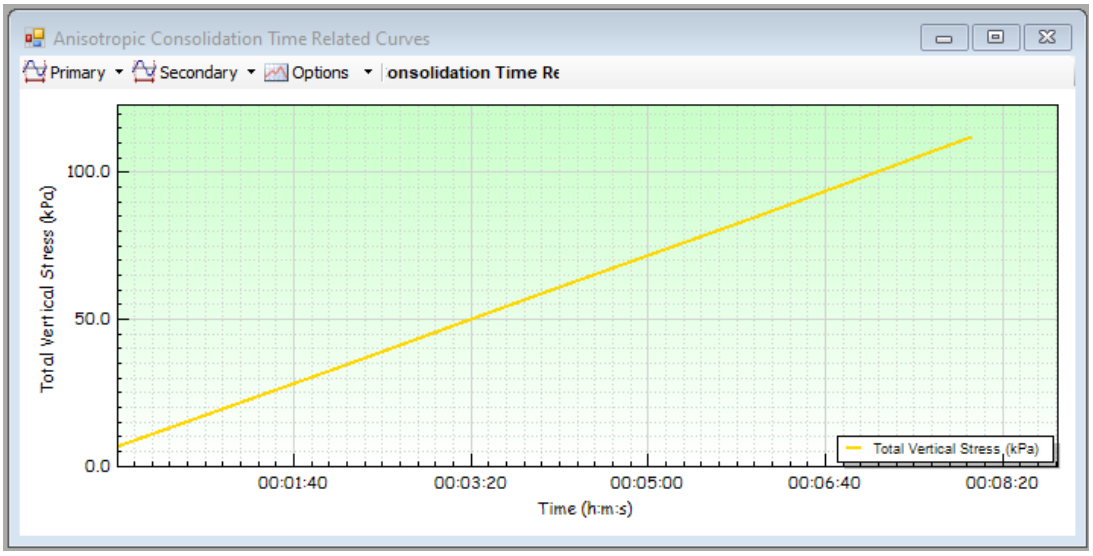

Figure 4.66: Anisotropic Consolidation Time Related Curve window.

Figure 4.66 shows the Cyclic Loading Time Related Curve window. The window shows the cyclic loading of the soil sample with respect to time. The primary axis is shown as horizontal load input, but this value can be changed to various values. The user can observe the waveform and determine whether the test is functioning properly. Expected outputs for this window consist of a steadily oscillating waveform and clearly defined peaks and valleys.

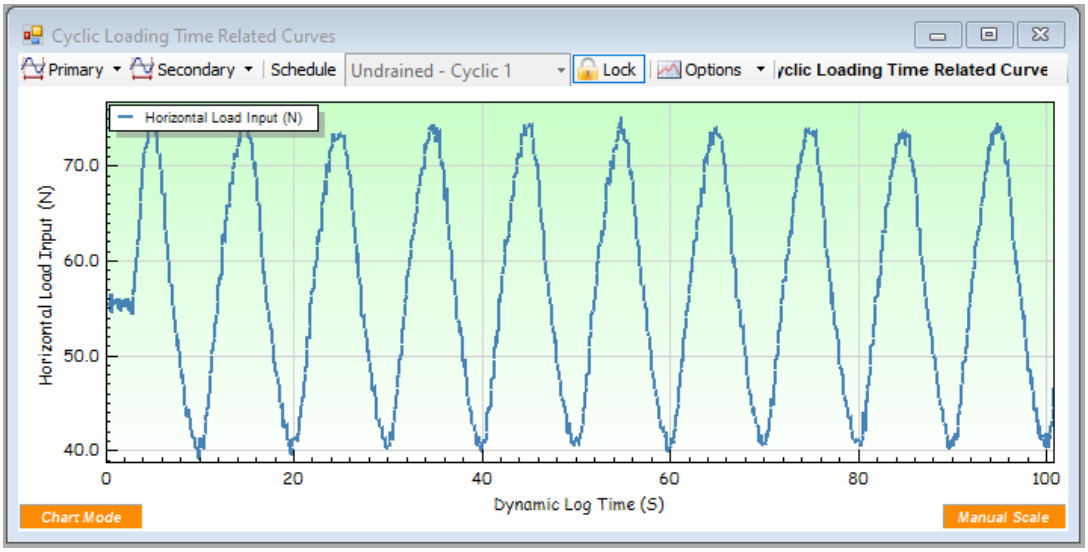

Figure 4.67: Cyclic Loading Time Related Curve window.

Figure 4.67 shows the Cyclic Loading Shear Strain Related Curve window. The window shows the hysteresis loop generated during the cyclic loading of the soil sample. This is another tool used to determine if the test is running properly. Expected outputs should resemble typical hysteresis loops. Larger deformations should correspond to larger loops that eventually break down in structure.

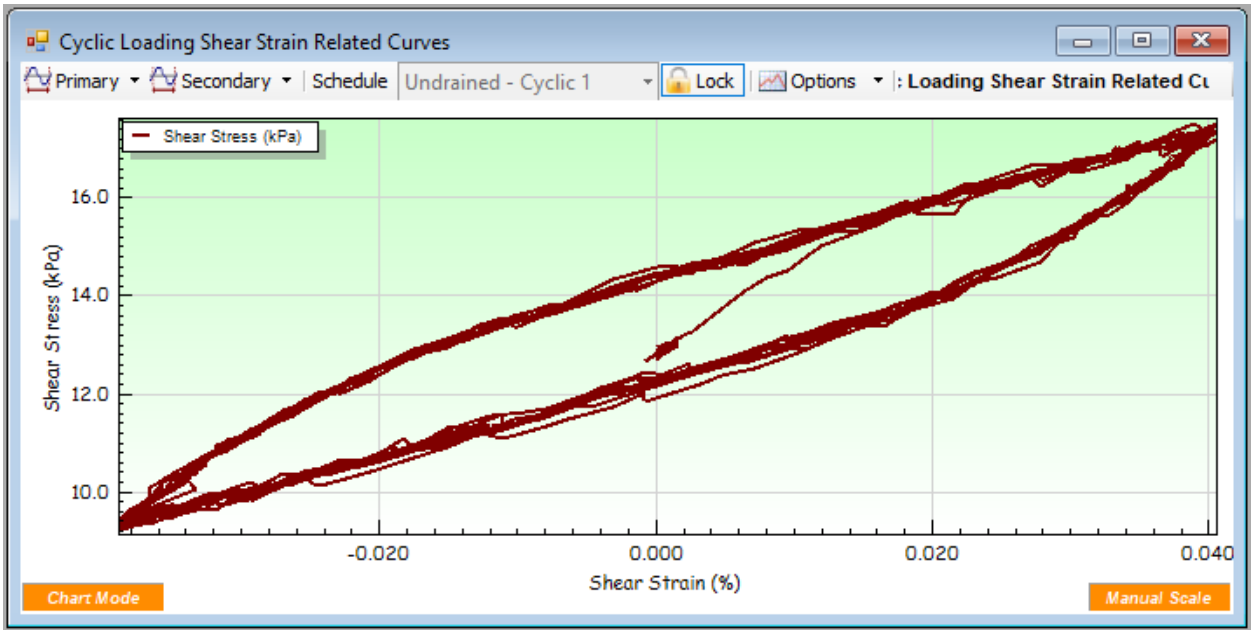

Figure 4.68: Cyclic Loading Shear Strain Related Curve window.

Chapter 5: Experimental Results from Thermo-Controlled Cyclic Simple Shear Testing

Chapter 5 presents thermo-controlled CSS test results for the three soil types used in this study. Test results are organized by soil type: dry clay (w=9.0%), optimum moisture content clay (w=13.6%), wet clay (w=17.0%), silt (w=14.8%), and clayey sand (w=10.0%). The same testing procedure was followed for all three soil types. Initially the soil sample is consolidated for 24 hours under a total vertical stress of 20 psi (137.9 kPa) and a total horizontal stress of 10.6 psi (73.1 kPa). After the 24-hour consolidation period, the drainage valve is closed, and the heater is set to the appropriate temperature corresponding to Table 4.3. During the heating process, the pressure control pump and vertical servo continue to regulate the total vertical and horizontal stress to account for thermal expansion of the water used for confinement. The soil undergoes a 24-hour undrained heating period. The drainage valve is left closed at this point for the remainder of the testing process to simulate undrained testing conditions.

For each soil type, four soil samples are needed to complete the testing process. A series of 20 undrained thermo-controlled CSS tests is performed for each temperature variation: 23^{o}C (room temperature RT), 40^{o}C, 50^{o}C, and 60^{o}C. The 20 undrained thermo-controlled CSS tests are performed under increasing shear strain amplitudes to provide a clear picture of the effects temperature has on shear modulus, G, for a wide array of shear strain amplitudes ranging from relatively small (γ = 0.001%) to large (γ = 10.0%). Each thermo-controlled CSS test is conducted at a cyclic frequency of f = 0.1 Hz for a total of N = 10 cycles.

Each section displays thermo-controlled experimental CSS test results in two different formats. First, results are presented on the basis of shear strain amplitude. For a given temperature, four sets of data are shown ranging from relatively small (γ = 0.035%) to large (γ = 10.0%) shear strain amplitudes. Each data set shows the first, fifth, and tenth cyclic loads to show how temperature interacts with successive load applications. Second, results are presented on the basis of temperature. For a given shear strain amplitude, data from four complete thermo-controlled CSS tests is presented to show how temperature effects shear modulus (slope of the hysteresis loops). One relatively small shear strain amplitude and one relatively large shear amplitude were chosen to provide a comparison of the effect increased temperature has on shear modulus at different strains. In general, the thermo-controlled CSS data shows a decrease in shear modulus for increasing temperatures.

5.1 - Typical Clayey Soil (CL) Response

Sections 5.1.1 – 5.1.3 show the typical clayey soil CL response for moisture contents ranging from dry of optimum (w=9.0%) to wet of optimum (w=17.0%). Varying water content for the clayey soil allows for an examination of the interaction between temperature and water content. The effect of water content on shear modulus has been thoroughly documented. Under similar conditions shear modulus is expected to decrease as water content increases. Intuitively stiffness is greater for dry soil than wet soil. Song et al. showed that modulus decreased under a given dynamic strain level for increasing water content (Song et al., 2017). Zhang et al. used a constant water triaxial test to study the modulus behavior of unsaturated soils compacted at various water contents, showing that modulus decreases with an increase in water content (Zhang et al., 2012). Zhang et al. used a resonant column test to evaluate the small strain shear modulus for a range of water contents, showing a decrease in the small strain shear modulus for increasing water contents (Zhang et al., 2021). Ng and Zhou used a thermo-controlled cyclic triaxial device to show

that while shear modulus increases with suction, samples under higher suction are more susceptible to thermal degradation (Ng and Zhou 2014).

5.1.1 - CL Soil Compacted Dry of Optimum Moisture Content (w=9.0%)

Figures 5.1 – 5.6 show various experimental test data from thermo-controlled CSS testing of CL soil compacted dry of optimum moisture content (w=9.0%). Figures 5.1 – 5.4 show typical soil response on the basis of shear strain amplitude. The figures are arranged from smaller strains Figure 5.1(a) to larger strains Figure 5.1(d) with cycles 1, 5, and 10 highlighted to show the effects of temperature on successive cyclic loading applications. The data shows that regardless of temperature, cyclic load application up to N=10 had little effect on shear modulus for small to medium shear strain amplitudes ($\gamma < 1.0\%$). For larger shear strain amplitudes ($\gamma > 1.0\%$) increasing cyclic load application caused a significant decrease in peak shear stress for a fixed shear strain value. Figures 5.1(c, d) – 5.4(c, d) show that the majority of the decrease in peak shear stress happens by cycle N=5, with the decrease becoming less pronounced at higher temperatures. The four shear strain amplitude values are kept constant in the presented data to show how increasing temperature affects shear stiffness at varying shear strain values. For a fixed shear strain amplitude, peak shear stress measurably decreased as temperature increased thus indicating a reduction in shear modulus. This effect can most clearly be seen when comparing Figure 5.1 with Figure 5.4.

Figures 5.5 – 5.6 show typical soil response on the basis of soil temperature. The figures are arranged from RT (room temperature) Figure 5.5(a) to 60^{o}C Figure 5.5(d) for a given shear strain amplitude. A small strain amplitude and a large strain amplitude were chosen to visually compare the effects of temperature at small and large cyclic shear deformations. The figures show all ten cyclic load applications for a given temperature and shear strain combination. Figure 5.5 shows a slight reduction in peak shear stress for increasing temperatures at small shear strain amplitudes ($\gamma = 0.035\%$). Figure 5.6 shows a similar trend; however, the effect of temperature is much greater at large shear strain amplitudes ($\gamma = 8.0\%$) causing a significant reduction in peak shear stress and by extension shear modulus.

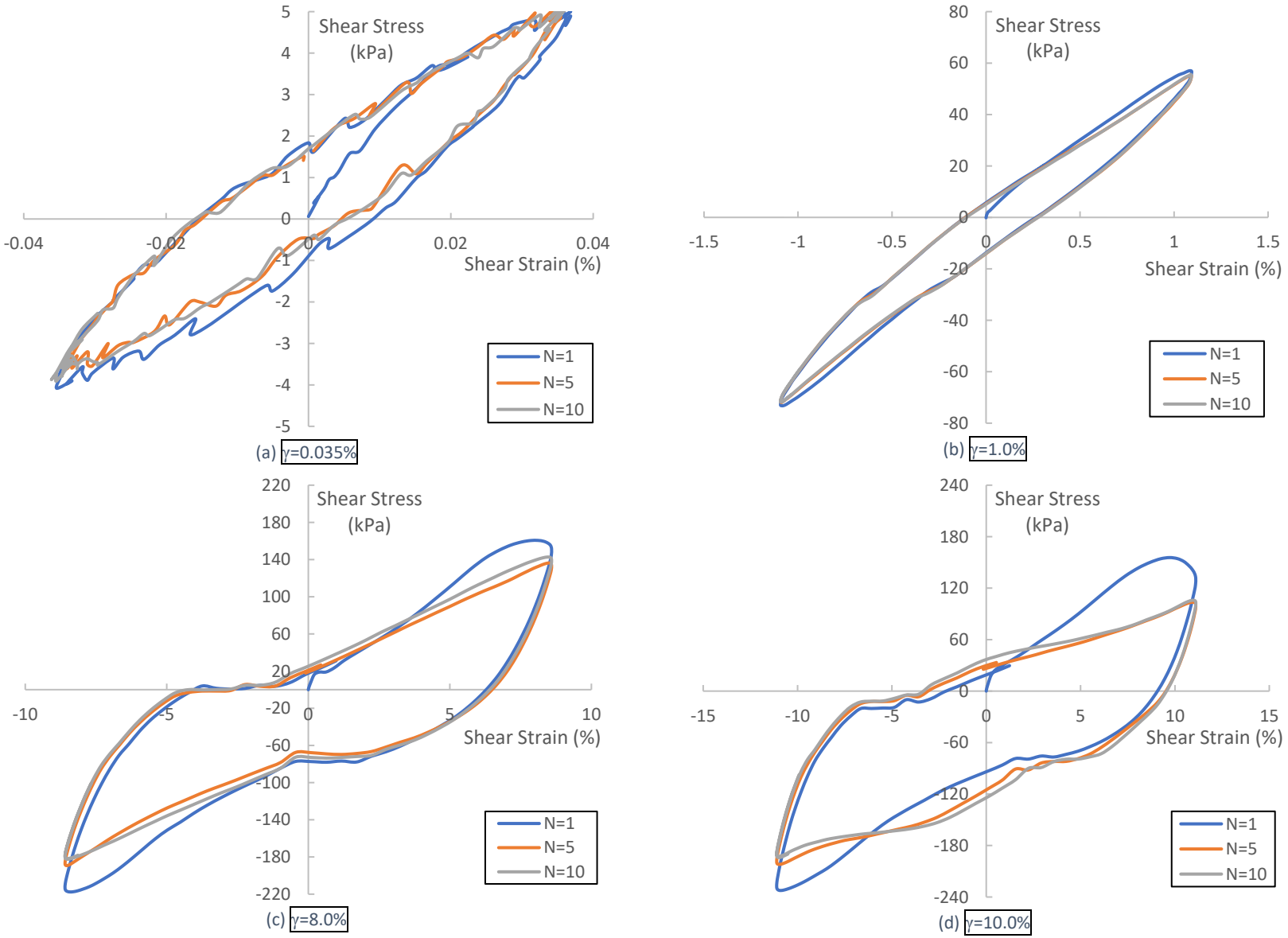

Figure 5.1: Typical CL Soil Response (w=9.0%) on the Basis of Shear Strain Amplitude for RT

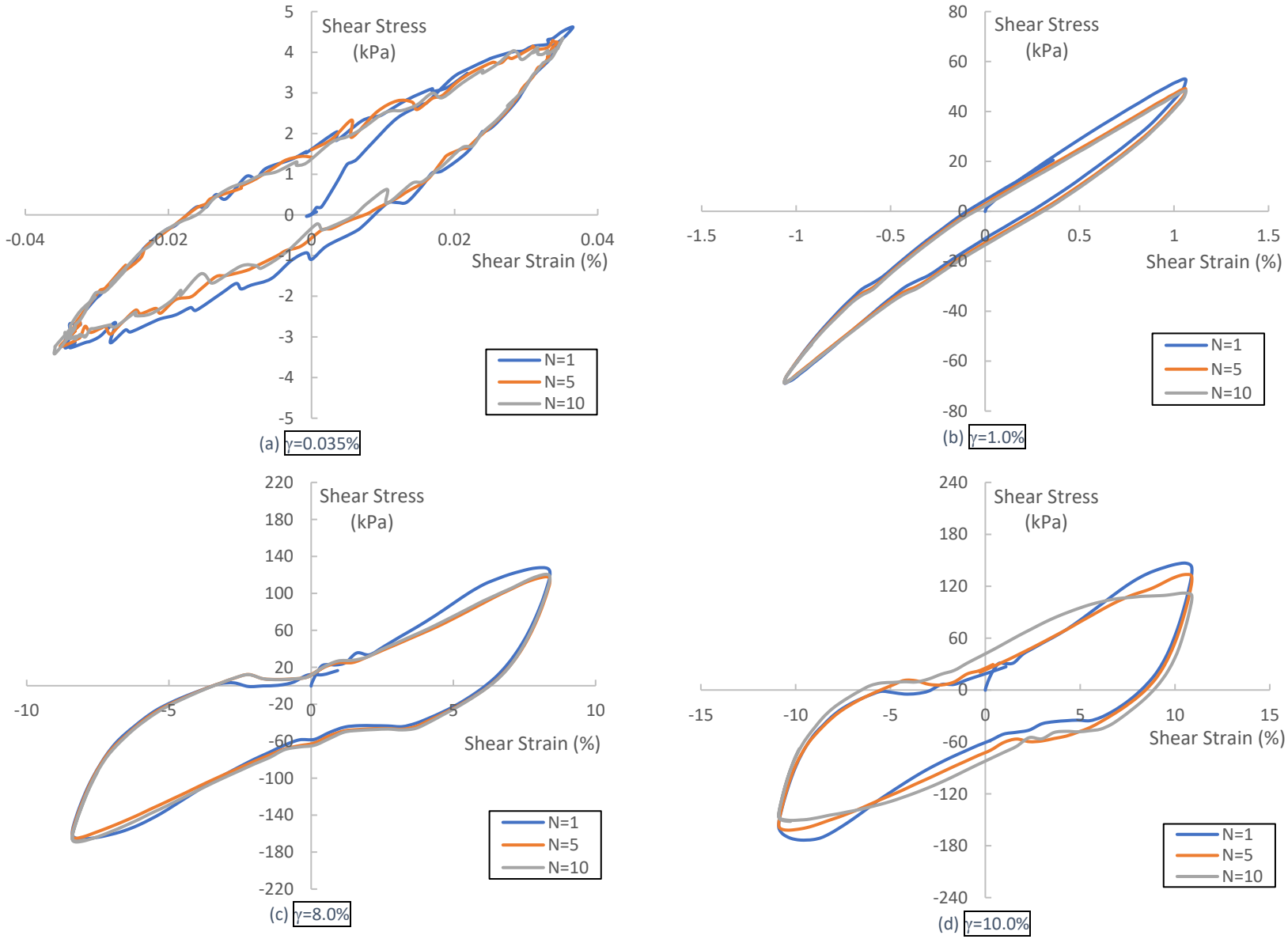

Figure 5.2: Typical CL Soil Response (w=9.0%) on the Basis of Shear Strain Amplitude for 40°C

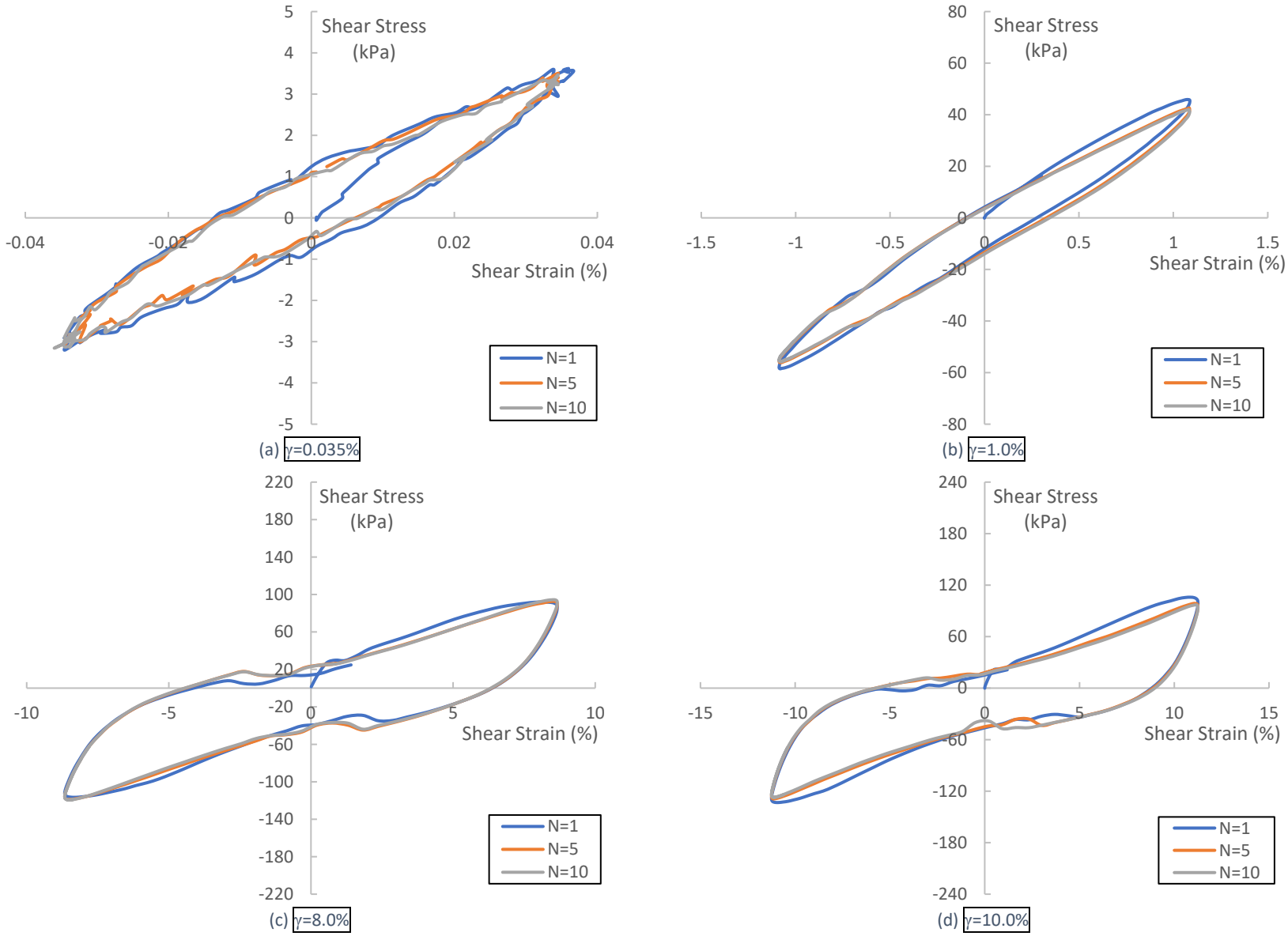

Figure 5.3: Typical CL Soil Response (w=9.0%) on the Basis of Shear Strain Amplitude for 50°C

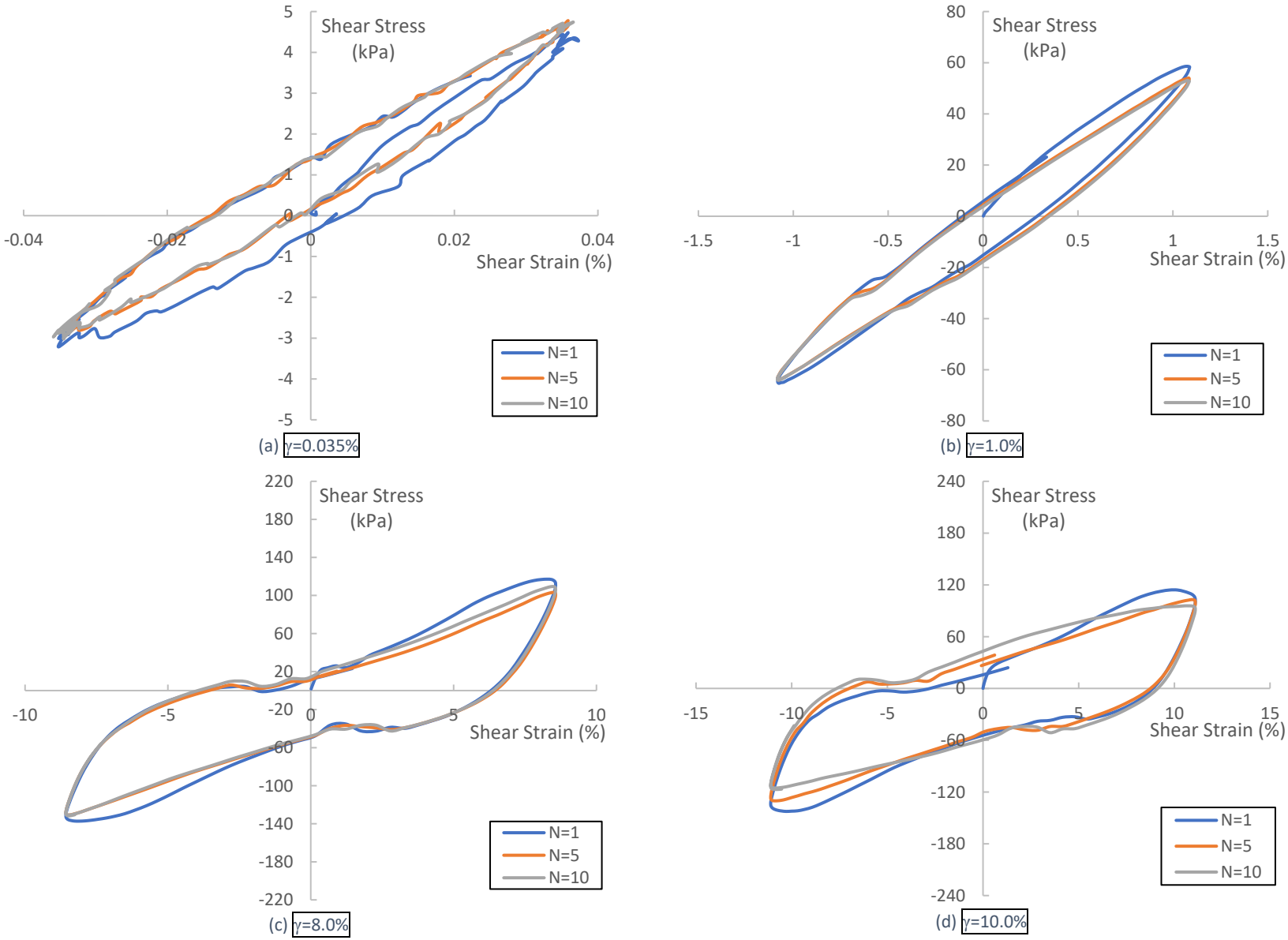

Figure 5.4: Typical CL Soil Response (w=9.0%) on the Basis of Shear Strain Amplitude for 60°C

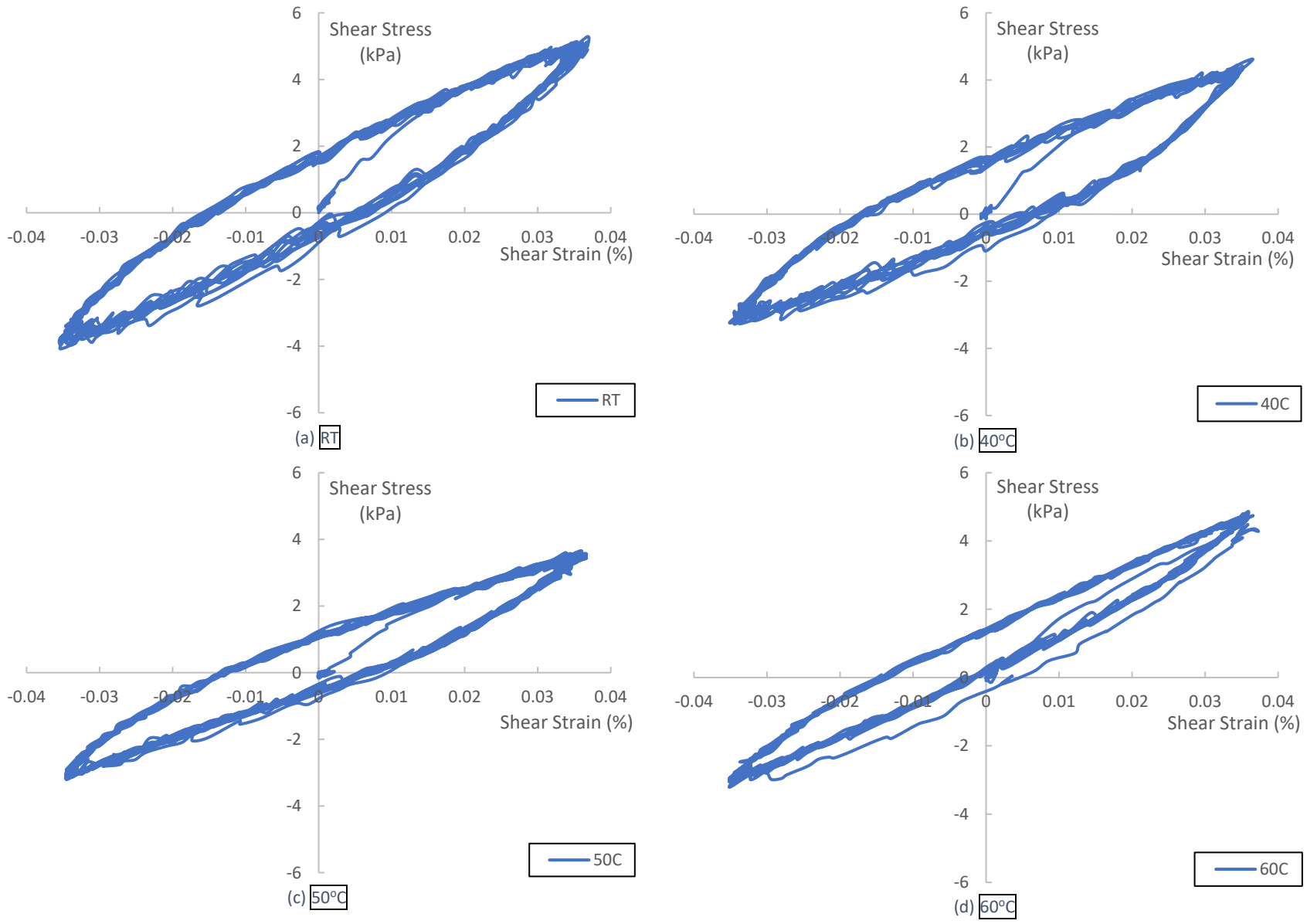

Figure 5.5: Typical CL Soil Response (w=9.0%) on the Basis of Soil Temperature for γ = 0.035%

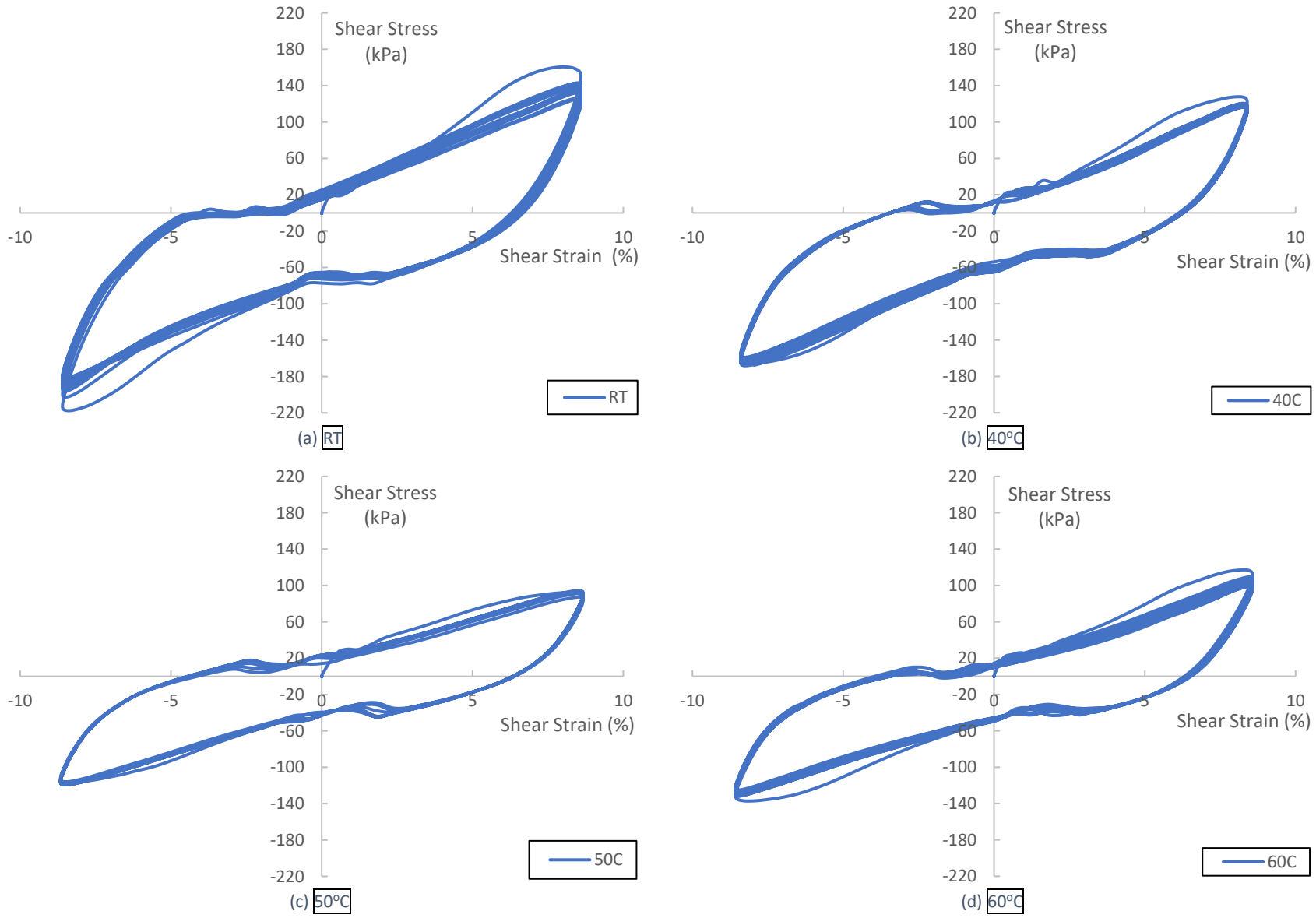

Figure 5.6: Typical CL Soil Response (w=9.0%) on the Basis of Soil Temperature for γ = 8.0%

5.1.2 - CL Soil Compacted at Optimum Moisture Content (w=13.6%)

Figures 5.7 – 5.12 show various experimental test data from thermo-controlled CSS testing of CL soil compacted at optimum moisture content (w=13.6%). Figures 5.7 – 5.10 show typical soil response on the basis of shear strain amplitude. The figures are arranged similarly to those in the previous section. Like the previous section, the data shows that regardless of temperature, cyclic load application up to N=10 had little effect on shear modulus for small to medium shear strain amplitudes ($\gamma < 1.0\%$). For larger shear strain amplitudes ($\gamma > 1.0\%$) increasing cyclic load application caused a significant decrease in peak shear stress for a fixed shear strain value. Figures 5.7(c, d) – 5.10(c, d) show that the majority of the decrease in peak shear stress happens by cycle N=5, with the decrease becoming less pronounced at higher temperatures. For a fixed shear strain amplitude, peak shear stress measurably decreased as temperature increased thus corroborating a reduction in shear modulus. This effect can most clearly be seen when comparing Figure 5.7(c) ($\tau = 60$ kPa) with Figure 5.10(c) ($\tau = 40$ kPa).

Figures 5.11 – 5.12 show typical soil response on the basis of soil temperature. The figures are arranged similarly to the previous section. Figure 5.11 shows a slight reduction in peak shear stress for increasing temperatures at small shear strain amplitudes ($\gamma = 0.035\%$). Figure 5.12 shows a similar trend; however, the effect of temperature is much greater at large shear strain amplitudes ($\gamma = 4.0\%$) causing a significant reduction in peak shear stress and by extension shear modulus.

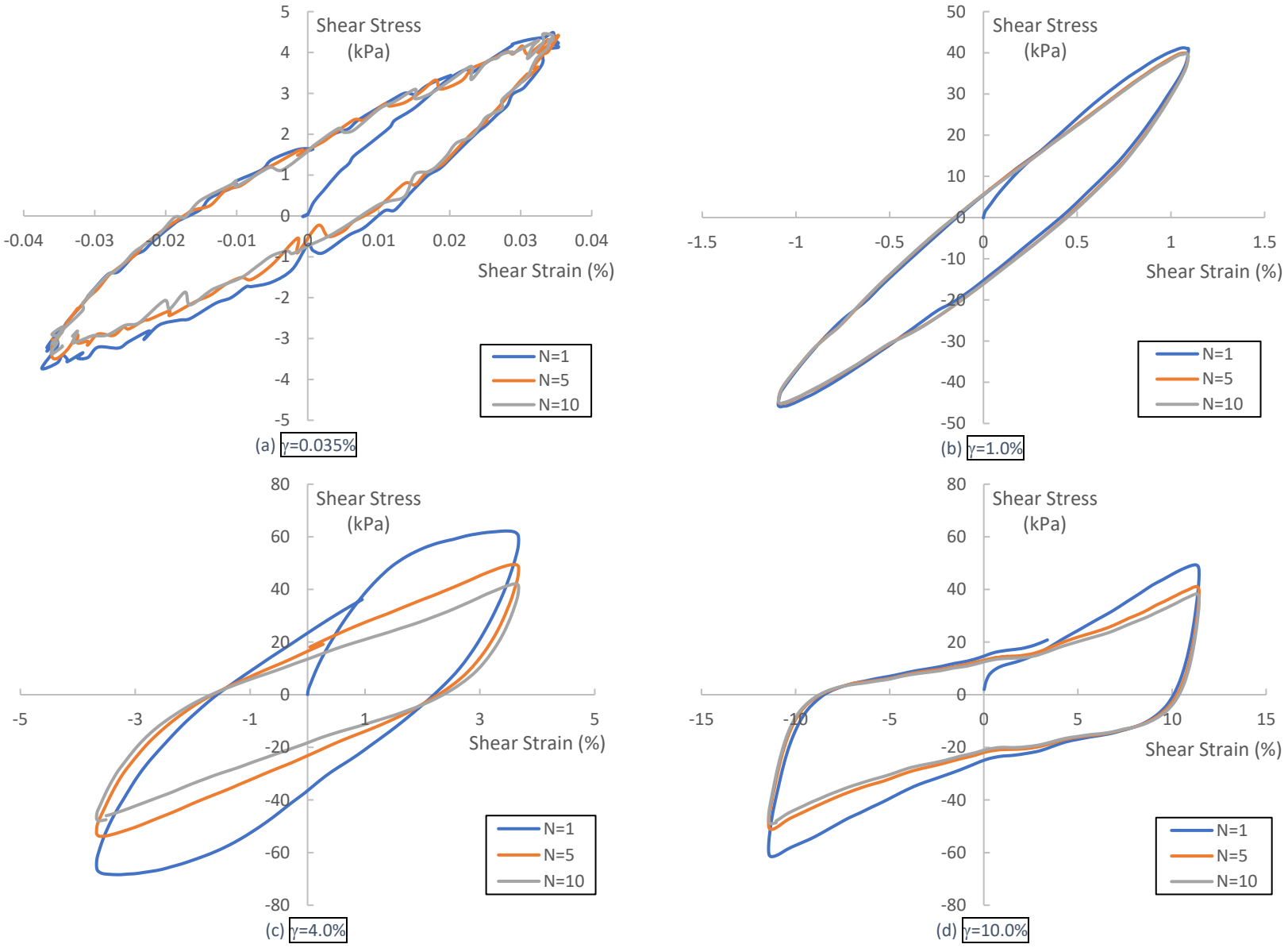

Figure 5.7: Typical CL Soil Response (w=13.6%) on the Basis of Shear Strain Amplitude for RT

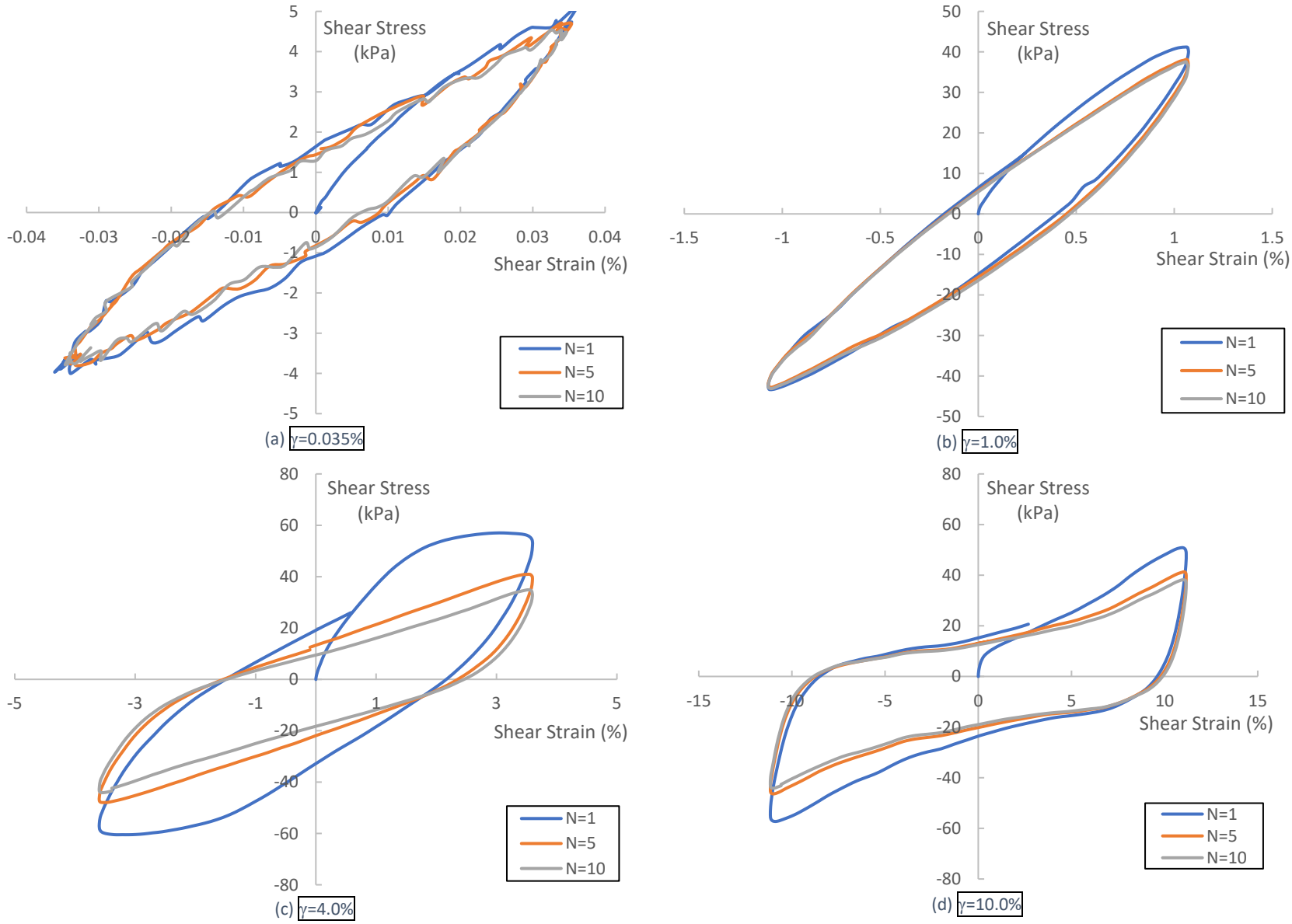

Figure 5.8: Typical CL Soil Response (w=13.6%) on the Basis of Shear Strain Amplitude for 40°C

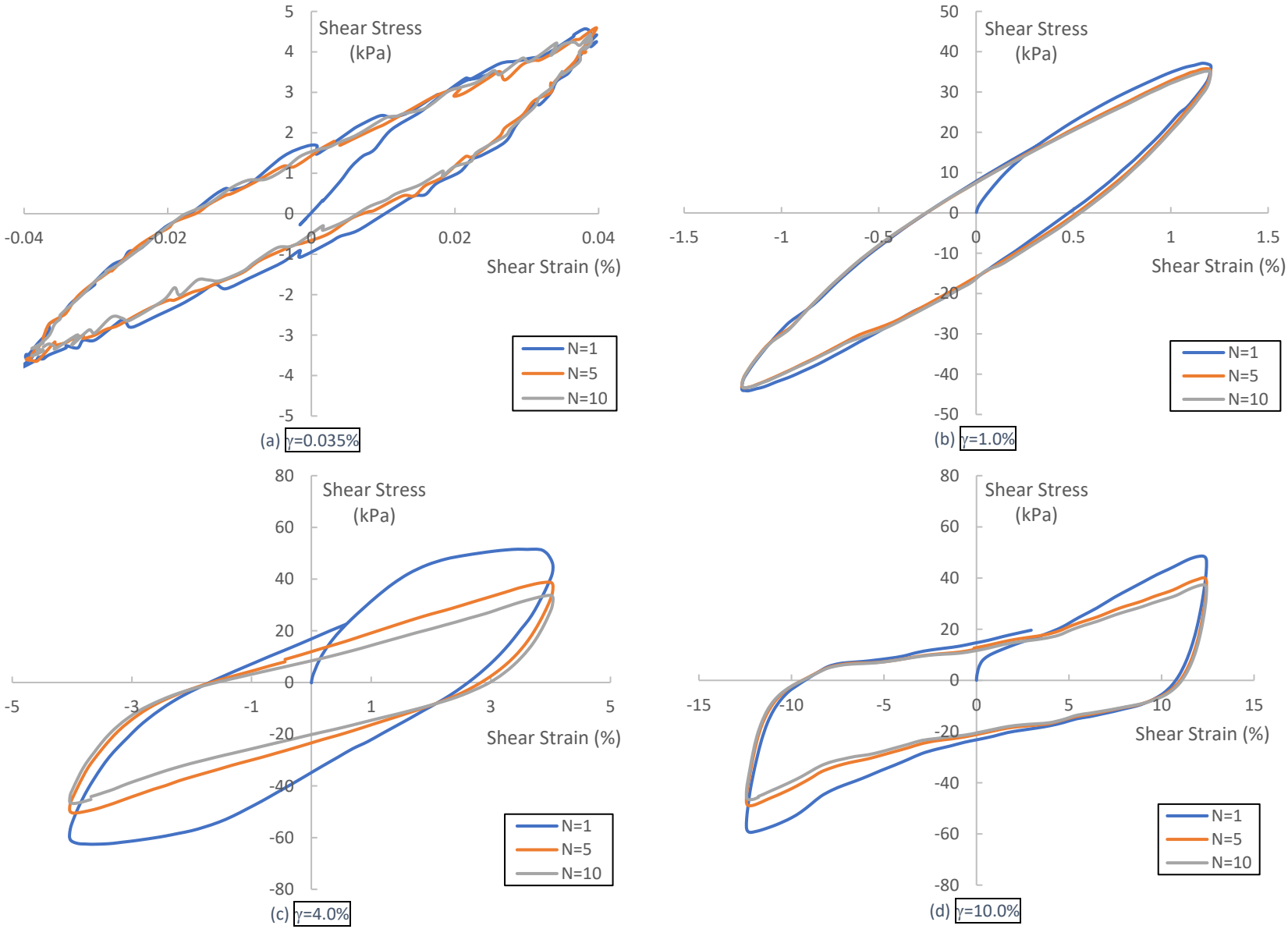

Figure 5.9: Typical CL Soil Response (w=13.6%) on the Basis of Shear Strain Amplitude for 50°C

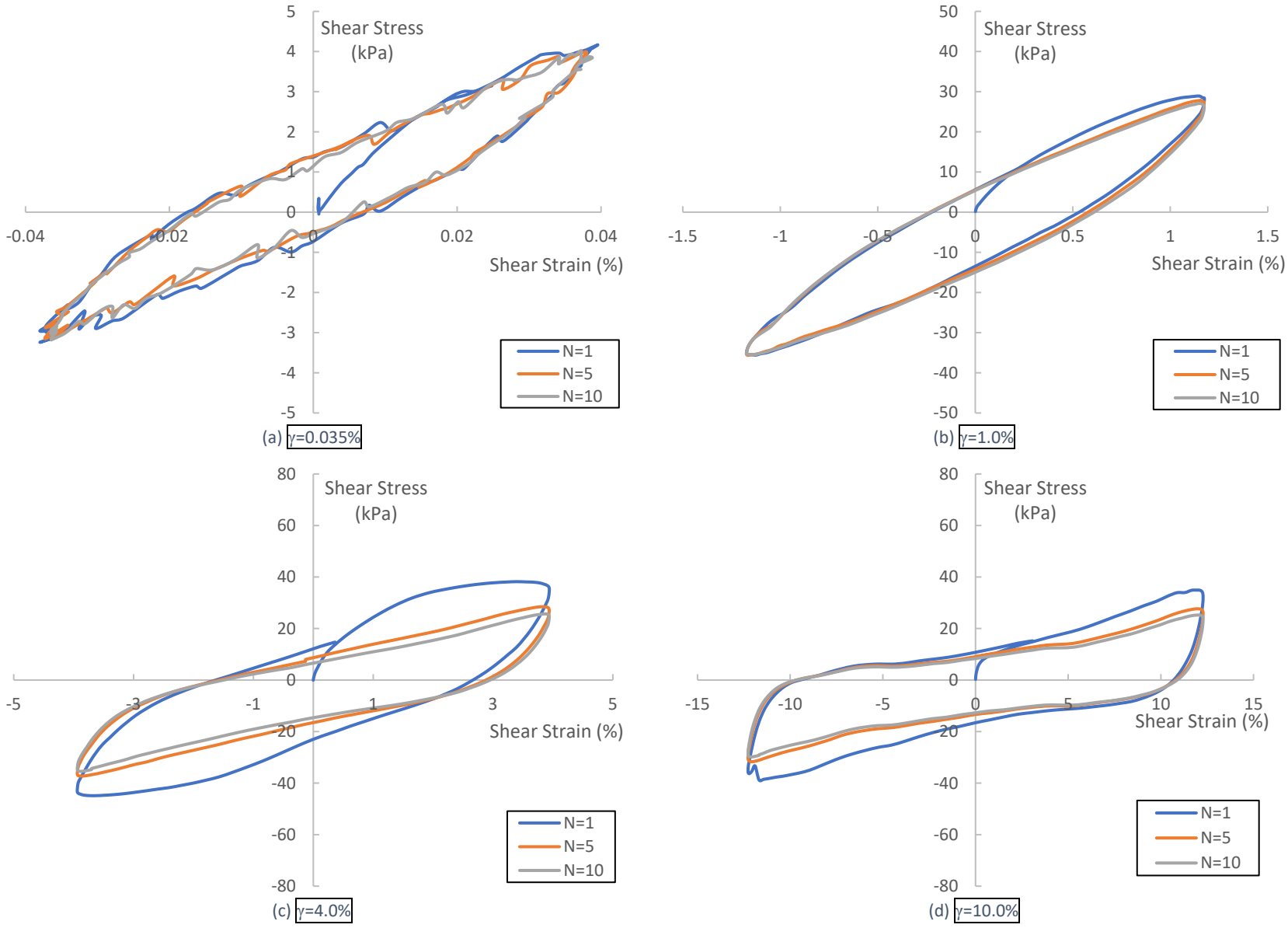

Figure 5.10: Typical CL Soil Response (w=13.6%) on the Basis of Shear Strain Amplitude for 60°C

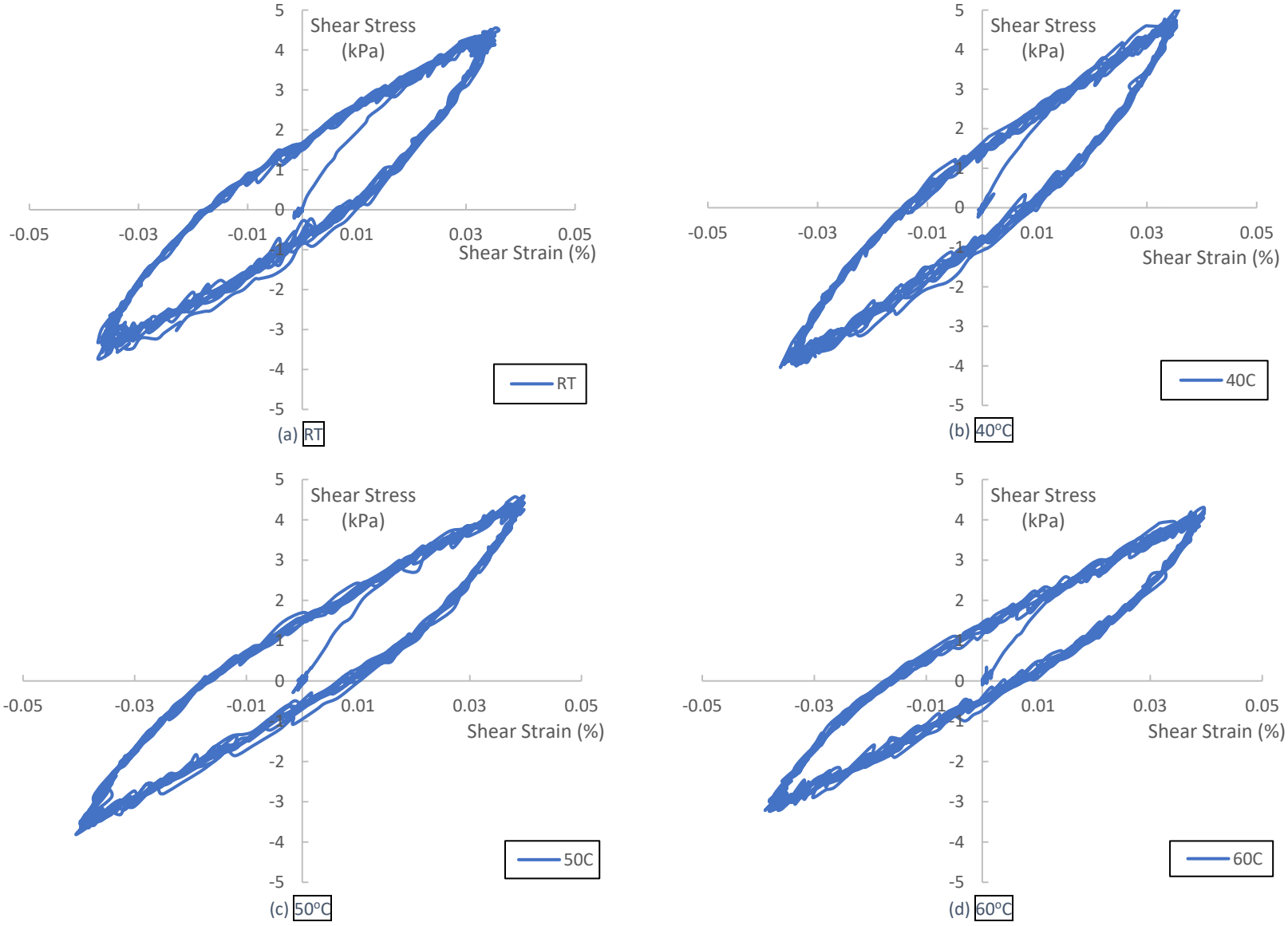

Figure 5.11: Typical CL Soil Response (w=13.6%) on the Basis of Soil Temperature for γ = 0.035%

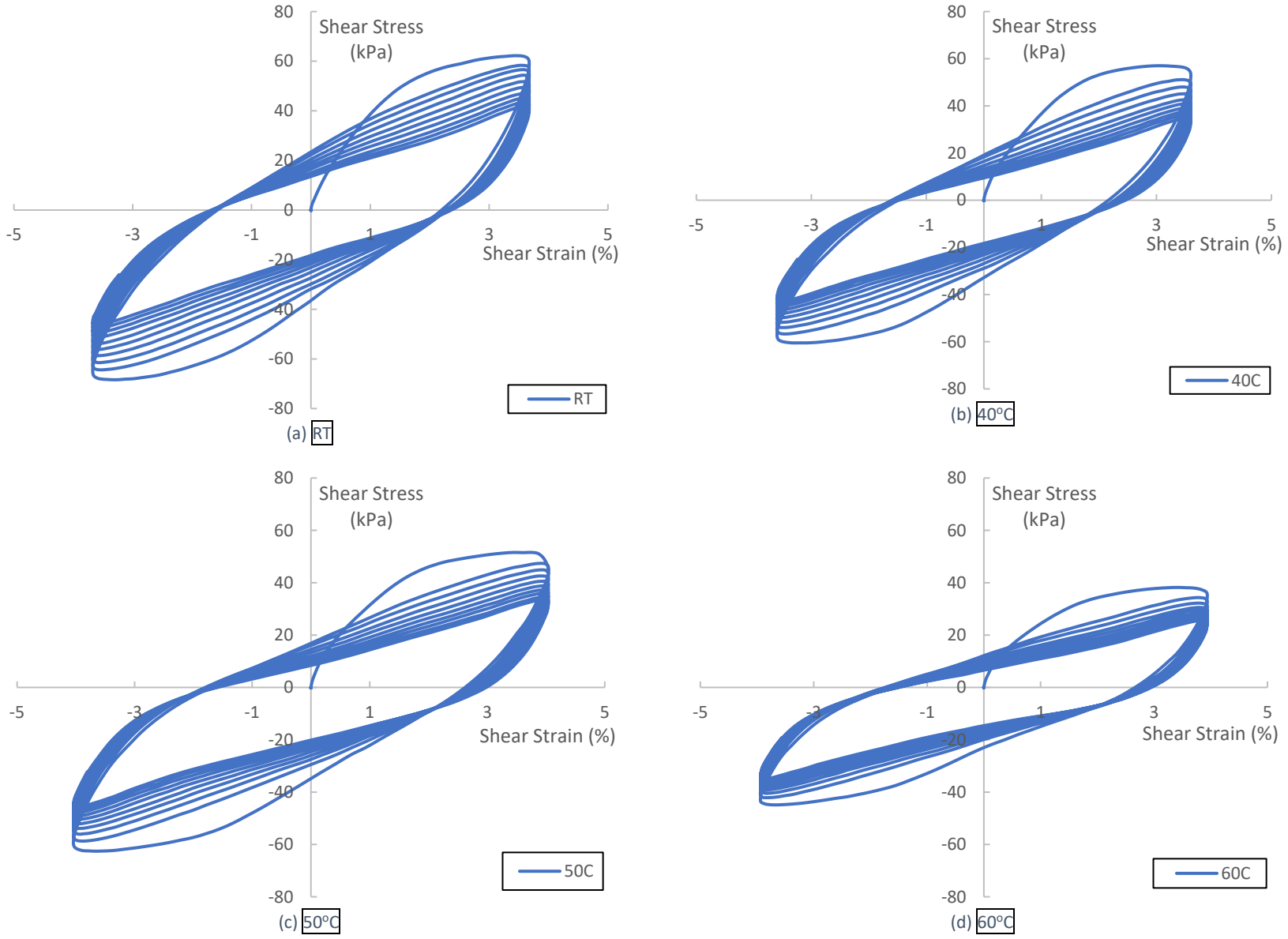

Figure 5.12: Typical CL Soil Response (w=13.6%) on the Basis of Soil Temperature for γ = 4.0%

5.1.3 - CL Soil Compacted Wet of Optimum Moisture Content (w=17.0%)

Figures 5.13 – 5.18 show various experimental test data from thermo-controlled CSS testing of CL soil compacted wet of optimum moisture content (w=17.0%). Figures 5.13 – 5.16 show typical soil response on the basis of shear strain amplitude. The figures are arranged similarly to those in the previous sections. Like the previous sections, the data shows that regardless of temperature, cyclic load application up to N=10 had little effect on shear modulus for small to medium shear strain amplitudes ($\gamma < 1.0\%$). For larger shear strain amplitudes ($\gamma > 1.0\%$) increasing cyclic load application caused a significant decrease in peak shear stress for a fixed shear strain value. Figures 5.13(c, d) – 5.16(c, d) show that the majority of the decrease in peak shear stress happens by cycle N=5, with the decrease per cyclic load application staying relatively constant as temperature increases. For a fixed shear strain amplitude, peak shear stress measurably decreased as temperature increased for large shear strains, substantiating previous observations of a reduction in shear modulus with increasing soil temperatures. This effect can most clearly be seen when comparing Figure 5.13(c) ($\tau = 60$ kPa) with Figure 5.16(c) ($\tau = 50$ kPa).

Figures 5.17 – 5.18 show typical soil response on the basis of soil temperature. The figures are arranged similarly to the previous sections. Figure 5.17 shows no reduction in peak shear stress for increasing temperatures at small shear strain amplitudes ($\gamma = 0.035\%$). However, Figure 5.18 shows the effect of temperature is much greater at large shear strain amplitudes ($\gamma = 6.0\%$) causing a significant reduction in peak shear stress and by extension shear modulus.

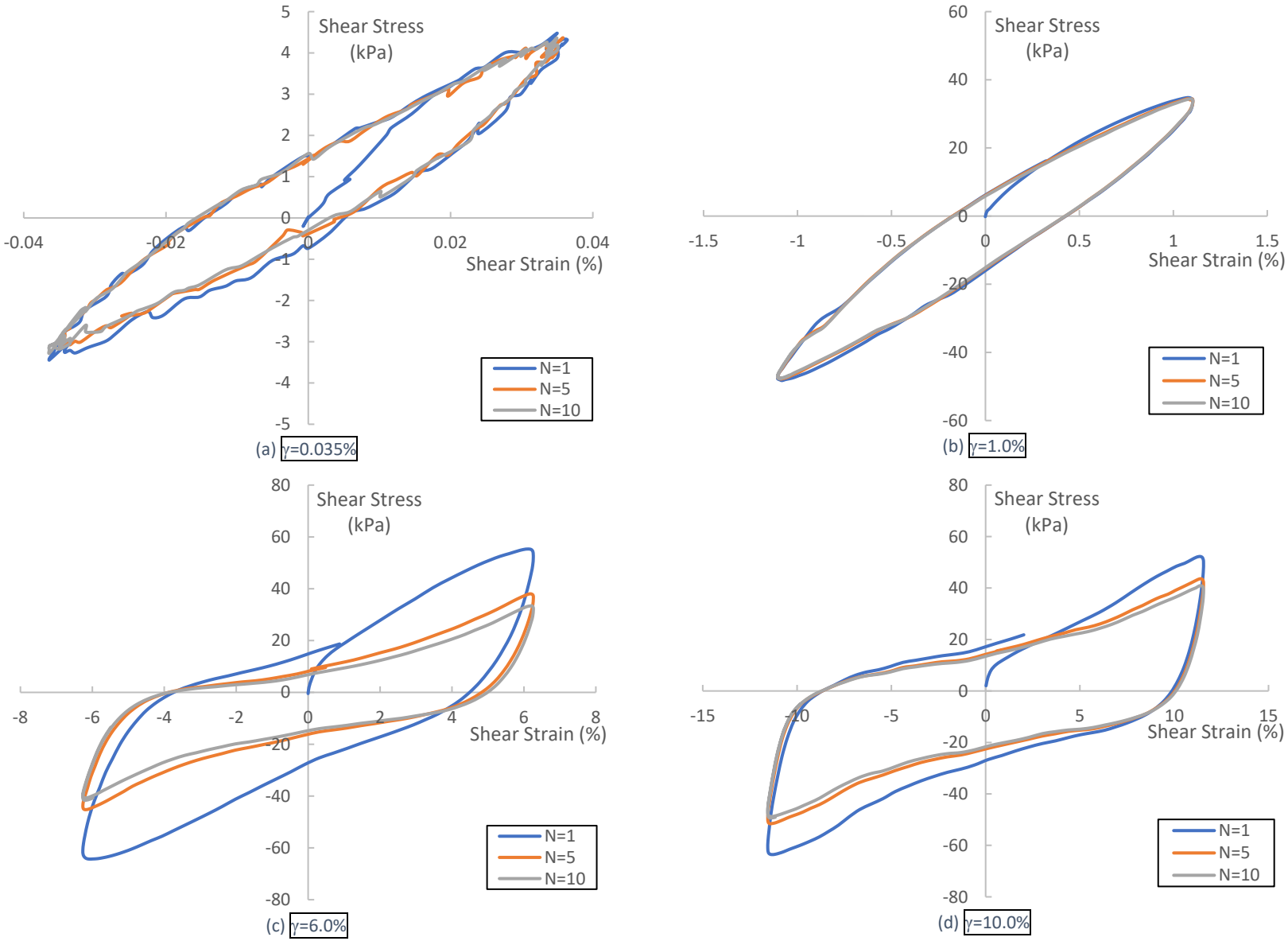

Figure 5.13: Typical CL Soil Response (w=17.0%) on the Basis of Shear Strain Amplitude for RT

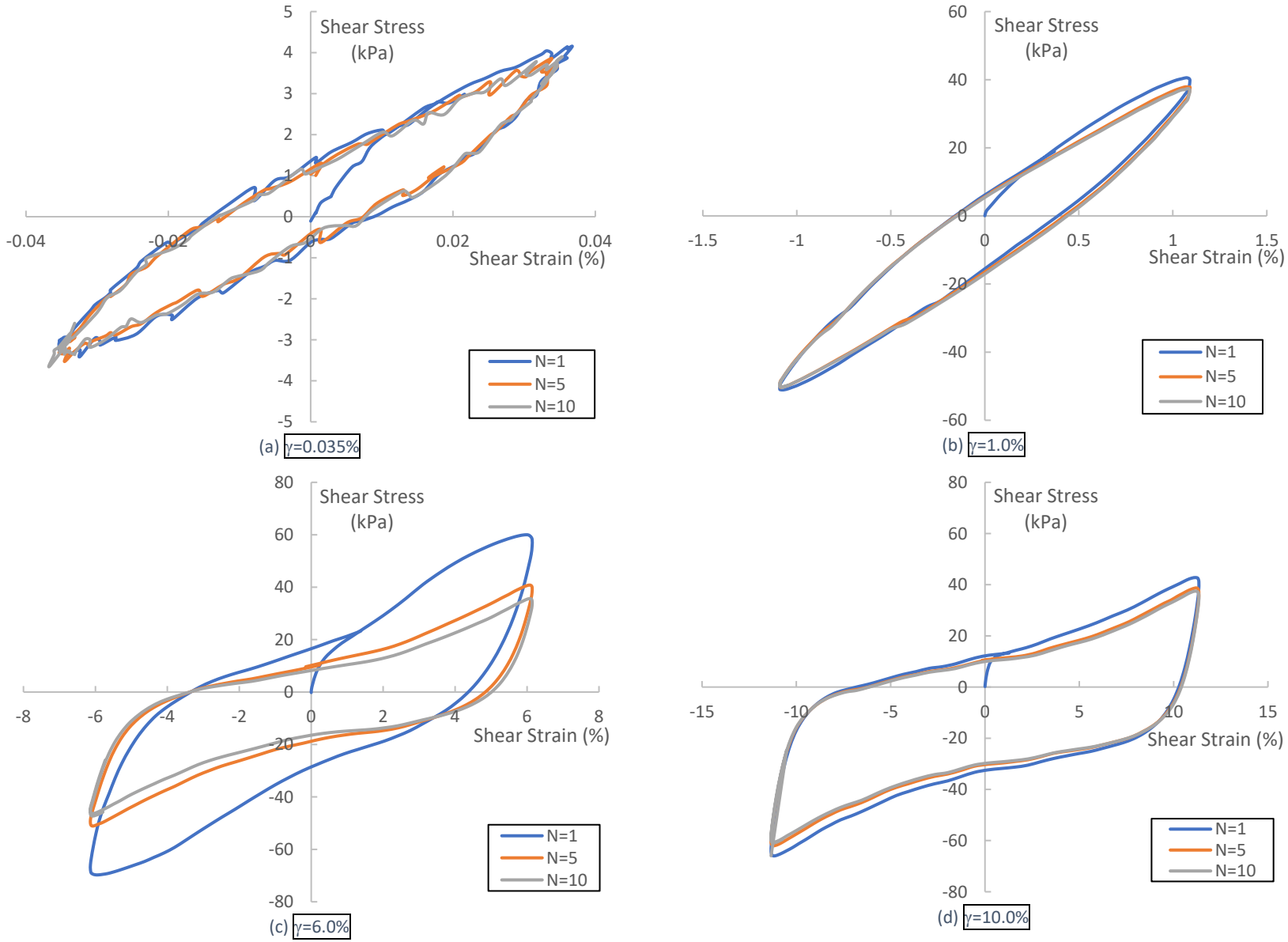

Figure 5.14: Typical CL Soil Response (w=17.0%) on the Basis of Shear Strain Amplitude for 40°C

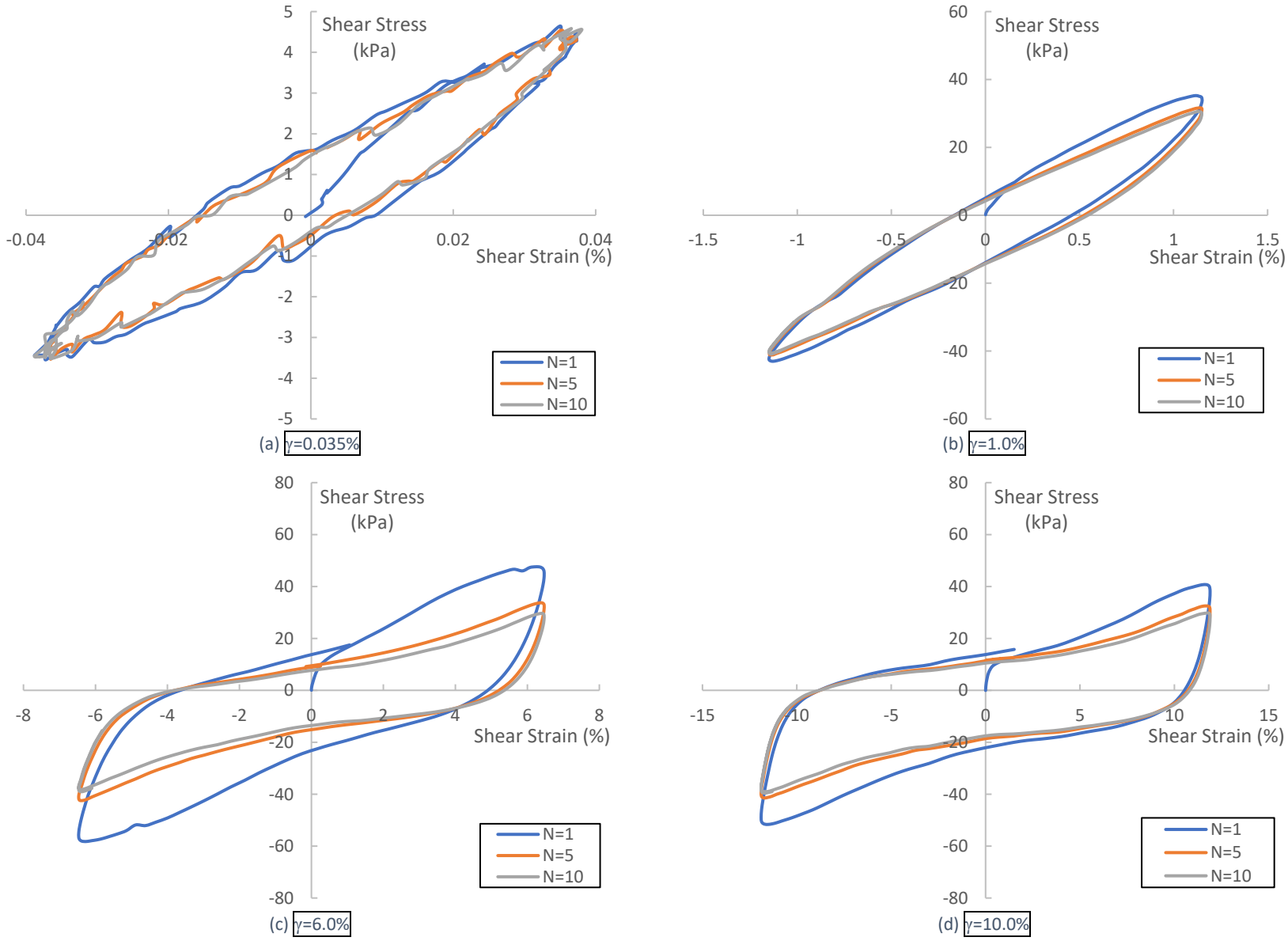

Figure 5.15: Typical CL Soil Response (w=17.0%) on the Basis of Shear Strain Amplitude for 50°C

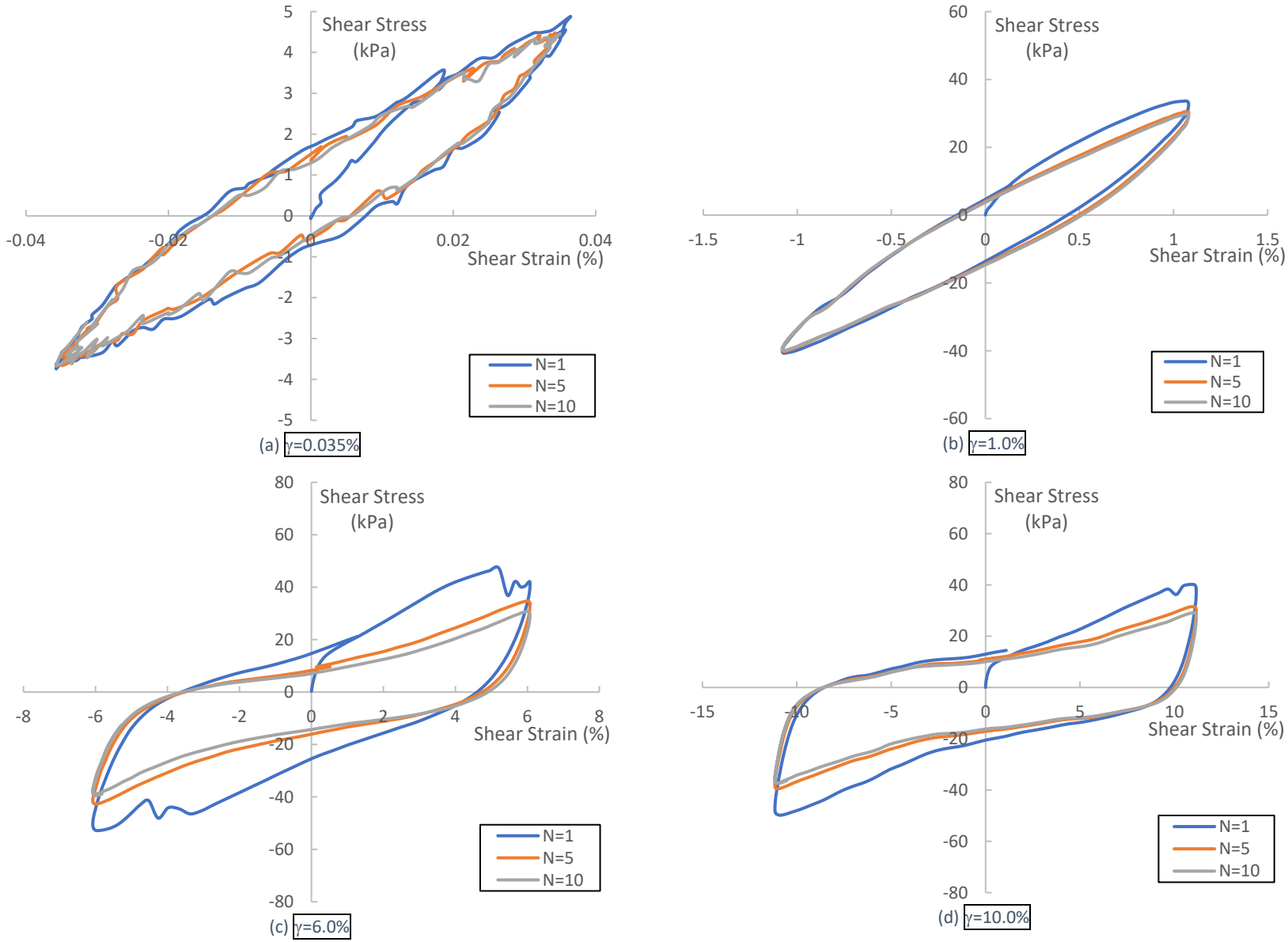

Figure 5.16: Typical CL Soil Response (w=17.0%) on the Basis of Shear Strain Amplitude for 60°C

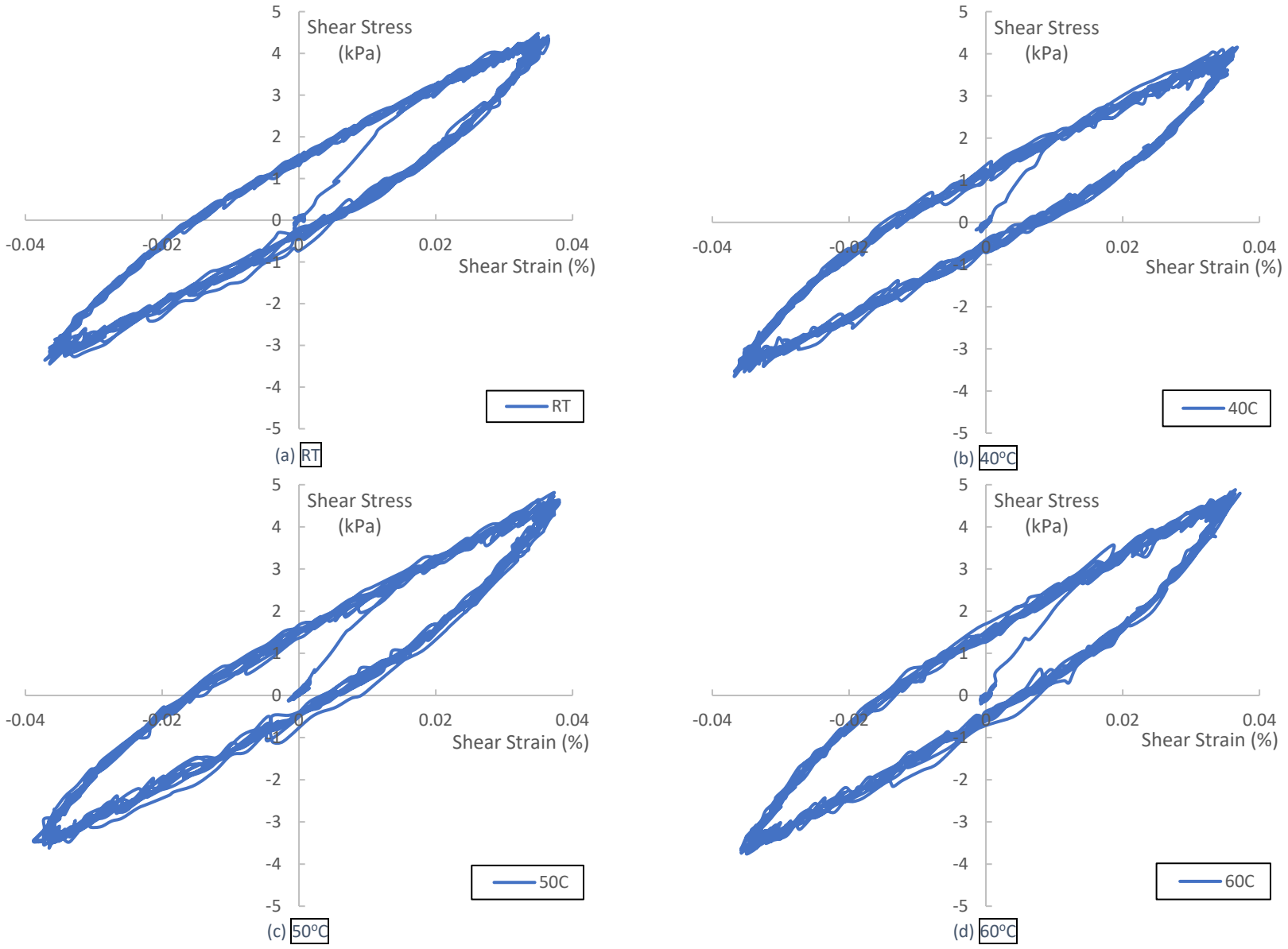

Figure 5.17: Typical CL Soil Response (w=17.0%) on the Basis of Soil Temperature for γ = 0.035%

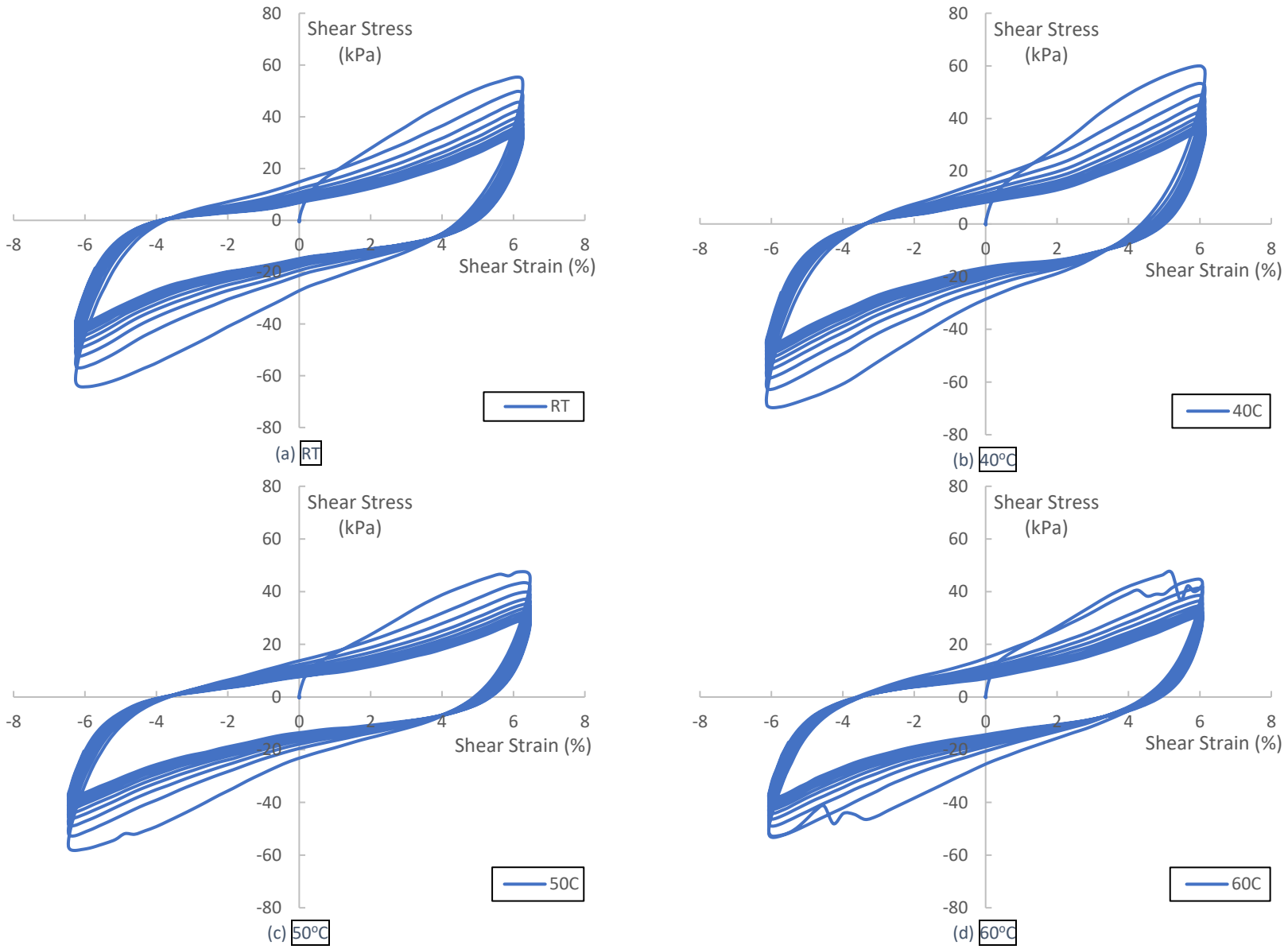

Figure 5.18: Typical CL Soil Response (w=17.0%) on the Basis of Soil Temperature for γ = 6.0%

5.2 - Typical Silty Soil (ML) Response

Figures 5.19 – 5.24 show various experimental test data from thermo-controlled CSS testing of ML soil compacted at optimum moisture content (w=14.8%). Figures 5.19 – 5.22 show typical soil response on the basis of shear strain amplitude. The figures are arranged similarly to those in the previous sections. Like the previous sections, the data shows that regardless of temperature, cyclic load application up to N=10 had little effect on shear modulus for small to moderately large shear strain amplitudes (γ < 4.0%). For larger shear strain amplitudes (γ > 4.0%) increasing cyclic load application caused a significant decrease in peak shear stress for a fixed shear strain value. Figures 5.19(d) – 5.22(d) show that the majority of the decrease in peak shear stress happens by cycle N=5, with the decrease becoming less pronounced at higher temperatures. For a fixed shear strain amplitude, peak shear stress measurably decreased as temperature increased indicating a reduction in shear modulus. This effect can most clearly be seen when comparing Figure 5.19(c) (τ = 70 kPa) with Figure 5.22(c) (τ = 50 kPa).

Figures 5.23 – 5.24 show typical soil response on the basis of soil temperature. The figures are arranged similarly to the previous sections. Figure 5.23 shows no reduction in peak shear stress for increasing temperatures from RT to 50^{o}C and a slight increase in peak shear stress for 60^{o}C at small shear strain amplitudes (γ = 0.035%). However, Figure 5.24 shows the effect of temperature is much greater at large shear strain amplitudes (γ = 10.0%). Even though the peak shear stress reduction was greatest for the 40^{o}C sample (Figure 5.24(b)), the overall trend shows peak shear stress is lower for samples tested at higher temperatures (40^{o}C – 60^{o}C) when compared to RT values, hence indicating a significant reduction in peak shear stress and by extension shear modulus with increasing soil temperature.

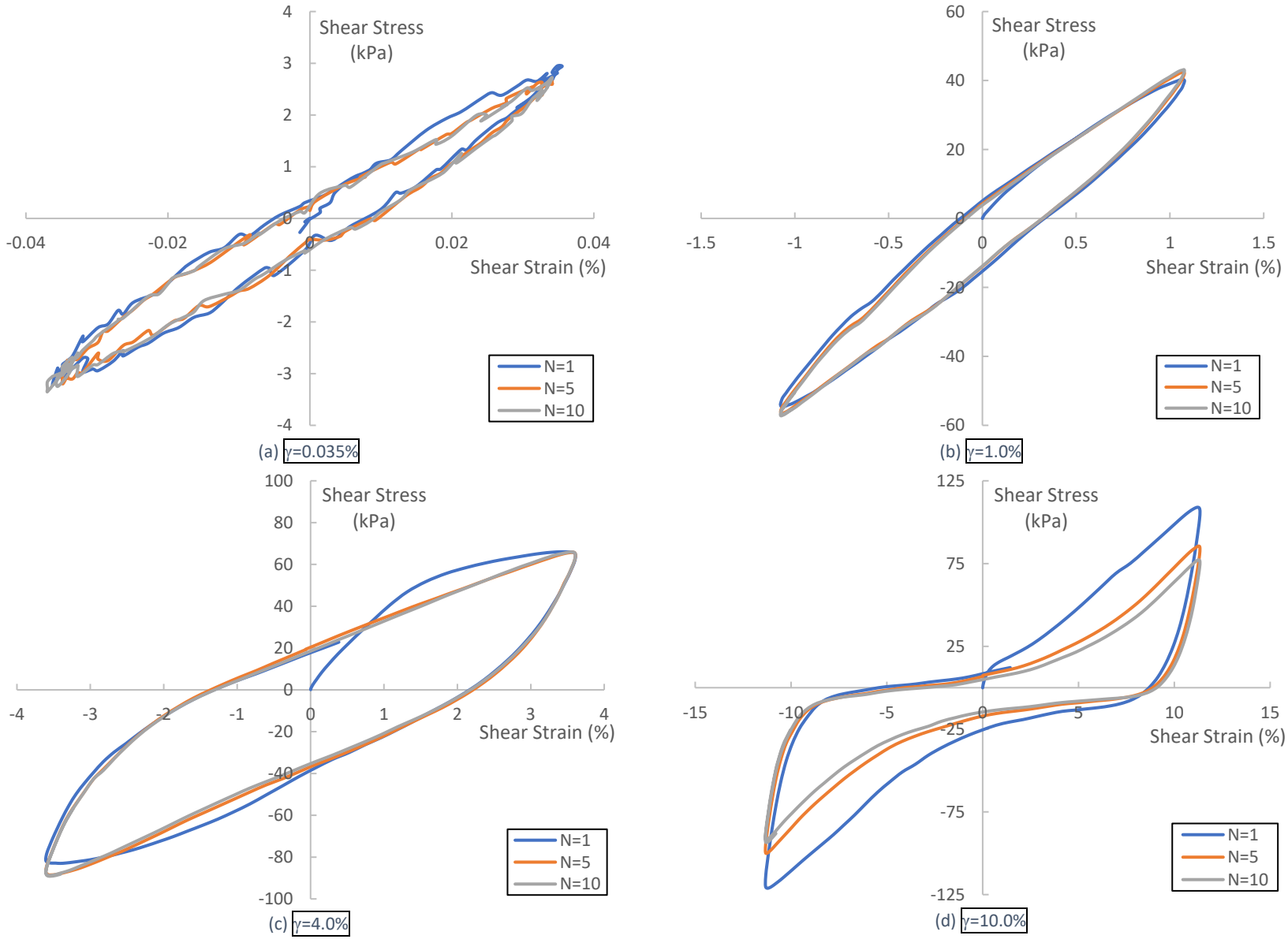

Figure 5.19: Typical ML Soil Response (w=14.8%) on the Basis of Shear Strain Amplitude for RT

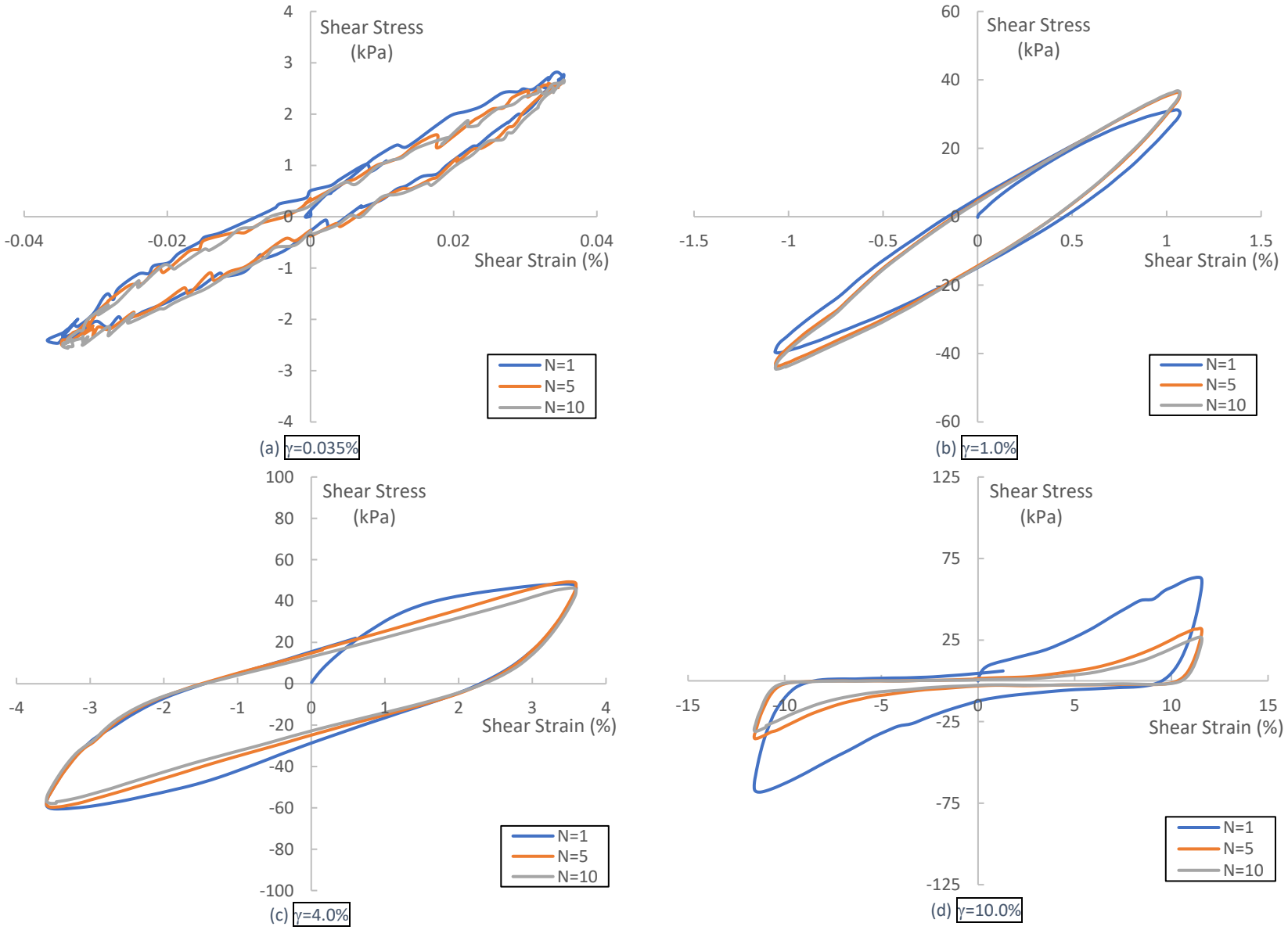

Figure 5.20: Typical ML Soil Response (w=14.8%) on the Basis of Shear Strain Amplitude for 40°C

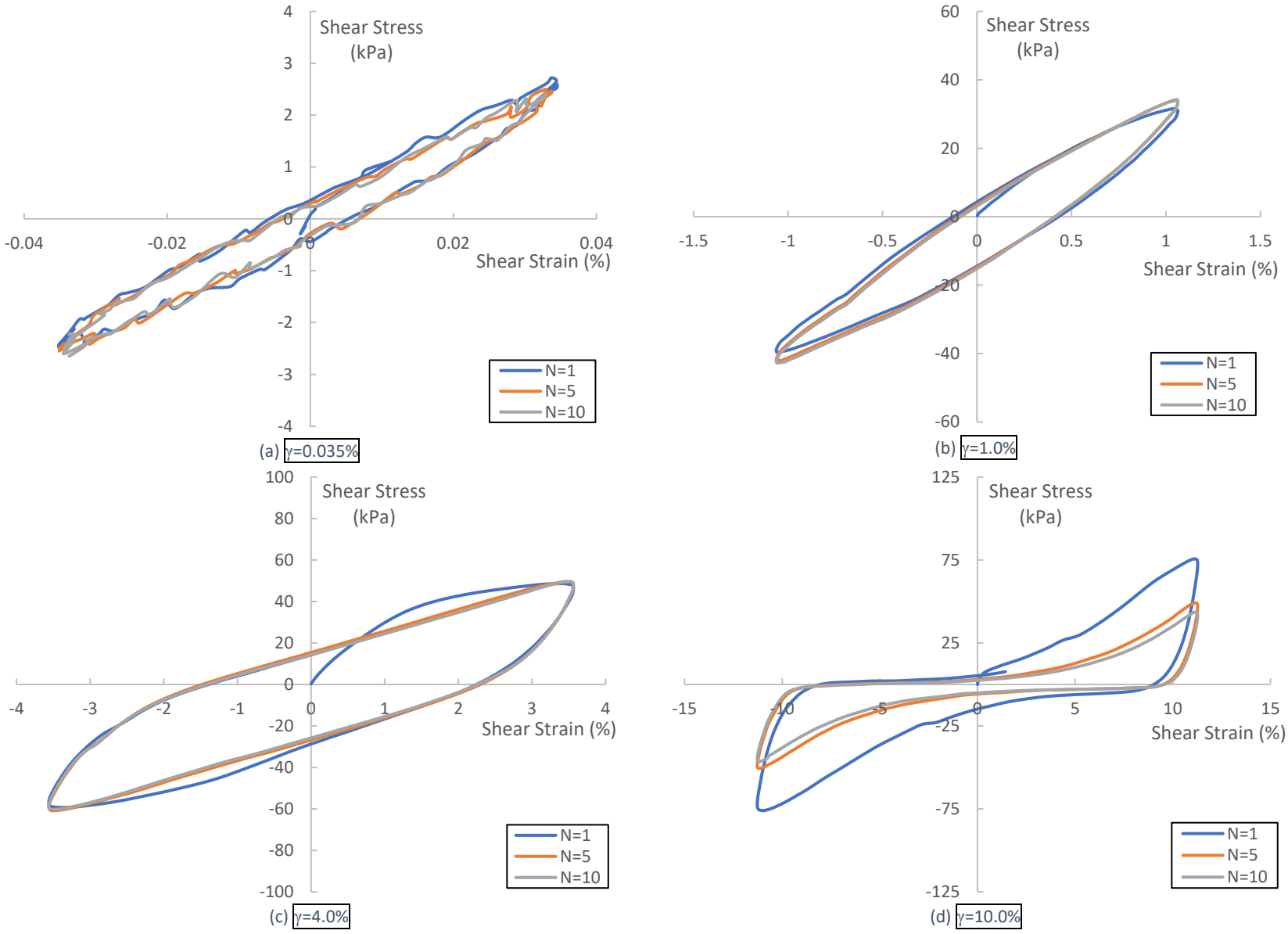

Figure 5.21: Typical ML Soil Response (w=14.8%) on the Basis of Shear Strain Amplitude for 50°C

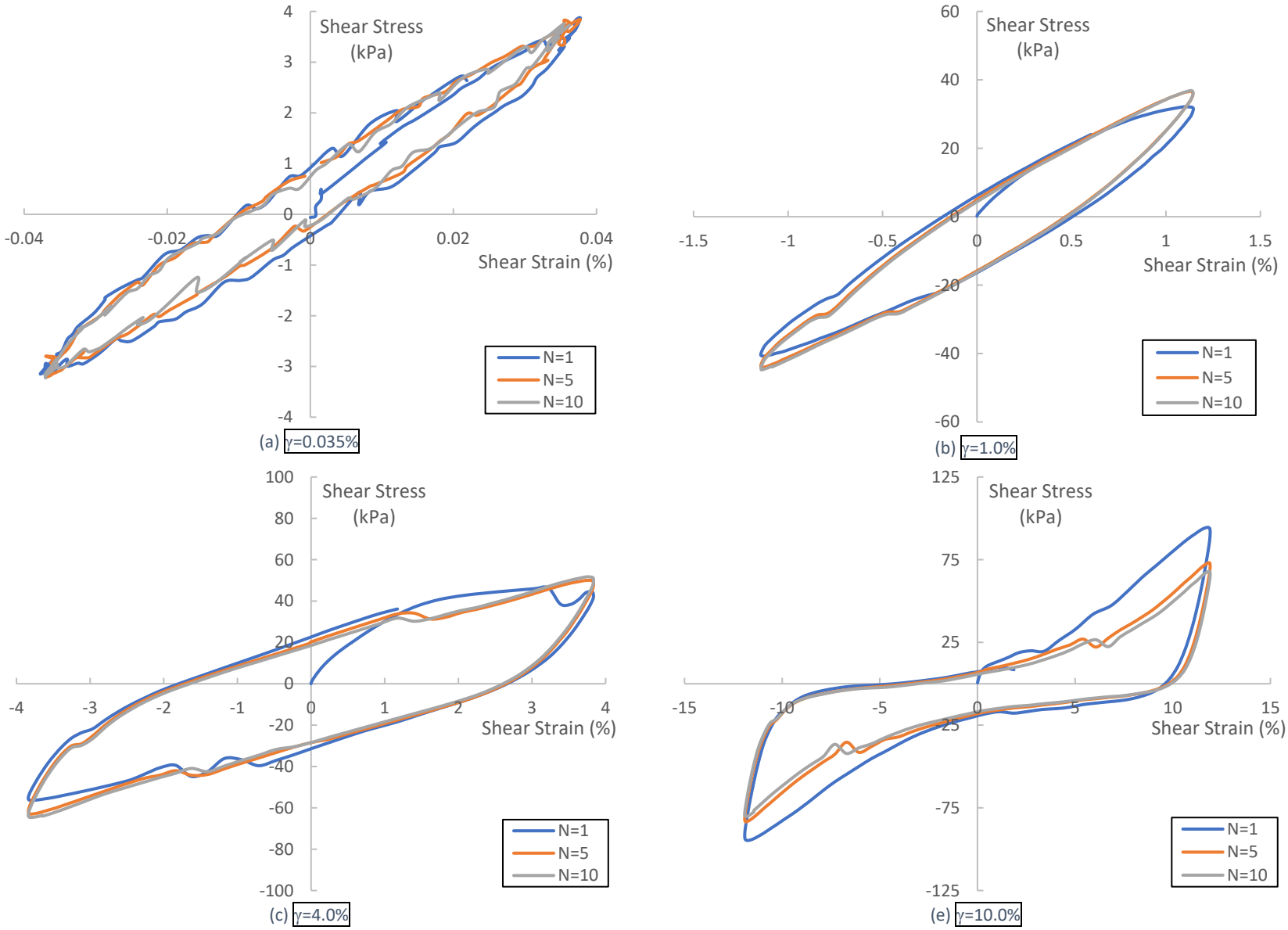

Figure 5.22: Typical ML Soil Response (w=14.8%) on the Basis of Shear Strain Amplitude for 60°C

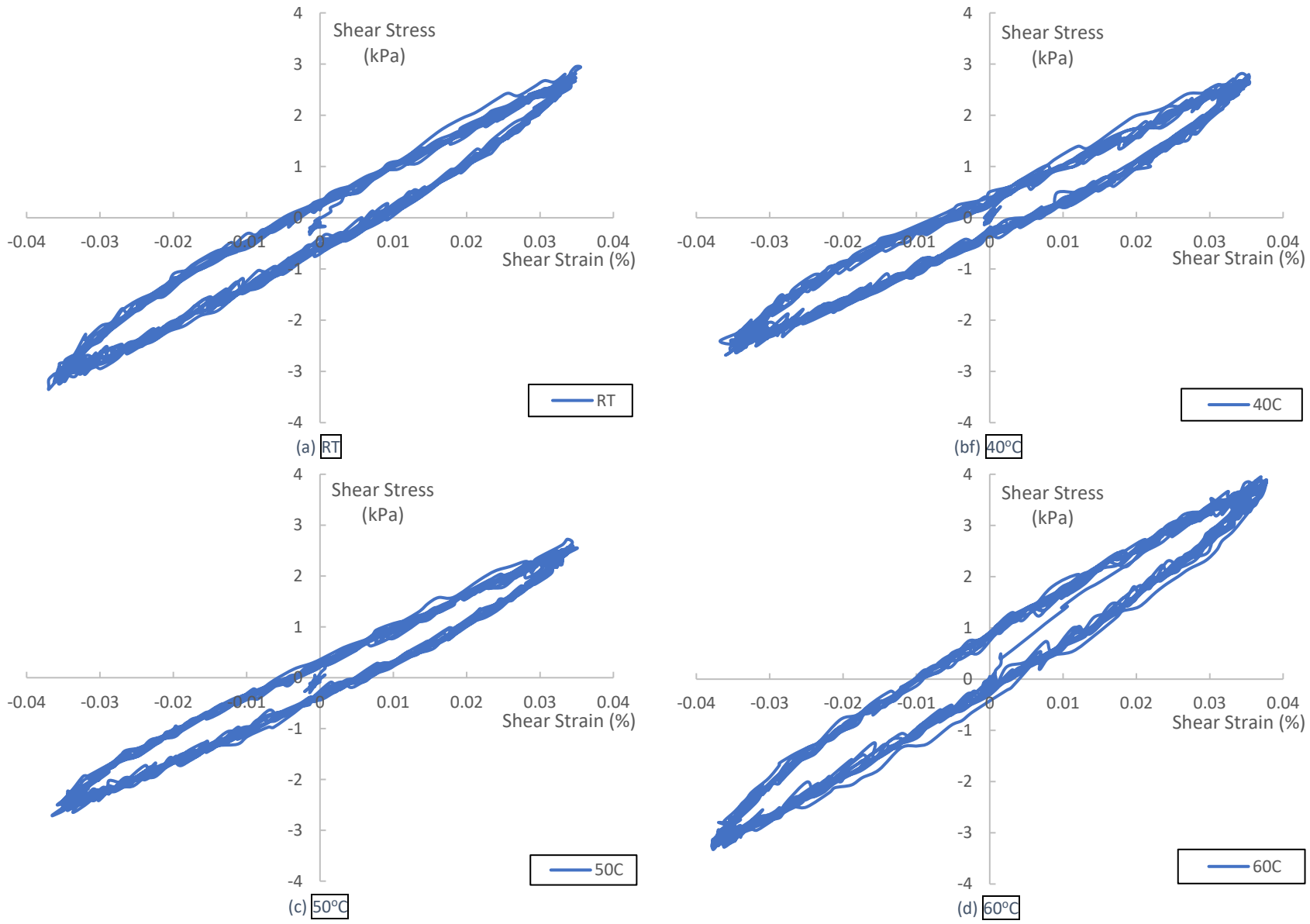

Figure 5.23: Typical ML Soil Response (w=14.8%) on the Basis of Soil Temperature for γ = 0.035%

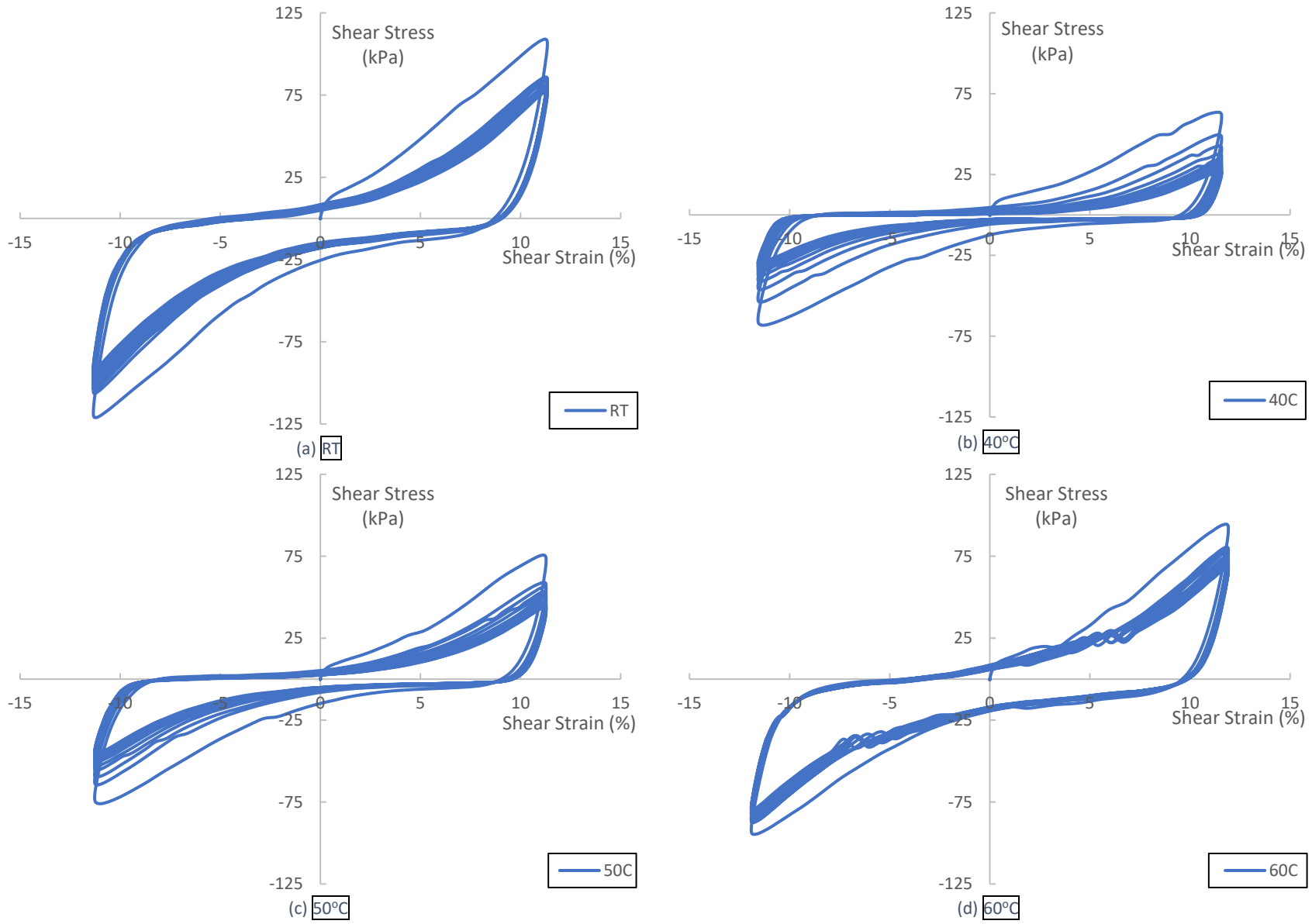

Figure 5.24: Typical ML Soil Response (w=14.8%) on the Basis of Soil Temperature for γ = 10.0%

5.3 - Typical Sandy Soil (SC) Response

Figures 5.25 – 5.30 show various experimental test data from thermo-controlled CSS testing of SC soil compacted at optimum moisture content (w=10.0%). Figures 5.25 – 5.28 show typical soil response on the basis of shear strain amplitude. The figures are arranged similarly to those in the previous sections. Like the previous sections, the data shows that regardless of temperature, cyclic load application up to N=10 had little effect on shear modulus for small to medium shear strain amplitudes ($\gamma < 1.0\%$). For larger shear strain amplitudes ($\gamma > 1.0\%$) increasing cyclic load application caused a significant decrease in peak shear stress for a fixed shear strain value. Figures 5.25(c, d) – 5.28(c, d) show that the majority of the decrease in peak shear stress happens by cycle N=5, with the decrease per cyclic load application staying relatively constant as temperature increases. For a fixed shear strain amplitude, peak shear stress measurably decreased as temperature increased for large shear strains indicating a reduction in shear modulus. This effect can most clearly be seen when comparing Figure 5.25(c) ($\tau = 90$ kPa) with Figure 5.28(c) ($\tau = 70$ kPa).

Figures 5.29 – 5.30 show typical soil response on the basis of soil temperature. The figures are arranged similarly to the previous sections. Figure 5.29 shows no reduction in peak shear stress for increasing temperatures at small shear strain amplitudes ($\gamma = 0.035\%$). However, Figure 5.30 shows a similar effect to the other soil types. As shear strain amplitude increases, the effect of temperature is more pronounced. At a large shear strain amplitude ($\gamma = 6.0\%$), peak shear stress is noticeably reduced and by extension shear modulus decreases significantly.

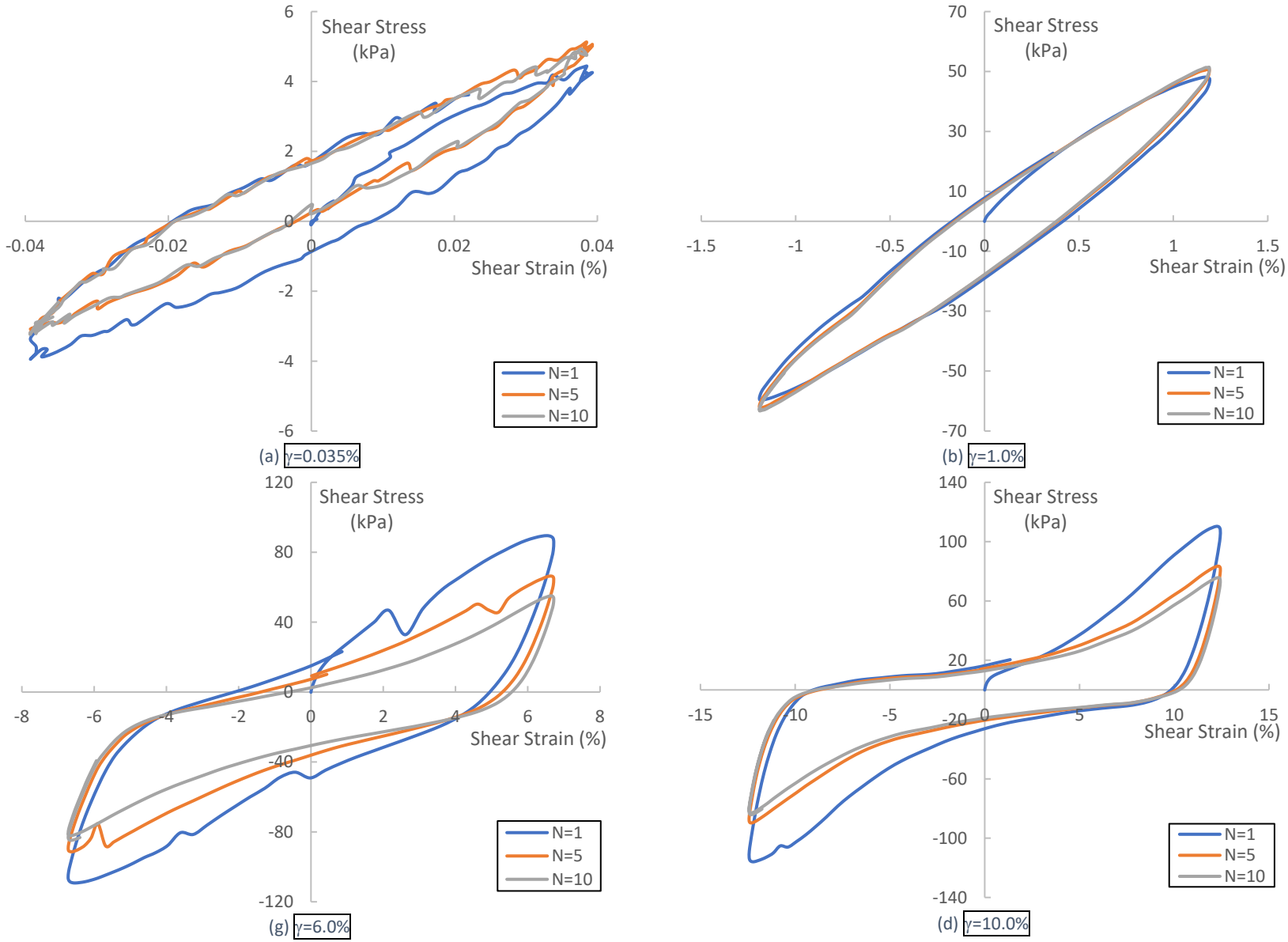

Figure 5.25: Typical SC Soil Response (w=10.0%) on the Basis of Shear Strain Amplitude for RT

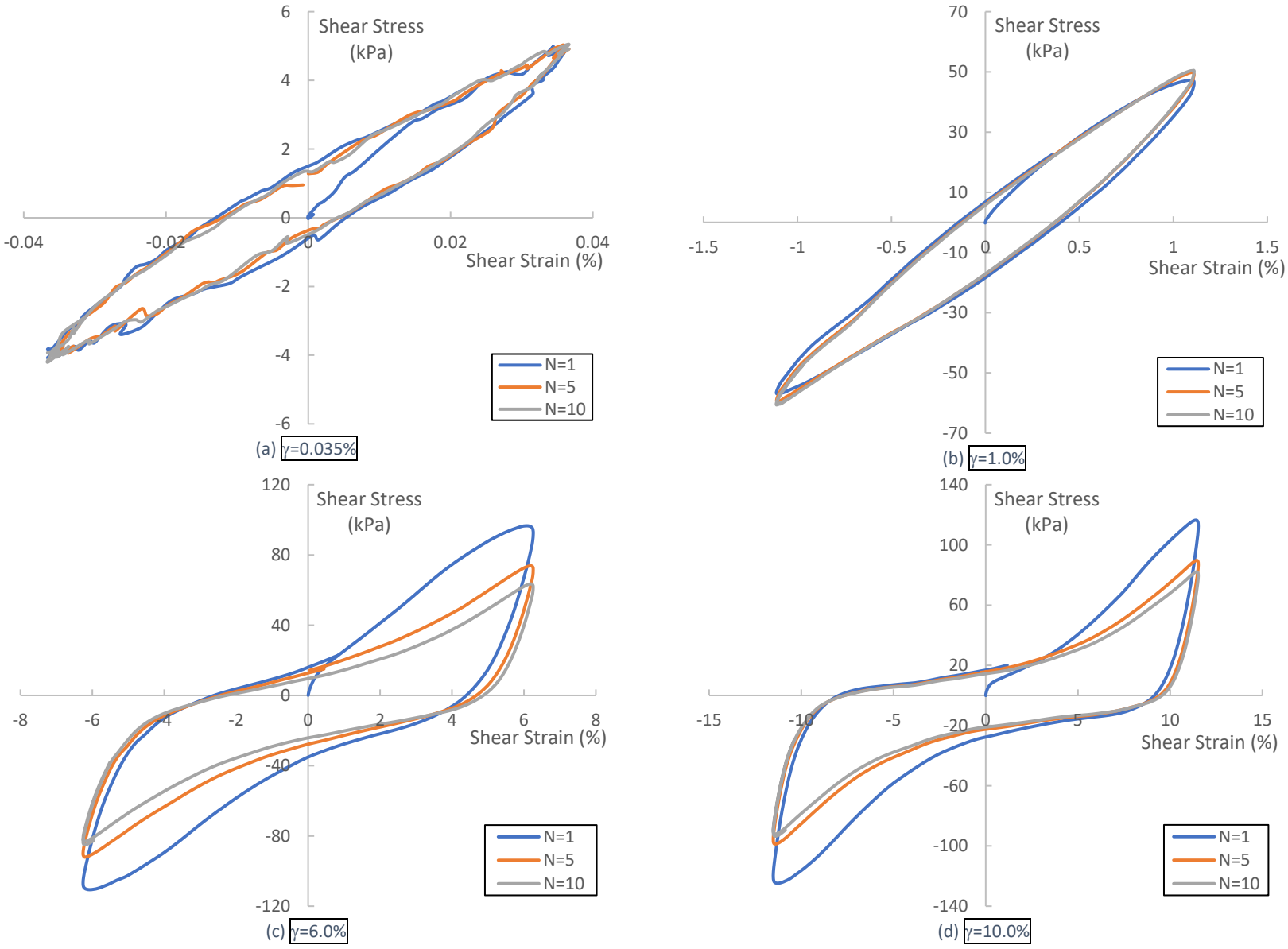

Figure 5.26: Typical SC Soil Response (w=10.0%) on the Basis of Shear Strain Amplitude for 40°C

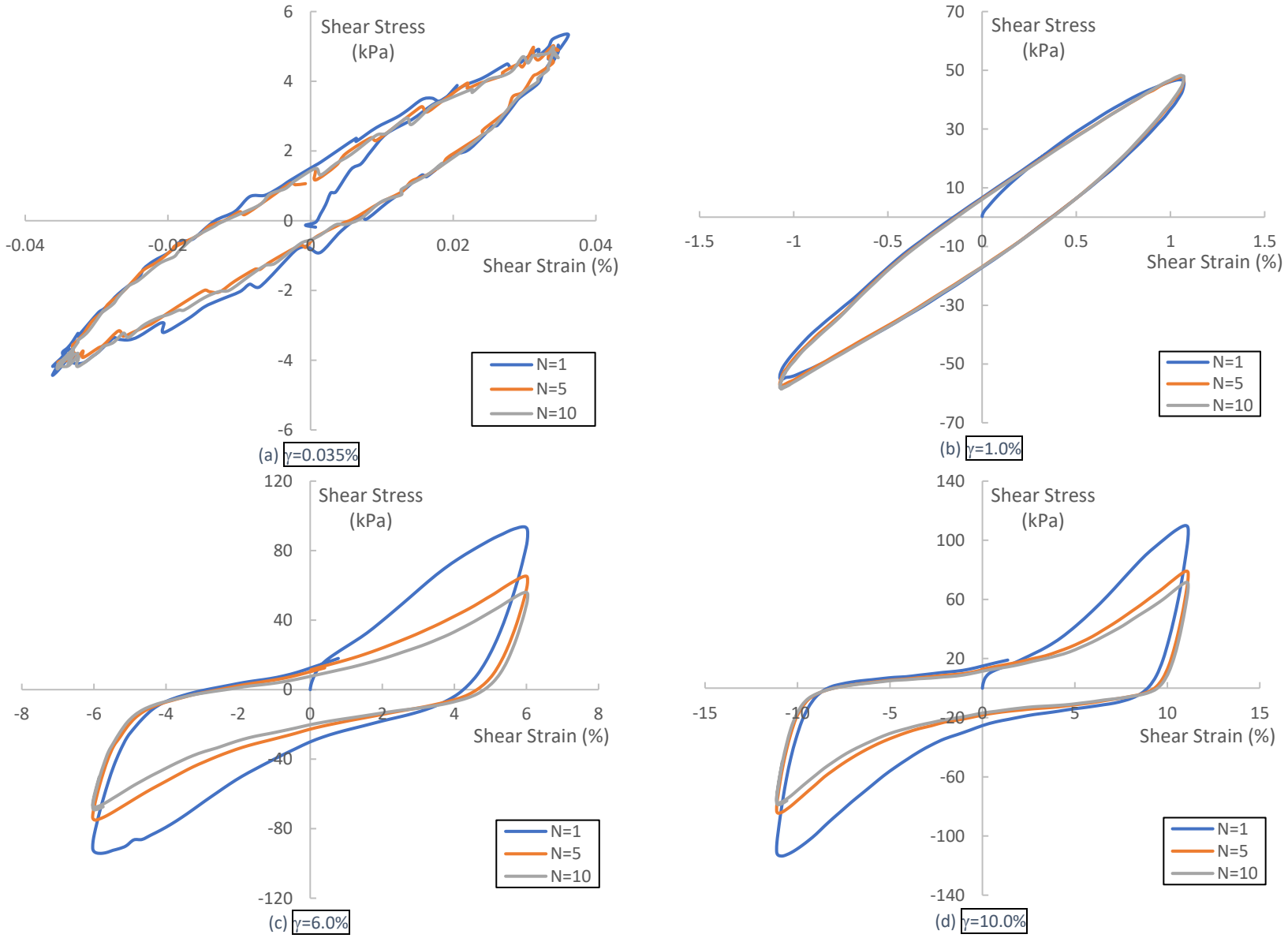

Figure 5.27: Typical SC Soil Response (w=10.0%) on the Basis of Shear Strain Amplitude for 50°C

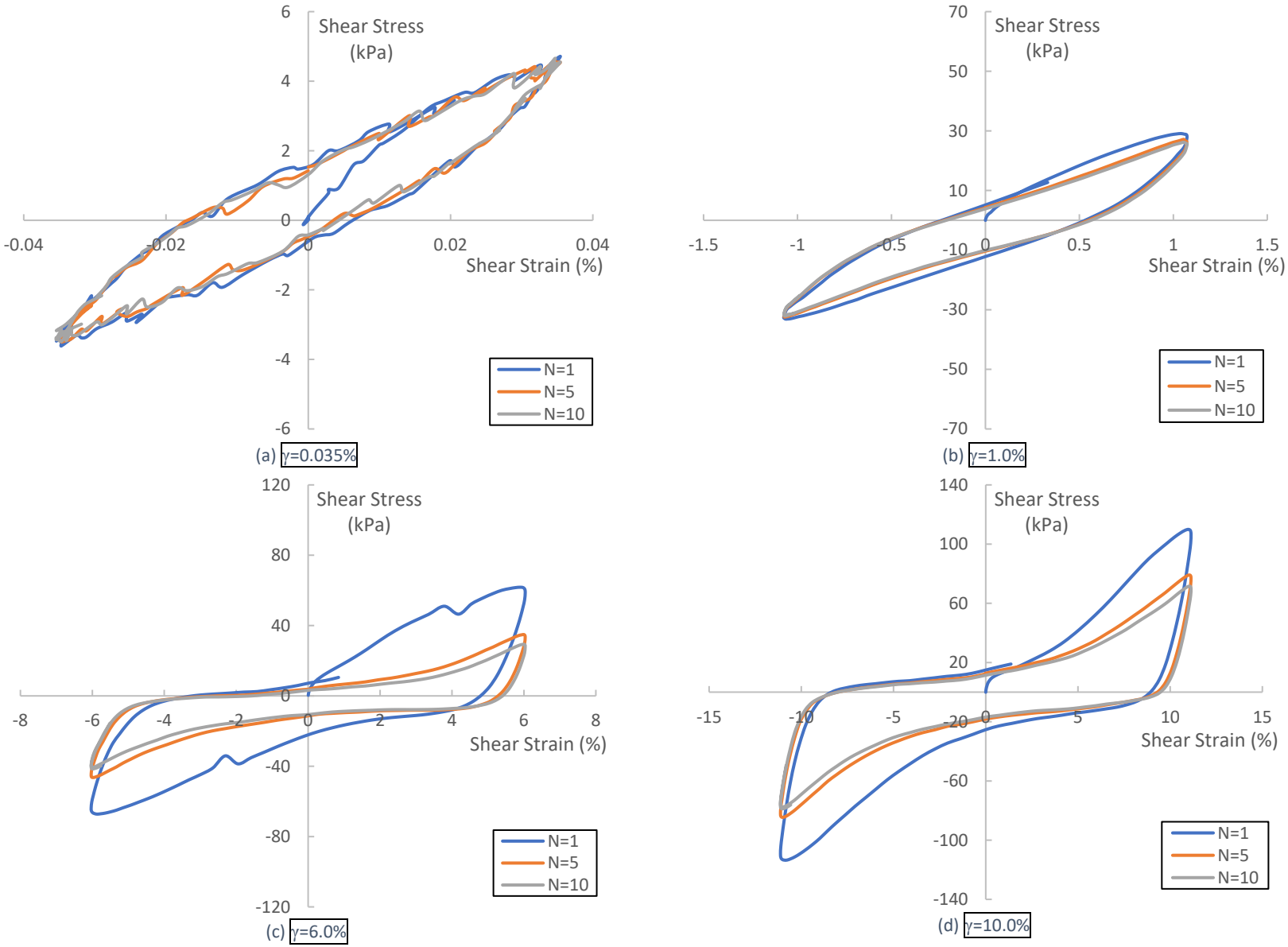

Figure 5.28: Typical SC Soil Response (w=10.0%) on the Basis of Shear Strain Amplitude for 60°C

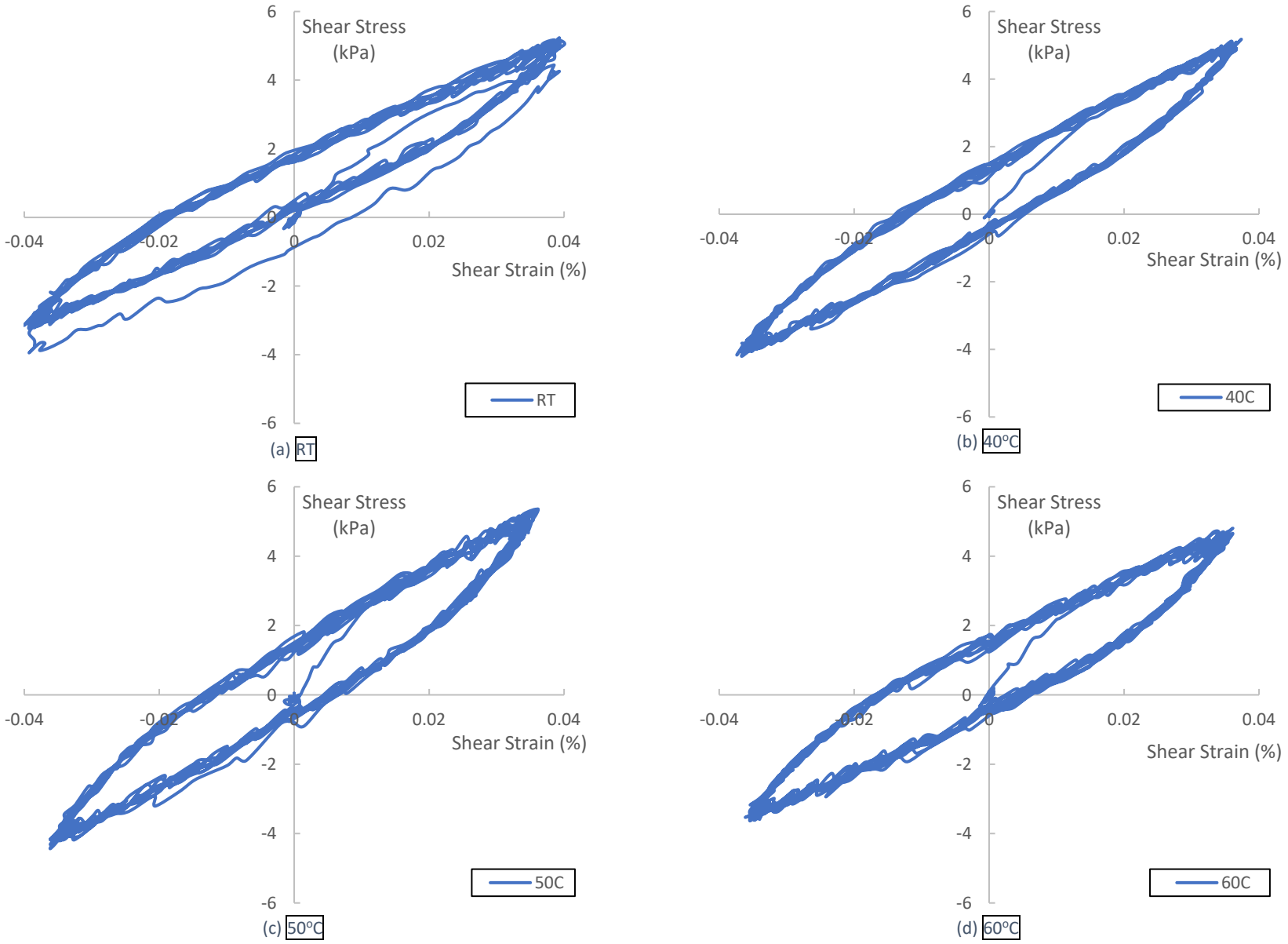

Figure 5.29: Typical SC Soil Response (w=10.0%) on the Basis of Soil Temperature for γ = 0.035%

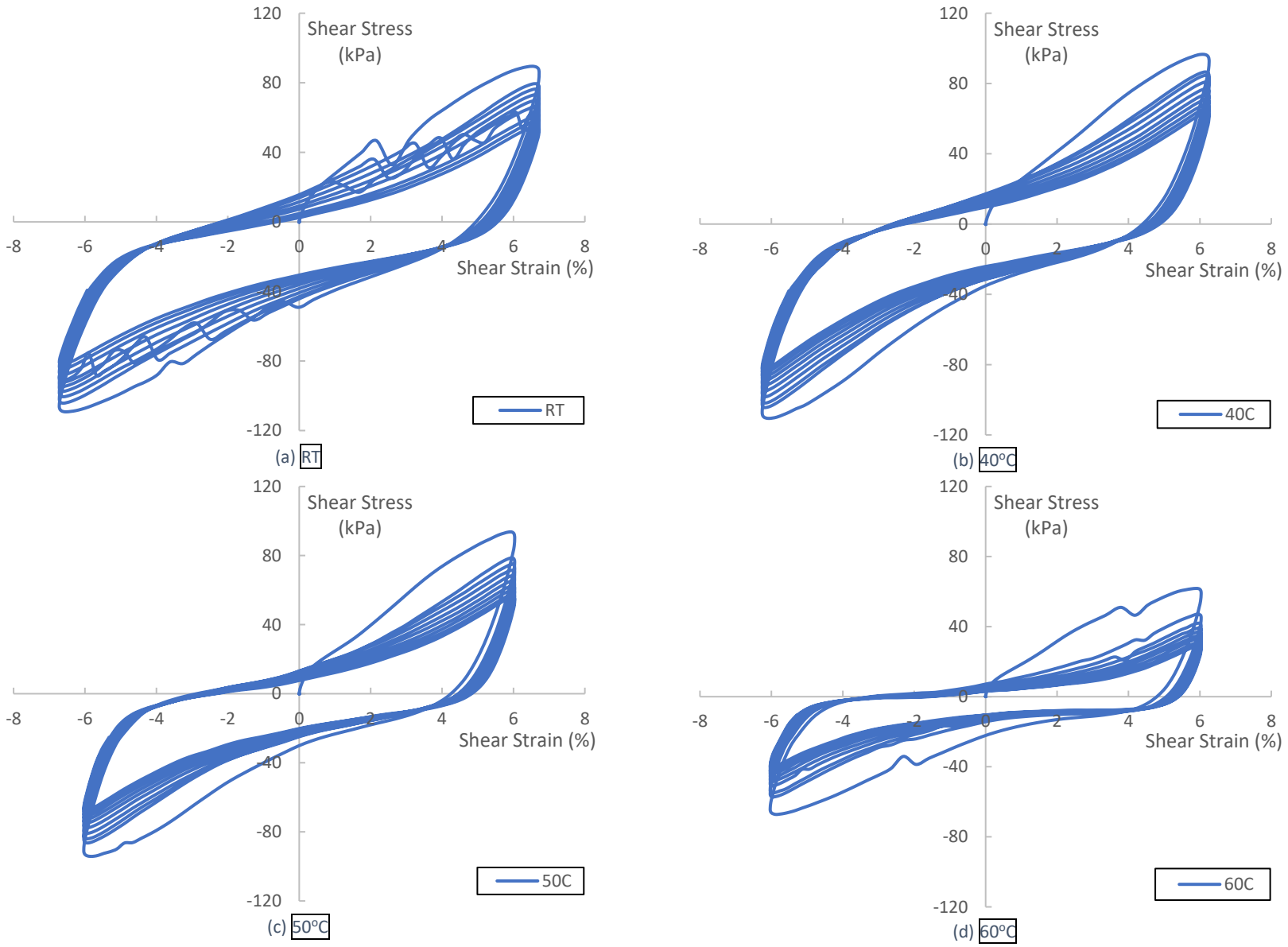

Figure 5.30: Typical SC Soil Response (w=10.0%) on the Basis of Soil Temperature for γ = 6.0%

Chapter 6: Bilinear Modeling of Shear Modulus

This chapter presents the bilinear modeling of large shear strain amplitude (γ > 1.0%) thermo-controlled CSS test results for the three soil types used in this study. Test results are organized by soil type: dry clay (w=9.0%), optimum moisture content clay (w=13.6%), wet clay (w=17.0%), silt (w=14.8%), and clayey sand (w=10.0%). The same testing procedure was followed for all three soil types as described in chapters 3 and 5. Prior to showing the experimental results, the bilinear model framework is thoroughly explained.

Each section displays thermo-controlled experimental CSS test results in three different formats. First, results are presented on the basis of number of cycles, N, for a fixed shear strain amplitude. For a given temperature, three sets of data are shown ranging from the first cyclic load application (N=1) to the last cyclic load application (N=10). The bilinear model was applied to each data set to determine the parameters G_1 and G_2. Second, results are presented on the basis of temperature. For a given shear strain amplitude and cycle, data from four cyclic load applications are shown for temperatures ranging from RT to 60^{o}C. Viewing the results on the basis of temperature gives a good visual depiction of the effects of temperature at large strains. Finally, G_1 and G_2 parameters are compared for a given soil type, clearly showing temperatures effect on stiffness at large shear strain amplitudes. In general, the bilinear model parameters G_1 and G_2 decrease for an increase shear strain amplitude, number of cycles, and temperature.

6.1 - Bilinear Model Framework

At large shear strain amplitudes the stress-strain hysteresis loop generated from a CSS test tends to degrade from the typical oval shape and the secant shear modulus provides a poor method for evaluating soil response. Thiers and Seed proposed the bilinear model to better evaluate the stiffness degradation of soils at large shear strain amplitudes. The characteristics of the best representation of any stress strain relationship will vary with the magnitude of the peak cyclic strain involved. The variation of stress and strain during a typical loading cycle is shown in Figure 6.1(a). For large deformations, strain > 0.5%, it is advisable to represent such a relationship in the form of the bilinear model shown in Figure 6.1(b). The bilinear model "provides a suitably convenient approximation for many purposes" (Thiers and Seed, 1968). The material parameters defining the model are defined in the following way: behavior during material loading is controlled by the modulus G_1 until a limiting strain, γ_y, is reached, at which point deformation is determined by the modulus G_2. When direction of strain is reversed behavior is again determined by G_1 until a strain change of $2\gamma_y$ has developed and G_2 again controls the behavior.

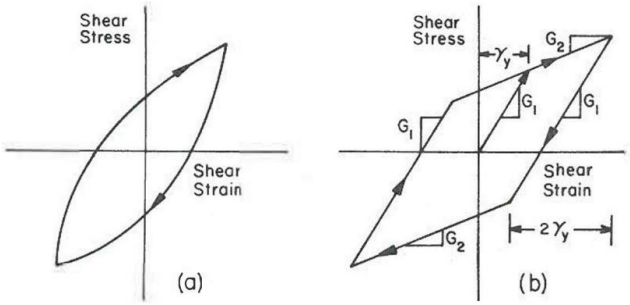

Figure 6.1: Stress-Strain Curve and Bilinear Model. (Thiers and Seed, 1968)

A Norwegian Geotechnical Institute (NGI) device used for simple shear testing was modified to produce the desired cyclic loading conditions. Figure 6.2 shows the typical stress-strain curves generated from cyclic

simple shear test. In this test, the sample was cycled through a double amplitude of 0.8 mm resulting in a peak strain of 4.0% for 200 cycles. Cycles 1, 50, and 200 are shown in Figure 6.2.

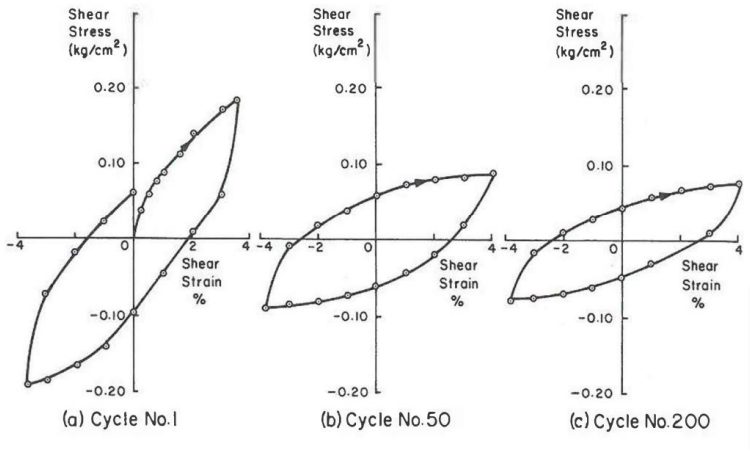

Figure 6.2: Typical Stress-Strain Curves. (Thiers and Seed, 1968)

The change in form of these stress-strain relationships may be studied and expressed by representing any relationship with the bilinear model shown in Figure 6.1(b) and examining the variation of the model parameters G_1, G_2, and γ_y. Figure 6.3 shows the best fit bilinear models for curves shown in Figure 6.2. Comparing G_1 and G_2 values allows for a better qualitative and quantitative comparison than comparing secant shear modulus for large shear strain amplitudes. It should be noted that "although construction of the parallelogram models requires some degree of judgement and approximation, their use can be justified by the fact that they provide the best approximation of actual properties which can be handled in analytical procedures at present" (Thiers and Seed, 1968).

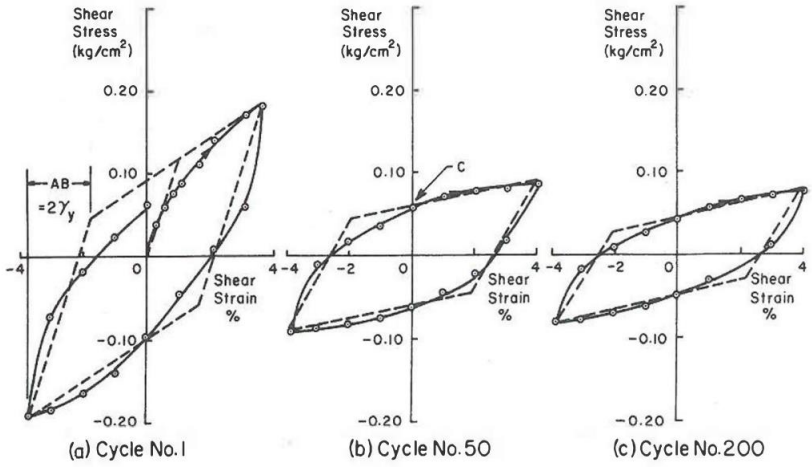

Figure 6.3: Bilinear Models of Stress-Strain Curves. (Thiers and Seed, 1968)

6.2 - Bilinear Modeling of Clayey Soil (CL) Response

Sections 6.2.1 – 6.2.3 show the bilinear model applied to thermo-controlled CSS data for large shear strain amplitudes of CL soil. Moisture contents ranged from dry of optimum (w=9.0%) to wet of optimum (w=17.0%). Varying water content for the clayey soil allows for an examination of the interaction between temperature and water content. In general suction increases as water content decreases, as suction increases shear modulus is expected to also increase; however, samples under higher suction are more susceptible to temperature induced decreases in shear modulus.

6.2.1 – CL Soil Compacted Dry of Optimum Moisture Content (w=9.0%)

Figures 6.4 – 6.12 show various experimental test data from thermo-controlled CSS testing of CL soil compacted dry of optimum moisture content (w=9.0%). Figures 6.4 – 6.7 show typical soil response on the basis of number of cycles N=1, 5, 10, for a fixed shear strain amplitude and temperature. The figures are arranged from room temperature Figure 6.4 to 60^{o}C Figure 6.7 with cycles 1, 5, and 10 highlighted to show the effects of temperature on successive cyclic loading applications. The data shows that increasing cyclic load application caused a significant decrease in bilinear parameter G_2 for a fixed shear strain value. Figures 6.4 – 6.7 show that the majority of the decrease in G_2 occurs by cycle N=5.

Figures 6.8 – 6.10 show typical soil response on the basis of soil temperature for a fixed cyclic load application and shear strain amplitude. The figures are arranged from RT (23^{o}C) Figure 6.8(a) to 60^{o}C Figure 6.8(d) for a given shear strain amplitude and load cycle. Shear strain amplitude was kept constant for Figures 6.8 – 6.10 to show how temperature affects the cyclic soil response at a given cyclic load application. The figures highlight cycle N=1 (Figure 6.8), N=5 (Figure 6.9), and N=10 (Figure 6.10). Figures 6.8 – 6.10 show a reduction in parameter G_2 for increasing temperatures, indicating a reduction in shear modulus.

Figures 6.11 and 6.12 show bilinear model parameters G_1 and G_2. G_1 values remain fairly constant as temperature, number of cycles, and shear strain amplitude increase (Figure 6.11). G_2 values significantly decrease as temperature, number of cycles, and shear strain amplitude increase (Figure 6.12). Figure 6.12(c, d) shows G_2 values are lower in the tests conducted at increased temperatures. G_2 values decrease as shear strain amplitude increases, with the majority of the reduction taking place by cycle N=5. The rate of decrease for parameter G_2, shown visually by the slope of the trendlines in Figure 6.12, appears to be greater for increased temperatures. Values for G_1 and G_2 are shown in Table 6.1.

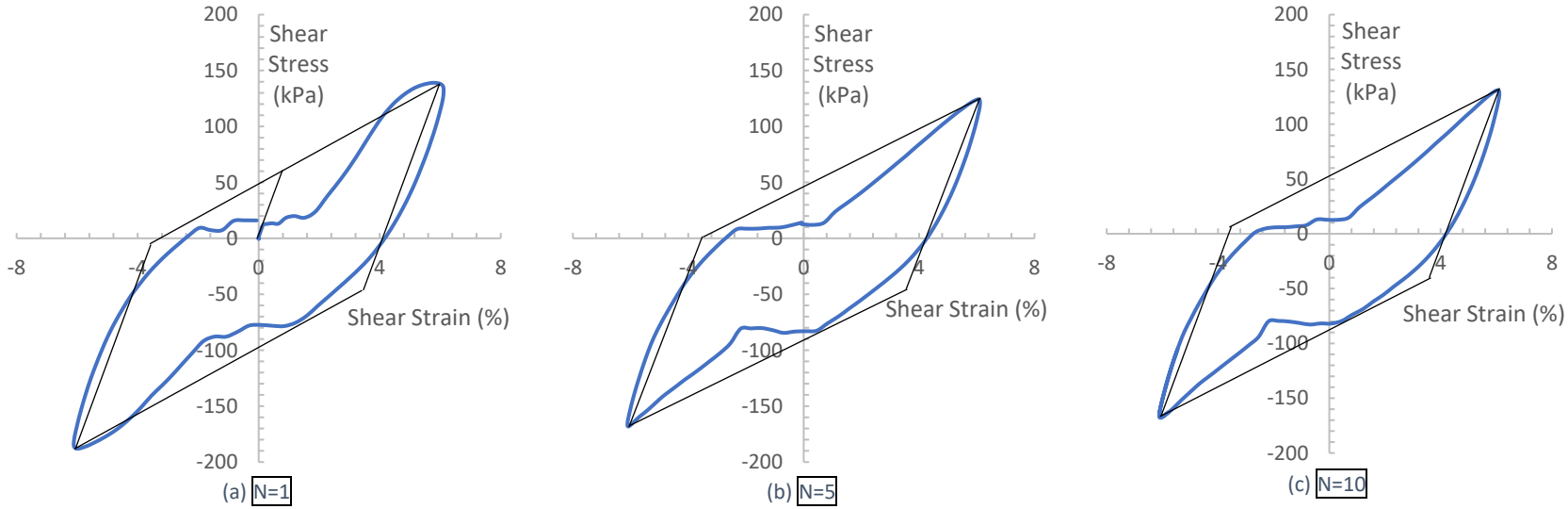

Figure 6.4: Bilinear Modeling of CL Soil Response (w=9.0%) on the Basis of Number of Cycles for RT, γ=6.0%

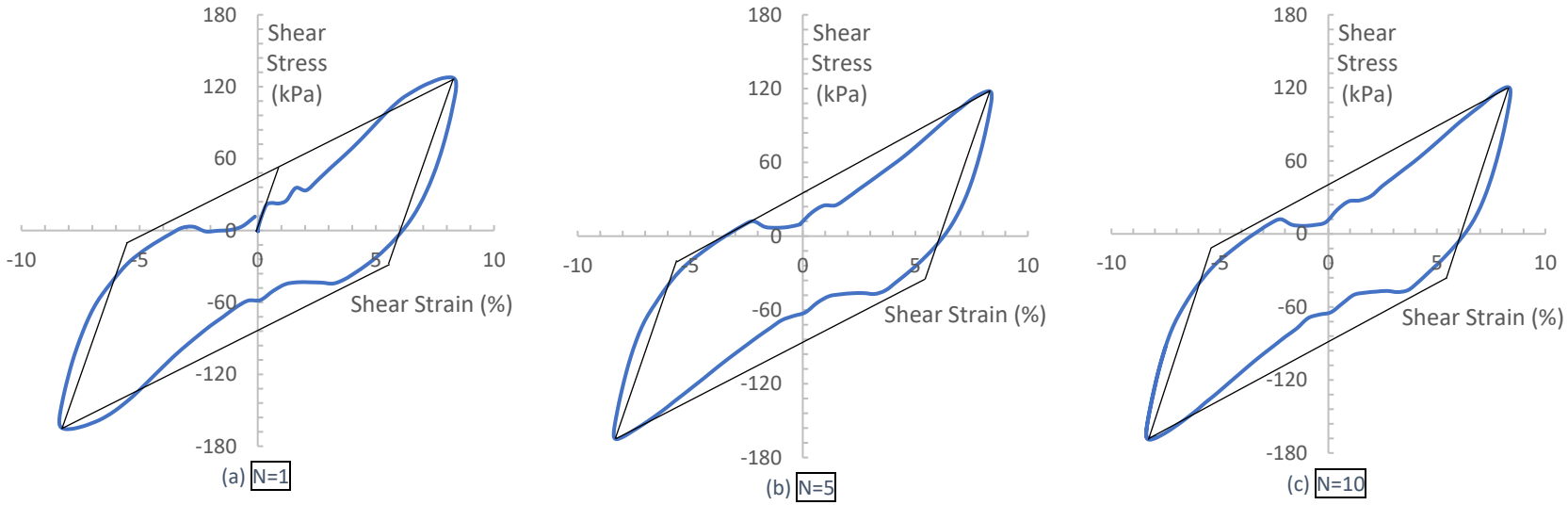

Figure 6.5: Bilinear Modeling of CL Soil Response (w=9.0%) on the Basis of Number of Cycles for 40°C, γ=8.0%

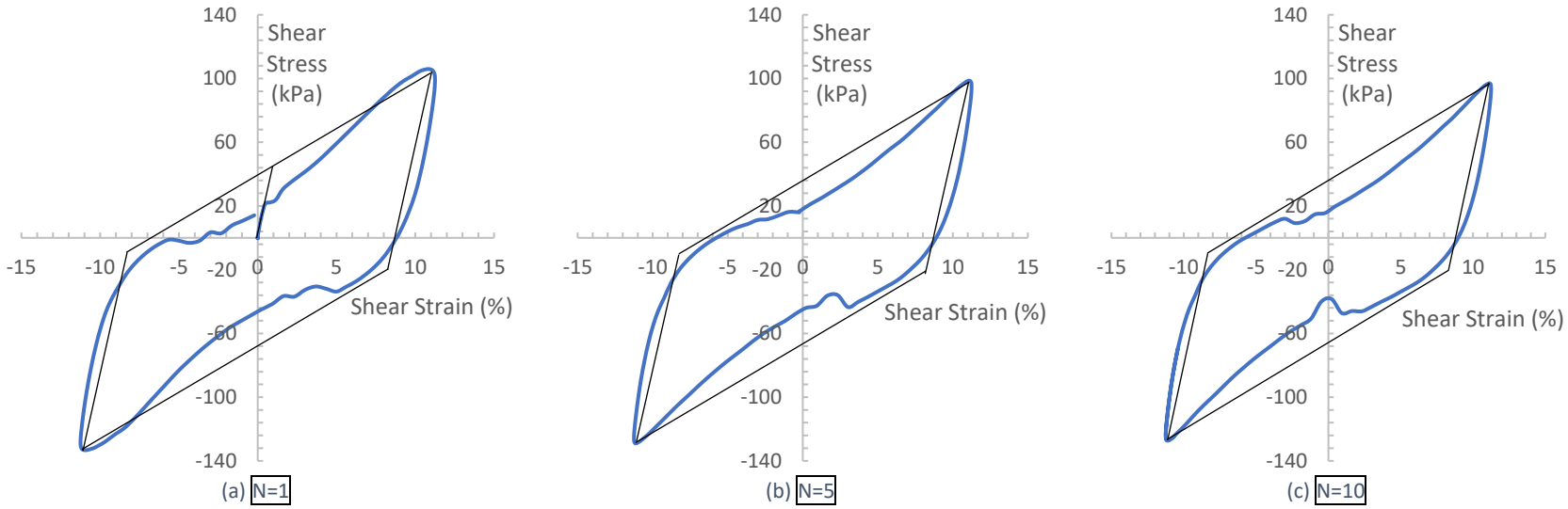

Figure 6.6: Bilinear Modeling of CL Soil Response (w=9.0%) on the Basis of Number of Cycles for 50°C, γ=10.0%

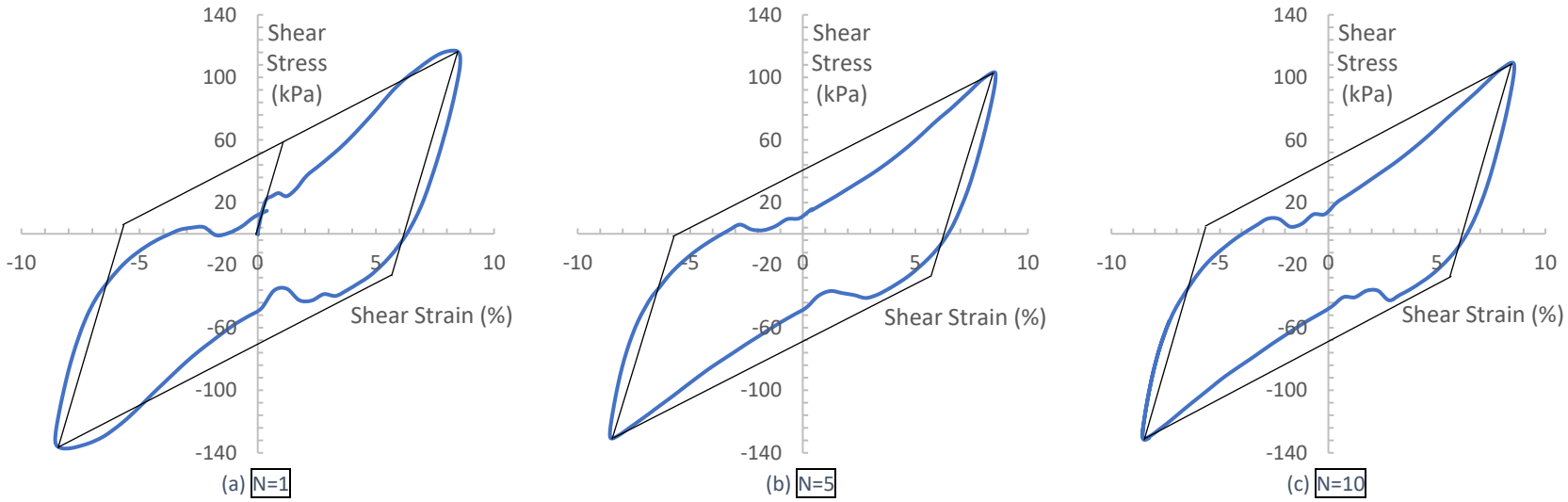

Figure 6.7: Bilinear Modeling of CL Soil Response (w=9.0%) on the Basis of Number of Cycles for 60°C, γ=8.0%

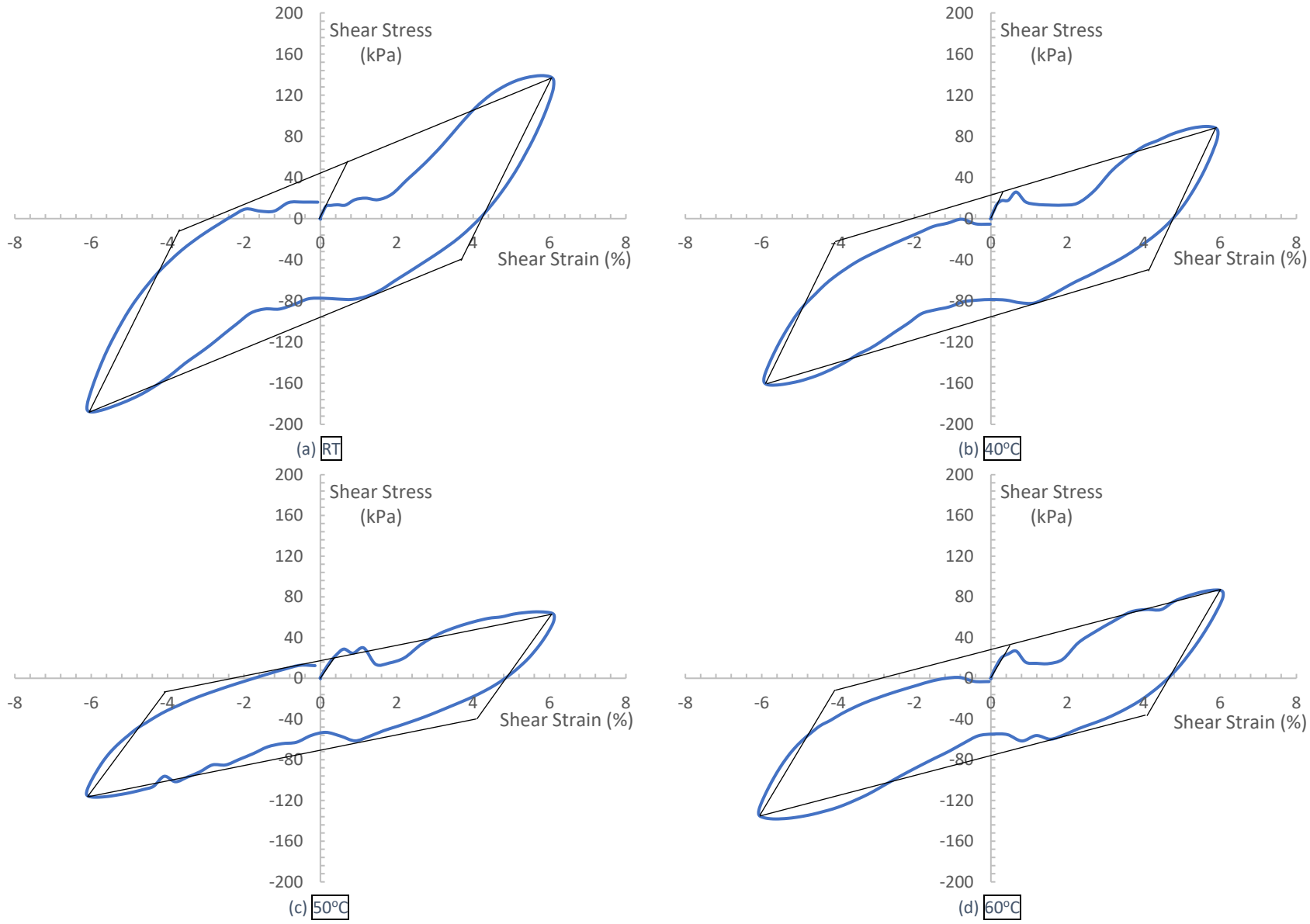

Figure 6.8: Bilinear Modeling of CL Soil Response (w=9.0%) on the Basis of Soil Temperature for N=1, γ = 6.0%

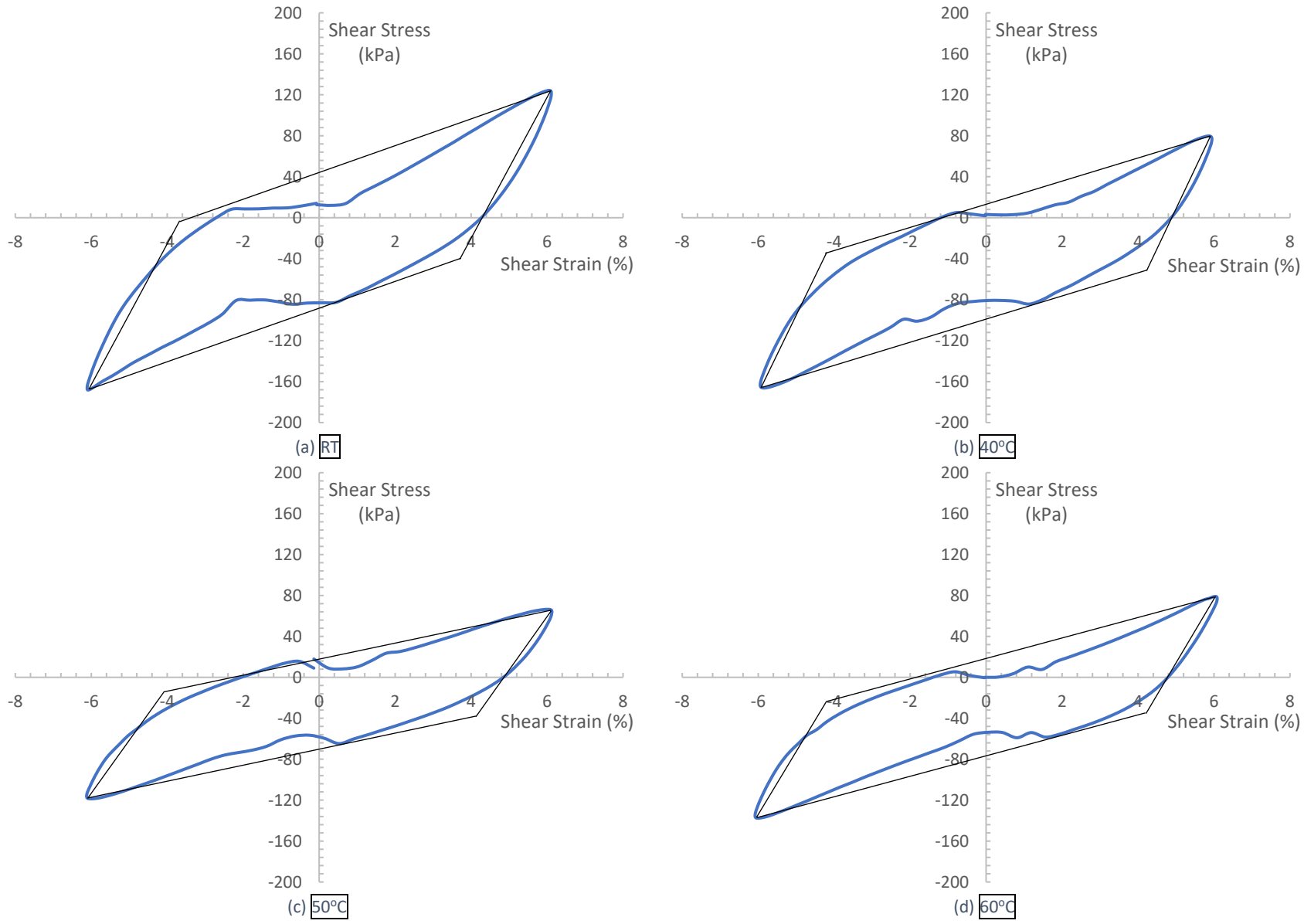

Figure 6.9: Bilinear Modeling of CL Soil Response (w=9.0%) on the Basis of Soil Temperature for N=5, γ = 6.0%

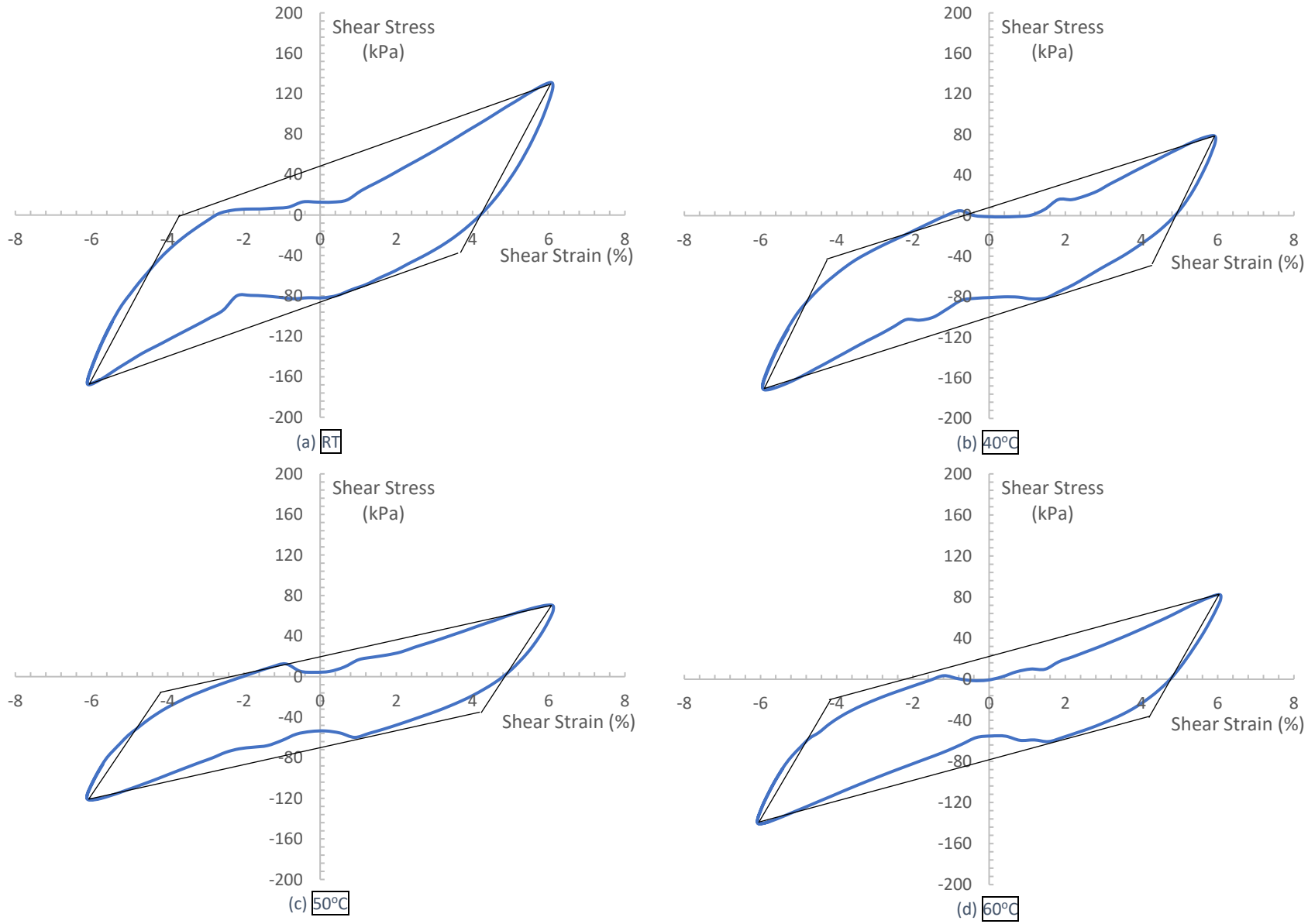

Figure 6.10: Bilinear Modeling of CL Soil Response (w=9.0%) on the Basis of Soil Temperature for N=10, γ = 6.0%

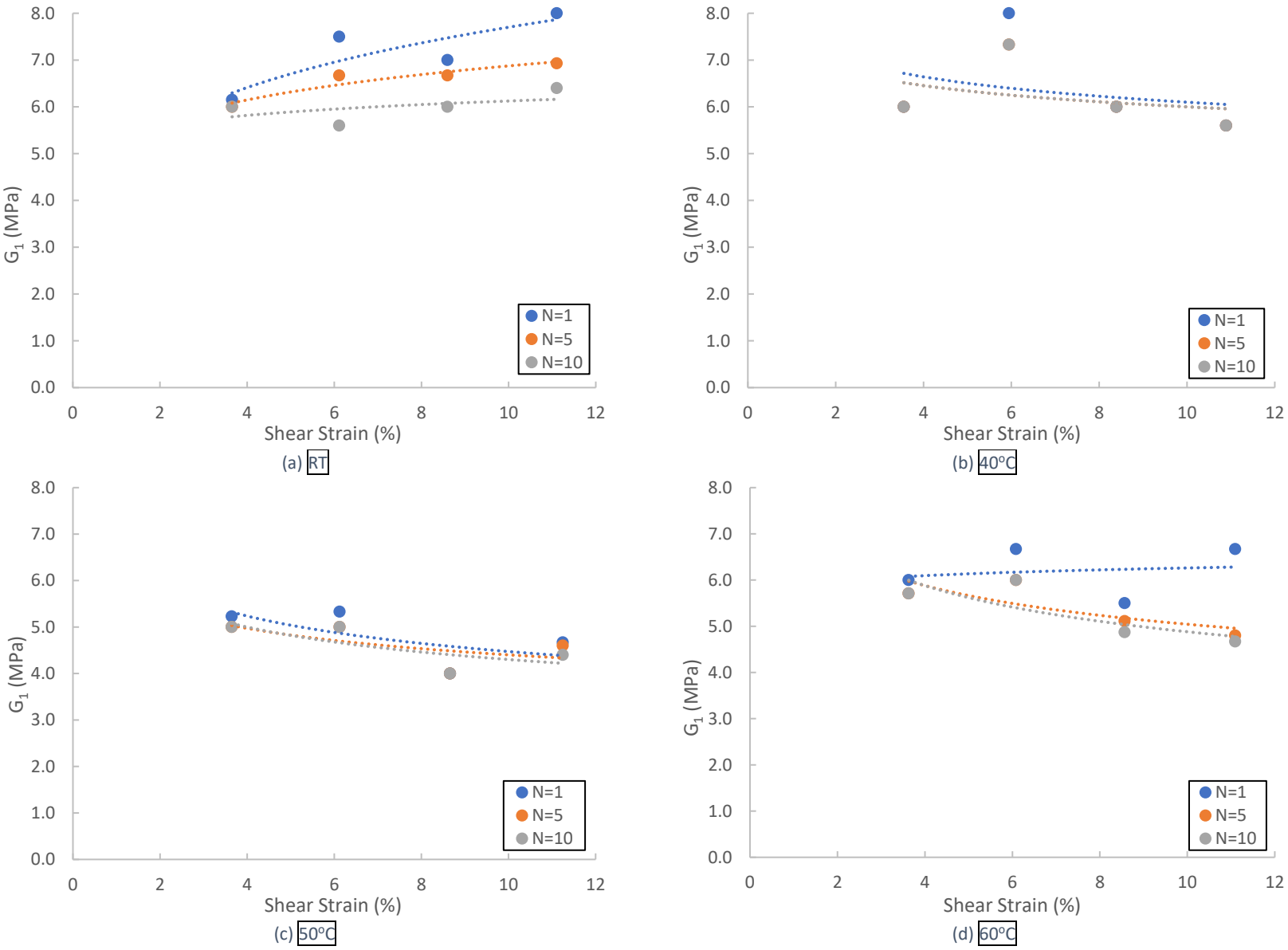

Figure 6.11: Bilinear Stiffness Parameter G_1 with Increasing Shear Strain and Number of Cycles for CL Soil (w=9.0%)

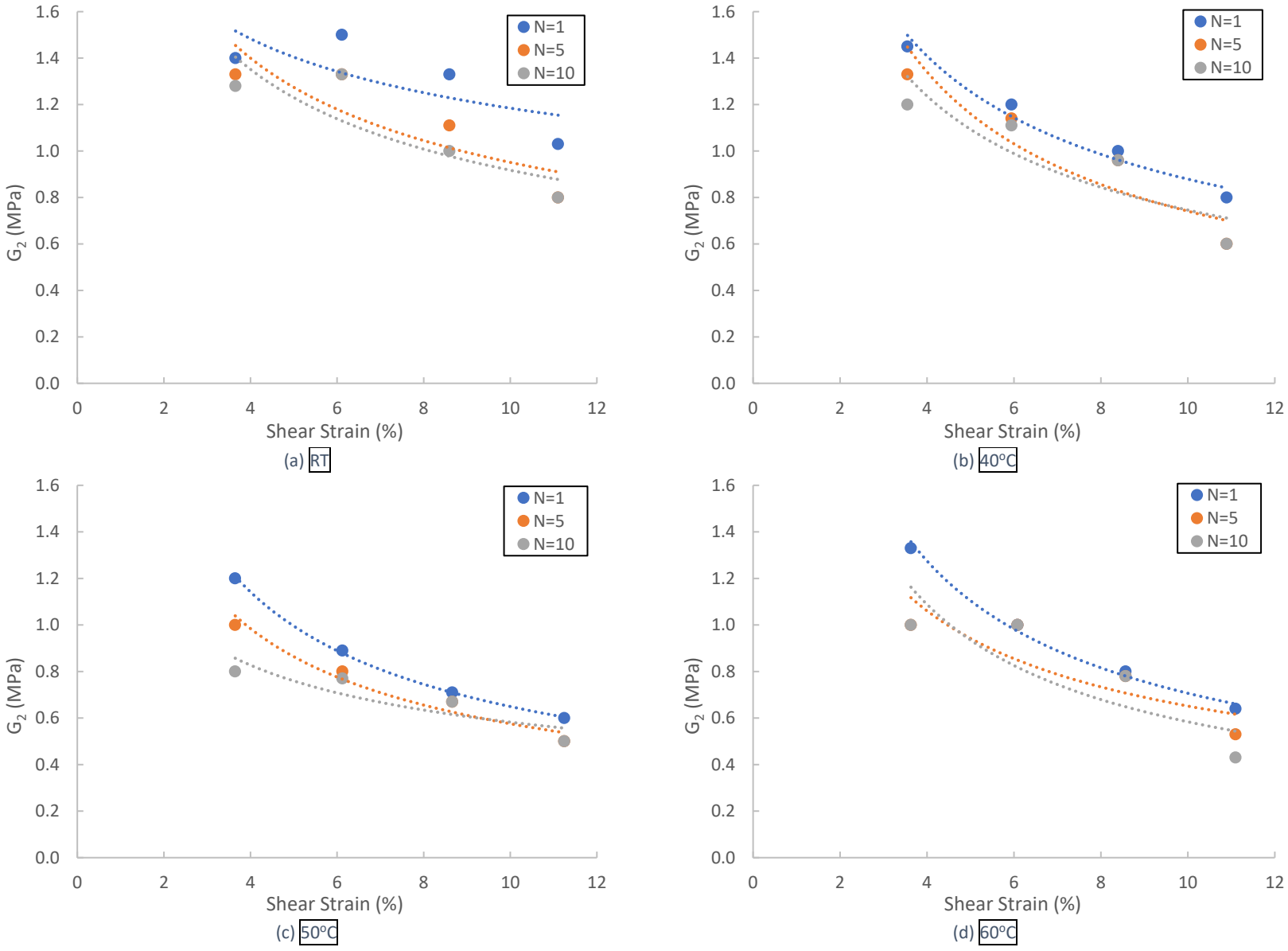

Figure 6.12: Bilinear Stiffness Parameter G_2 with Increasing Shear Strain and Number of Cycles for CL Soil (w=9.0%)

Table 6.1: G_1 and G_2 Values for CL Soil (w=9.0%)

RT						
	G_1 (MPa)			G_2 (MPa)		
Strain (%)	**N=1**	**N=5**	**N=10**	**N=1**	**N=5**	**N=10**
3.7	6.15	6.00	6.00	1.40	1.33	1.28
6.1	7.50	6.67	5.60	1.50	1.33	1.33
8.6	7.00	6.67	6.00	1.33	1.11	1.00
11.1	8.00	6.93	6.40	1.03	0.80	0.80
40C						
	G_1			G_2		
Strain	**N=1**	**N=5**	**N=10**	**N=1**	**N=5**	**N=10**
3.6	6.00	6.00	6.00	1.45	1.33	1.20
5.9	8.00	7.33	7.33	1.20	1.14	1.11
8.4	6.00	6.00	6.00	1.00	0.96	0.96
10.9	5.60	5.60	5.60	0.80	0.60	0.60
50C						
	G_1			G_2		
Strain	**N=1**	**N=5**	**N=10**	**N=1**	**N=5**	**N=10**
3.6	5.23	5.00	5.00	1.20	1.00	0.80
6.1	5.33	5.00	5.00	0.89	0.80	0.77
8.7	4.00	4.00	4.00	0.71	0.67	0.67
11.2	4.67	4.60	4.40	0.60	0.50	0.50
60C						
	G_1			G_2		
Strain	**N=1**	**N=5**	**N=10**	**N=1**	**N=5**	**N=10**
3.6	6.00	5.71	5.71	1.33	1.00	1.00
6.1	6.67	6.00	6.00	1.00	1.00	1.00
8.6	5.50	5.11	4.87	0.80	0.78	0.78
11.1	6.67	4.80	4.67	0.64	0.53	0.43

6.2.2 – CL Soil Compacted at Optimum Moisture Content (w=13.6%)

Figures 6.13 – 6.21 show various experimental test data from thermo-controlled CSS testing of CL soil compacted at optimum moisture content (w=13.6%). Figures 6.13 – 6.16 show typical soil response on the basis of number of cycles N=1, 5, 10, for a fixed shear strain amplitude and temperature. The figures are arranged similarly to those of the previous section. The data shows that increasing cyclic load application caused a significant decrease in bilinear parameter G_2 for a fixed shear strain value. Figures 6.13 – 6.16 show that the majority of the decrease in G_2 occurs by cycle N=5.

Figures 6.17 – 6.19 show typical soil response on the basis of soil temperature for a fixed cyclic load application and shear strain amplitude. Similar to the previous section, increasing temperatures caused a reduction in bilinear parameter G_2, indicating a reduction in shear modulus.

Figures 6.20 and 6.21 show bilinear model parameters G_1 and G_2. G_1 values remain fairly constant as temperature, number of cycles, and shear strain amplitude increase (Figure 6.20). G_2 values significantly decrease as temperature, number of cycles, and shear strain amplitude increase (Figure 6.21). Figure 6.21(c, d) shows G_2 values are lower in the tests conducted at increased temperatures. G_2 values decrease as shear strain amplitude increases, with the majority of the reduction taking place by cycle N=5. The rate of decrease for parameter G_2, shown visually by the slope of the trendlines in Figure 6.21, appears to be similar for all temperatures. Values for G_1 and G_2 are shown in Table 6.2.

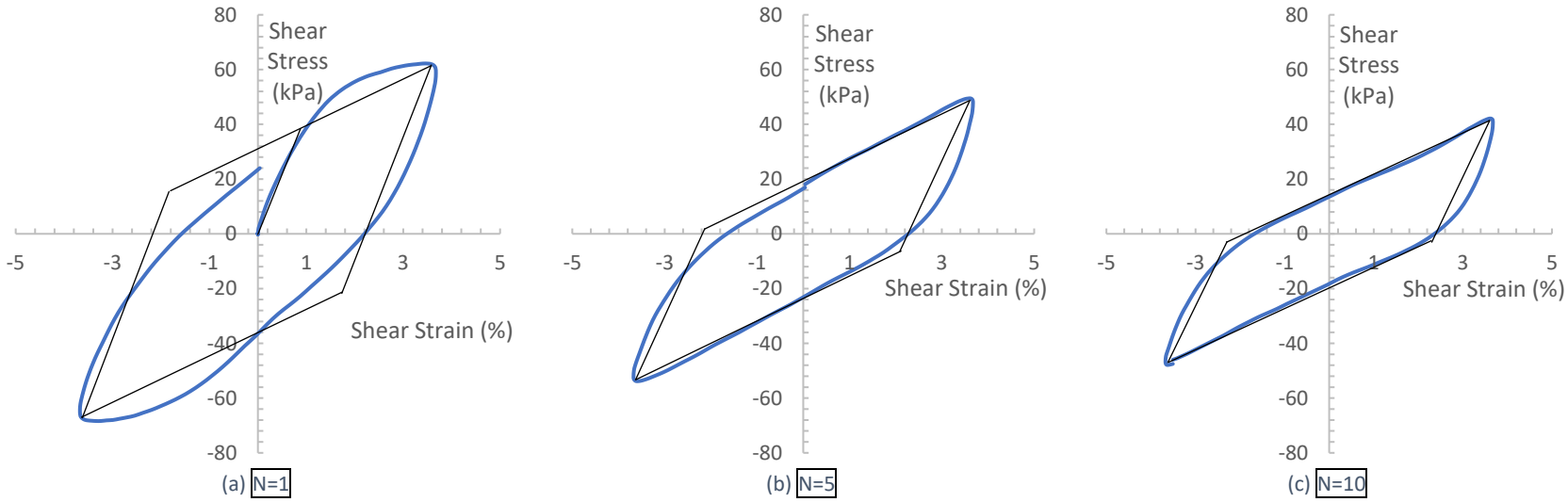

Figure 6.13: Bilinear Modeling of CL Soil Response (w=13.6%) on the Basis of Number of Cycles for RT, γ=4.0%

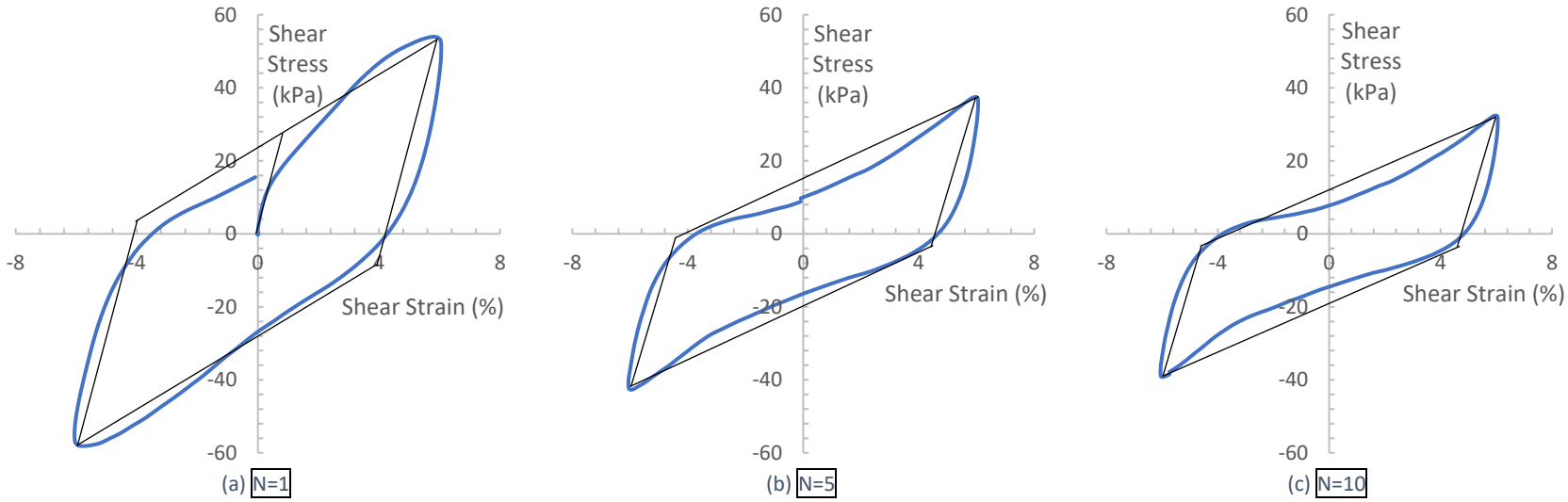

Figure 6.14: Bilinear Modeling of CL Soil Response (w=13.6%) on the Basis of Number of Cycles for 40°C, γ=6.0%

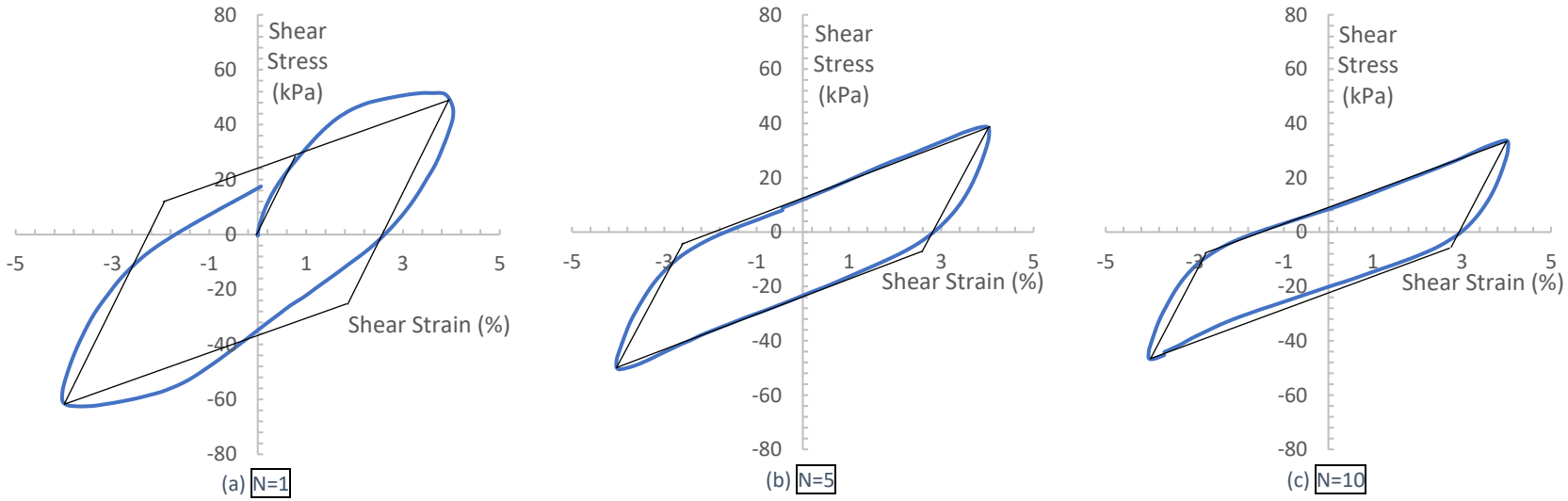

Figure 6.15: Bilinear Modeling of CL Soil Response (w=13.6%) on the Basis of Number of Cycles for 50°C, γ=4.0%

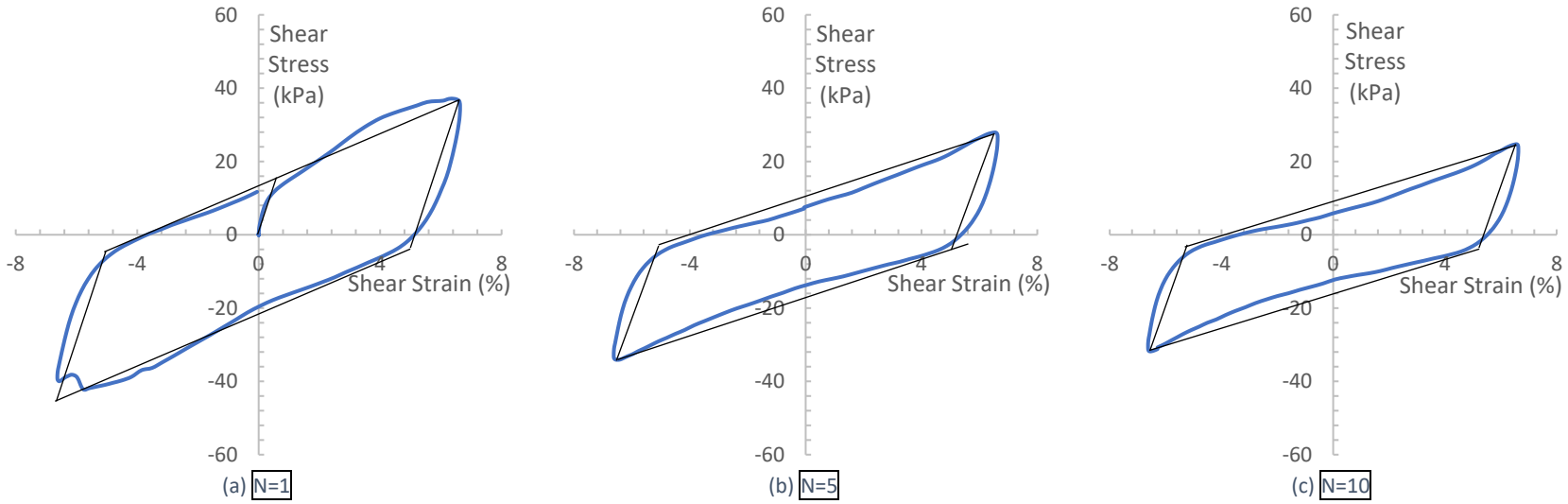

Figure 6.16: Bilinear Modeling of CL Soil Response (w=13.6%) on the Basis of Number of Cycles for 60°C, γ=6.0%

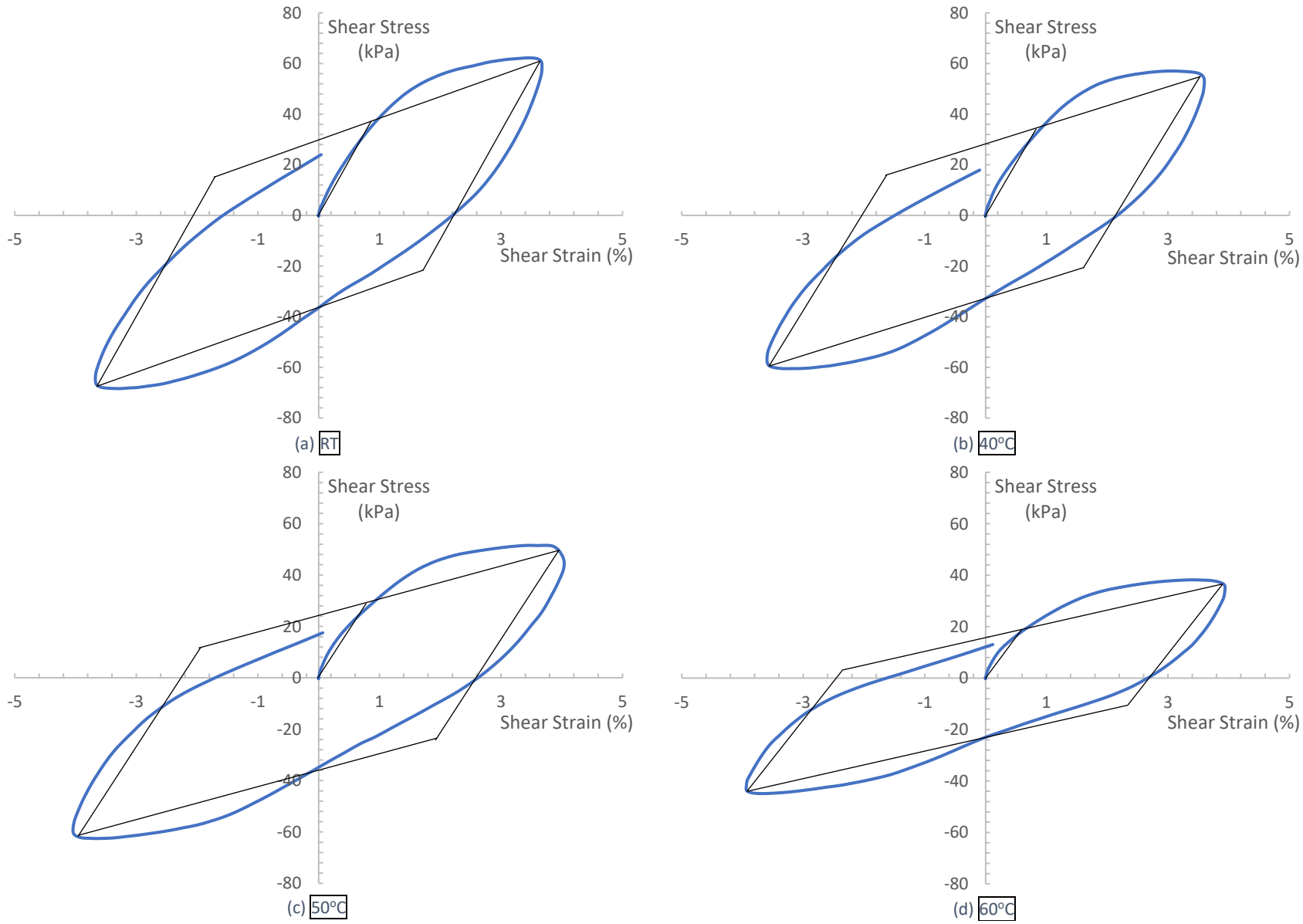

Figure 6.17: Bilinear Modeling of CL Soil Response (w=13.6%) on the Basis of Soil Temperature for N=1, γ = 4.0%

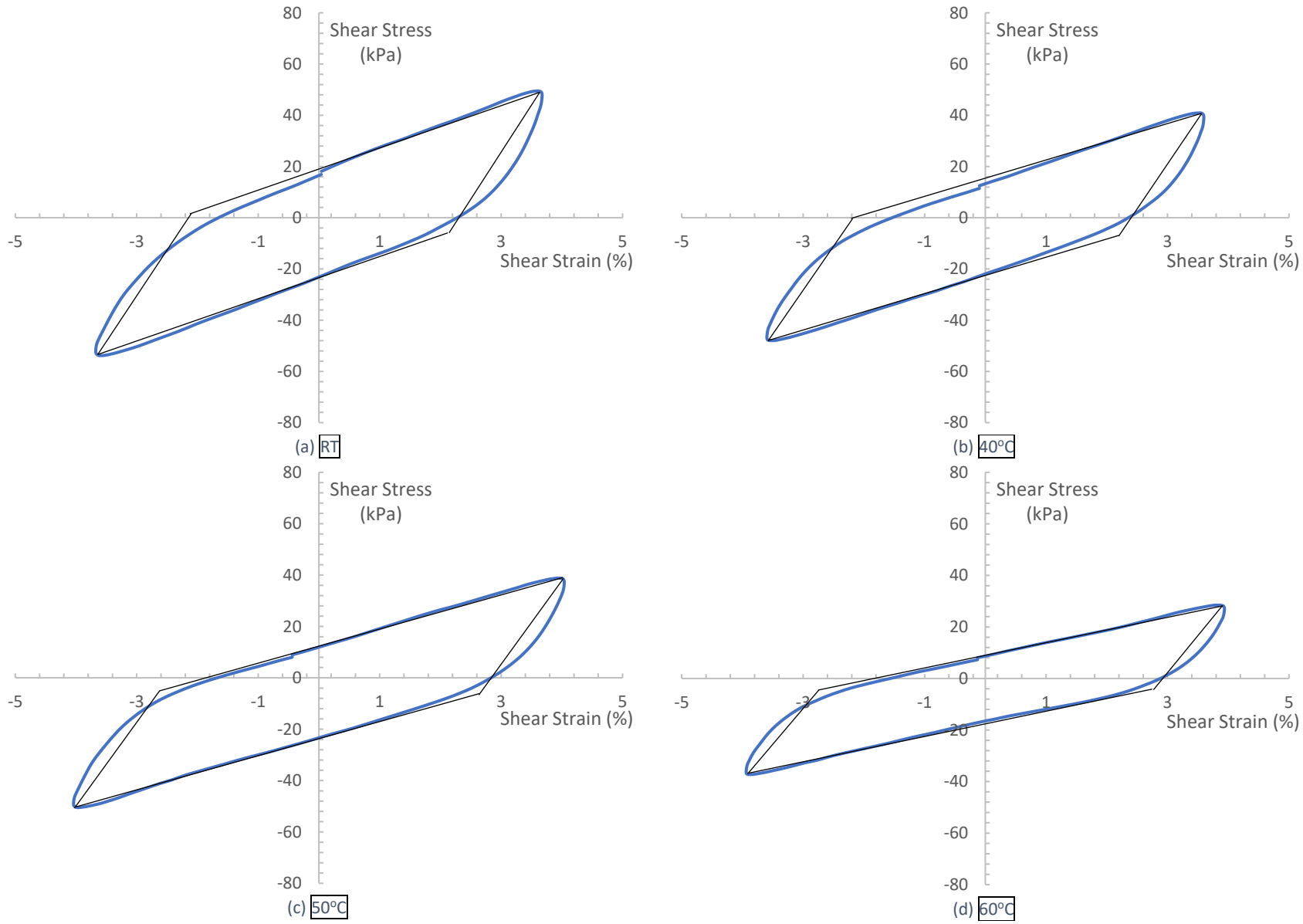

Figure 6.18: Bilinear Modeling of CL Soil Response (w=13.6%) on the Basis of Soil Temperature for N=5, γ = 4.0%

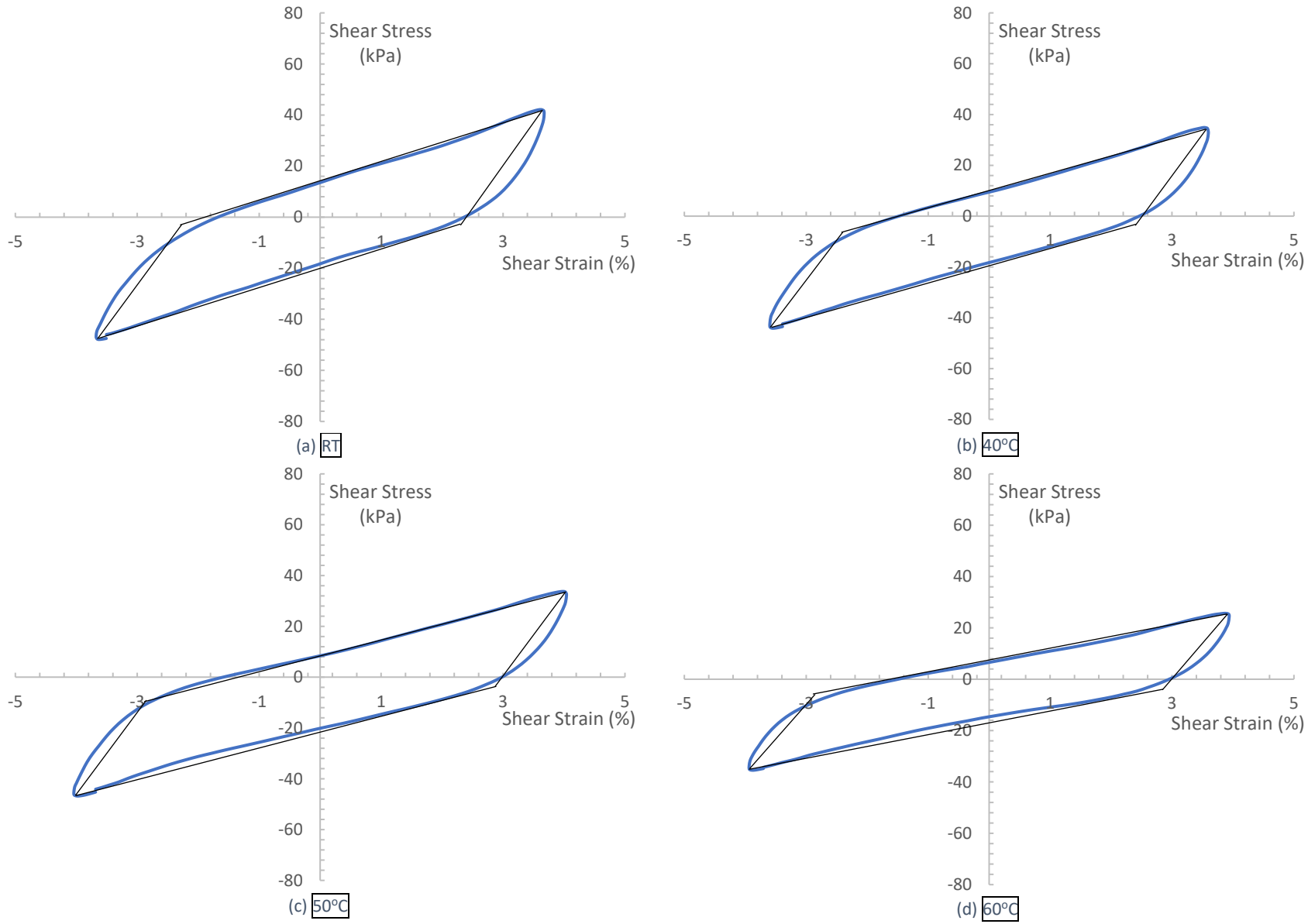

Figure 6.19: Bilinear Modeling of CL Soil Response (w=13.6%) on the Basis of Soil Temperature for N=10, γ = 4.0%

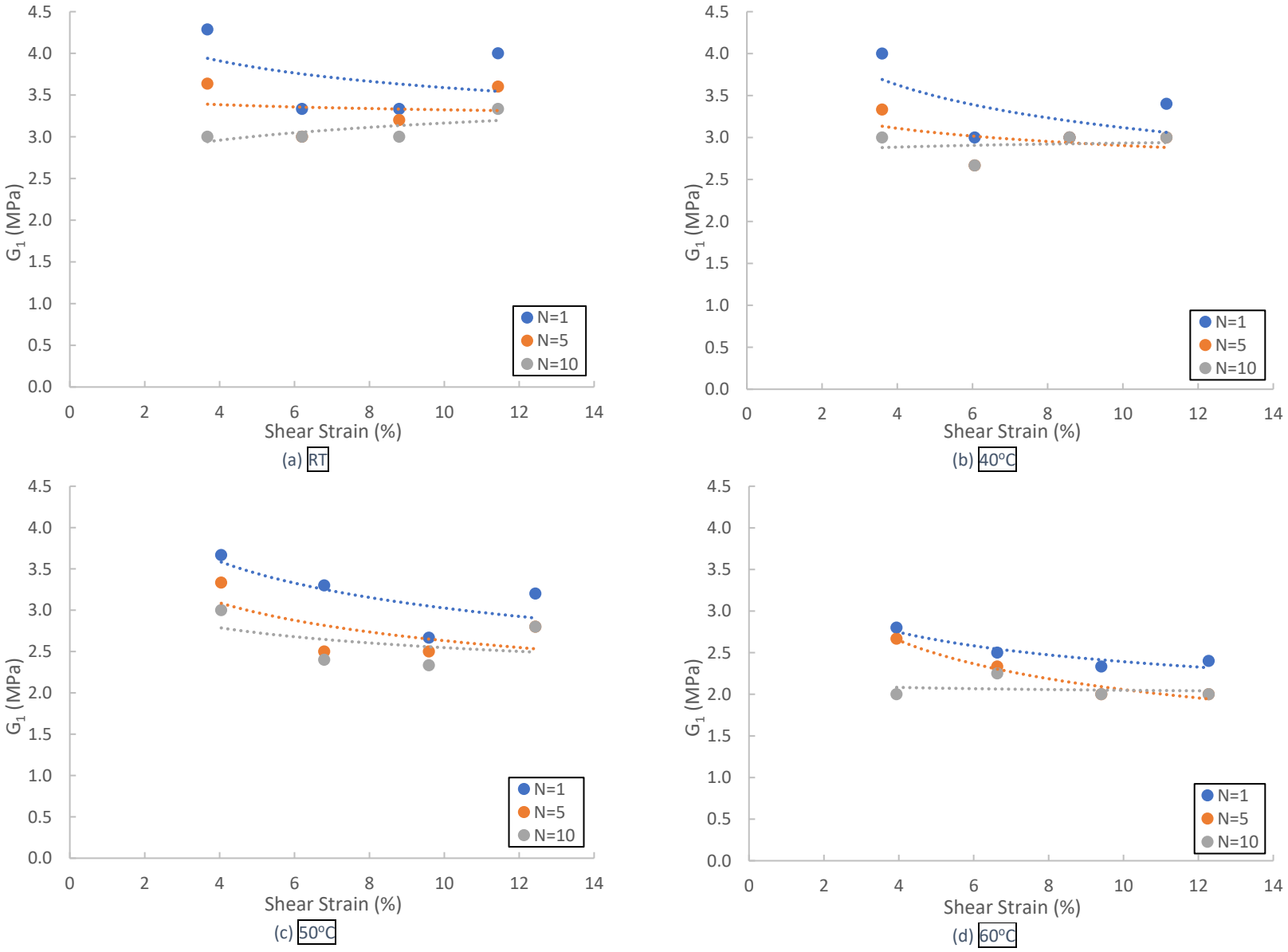

Figure 6.20: Bilinear Stiffness Parameter G_1 with Increasing Shear Strain and Number of Cycles for CL Soil (w=13.6%)

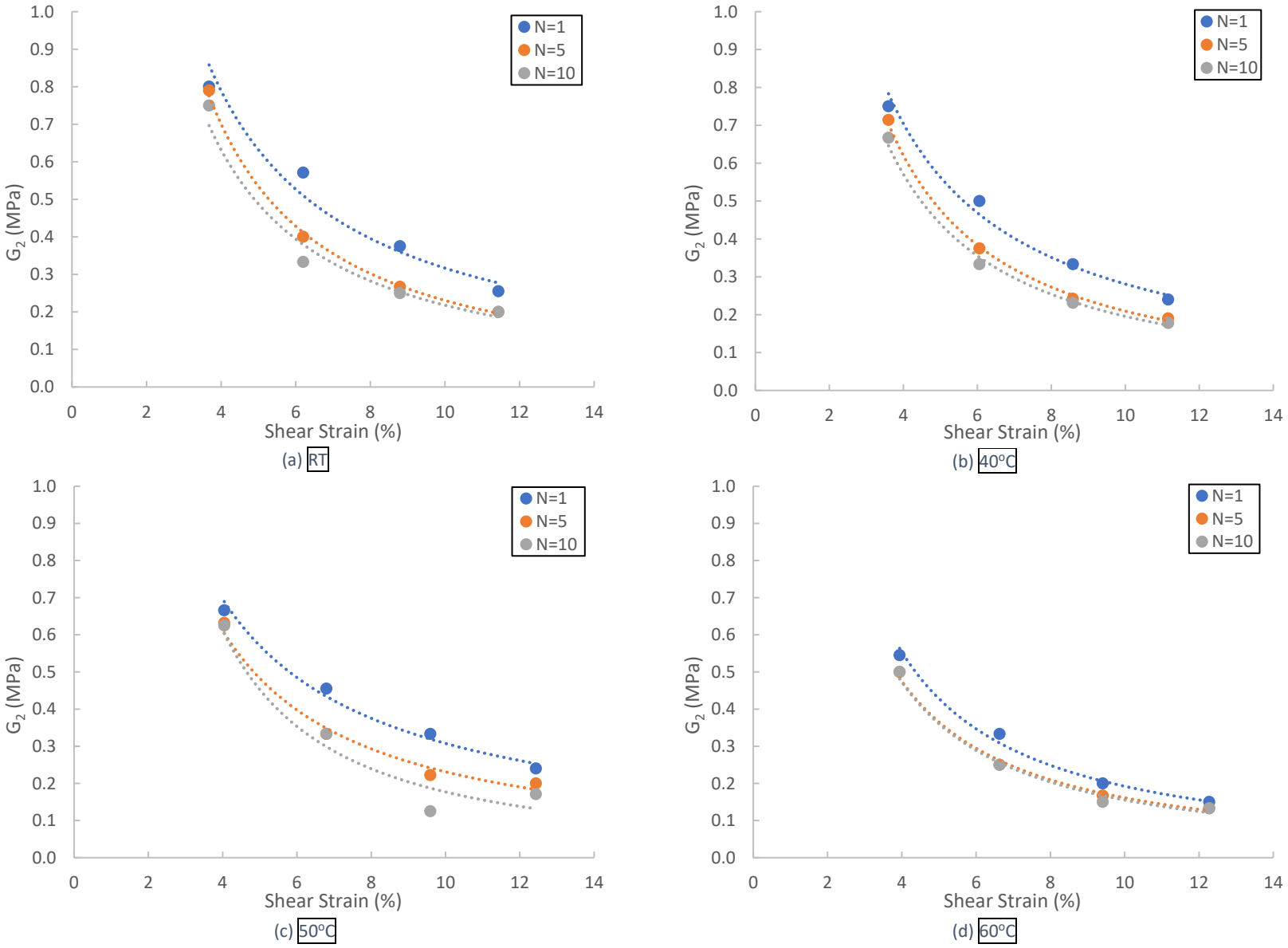

Figure 6.21: Bilinear Stiffness Parameter G_2 with Increasing Shear Strain and Number of Cycles for CL Soil (w=13.6%)

Table 6.2: G_1 and G_2 Values for CL Soil (w=13.6%)

RT						
	G_1 (MPa)			G_2 (MPa)		
Strain (%)	**N=1**	**N=5**	**N=10**	**N=1**	**N=5**	**N=10**
3.7	4.29	3.64	3.00	0.80	0.79	0.75
6.2	3.33	3.00	3.00	0.57	0.40	0.33
8.8	3.33	3.20	3.00	0.38	0.27	0.25
11.4	4.00	3.60	3.33	0.26	0.20	0.20
40C						
	G_1			G_2		
Strain	**N=1**	**N=5**	**N=10**	**N=1**	**N=5**	**N=10**
3.6	4.00	3.33	3.00	0.75	0.71	0.67
6.1	3.00	2.67	2.67	0.50	0.38	0.33
8.6	3.00	3.00	3.00	0.33	0.24	0.23
11.2	3.40	3.00	3.00	0.24	0.19	0.18
50C						
	G_1			G_2		
Strain	**N=1**	**N=5**	**N=10**	**N=1**	**N=5**	**N=10**
4.0	3.67	3.33	3.00	0.67	0.63	0.63
6.8	3.30	2.50	2.40	0.46	0.33	0.33
9.6	2.67	2.50	2.33	0.33	0.22	0.13
12.4	3.20	2.80	2.80	0.24	0.20	0.17
60C						
	G_1			G_2		
Strain	**N=1**	**N=5**	**N=10**	**N=1**	**N=5**	**N=10**
3.9	2.80	2.67	2.00	0.55	0.50	0.50
6.6	2.50	2.33	2.25	0.33	0.25	0.25
9.4	2.33	2.00	2.00	0.20	0.17	0.15
12.3	2.40	2.00	2.00	0.15	0.13	0.13

6.2.3 – CL Soil Compacted Wet of Optimum Moisture Content (w=17.0%)

Figures 6.22 – 6.30 show various experimental test data from thermo-controlled CSS testing of CL soil compacted at wet of optimum moisture content (w=17.0%). Figures 6.22 – 6.25 show typical soil response on the basis of number of cycles N=1, 5, 10, for a fixed shear strain amplitude and temperature. The figures are arranged similarly to those of the previous sections. The data shows that increasing cyclic load application caused a significant decrease in bilinear parameter G_2 for a fixed shear strain value. Figures 6.22 – 6.25 show that the majority of the decrease in G_2 occurs by cycle N=5.

Figures 6.26 – 6.28 show typical soil response on the basis of soil temperature for a fixed cyclic load application and shear strain amplitude. Similar to the previous sections, increasing temperatures caused a reduction in bilinear parameter G_2, indicating a reduction in shear modulus.

Figures 6.29 and 6.30 show bilinear model parameters G_1 and G_2. G_1 values remain fairly constant as temperature, number of cycles, and shear strain amplitude increase (Figure 6.29). G_2 values significantly decrease as temperature, number of cycles, and shear strain amplitude increase (Figure 6.30). Figure 6.30(c, d) shows G_2 values are lower in the tests conducted at increased temperatures. G_2 values decrease as shear strain amplitude increases, with the majority of the reduction taking place by cycle N=5. The rate of decrease for parameter G_2, shown visually by the slope of the trendlines in Figure 6.30, appears to be lower at higher temperatures. Values for G_1 and G_2 are shown in Table 6.3.

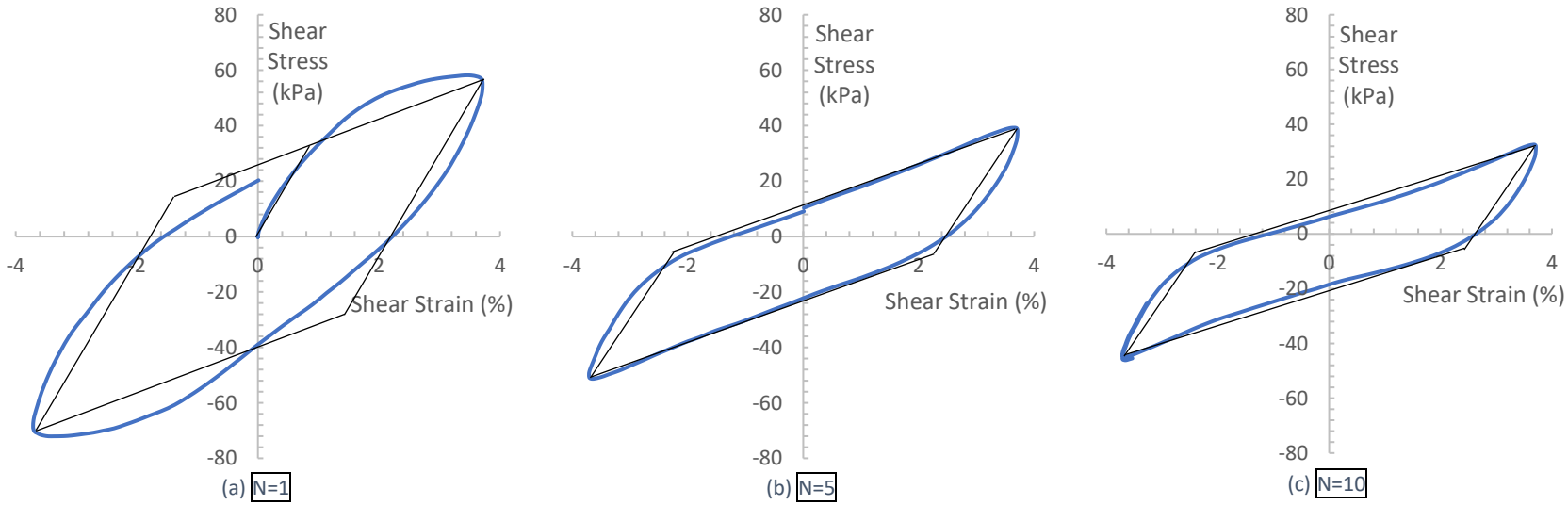

Figure 6.22: Bilinear Modeling of CL Soil Response (w=17.0%) on the Basis of Number of Cycles for RT, γ=4.0%

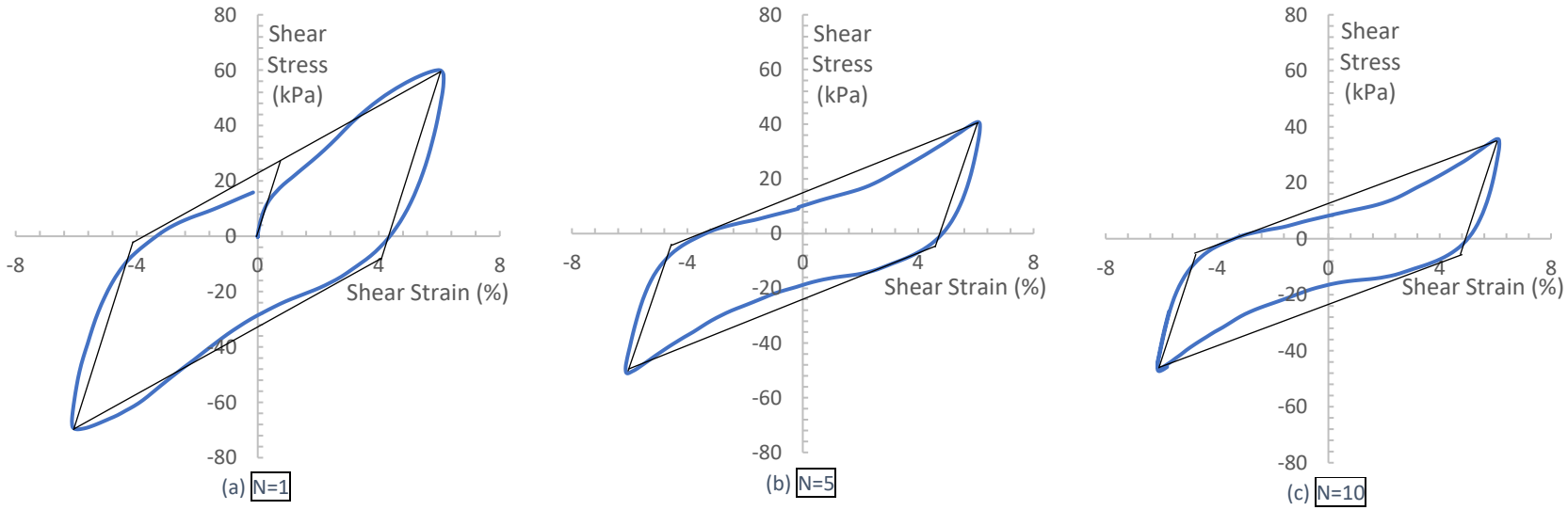

Figure 6.23: Bilinear Modeling of CL Soil Response (w=17.0%) on the Basis of Number of Cycles for 40°C, γ=6.0%

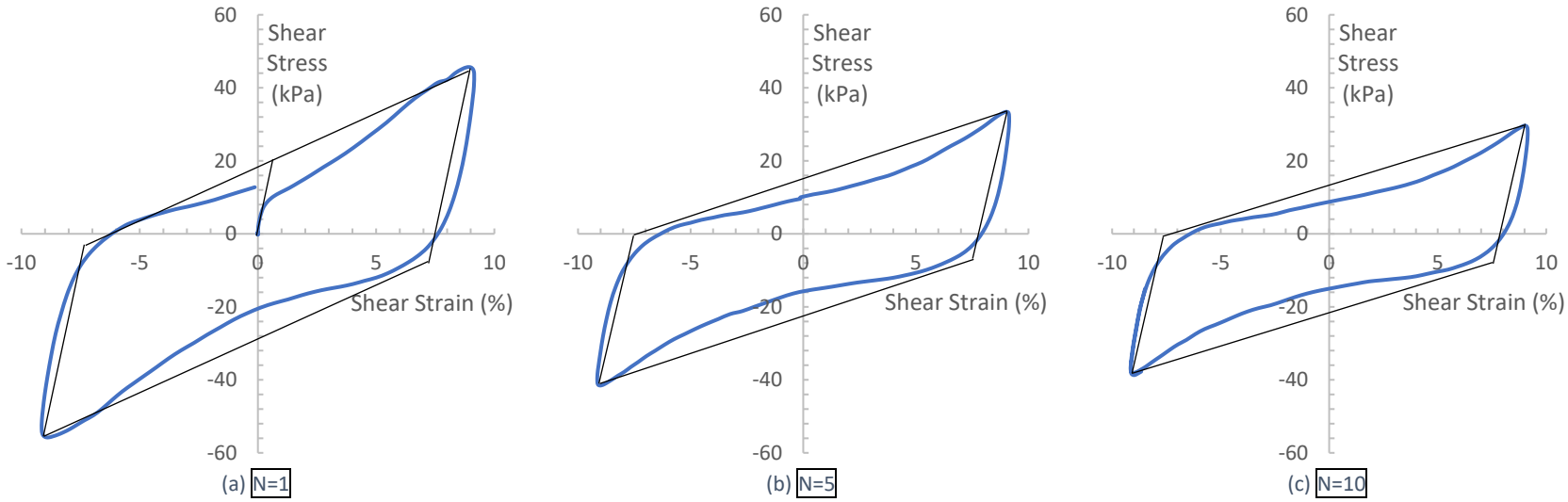

Figure 6.24: Bilinear Modeling of CL Soil Response (w=17.0%) on the Basis of Number of Cycles for 50°C, γ=8.0%

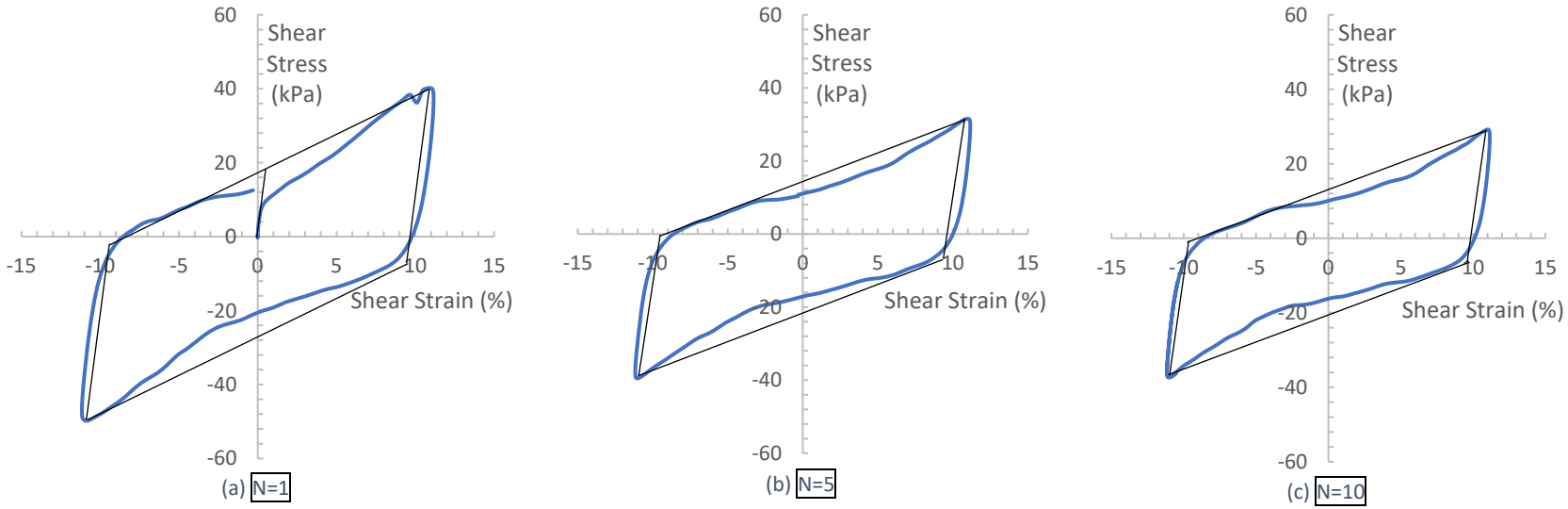

Figure 6.25: Bilinear Modeling of CL Soil Response (w=17.0%) on the Basis of Number of Cycles for 60°C, γ=10.0%

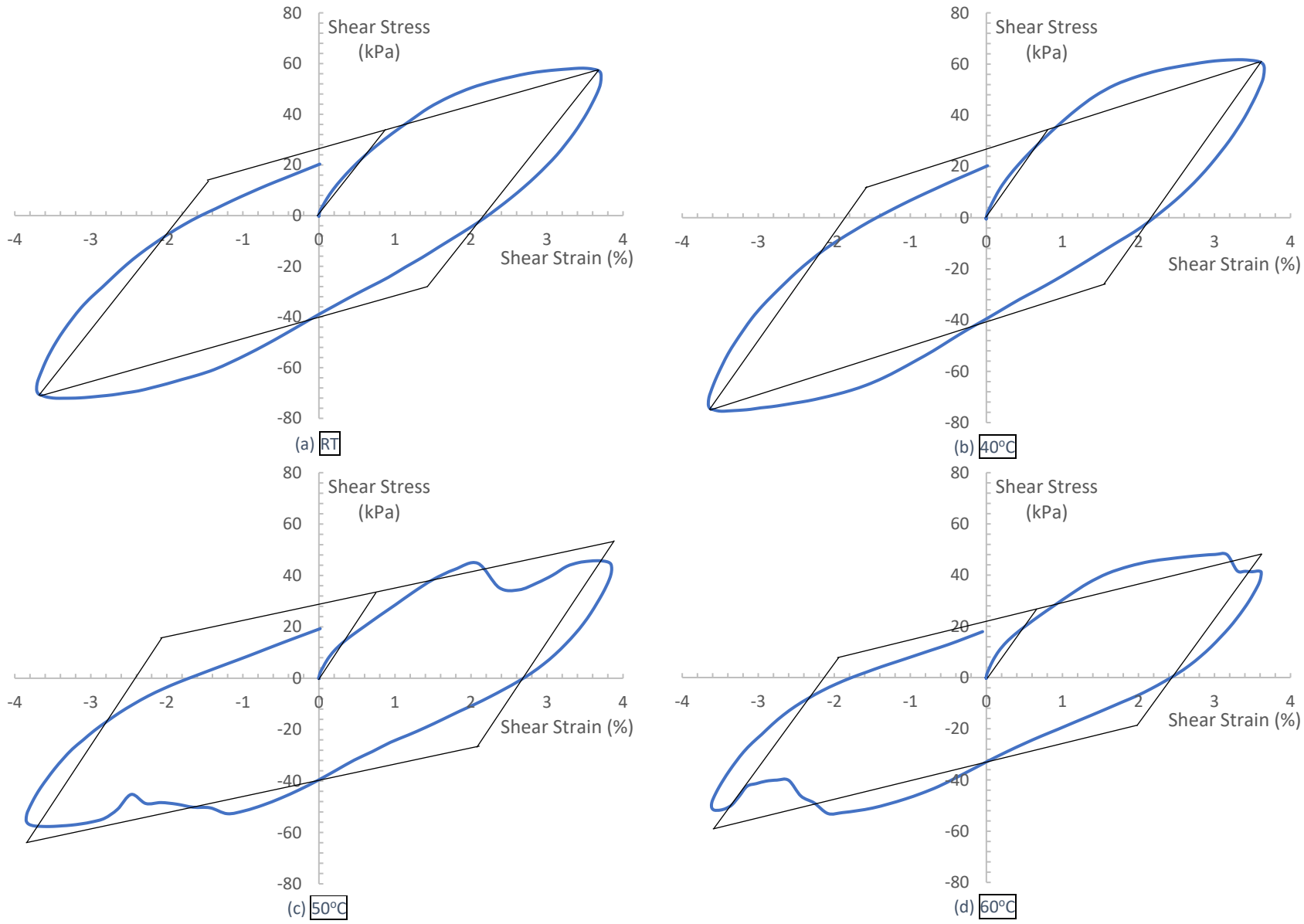

Figure 6.26: Bilinear Modeling of CL Soil Response (w=17.0%) on the Basis of Soil Temperature for N=1, γ = 4.0%

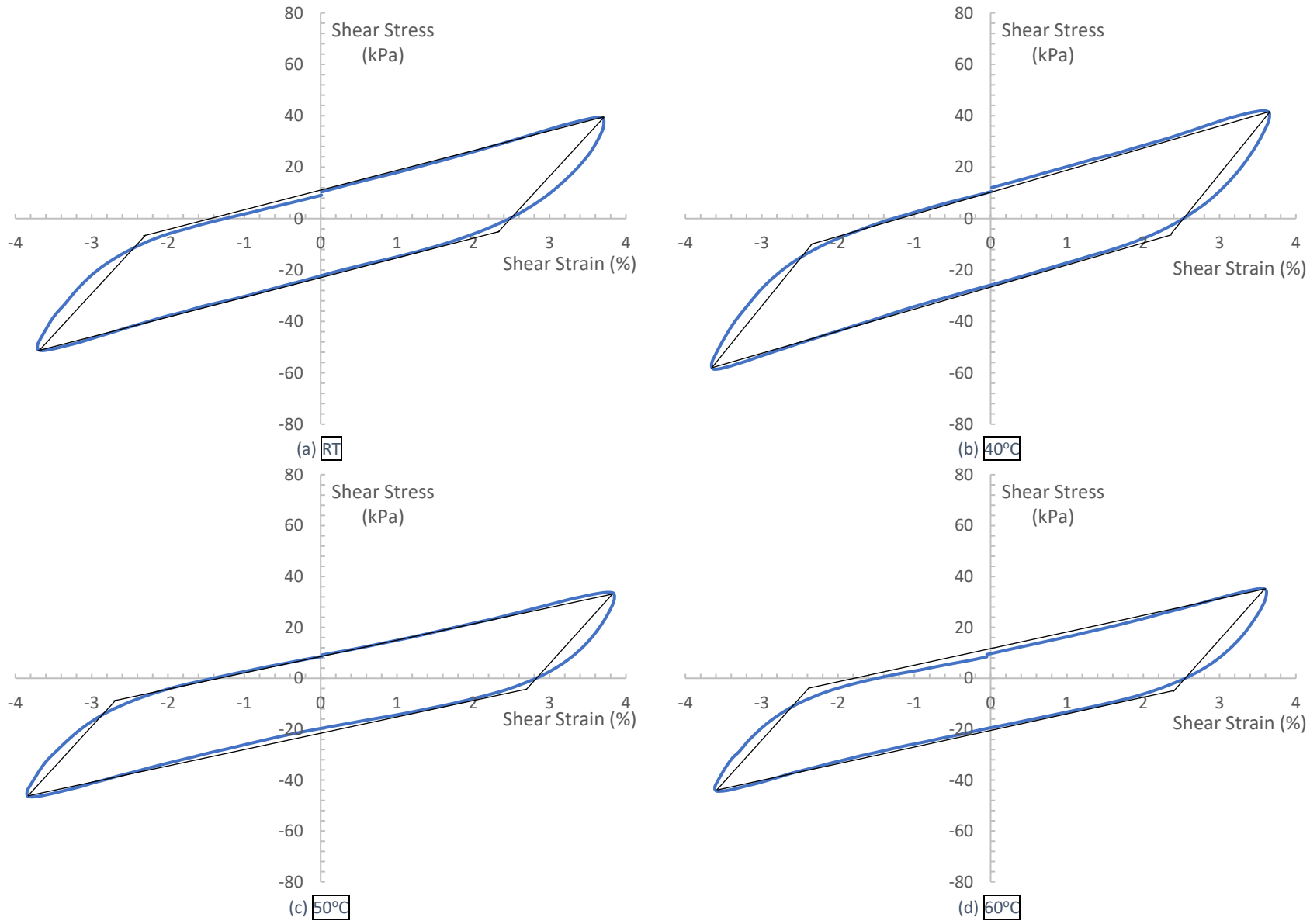

Figure 6.27: Bilinear Modeling of CL Soil Response (w=17.0%) on the Basis of Soil Temperature for N=5, γ = 4.0%

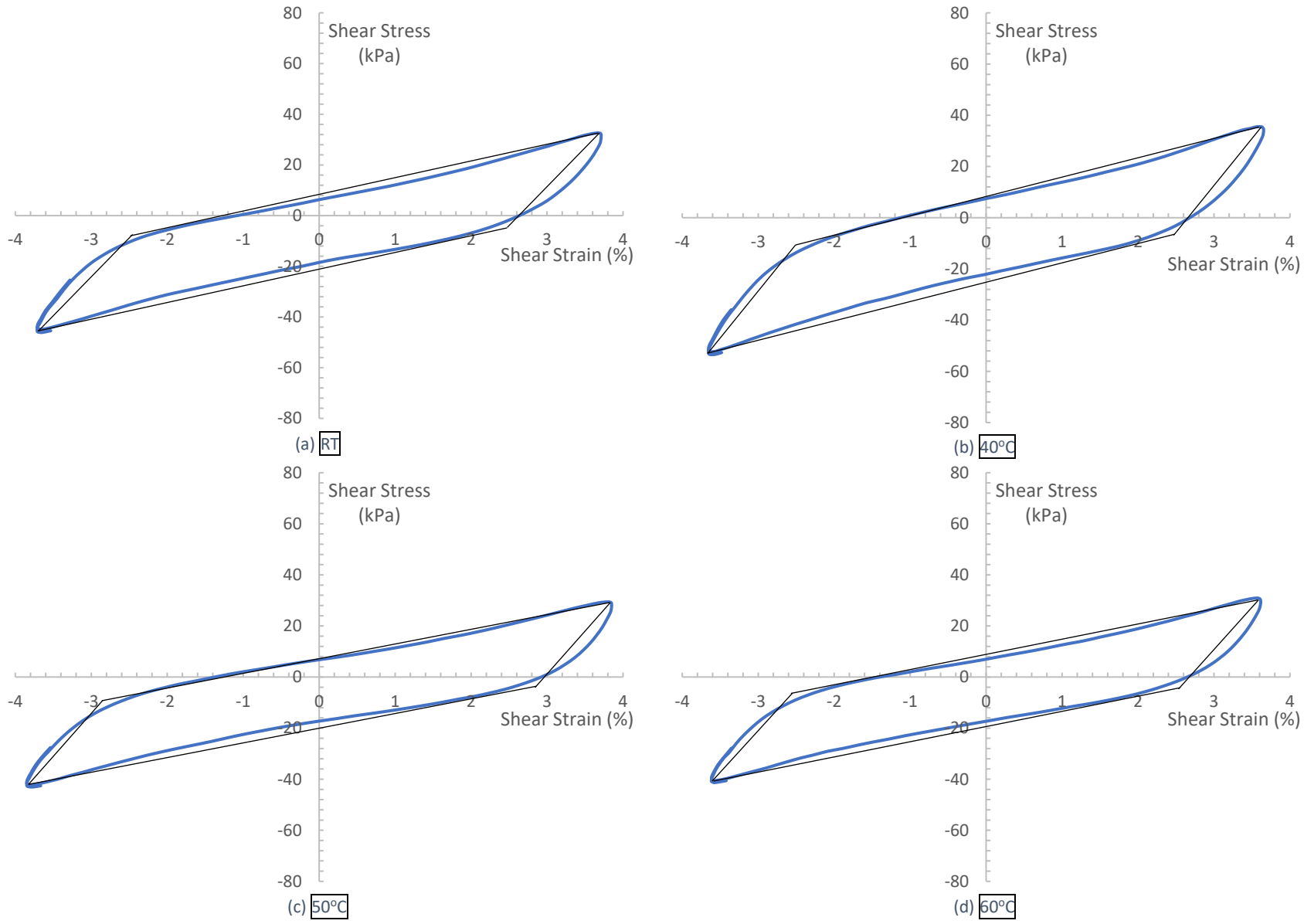

Figure 6.28: Bilinear Modeling of CL Soil Response (w=17.0%) on the Basis of Soil Temperature for N=10, γ = 4.0%

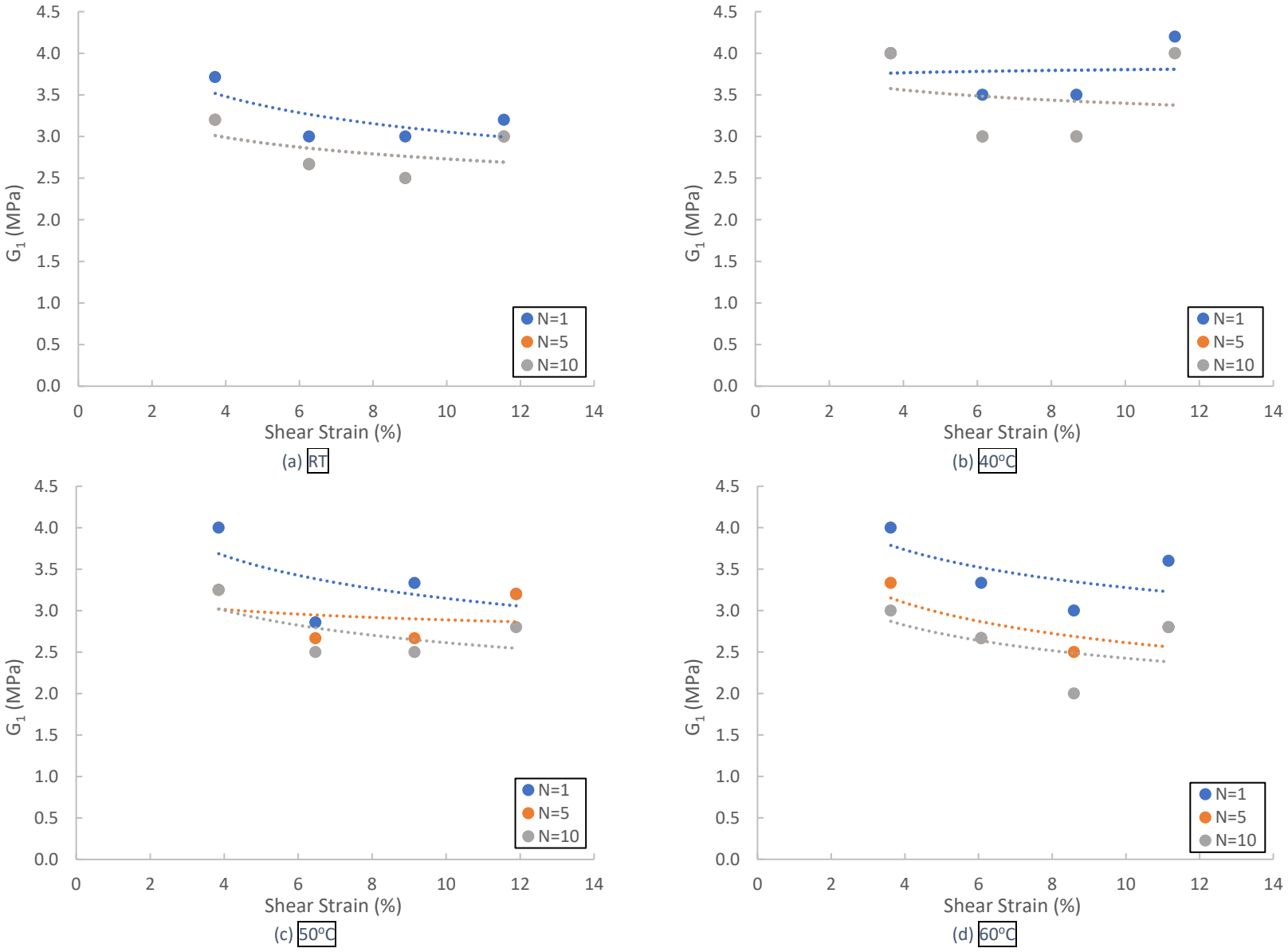

Figure 6.29: Bilinear Stiffness Parameter G_1 with Increasing Shear Strain and Number of Cycles for CL Soil (w=17.0%)

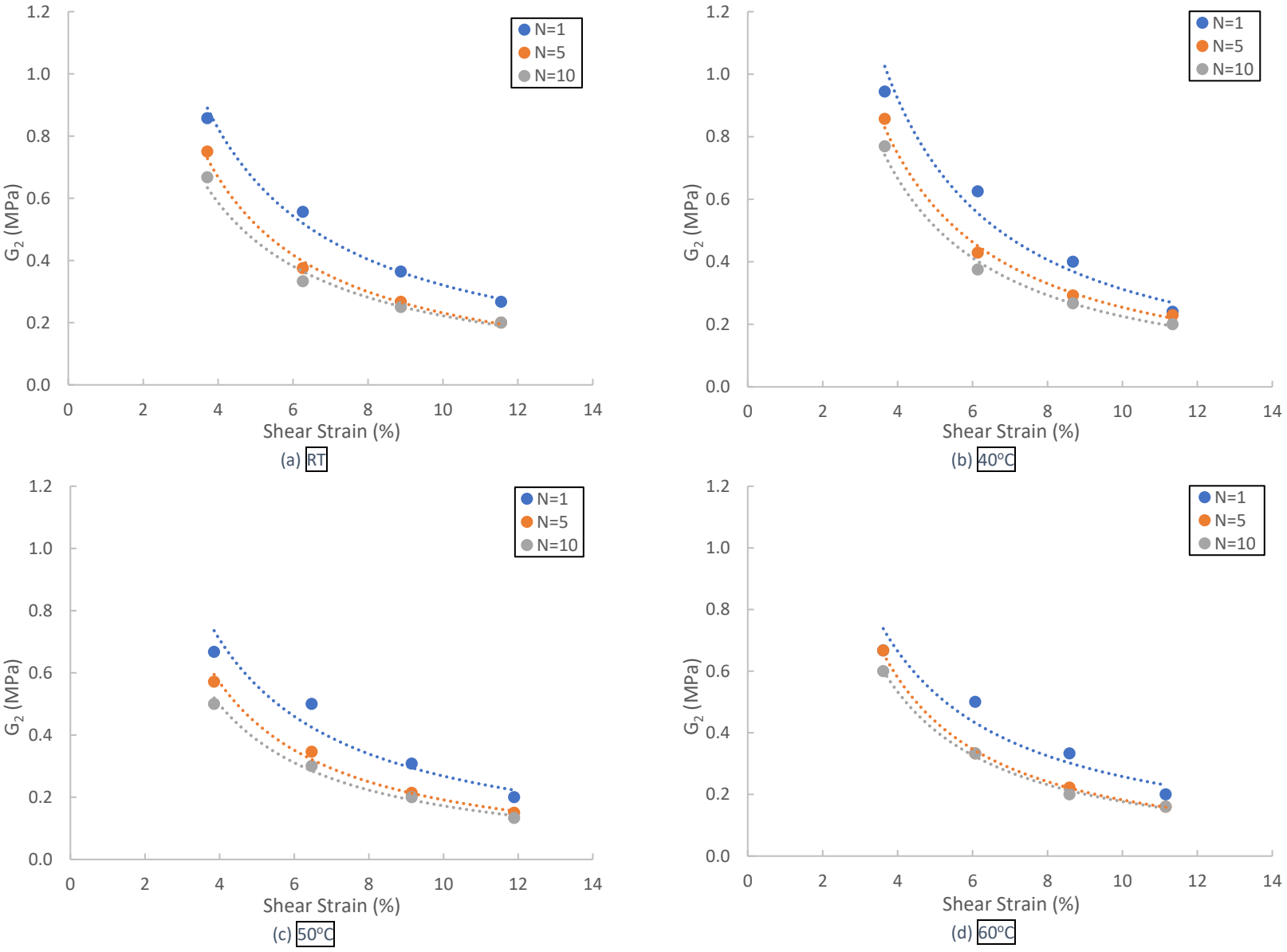

Figure 6.30: Bilinear Stiffness Parameter G_2 with Increasing Shear Strain and Number of Cycles for CL Soil (w=17.0%)

Table 6.3: G_1 and G_2 Values for CL Soil (w=17.0%)

RT						
	G_1 (MPa)			G_2 (MPa)		
Strain (%)	**N=1**	**N=5**	**N=10**	**N=1**	**N=5**	**N=10**
3.7	3.71	3.20	3.20	0.86	0.75	0.67
6.3	3.00	2.67	2.67	0.56	0.38	0.33
8.9	3.00	2.50	2.50	0.36	0.27	0.25
11.6	3.20	3.00	3.00	0.27	0.20	0.20
40C						
	G_1			G_2		
Strain	**N=1**	**N=5**	**N=10**	**N=1**	**N=5**	**N=10**
3.7	4.00	4.00	4.00	0.94	0.86	0.77
6.1	3.50	3.00	3.00	0.63	0.43	0.38
8.7	3.50	3.00	3.00	0.40	0.29	0.27
11.3	4.20	4.00	4.00	0.24	0.23	0.20
50C						
	G_1			G_2		
Strain	**N=1**	**N=5**	**N=10**	**N=1**	**N=5**	**N=10**
3.9	4.00	3.25	3.25	0.67	0.57	0.50
6.5	2.86	2.67	2.50	0.50	0.35	0.30
9.1	3.33	2.67	2.50	0.31	0.21	0.20
11.9	3.20	3.20	2.80	0.20	0.15	0.13
60C						
	G_1			G_2		
Strain	**N=1**	**N=5**	**N=10**	**N=1**	**N=5**	**N=10**
3.6	4.00	3.33	3.00	0.67	0.67	0.60
6.1	3.33	2.67	2.67	0.50	0.33	0.33
8.6	3.00	2.50	2.00	0.33	0.22	0.20
11.2	3.60	2.80	2.80	0.20	0.16	0.16

6.3 - Bilinear Modeling of Silty Soil (ML) Response

Figures 6.31 – 6.39 show various experimental test data from thermo-controlled CSS testing of ML soil compacted at optimum moisture content (w=14.8%). Figures 6.31 – 6.34 show typical soil response on the basis of number of cycles N=1, 5, 10, for a fixed shear strain amplitude and temperature. The figures are arranged similarly to those of the previous section. The data shows that increasing cyclic load application caused a decrease in bilinear parameter G_2 for a fixed shear strain value. Figures 6.31 – 6.34 show that the majority of the decrease in G_2 occurs by cycle N=5.

Figures 6.35 – 6.37 show typical soil response on the basis of soil temperature for a fixed cyclic load application and shear strain amplitude. In general, increasing temperatures caused a reduction in bilinear parameter G_2, indicating a reduction in shear modulus.

Figures 6.38 and 6.39 show bilinear model parameters G_1 and G_2. G_1 values decrease slightly as temperature, number of cycles, and shear strain amplitude increase (Figure 6.38). G_2 values decrease significantly as temperature, number of cycles, and shear strain amplitude increase (Figure 6.39). Figure 6.39(c, d) shows G_2 values are lower in the tests conducted at increased temperatures. G_2 values decrease as shear strain amplitude increases, with the majority of the reduction taking place by cycle N=5. The rate of decrease for parameter G_2, shown visually by the slope of the trendlines in Figure 6.39, appears to be greater for tests conducted at room temperature. Values for G_1 and G_2 shown in Table 6.4.

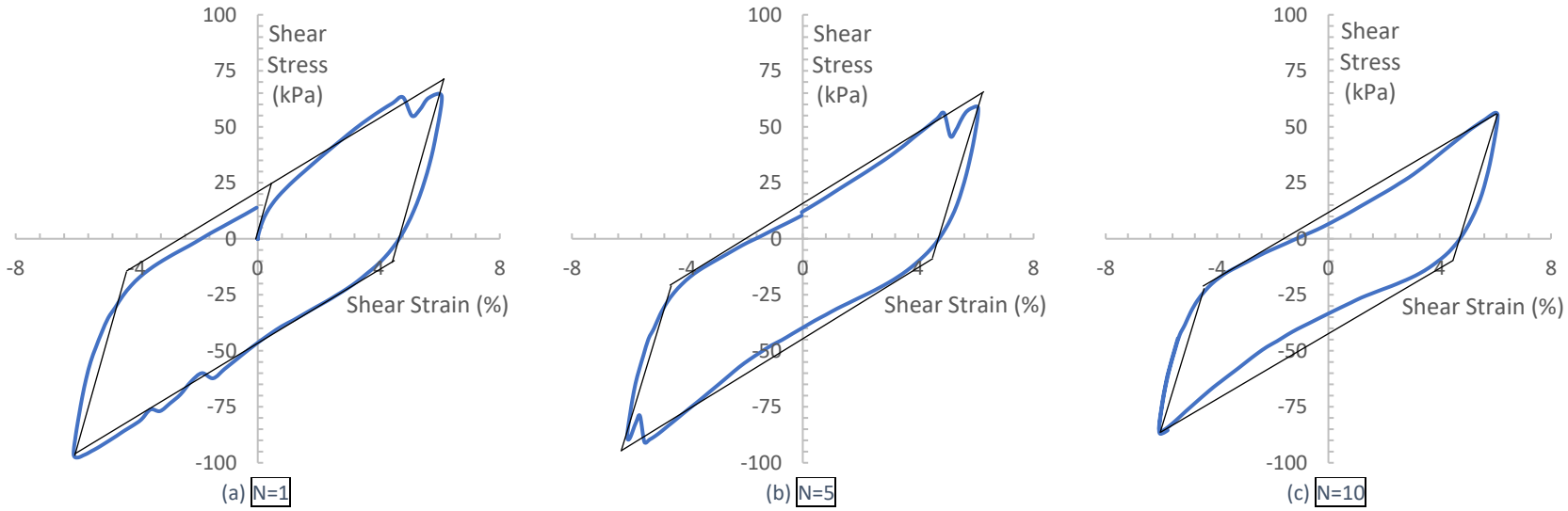

Figure 6.31: Bilinear Modeling of ML Soil Response (w=14.8%) on the Basis of Number of Cycles for RT, γ=6.0%

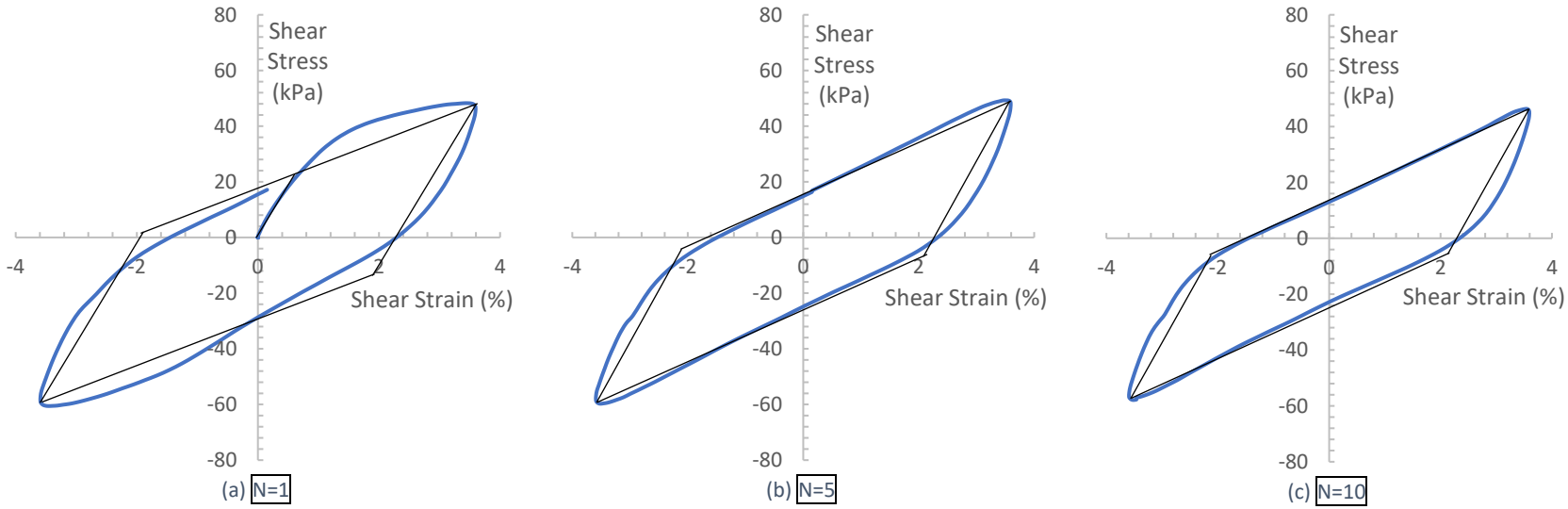

Figure 6.32: Bilinear Modeling of ML Soil Response (w=14.8%) on the Basis of Number of Cycles for 40°C, γ=4.0%

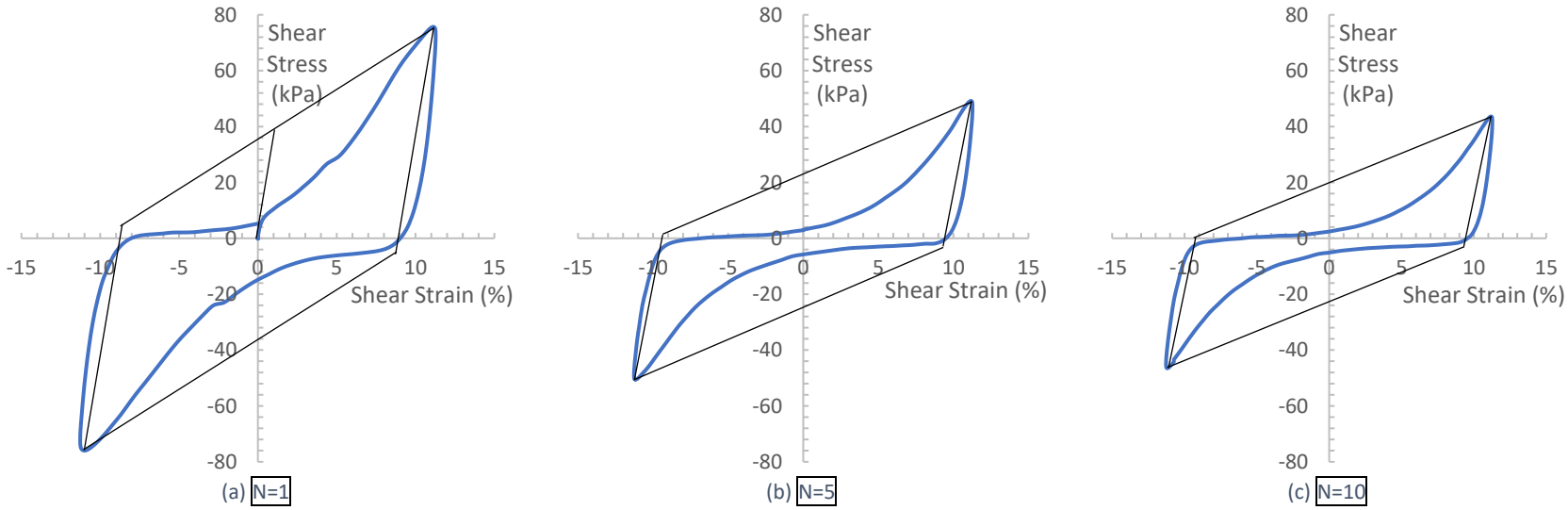

Figure 6.33: Bilinear Modeling of ML Soil Response (w=14.8%) on the Basis of Number of Cycles for 50°C, γ=10.0%

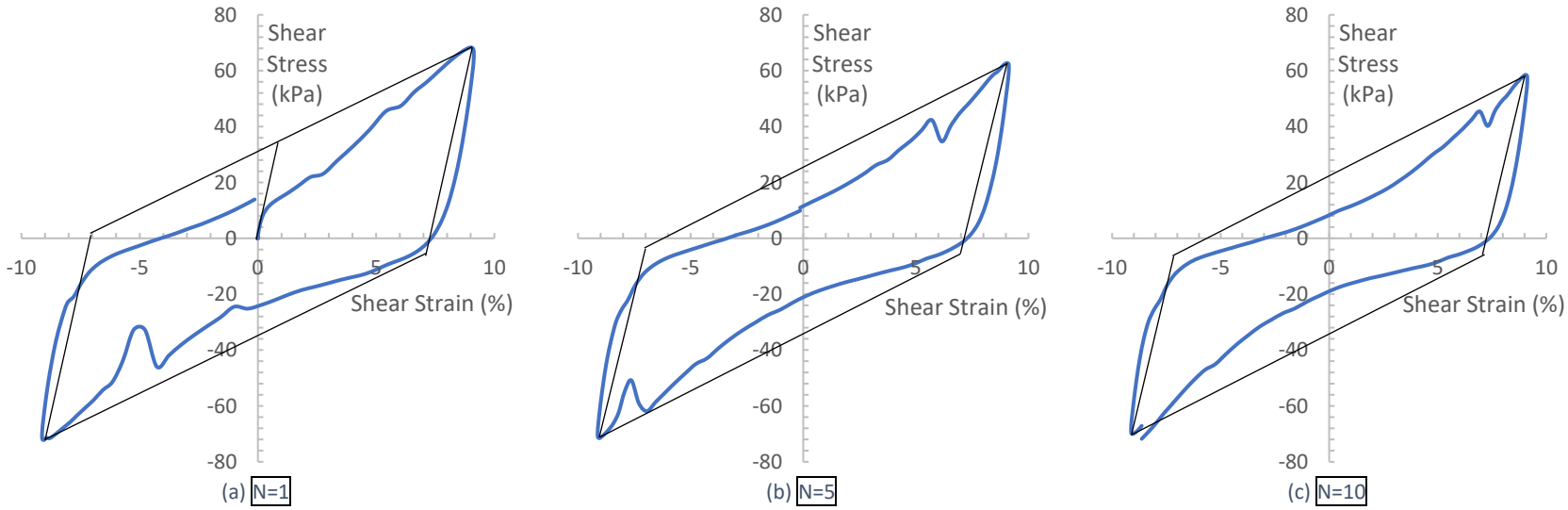

Figure 6.34: Bilinear Modeling of ML Soil Response (w=14.8%) on the Basis of Number of Cycles for 60°C, γ=8.0%

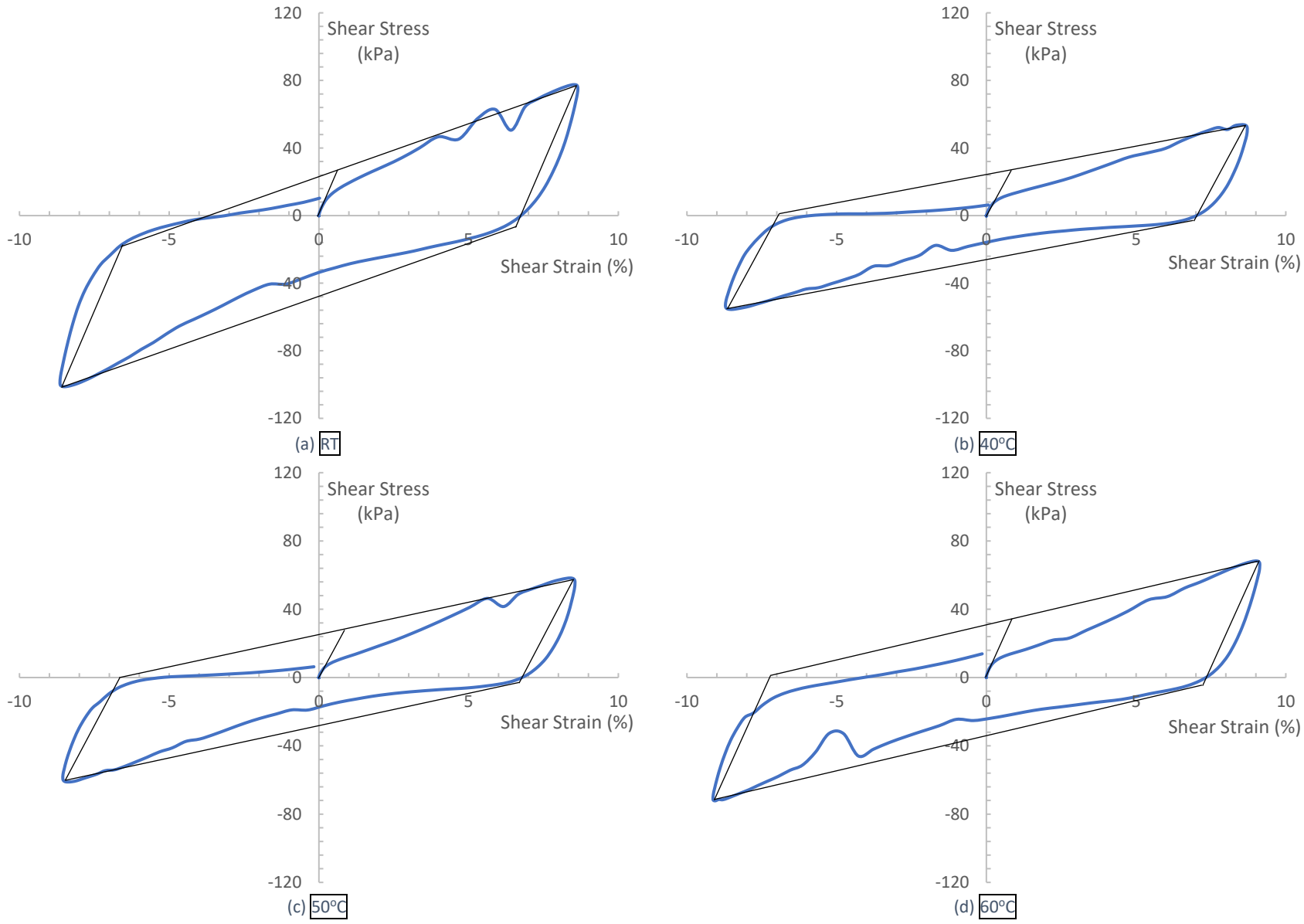

Figure 6.35: Bilinear Modeling of ML Soil Response (w=14.8%) on the Basis of Soil Temperature for N=1, γ = 8.0%

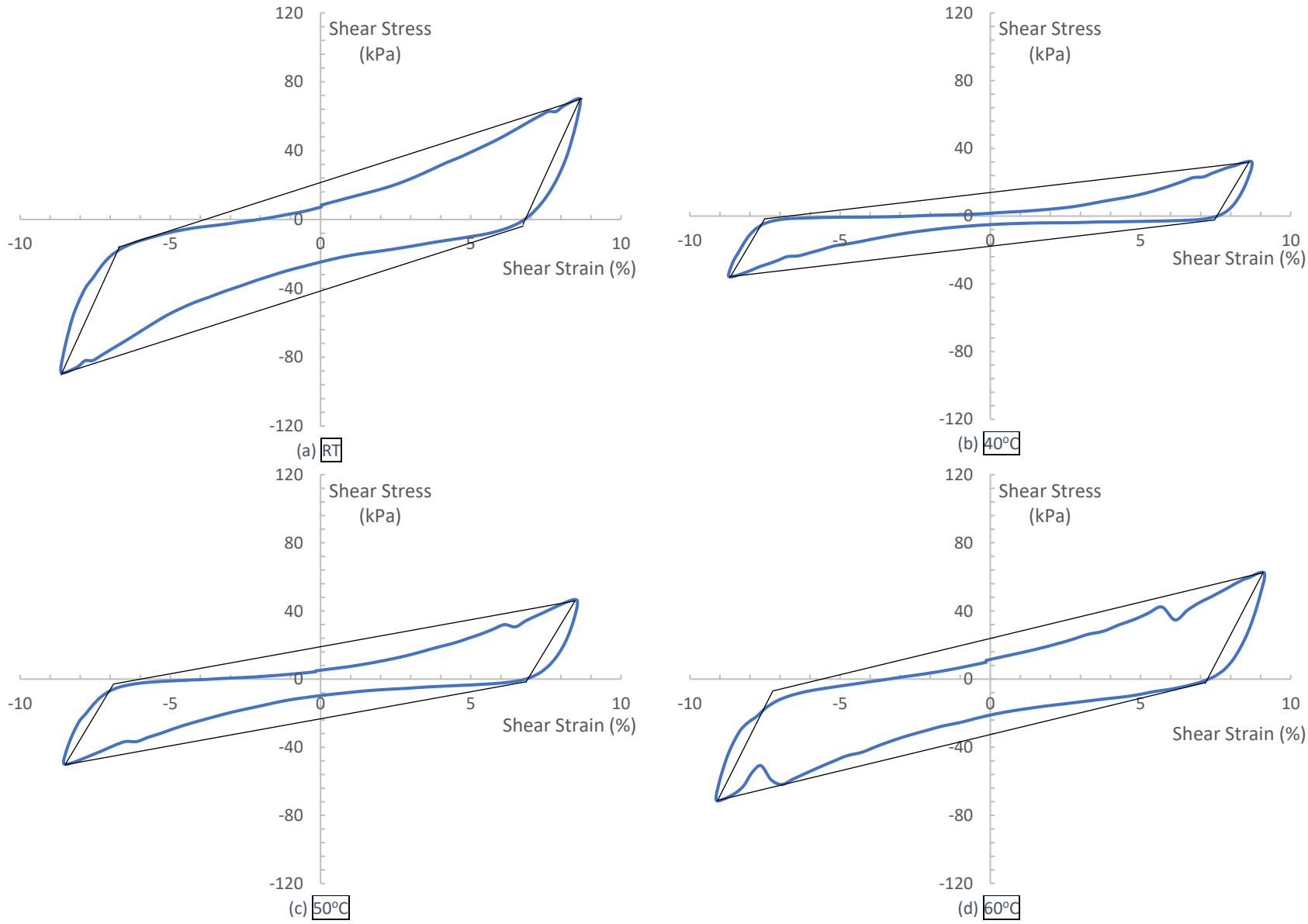

Figure 6.36: Bilinear Modeling of ML Soil Response (w=14.8%) on the Basis of Soil Temperature for N=5, γ = 8.0%

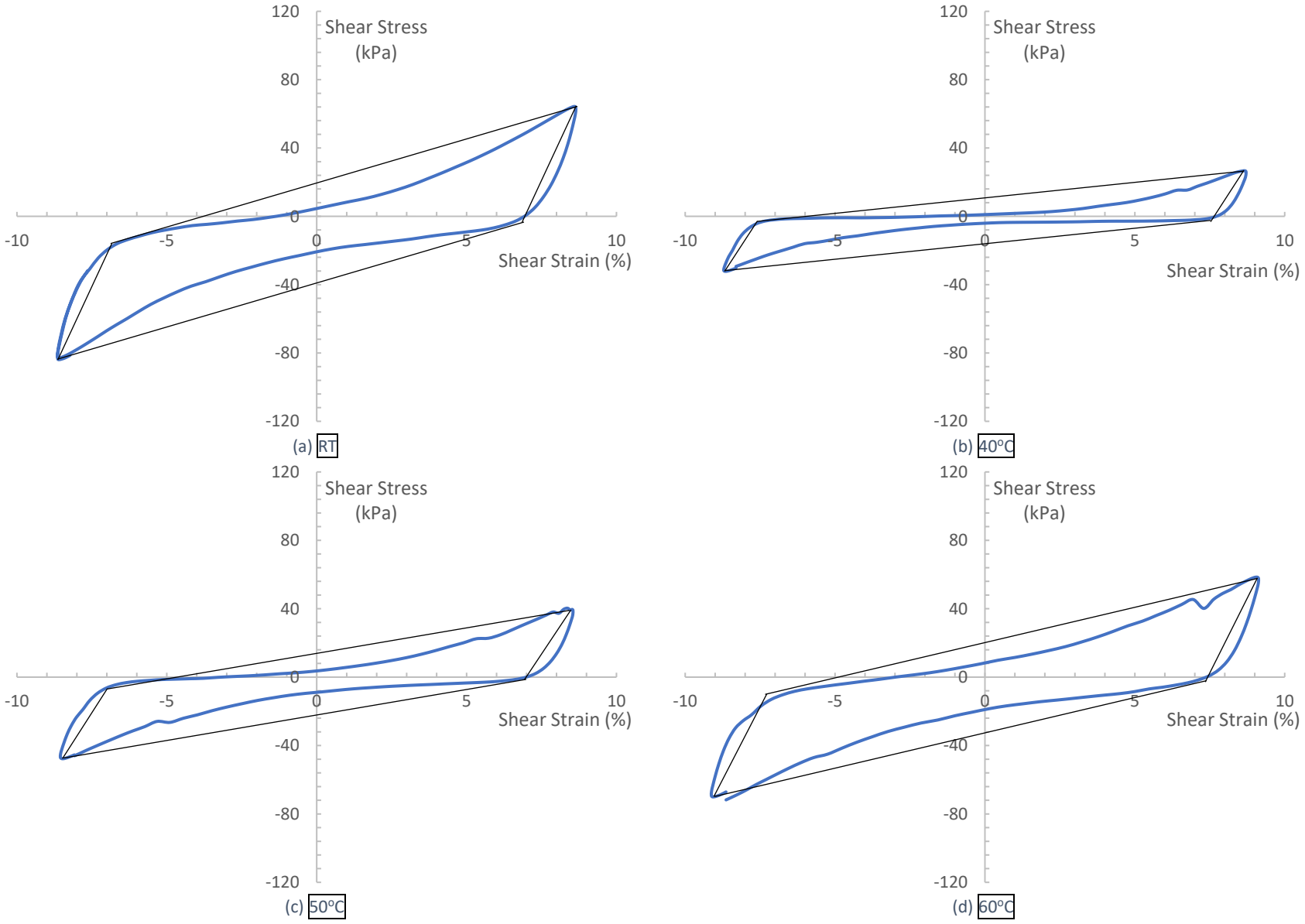

Figure 6.37: Bilinear Modeling of ML Soil Response (w=14.8%) on the Basis of Soil Temperature for N=10, γ = 8.0%

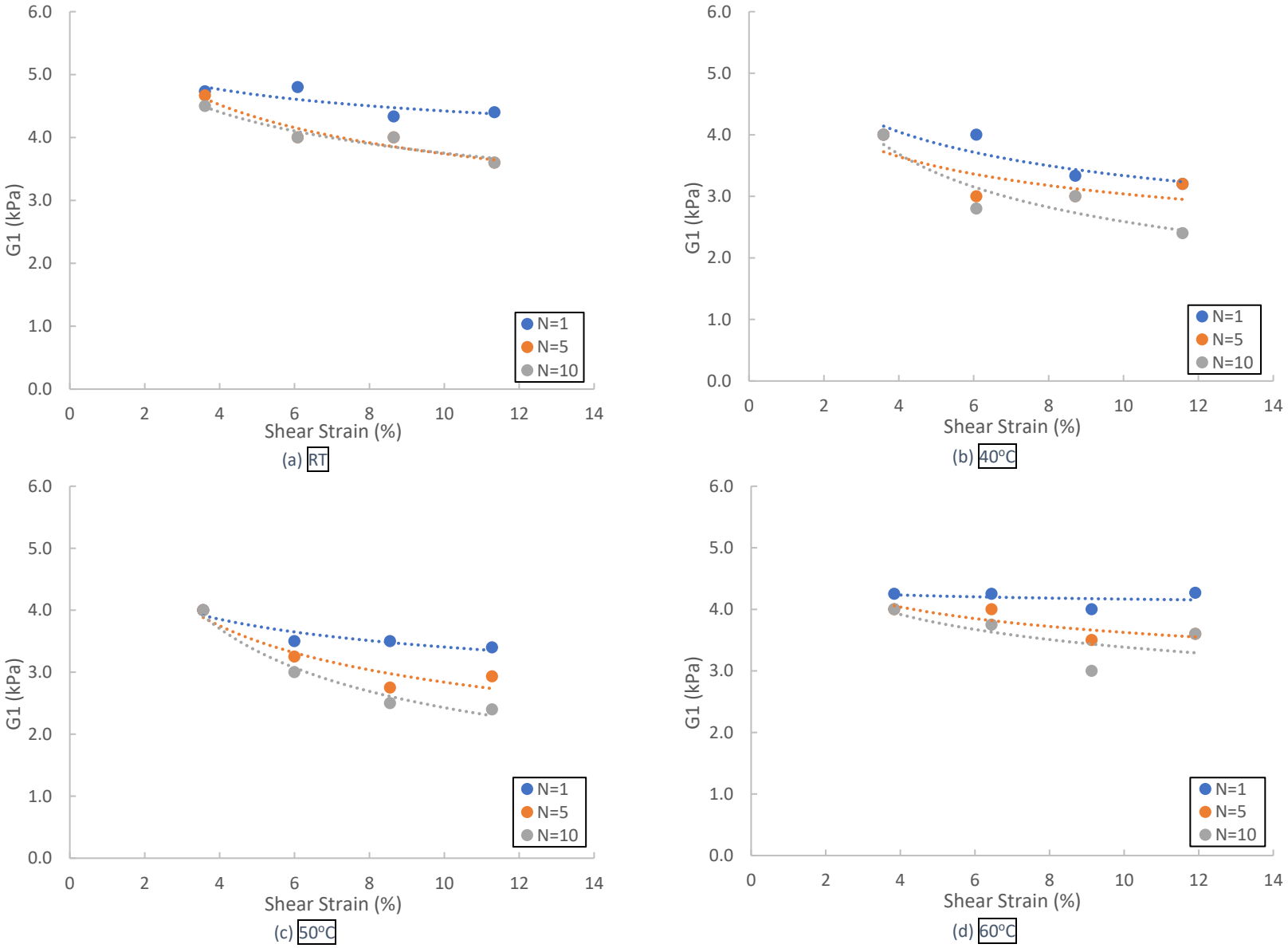

Figure 6.38: Bilinear Stiffness Parameter G_1 with Increasing Shear Strain and Number of Cycles for ML Soil (w=14.8%)

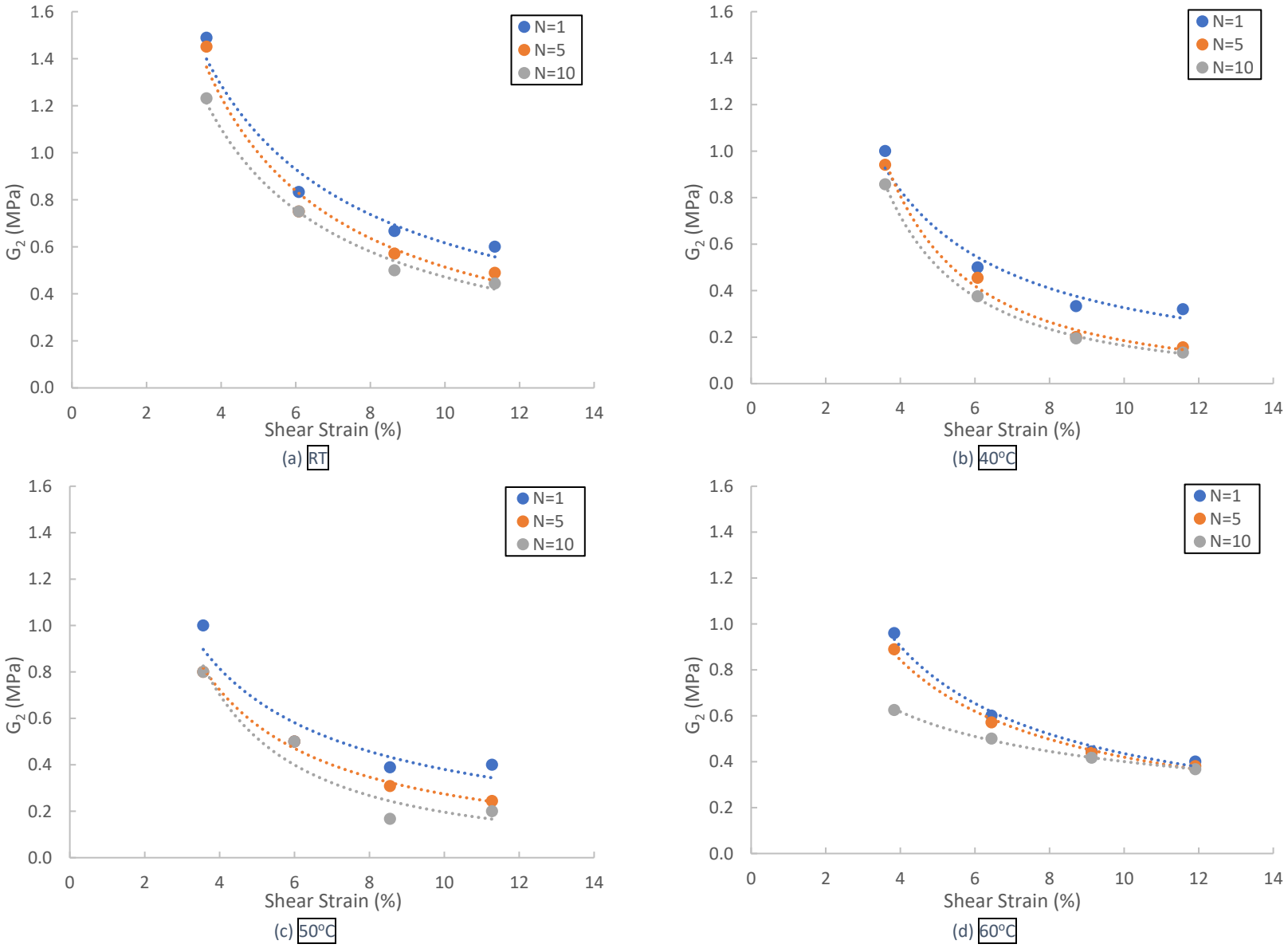

Figure 6.39: Bilinear Stiffness Parameter G_2 with Increasing Shear Strain and Number of Cycles for ML Soil (w=14.8%)

Table 6.4: G_1 and G_2 Values for ML Soil (w=14.8%)

RT						
	G_1 (MPa)			G_2 (MPa)		
Strain (%)	**N=1**	**N=5**	**N=10**	**N=1**	**N=5**	**N=10**
3.6	4.73	4.67	4.50	1.49	1.45	1.23
6.1	4.80	4.00	4.00	0.83	0.75	0.75
8.6	4.33	4.00	4.00	0.67	0.57	0.50
11.3	4.40	3.60	3.60	0.60	0.49	0.44
40C						
	G_1			G_2		
Strain	**N=1**	**N=5**	**N=10**	**N=1**	**N=5**	**N=10**
3.6	4.00	4.00	4.00	1.00	0.94	0.86
6.1	4.00	3.00	2.80	0.50	0.46	0.38
8.7	3.33	3.00	3.00	0.33	0.20	0.19
11.6	3.20	3.20	2.40	0.32	0.16	0.13
50C						
	G_1			G_2		
Strain	**N=1**	**N=5**	**N=10**	**N=1**	**N=5**	**N=10**
3.6	4.00	4.00	4.00	1.00	0.80	0.80
6	3.50	3.25	3.00	0.50	0.50	0.50
8.6	3.50	2.75	2.50	0.39	0.31	0.17
11.3	3.40	2.93	2.40	0.40	0.24	0.20
60C						
	G_1			G_2		
Strain	**N=1**	**N=5**	**N=10**	**N=1**	**N=5**	**N=10**
3.8	4.25	4.00	4.00	0.96	0.89	0.63
6.4	4.25	4.00	3.75	0.60	0.57	0.50
9.1	4.00	3.50	3.00	0.44	0.44	0.42
11.9	4.27	3.60	3.60	0.40	0.38	0.37

6.4 - Bilinear Modeling of Sandy Soil (SC) Response

Figures 6.40 – 6.48 show various experimental test data from thermo-controlled CSS testing of SC soil compacted at optimum moisture content (w=10.0%). Figures 6.40 – 6.43 show typical soil response on the basis of number of cycles N=1, 5, 10, for a fixed shear strain amplitude and temperature. The figures are arranged similarly to those of the previous section. The data shows that increasing cyclic load application caused a significant decrease in bilinear parameter G_2 for a fixed shear strain value. Figures 6.40 – 6.43 show that the majority of the decrease in G_2 occurs by cycle N=5.

Figures 6.44 – 6.46 show typical soil response on the basis of soil temperature for a fixed cyclic load application and shear strain amplitude. Similar to the previous section, increasing temperatures caused a reduction in bilinear parameter G_2, indicating a reduction in shear modulus.

Figures 6.47 and 6.48 show bilinear model parameters G_1 and G_2. G_1 values remain fairly constant as temperature, number of cycles, and shear strain amplitude increase (Figure 6.47). G_2 values significantly decrease as temperature, number of cycles, and shear strain amplitude increase (Figure 6.48). Figure 6.48(d) shows G_2 values are lower in the tests conducted at increased temperatures. G_2 values decrease as shear strain amplitude increases, with the majority of the reduction taking place by cycle N=5. The rate of decrease for parameter G_2, shown visually by the slope of the trendlines in Figure 6.48, appears to be similar for all temperatures. Values for G_1 and G_2 are shown in Table 6.5.

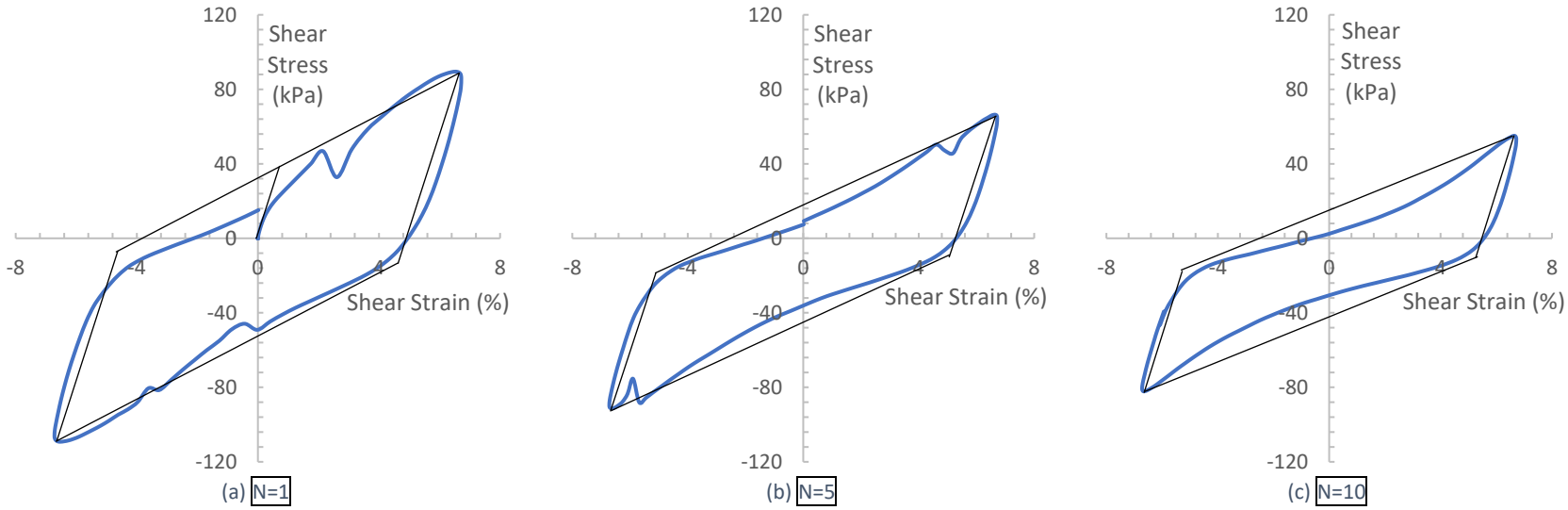

Figure 6.40: Bilinear Modeling of SC Soil Response (w=10.0%) on the Basis of Number of Cycles for RT, γ=6.0%

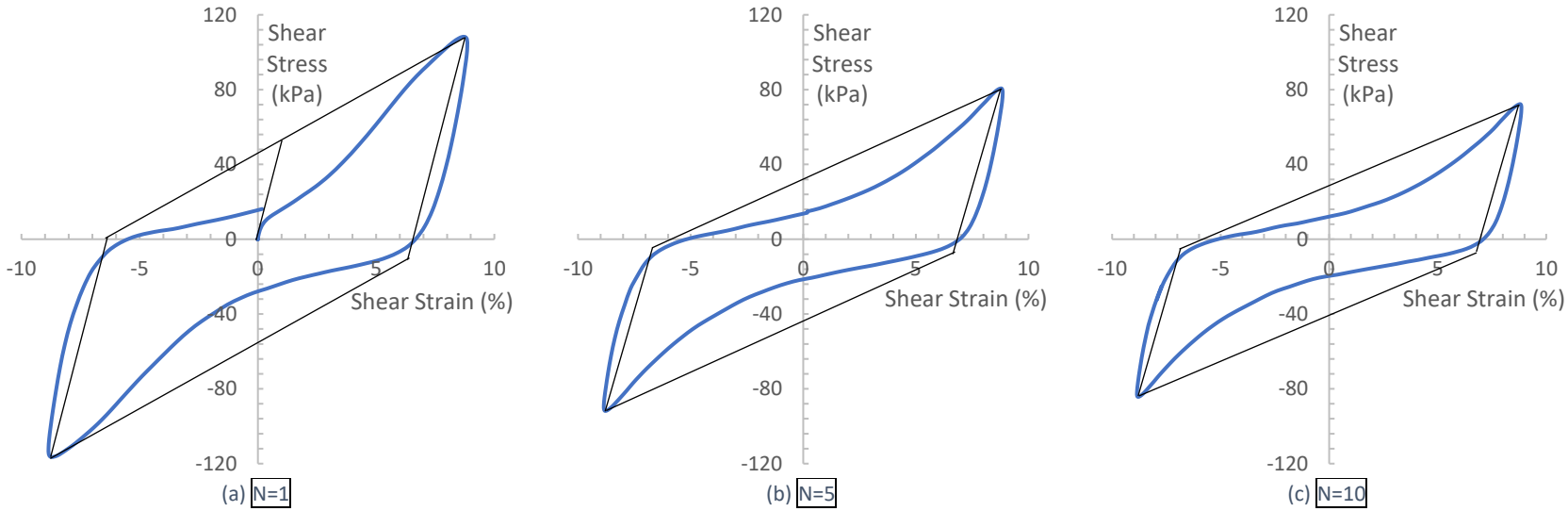

Figure 6.41: Bilinear Modeling of SC Soil Response (w=10.0%) on the Basis of Number of Cycles for 40°C, γ=8.0%

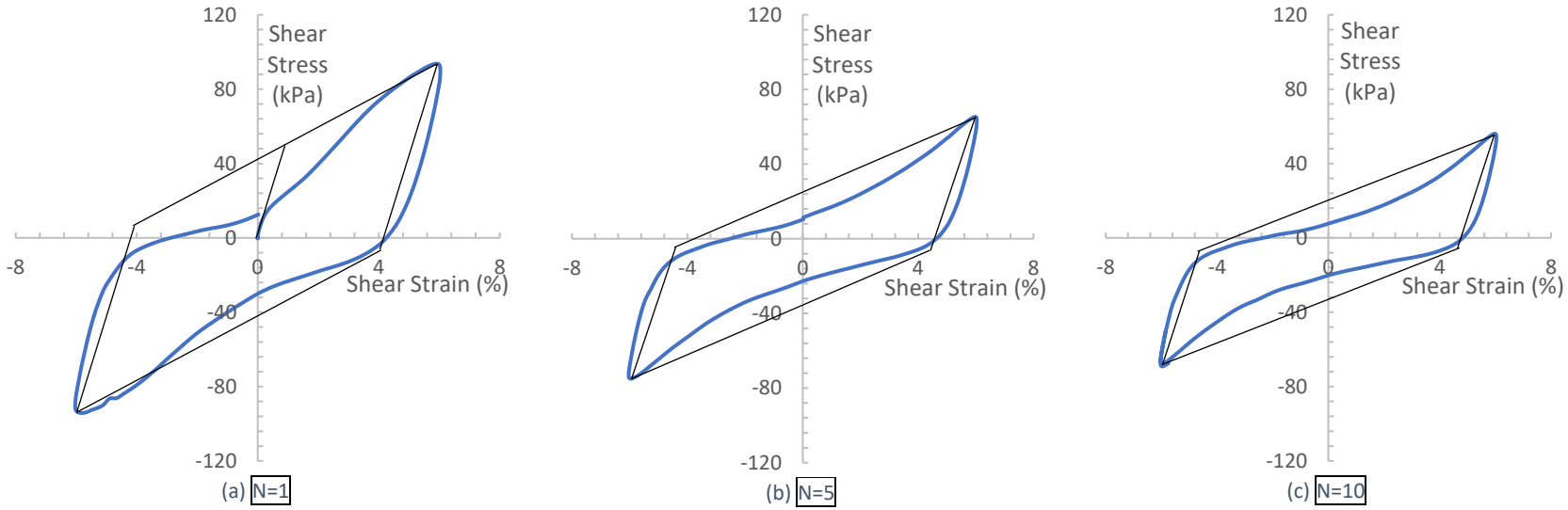

Figure 6.42: Bilinear Modeling of SC Soil Response (w=10.0%) on the Basis of Number of Cycles for 50°C, γ=6.0%

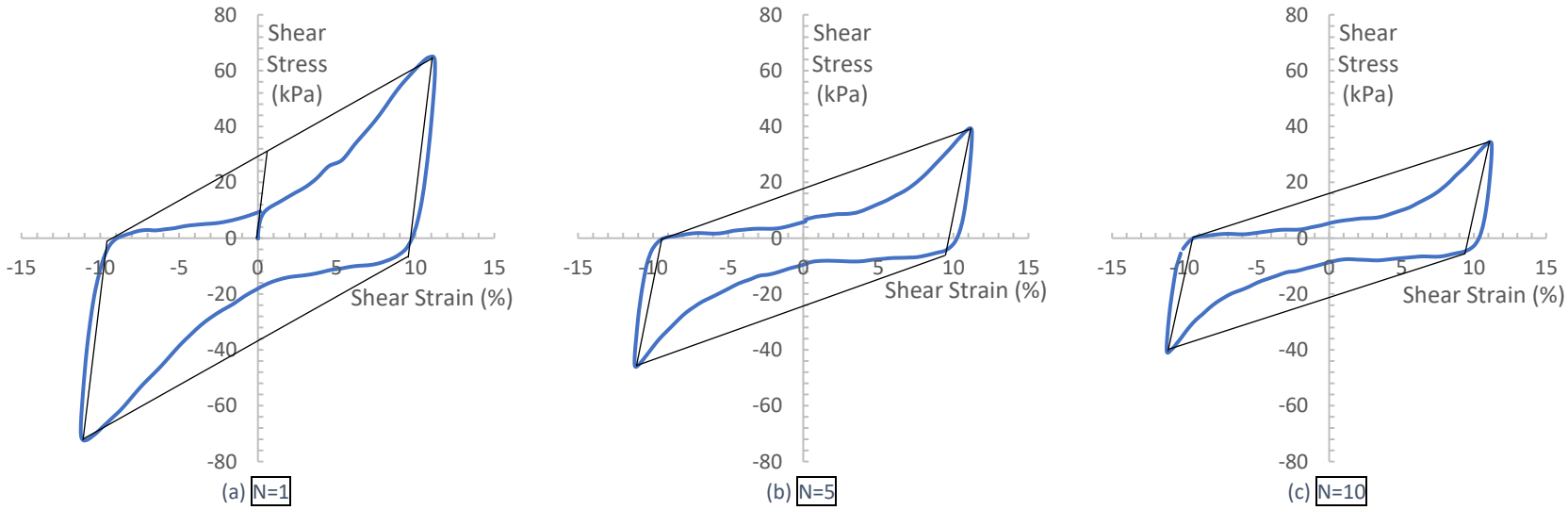

Figure 6.43: Bilinear Modeling of SC Soil Response (w=10.0%) on the Basis of Number of Cycles for 60°C, γ=10.0%

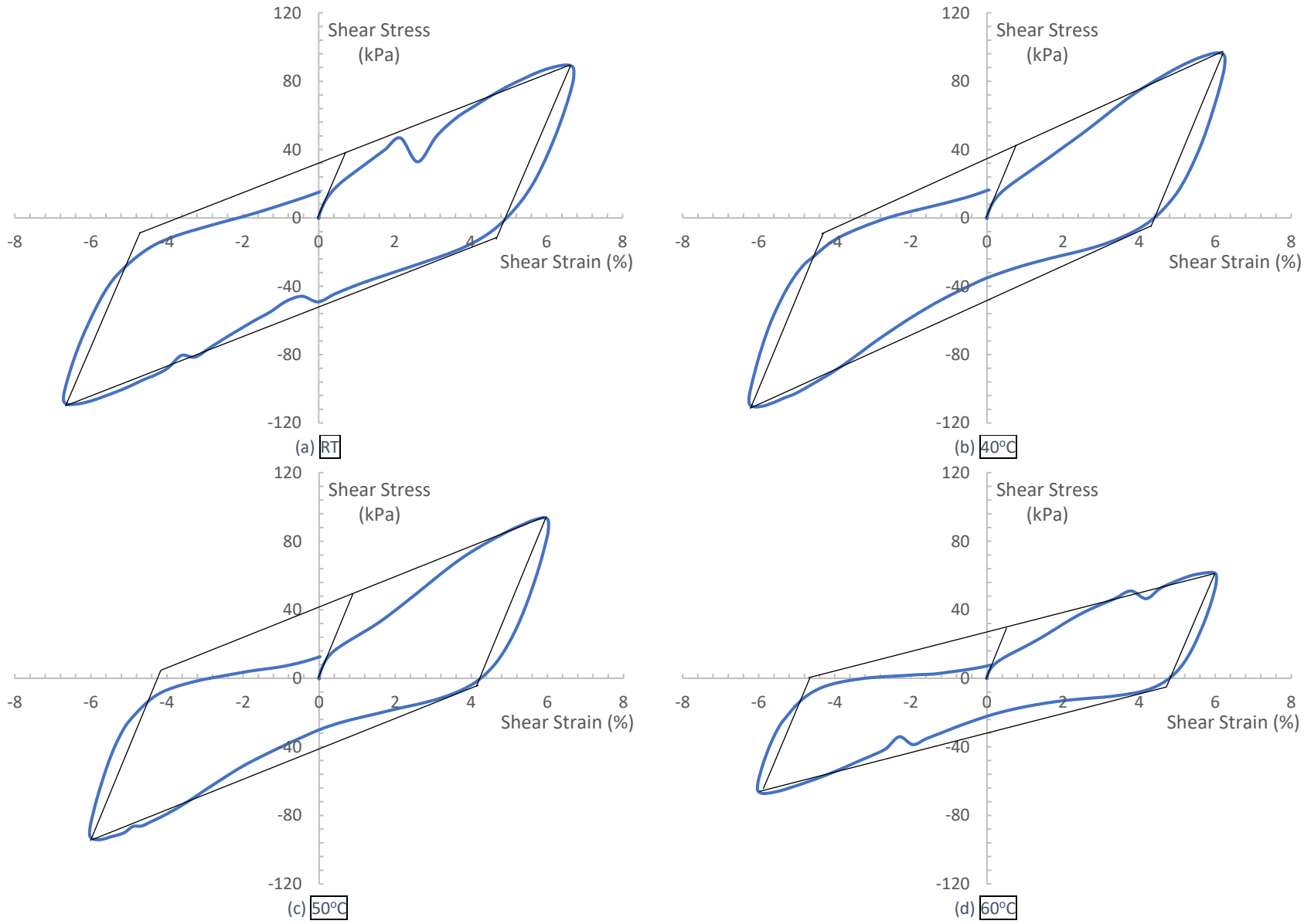

Figure 6.44: Bilinear Modeling of SC Soil Response (w=10.0%) on the Basis of Soil Temperature for N=1, γ = 6.0%

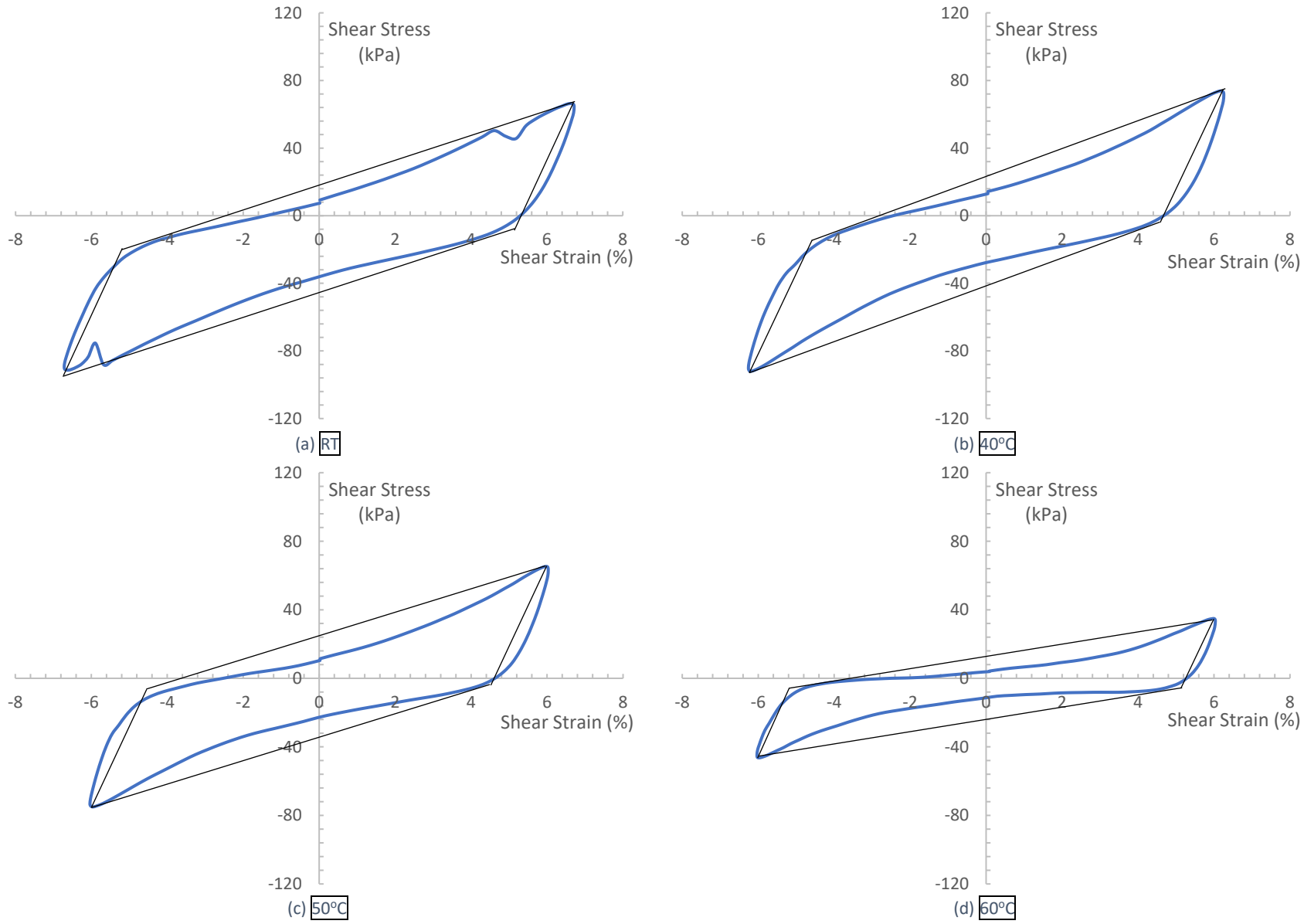

Figure 6.45: Bilinear Modeling of SC Soil Response (w=10.0%) on the Basis of Soil Temperature for N=5, γ = 6.0%

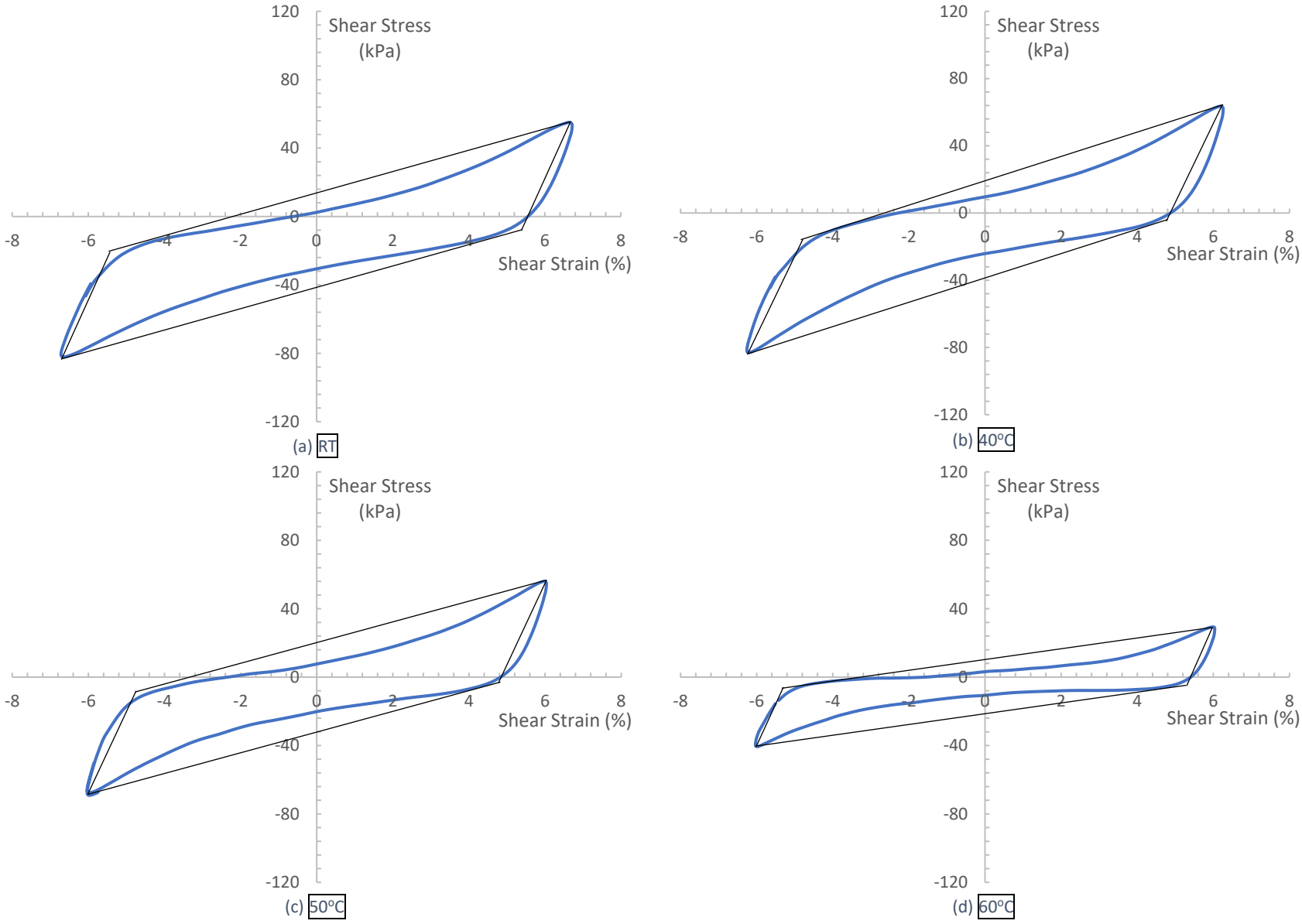

Figure 6.46: Bilinear Modeling of SC Soil Response (w=10.0%) on the Basis of Soil Temperature for N=10, γ = 6.0%

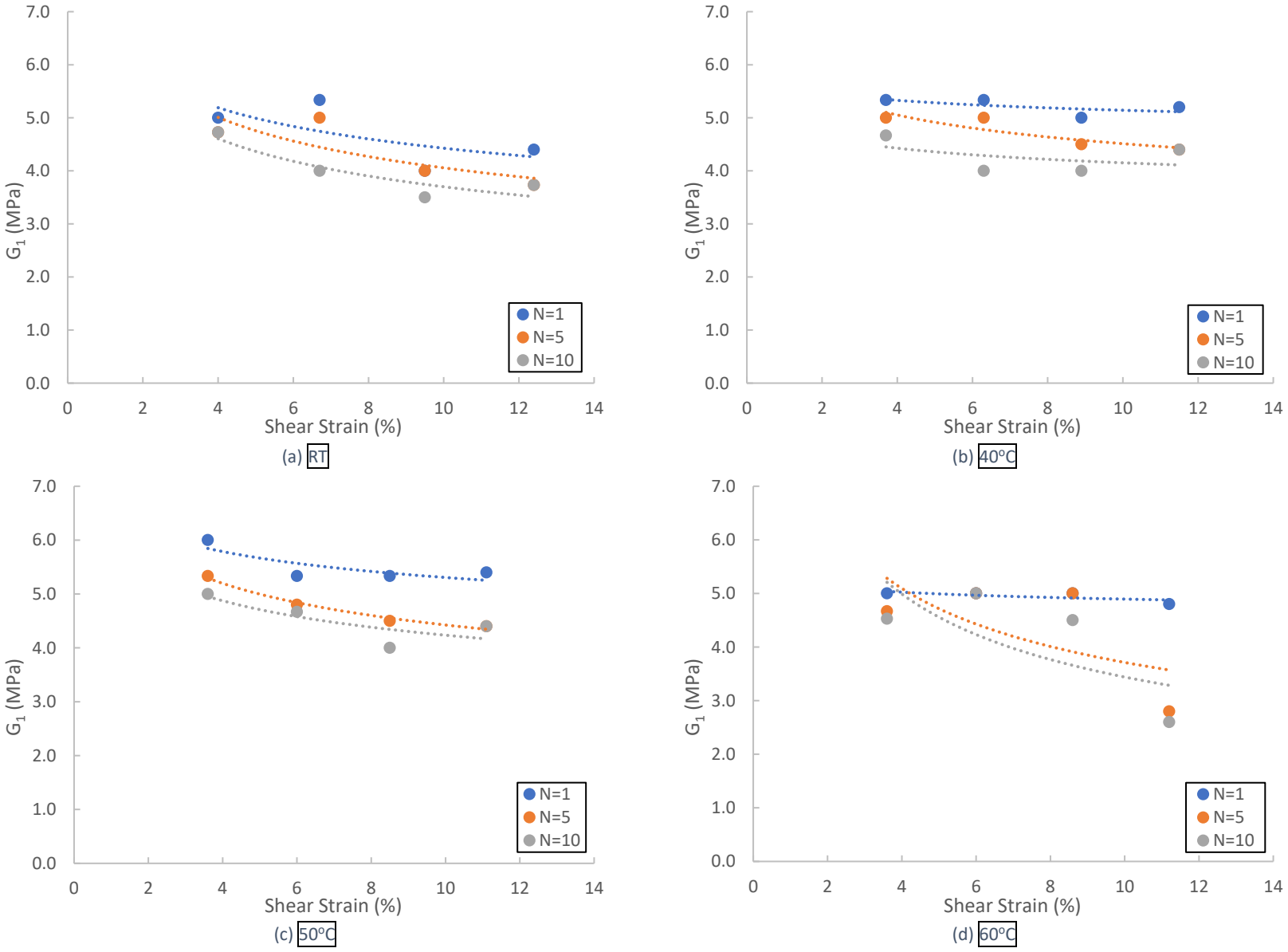

Figure 6.47: Bilinear Stiffness Parameter G_1 with Increasing Shear Strain and Number of Cycles for SC Soil (w=10.0%)

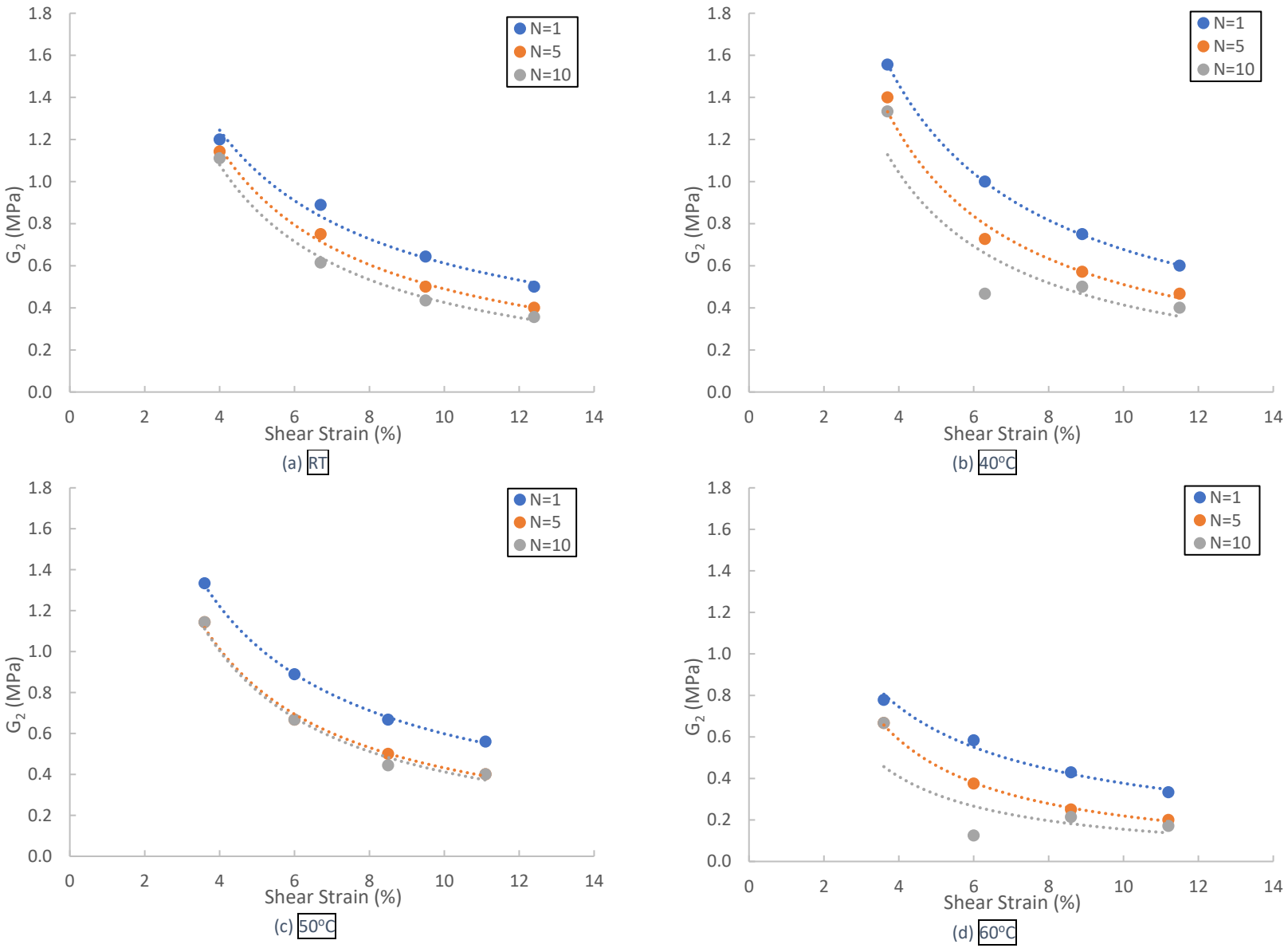

Figure 6.48: Bilinear Stiffness Parameter G_2 with Increasing Shear Strain and Number of Cycles for SC Soil (w=10.0%)

Table 6.5: G_1 and G_2 Values for SC Soil (w=10.0%)

RT						
	G_1 (MPa)			G_2 (MPa)		
Strain (%)	**N=1**	**N=5**	**N=10**	**N=1**	**N=5**	**N=10**
4	5.00	4.73	4.73	1.20	1.14	1.11
6.7	5.33	5.00	4.00	0.89	0.75	0.62
9.5	4.00	4.00	3.50	0.64	0.50	0.44
12.4	4.40	3.73	3.73	0.50	0.40	0.36
40C						
	G_1			G_2		
Strain	**N=1**	**N=5**	**N=10**	**N=1**	**N=5**	**N=10**
3.7	5.33	5.00	4.67	1.56	1.40	1.33
6.3	5.33	5.00	4.00	1.00	0.73	0.47
8.9	5.00	4.50	4.00	0.75	0.57	0.50
11.5	5.20	4.40	4.40	0.60	0.47	0.40
50C						
	G_1			G_2		
Strain	**N=1**	**N=5**	**N=10**	**N=1**	**N=5**	**N=10**
3.6	6.00	5.33	5.00	1.33	1.14	1.14
6	5.33	4.80	4.67	0.89	0.67	0.67
8.5	5.33	4.50	4.00	0.67	0.50	0.44
11.1	5.40	4.40	4.40	0.56	0.40	0.40
60C						
	G_1			G_2		
Strain	**N=1**	**N=5**	**N=10**	**N=1**	**N=5**	**N=10**
3.6	5.00	4.67	4.53	0.78	0.67	0.67
6	5.00	5.00	5.00	0.58	0.38	0.13
8.6	5.00	5.00	4.50	0.43	0.25	0.21
11.2	4.80	2.80	2.60	0.33	0.20	0.17

Chapter 7: Nonlinear Modeling of Shear Modulus and Damping Ratio

Dynamic soil response is primarily dictated by shear modulus and damping ratio, which describe the stiffness and energy dissipation during cyclic loading. To use these parameters to predict soil response during future cyclic loading events, it is important to accurately fit a representative numerical model to the lab data. The following chapter presents the shear modulus and material damping curves based on shear strain amplitude for the three soil types used in this study. Typically, an increase in shear strain amplitude causes a decrease in shear modulus and an increase in damping. One of the most prominent material models for predicting soil behavior is the Ramberg-Osgood model. For the purposes of this study, the Ramberg-Osgood model is used.

7.1 - Ramberg-Osgood Model Framework

In 1943 Ramberg and Osgood proposed three parameters (Young's modulus and two secant yield strengths) for modeling the non-linear stress-strain response curve under monotonic loading conditions of high strength materials used in aircraft construction, namely: aluminum alloy, stainless steel, and carbon steel sheets for the National Advisory Committee for Aeronautics. Prior to Ramberg and Osgood, stress-strain behavior of low strength metals was modeled using two parameters (Young's modulus and yield strength). The Ramberg-Osgood model is shown in Equation 7.1:

$$\varepsilon = \frac{\sigma}{E} + K\left(\frac{\sigma}{E}\right)^{n} \tag{7.1}$$

where ε is strain, σ is stress, and E is Young's modulus. K and n are constants that depend on the material being considered. The first term in the equation is equal to the elastic strain response and the second term accounts for the plastic strain response (Ramberg and Osgood, 1943). The model was adapted for soil response and typically takes the form of Equation 7.2 for modeling shear modulus degradation:

$$\frac{G_{sec}}{G_{max}} = \left(\frac{1}{1 + \alpha\left|\frac{\tau}{C\tau_{max}}\right|^{R-1}}\right) \tag{7.2}$$

where G_{sec} is the secant shear modulus, G_{max} is the small strain shear modulus, τ is shear stress, and τ_{max} is the maximum shear stress. α, C, and R are curve fitting constants (Ahmad and Ray, 2021). For convenience, shear stress τ and maximum shear stress τ_{max} have been replaced with shear strain γ and maximum shear strain γ_{max}. To use the Ramberg-Osgood model for material damping ratio, the original equation takes the form of Equation 7.3:

$$D = \frac{2(R-1)}{\pi(R+1)}\left(1 - \frac{G_{sec}}{G_{max}}\right) \tag{7.3}$$

where D is the material damping ratio, R is a curve fitting constant, G_{sec} is the secant shear modulus, and G_{max} is the small strain shear modulus (Ueng and Chen 1992). While not used for this study, it is important to note that the Ramberg-Osgood model is capable of modeling soil hysteresis loops generated by cyclic loading. The original equation can be modified with Masing's rule to obtain the unloading-reloading curve from Equation 7.4:

$$\gamma = 2\left[\frac{\tau - \tau_i}{2G_{max}}\left(1 + \alpha\left|\frac{\tau - \tau_i}{2C\tau_{max}}\right|^{R-1}\right)\right] + \gamma_i \tag{7.4}$$

where τ_i and γ_i are the shear stress and the shear strain at the turning point respectively (Ahmad and Ray 2021).

7.2 - Shear Modulus and Material Damping Degradation of CL Soil (w=9.0%)

Figure 7.1 shows the shear modulus (a) and material damping (b) degradation curves for thermo-controlled CSS testing of clay soil (CL) samples compacted dry of optimum moisture content. Shear modulus degradation data is included for tests conducted at all temperature variations (RT, 40°C, 50°C, and 60°C). For dry clay, the degradation rate of shear modulus was greater for samples tested at RT versus samples tested at 60°C. This effect is clearly seen in Figure 7.1. At any shear strain amplitude, a soil sample at RT will experience a faster shear modulus degradation than a sample heated to 60°C. RT and 60°C resonant column (RC) data are also included, and while limited to primarily low shear strain amplitudes, appear to show a contradictory trend.

For simplicity, material damping data is only included for the RT and 60°C tests for shear strain amplitudes greater than 0.1%. For shear strain amplitudes lower than 0.1%, the inconsistency of the hysteresis loops leads to excessive scattering of the damping data. Figure 7.1(b) shows that as temperature increases damping slightly decreases. The parameters used to best fit the Ramberg-Osgood model (R-O) to the shear modulus degradation and material damping data for RT and 60°C tests are shown in Table 7.1.

Table 7.1: Ramberg-Osgood Model Parameters for CL Soil (w=9.0%)

Normalized Shear Modulus				
	α	**C**	**R**	**γ_{max} (%)**
RT	0.2	0.0005	1.74	10.0
60C	0.1	0.0007	1.70	10.0
Damping Ratio (%)				
RT	3.0	0.4	2.05	10.0
60C	3.0	0.5	2.10	10.0

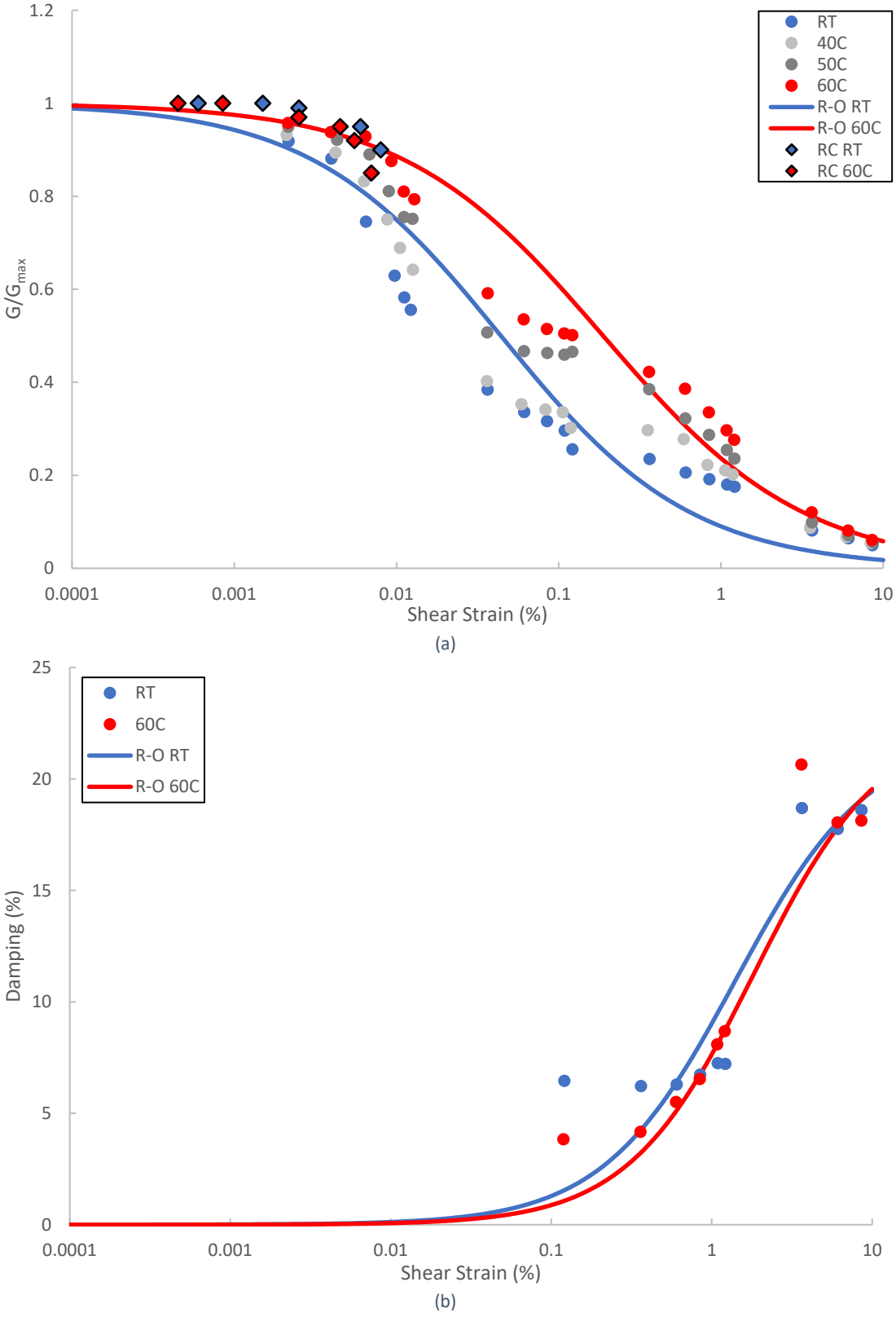

Figure 7.1: Thermal sensitivity of (a) shear modulus and (b) material damping degradation of CL Soil (w=9.0%) with increasing shear strain amplitude

7.3 - Shear Modulus and Material Damping Degradation of CL Soil (w=13.6%)

Figure 7.2 shows the shear modulus (a) and material damping (b) degradation curves for thermo-controlled CSS testing of clay soil (CL) samples compacted at optimum moisture content. Shear modulus degradation data is included for tests conducted at all temperature variations (RT, 40°C, 50°C, and 60°C). For clay, the degradation rate of shear modulus was similar for all temperatures. This effect is clearly seen in Figure 7.2. At any shear strain amplitude, a soil sample at RT will experience roughly the same shear modulus degradation as a sample heated to 60°C. RT and 60°C RC data are also included and appear to show a similar trend.

For simplicity, material damping data is only included for the RT and 60°C tests for shear strain amplitudes greater than 0.1%. For shear strain amplitudes lower than 0.1%, the inconsistency of the hysteresis loops leads to excessive scattering of the damping data. Figure 7.2(b) shows that damping remained consistent as temperature increased. The parameters used to best fit the R-O model to the shear modulus degradation and material damping data are shown in Table 7.2.

Table 7.2: Ramberg-Osgood Model Parameters for CL Soil (w=13.6%)

Normalized Shear Modulus				
	α	**C**	**R**	**γ_{max} (%)**
FIT	0.3	0.001	1.7	10.0
Damping Ratio (%)				
FIT	3.0	0.25	2.2	10.0

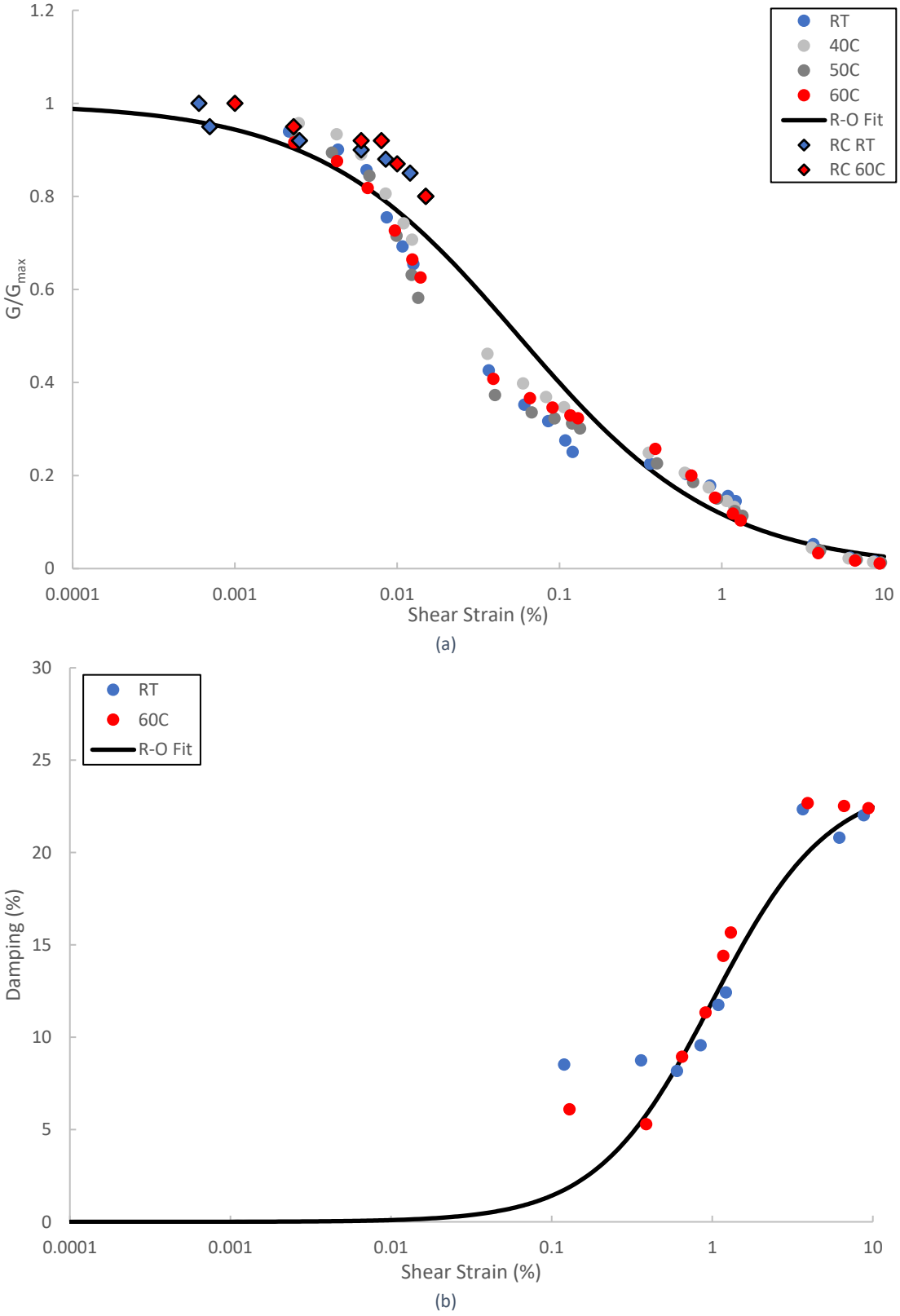

Figure 7.2: Thermal sensitivity of (a) shear modulus and (b) material damping degradation of CL Soil (w=13.6%) with increasing shear strain amplitude

7.4 - Shear Modulus and Material Damping Degradation of CL Soil (w=17.0%)

Figure 7.3 shows the shear modulus (a) and material damping (b) degradation curves for thermo-controlled CSS testing of clay soil (CL) samples compacted wet of optimum moisture content. Shear modulus degradation data is included for tests conducted at all temperature variations (RT, 40°C, 50°C, and 60°C). For wet clay, the degradation rate of shear modulus was similar for all temperatures. This effect is clearly seen in Figure 7.3. At any shear strain amplitude, a soil sample at RT will experience roughly the same shear modulus degradation as a sample heated to 60°C. RT and 60°C RC data are also included, and while limited to primarily low shear strain amplitudes, appear to show a similar trend.

For simplicity, material damping data is only included for the RT and 60°C tests for shear strain amplitudes greater than 0.1%. For shear strain amplitudes lower than 0.1%, the inconsistency of the hysteresis loops leads to excessive scattering of the damping data. Figure 7.3(b) shows that damping remained constant as temperature increased. The parameters used to best fit the R-O model to the shear modulus degradation and material damping data for RT and 60°C tests are shown in Table 7.3.

Table 7.3: Ramberg-Osgood Model Parameters for CL Soil (w=17.0%)

Normalized Shear Modulus				
	α	**C**	**R**	**γ_{max} (%)**
FIT	0.3	0.0007	1.70	10.0
Damping Ratio (%)				
FIT	3.0	0.25	2.15	10.0

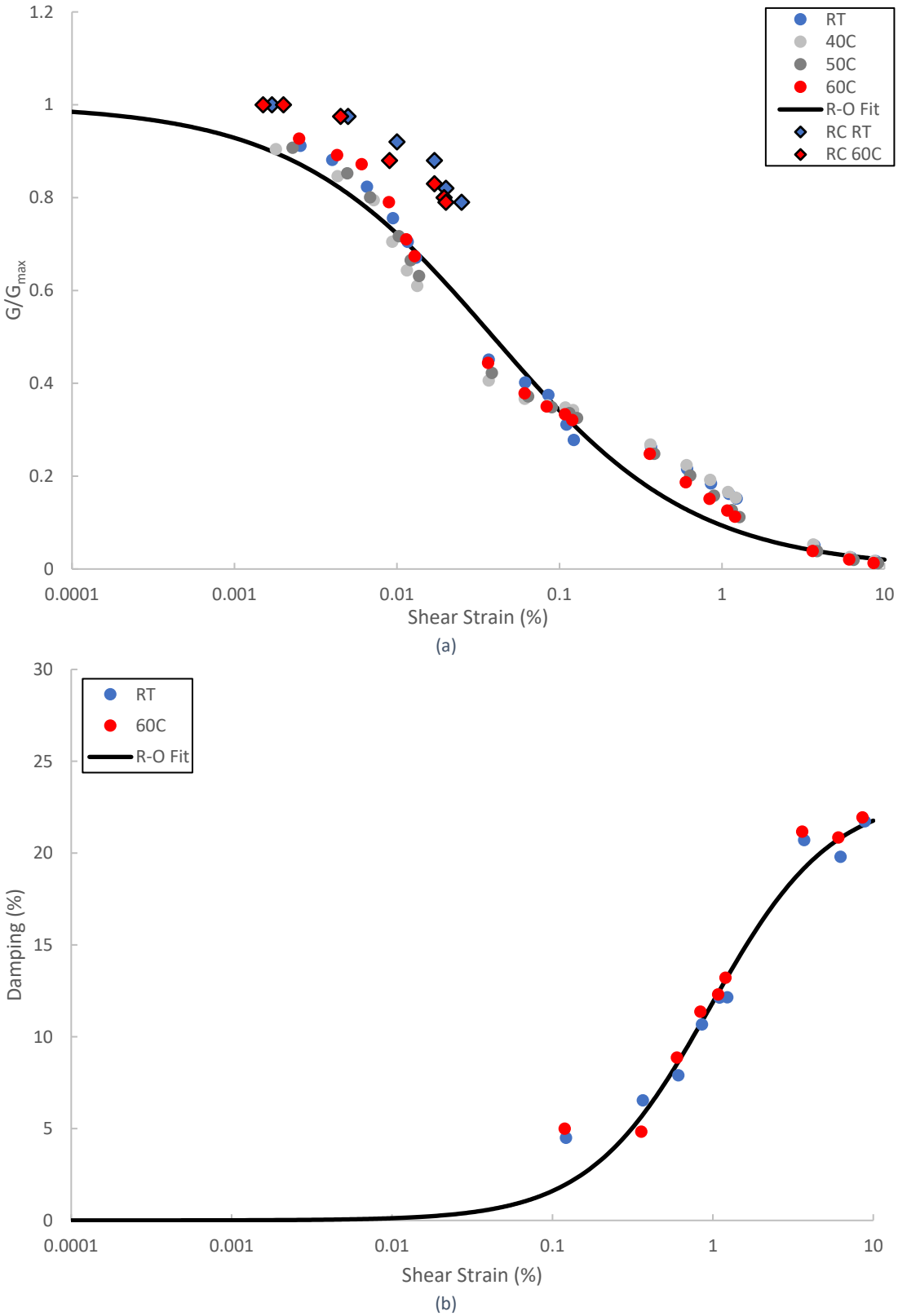

Figure 7.3: Thermal sensitivity of (a) shear modulus and (b) material damping degradation of CL Soil (w=17.0%) with increasing shear strain amplitude

7.5 - Shear Modulus and Material Damping Degradation of ML Soil (w=14.8%)

Figure 7.4 shows the shear modulus (a) and material damping (b) degradation curves for thermo-controlled CSS testing of silty soil (ML) samples compacted at optimum moisture content. Shear modulus degradation data is included for tests conducted at all temperature variations (RT, 40°C, 50°C, and 60°C). For silt, the degradation rate of shear modulus was greater for samples tested at 60°C versus samples tested at RT. This effect is clearly seen in Figure 7.4. At any shear strain amplitude, a soil sample heated to 60°C will experience a faster shear modulus degradation than a sample at RT. RT and 60°C RC data are also included. The RC data for silt did not show a noticeable effect of temperature.

For simplicity, material damping data is only included for the RT and 60°C tests for shear strain amplitudes greater than 0.1%. For shear strain amplitudes lower than 0.1%, the inconsistency of the hysteresis loops leads to excessive scattering of the damping data. Figure 7.4(b) shows that as temperature increases damping increases. The parameters used to best fit the R-O model to the shear modulus degradation and material damping data for RT and 60°C tests are shown in Table 7.4.

Table 7.4: Ramberg-Osgood Model Parameters for ML Soil (w=14.8%)

Normalized Shear Modulus				
	α	**C**	**R**	**γ_{max} (%)**
RT	0.25	0.0006	1.48	10.0
60C	0.38	0.0010	1.60	10.0
Damping Ratio (%)				
RT	3.0	0.4	2.1	10.0
60C	1.3	0.1	2.1	10.0

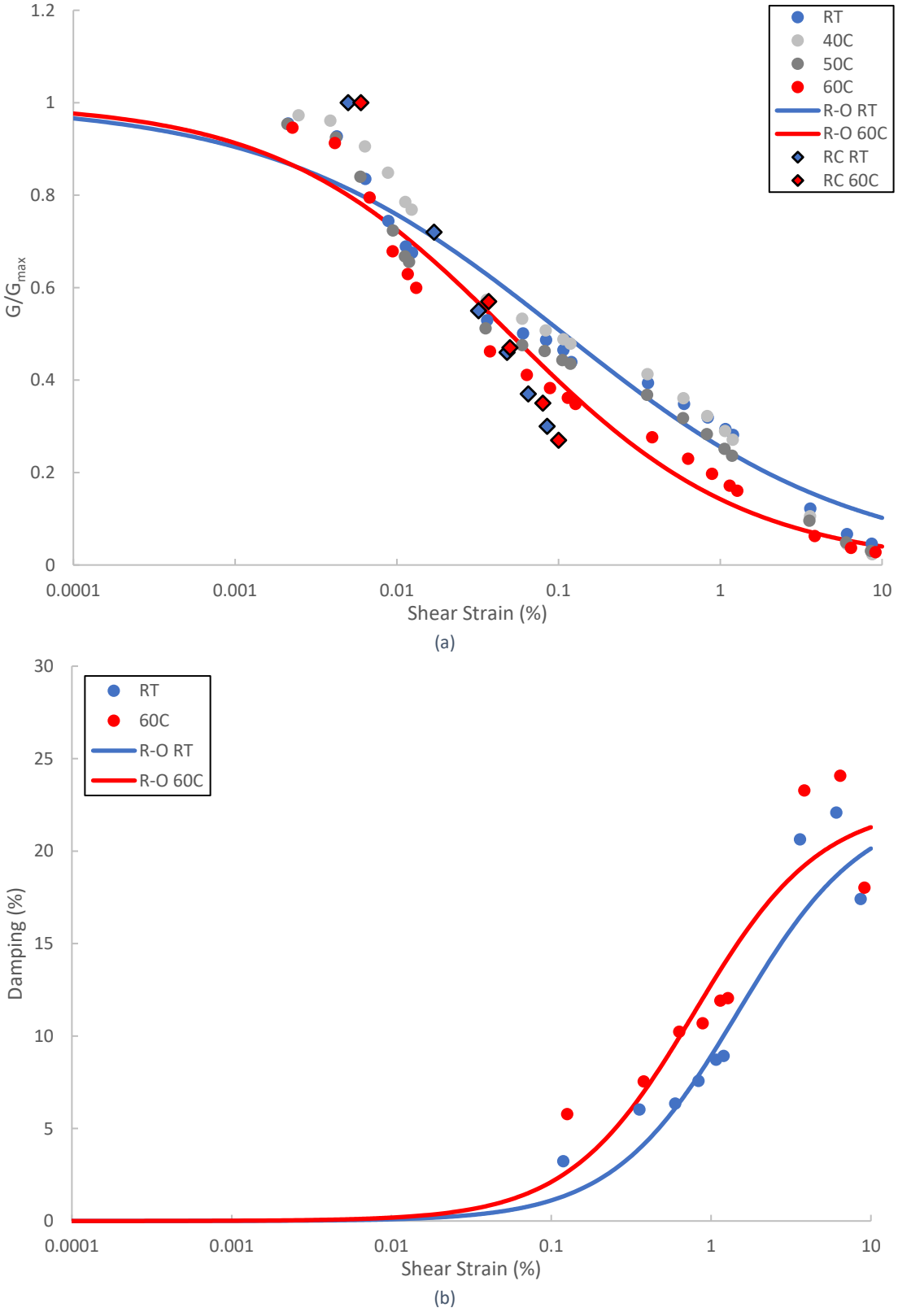

Figure 7.4: Thermal sensitivity of (a) shear modulus and (b) material damping degradation of ML Soil (w=14.8%) with increasing shear strain amplitude

7.6 - Shear Modulus and Material Damping Degradation of SC Soil (w=10.0%)

Figure 7.5 shows the shear modulus (a) and material damping (b) degradation curves for thermo-controlled CSS testing of sandy soil (SC) samples compacted at optimum moisture content. Shear modulus degradation data is included for tests conducted at all temperature variations (RT, 40°C, 50°C, and 60°C). For sand, the degradation rate of shear modulus was greater for samples tested at 60°C versus samples tested at RT. This effect is clearly seen in Figure 7.5. At any shear strain amplitude, a soil sample heated to 60°C will experience a faster shear modulus degradation than a sample at RT. RT and 60°C RC data are also included and shows a similar trend to the thermo-controlled CSS test data.

For simplicity, material damping data is only included for the RT and 60°C tests for shear strain amplitudes greater than 0.1%. For shear strain amplitudes lower than 0.1%, the inconsistency of the hysteresis loops leads to excessive scattering of the damping data. Figure 7.5(b) shows that as temperature increases damping increases. The parameters used to best fit the R-O model to the shear modulus degradation and material damping data for RT and 60°C tests are shown in Table 7.5.

Table 7.5: Ramberg-Osgood Model Parameters for SC Soil (w=10.0%)

Normalized Shear Modulus				
	α	**C**	**R**	**γ_{max} (%)**
RT	0.3	0.0007	1.55	10.0
60C	0.3	0.0008	1.80	10.0
Damping Ratio (%)				
RT	3.0	0.30	2.03	10.0
60C	3.0	0.15	1.95	10.0

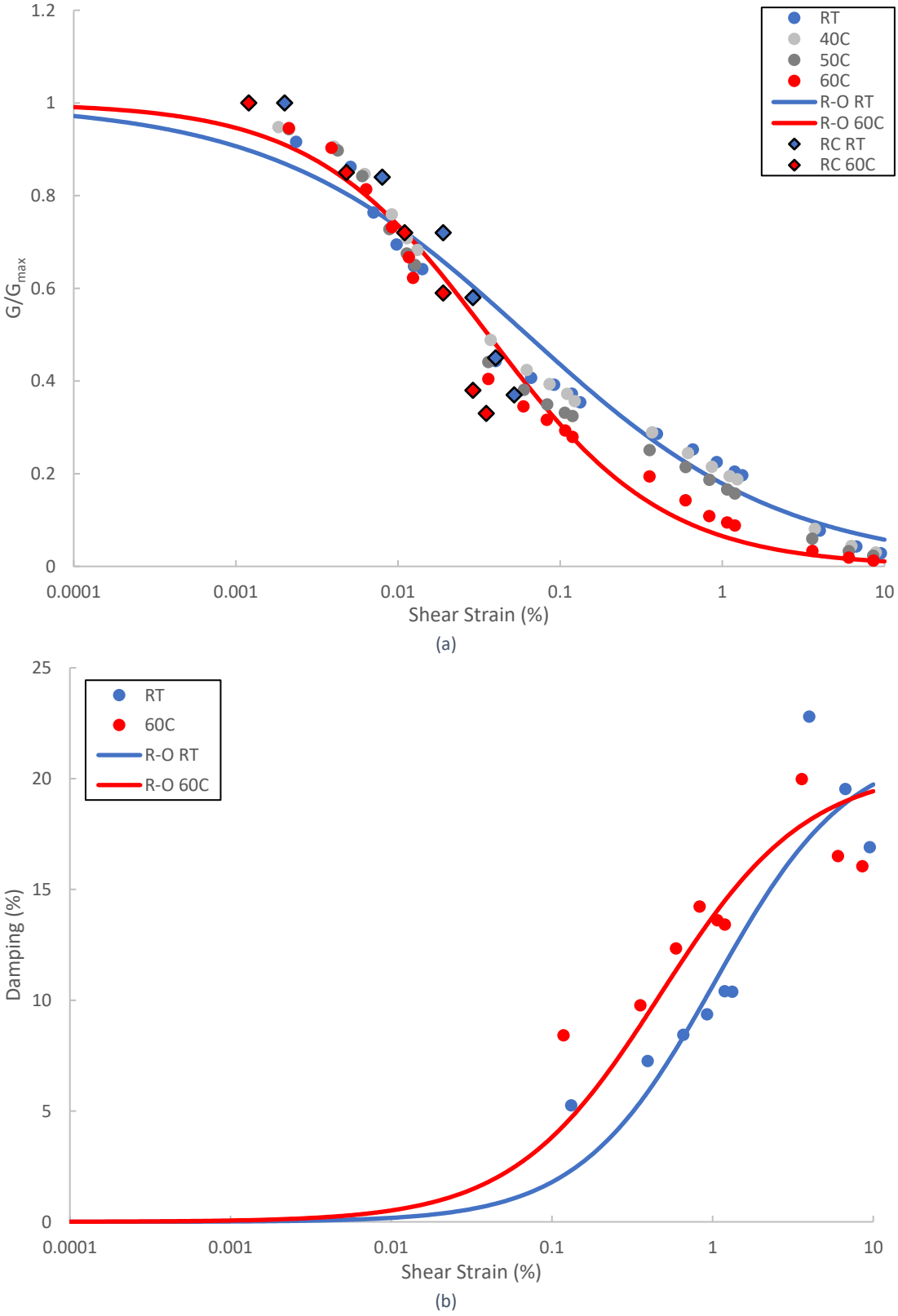

Figure 7.5: Thermal sensitivity of (a) shear modulus and (b) material damping degradation of SC Soil (w=10.0%) with increasing shear strain amplitude

Figure 7.6 shows RT and 60°C G/G_{max} data for all soil types. The data is plotted against the upper and lower bounds of the Wang and Borden 1996 figure of compiled shear modulus reduction data for various soil types. This is shown primarily to add validity to the present study by verifying the thermo-controlled CSS test data falls into the range of typically expected values.

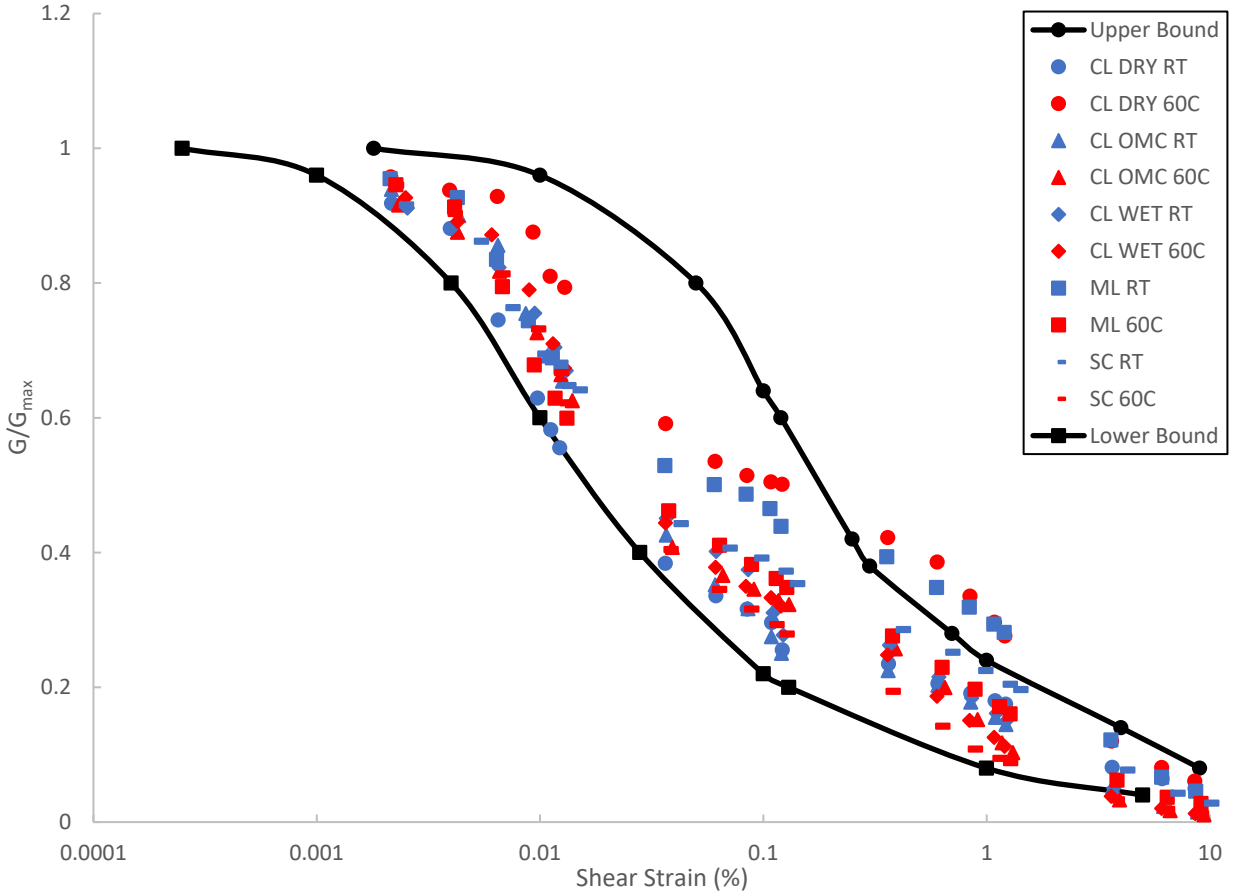

Figure 7.6: RT and 60°C G/G_{max} data for all soil types plotted against upper and lower bounds as defined by Wang and Borden. (Wang and Borden, 1996)

Chapter 8: Conclusions and Recommendations

A comprehensive series of thermo-controlled cyclic simple shear tests were conducted for small to large shear strain amplitudes (0.001% to 10.0%) to investigate the effects of temperature on the main dynamic properties of soils, shear modulus (G) and damping ratio (D). For the purposes of this study and future investigations, an existing CSS device was upgraded to allow for thermo-controlled testing. Calibration tests were performed to verify functionality of the newly adapted device. After demonstrating proper functionality, soil samples consisting of CL (w=9.0%), CL (w=13.6%), CL (w=17.0%), ML (w=14.8%), and SC (w=10.0%) were consolidated at 20 psi total vertical stress and heated to increasing temperatures of 23°C (RT), 40°C, 50°C, and 60°C prior to cyclic loading. All soil samples were subjected to the same thermo-stress history.

The influence of increased temperatures on shear modulus (G), shear modulus degradation (G/G_{max}), and damping ratio (D) were thoroughly documented via the experimental results presented in this study. A qualitative analysis of experiment data was aided by the use of the Bilinear and Ramberg-Osgood models. Parameter values for both models were included in the preceding chapters.

The main conclusions from both the thermo-calibration and thermo-controlled testing phases of this study can be summarized as follows:

1. Thermo-calibration data presented in Chapter 4 shows that the thermo-control function of the CSS device works properly. The device is capable of producing reasonably constant soil temperatures of 40°C, 50°C, and 60°C with virtually no temperature variation inside the soil sample.
2. In general, the experimental data showed that for a given shear strain amplitude, increased soil temperatures caused a significant decrease in peak shear stress and by extension shear modulus for all soil types. The detrimental effect of temperature on shear modulus was more pronounced at greater shear strain amplitudes (γ > 1.0%). Additionally, comparing CSS data for CL soil showed that the shear modulus reduction was greater in the dry samples (w=9.0%) than the wet samples (w=17.0%). The decrease in peak shear stress typically occurred between the first (N=1) and fifth (N=5) cyclic load applications for all soil types and temperature variations as generally observed from conventional cyclic loading testing on soils.
3. At large shear strain amplitudes (γ > 1.0%), hysteresis loops generated via cyclic load applications degrade significantly. Due to the excessive degradation, the secant shear modulus was not an accurate tool for comparison. To analyze stiffness of samples for large shear strain amplitudes the bilinear model proposed by Thiers and Seed (1968) was used. For all soil types, both the G_1 and G_2 parameters decreased as soil temperature increased. For a given temperature, the G_1 parameter remained relatively constant and the G_2 parameter significantly decreased with increasing shear strain amplitudes. The majority of the decrease in the G_1 and G_2 parameters occurred by the fifth (N=5) cyclic load application.
4. Thermal sensitivity trends varied between the soil types as shown in the shear modulus degradation data (G/G_{max}). For CL soil, dry samples showed a slower rate of shear modulus degradation at increased temperatures. Temperature did not appear to affect the degradation rate of shear modulus for optimum and wet samples. Thermal sensitivity was greater in the cohesionless soil samples. Both ML and SC samples showed faster shear modulus degradation rates under increased temperatures.

5. Material damping ratio was shown for room temperature (RT) and 60°C tests for all soil types. As expected, damping behaves inversely to shear modulus. For damping, a reduction in stiffness is characterized by an increase in damping ratio. The damping trends were similar to those observed in the shear modulus degradation data. For CL soil, dry samples showed a slight decrease in damping ratio at increased temperatures with optimum and wet samples showing no variation with temperature. Both ML and SC samples showed an increase in damping ratio for samples tested at increased temperatures.
6. All data, regardless of soil type or temperature, fall within the upper and lower bounds adapted from Wang and Borden (1996) for a wide variety of clayey, silty, and sandy soils under isothermal testing conditions.

Recommendations for further testing are given below.

1. The thermo-control method consisted of two heating elements inserted into the base of the CSS device. It was more economical to use existing heating elements present in the lab. However, the heating elements are too long for the device resulting in a significant length being exposed to the device operator. The elements are extremely hot prior to temperature equalization inside the chamber and could potentially be hazardous to the operator. An improved design incorporating appropriately sized heating elements would be safer for the device operator and increase thermal efficiency of the system.
2. In order to perform thermal calibration of the CSS device, the vertical loading assembly was removed to allow for insertion of thermocouple wire probes into the soil sample. This configuration allowed for the device to be filled with water as would be the case during testing, however, the device could not be pressurized in this state. Pressurized heating may produce slightly more accurate calibration data.
3. All tests were conducted at 20 psi total vertical stress, which is reasonably close to the typical average of overburden pressures reported in a wide variety of geosystems subject to thermal gradients in the field. Future testing should investigate thermal sensitivity for various total vertical stress values.
4. Due to scattering, damping ratio values for small shear strain amplitudes ($\gamma < 0.1\%$) was difficult to determine from raw data. Furthermore, the hysteresis loop degradation for larger shear strain amplitudes ($\gamma > 4.0\%$) caused similar problems. This problem could be mitigated with the modified Ramberg-Osgood model. Masing's criteria allows the R-O model to procedurally generate hysteresis loops that may assist in damping calculations. The Bilinear model could be another potential solution. The representative parallelograms used to determine G_1 and G_2 could also be used to calculate a slightly over-estimated area of the hysteresis loop.
5. Due to limitations of the CSS device, rather small strain shear modulus G_{max} could not be obtained experimentally. Improvements in mechanical precision of the horizontal servo could increase accuracy at small shear strain amplitudes ($\gamma < 0.001\%$).

References

[1] Ahmad, M., & Ray, R. (2021). Comparison between Ramberg-Osgood and Hardin-Drnevich soil models in Midas GTS NX. *Pollack Periodica*, 16(3), 52-57.

[2] Al-Hunaidi, M. O., Chen, P. A., Rainer, J. H., & Tremblay, M. (1996). Shear moduli and damping in frozen and unfrozen clay by resonant column tests. *Canadian Geotechnical Journal*, *33*(3), 510-514.

[3] Alsherif, N. A., & McCartney, J. S. (2015). Yielding of Silt at High Temperature and Suction Magnitudes. *Geotechnical and Geological Engineering,34*(2), 501-514. doi:10.1007/s10706-015-9961-x

[4] Anderson, D. G., & Stokoe, K. H. (1977). Shear Modulus: a Time-Dependent soil property. *Dynamic Geotechnical Testing*, STP 654, 66–90. https://doi.org/10.1520/STP35672S

[5] Ashmawy, A. K.; Salgado, R.; Guha, S.; and Drnevich, V. P. (1995). Soil Damping and Its Use in Dynamic Analyses. *International Conferences on Recent Advances in Geotechnical Earthquake Engineering and Soil Dynamics. 9*. http://scholarsmine.mst.edu/icrageesd/03icragees d/session01/9

[6] Bilesavar, R. D. (2020). Dynamic properties of cohesive-frictional soils via thermo-controlled resonant column testing (Doctoral dissertation, The University of Texas at Arlington).

[7] Cekerevac, C., & Laloui, L. (2004). Experimental study of thermal effects on the mechanical behaviour of a clay. *International Journal for Numerical and Analytical Methods in Geomechanics,28*(3), 209-228. doi:10.1002/nag.332

[8] Cekerevac, C., Laloui, L., & Vulliet, L. (2005). A Novel Triaxial Apparatus for Thermo-Mechanical Testing of Soils. *Geotechnical Testing Journal,28*(2), 161-170. doi:10.1520/gtj12311

[9] Cooper, P., Grubelich, M. C., & Bauer, S. J. (2011, September). Potential Hazards of Compressed Air Energy Storage in Depleted Natural Gas Reservoirs. U.S. Department of Energy. https://doi.org/10.2172/1029814

[10] Darendeli, M. B., Stokoe, K. H., II, & Rathje, E. M. Importance of confining pressure on nonlinear soil behavior and its impact on earthquake response predictions of deep sites. *15th International Conference on Soil Mechanics and Foundation Engineering*.

[11] Das, B. M. (1992). Principles of Soil Dynamics (1st ed.). PWS-KENT.

[12] Dobry, R. & Vucetic, M. (1987). Dynamic properties and seismic response of soft clay deposits.

[13] Fichman, B. T. (2012, September). *Annual Energy Review 2011*. https://doi.org/10.2172/1212312

[14] Ghasemi-Fare, O., & Basu, P. (2016). Predictive assessment of heat exchange performance of geothermal piles. *Renewable Energy,86*, 1178-1196. doi:10.1016/j.renene.2015.0 8.078

[15] Guo, Y., Golchin, A., Hicks, M. A., Liu, S., Zhang, G., & Vardon, P. J. (2023). Experimental investigation of soil–structure interface behaviour under monotonic and cyclic thermal loading. *Acta Geotechnica*, 1-24.

[16] Hardin, B. D., & Drnevich, V. P. (1972). Shear modulus and damping in soils: Measurement and parameter Effects. *Journal of the Soil Mechanics and Foundations Division*, 98(6), 603–624. https://doi.org/10.1061/jsfeaq.0001756

[17] IRENA and IGA (2023), Global geothermal market and technology assessment, International Renewable Energy Agency, Abu Dhabi; International Geothermal Association, The Hague.

[18] Kuntiwattanakul, P., Towhata, I., Ohishi, K., & Seko, I. (1995). Temperature effects on undrained shear characteristics of clay. *Soils and Foundations*, 35(1), 147–162. https://doi.org/10.3208/sandf1972.35.147

[19] Lanzo, G., & Vucetic, M. (1999). Effect of Soil Plasticity on Damping Ratio at Small Cyclic Strains. *Soils And Foundations,39*(4), 131-141. doi:10.3208/sandf.39.4_131

[20] Le, K. N. & Ghayoomi, M. Suction-controlled dynamic simple shear apparatus for measurement of dynamic properties of unsaturated soils. (2016).

[21] Matek, B. (2013). 2013 Annual US Geothermal Power Production and Development Report. Geothermal Energy Association. http://geo-energy.org/reports.aspx

[22] Matek, B. (2013). 2013 Geothermal Power: International Market Overview. Geothermal Energy Association. http://geo-energy.org/reports.aspx

[23] Matek, B. (2016). 2016 Annual US & Global Geothermal Power Production Report. Geothermal Energy Association. http://geo-energy.org/reports.aspx

[24] Meidani, M., Shafiei, A., Habibagahi, G., Jafari, M. K., Mohri, Y., Ghahramani, A., & Chang, C. S. (2008). Granule shape effect on the shear modulus and damping ratio of mixed gravel and clay. *Iranian Journal of Science and Technology Transaction B-engineering 32* (2008): 501-518.

[25] Mortezaie, A. R., & Vucetic, M. (2013). Effect of frequency and vertical stress on cyclic degradation and pore water pressure in clay in the NGI simple shear device. *Journal of Geotechnical and Geoenvironmental Engineering*, 139(10), 1727-1737.

[26] Ng, C.W.W. & Zhou, C. (2014). Cyclic behaviour of an unsaturated silt at various suctions and temperatures. *Géotechnique*. 64. 709-720. 10.1680/geot.14.P.015.

[27] Nong Z, Park S.S., Jeong S.W., Lee D.E. Effect of Cyclic Loading Frequency on Liquefaction Prediction of Sand. *Applied Sciences*. 2020; 10(13):4502. https://doi.org/10.3390/app10134502

[28] Normandeau, D. E. & Zimmie, T. F., The Effect of Frequency of Cyclic Loading on Earth Structures and Foundation Soils (1991). *International Conferences on Recent Advances in Geotechnical Earthquake Engineering and Soil Dynamics*. 39. https://scholarsmine.mst.edu/icrageesd/02icrageesd/session01/39

[29] Olgun, G., Ozudogru, T., Abdelaziz, S., & Senol, A. (2015). Long-term performance of heat exchanger piles. *Acta Geotechnica*. 10. 553-569. doi:10.1007/s11440-014-0334-z.

[30] Ramberg, W., & Osgood, W. R. (1943). Description of stress-strain curves by three parameters (No. NACA-TN-902).

[31] Shahbaz, Chaudhry Muhammad, Effect of saturation and plasticity on dynamic properties of silt" (1993). Masters Theses. 1271.

[32] Silver, M., & Seed, B. Volume Changes in Sands During Cyclic Loading. *Journal of the Soil Mechanics and Foundations Division*, vol. 97, no. 9, Sept. 1971, pp. 1171–82. American Society of Civil Engineers, https://doi.org/10.1061/JSFEAQ.0001658.

[33] Song, B., Chen, W., Wu, W., & Jiang, Y. Experimental study on the dynamic properties of sliding zone soil of a landslide under varying water content. *China Earthq. Eng*. J. 2017, 39, 744–758. (In Chinese).

[34] Stewart, J., Kioumars, A., & Hashash, Y.M.A.. (2014). Guidelines for performing hazard-consistent one-dimensional ground response analysis for ground motion prediction. ResearchGate.

[35] Suprunenko, G. (2015). Suction-controlled cyclic triaxial test to measure strain-dependent dynamic shear modulus of unsaturated sand (Doctoral dissertation, University of New Hampshire).

[36] Tang, A., Cui, Y., & Barnel, N. (2007). A New Isotropic Cell for Studying the Thermo-Mechanical Behavior of Unsaturated Expansive Clays. *Geotechnical Testing Journal,30*(5), 341-348. doi:10.1520/gtj100623

[37] Thiers, G. R., & Seed, H. B. (1968). Cyclic Stress-Strain Characteristics of Clay. *Journal of the Soil Mechanics and Foundations Division*, 94(2), 555–569. https://doi.org/10.1061/jsfeaq.0001110

[38] 20% Wind Energy by 2030: Increasing Wind Energy's Contribution to U.S. Electricity Supply. U.S. Department of Energy, 1 July 2008, https://doi.org/10.2172/1216732.

[39] Uchaipichat, A., & Khalili, N. (2009). Experimental investigation of thermo-hydro-mechanical behaviour of an unsaturated silt. *Géotechnique,59*(4), 339-353. doi:10.1680/geot.2009.59.4.339

[40] Ueng, T. S., & Chen, J. C. (1992). Computational procedures for determining parameters in Ramberg-Osgood elastoplastic model based on modulus and damping versus strain (No. UCRL-ID-111487). *Lawrence Livermore National Lab*. (LLNL), Livermore, CA (United States).

[41] U.S. Energy Information Administration - EIA - independent statistics and analysis. Electricity generation from wind - U.S. Energy Information Administration (EIA).

[42] Vassallo, R., Mancuso, C., & Vinale, F. (2007). Effects of net stress and suction history on the small strain stiffness of a compacted clayey silt. *Canadian Geotechnical Journal,44*(4), 447-462. doi:10.1139/t06-129

[43] VJ Tech Limited: Soil and Rock Testing Equipment. (2023). https://www.vjtech.co.uk/

[44] Vucetic, M., & Dobry, R. (1991). Effect of Soil Plasticity on Cyclic Response. *Journal of Geotechnical Engineering,117*(1), 89-107. doi:10.1061/(asce)0733-9410(1991)117:1(89)

[45] Wang, C. E., & Borden, R. H. (1996). Deformation characteristics of Piedmont residual soils. *Journal of Geotechnical Engineering*, 122(10), 822-830.

[46] Yu, X., Sun, R., Yuan, X., Chen, Z., & Zhang, J. Resonant Column Test on the Frozen Silt Soil Modulus and Damping at Different Temperatures, *Periodica Polytechnica Civil Engineering*, 61(4), pp. 762–769, 2017. https://doi.org/10.3311/PPci.10349

[47] Zhang, D., Liu, S., & Zhang, T. Water content and modulus relationship of a compacted unsaturated soil. J. Southeast Univ. 2012, 28, 209–214.

[48] Zhang L, Zhang S, Liu X, & Sun Y. Characterizing the Effect of Water Content on Small-Strain Shear Modulus of Qiantang Silt. *Journal of Marine Science and Engineering*. 2021; 9(12):1363. https://doi.org/10.3390/jmse9121363

[49] Zhou, Y., Deng, Z., Fan, Z., & Liu, W. (2021b). Shear Strength Deterioration of Compacted Residual Soils under a Wind Turbine due to Drying-Wetting Cycles and Vibrations. *Advances in Civil Engineering*, 2021, 1–10. https://doi.org/10.1155/2021/8628842

[50] Zhou, Y., Li, M., He, Q., & Wen, K. (2018). Deformation and Damping Characteristics of Lightweight Clay-EPS Soil under Cyclic Loading. *Advances in Civil Engineering*. https://doi.org/10.1155/2018/8093719